

Laminate Integration Platforms for Millimeter-Wave RoF Photodiode Modules

Von der Fakultät für Ingenieurwissenschaften
Abteilung Elektrotechnik und Informationstechnik
der Universität Duisburg-Essen

zur Erlangung des akademischen Grades
Doktor der Ingenieurwissenschaften

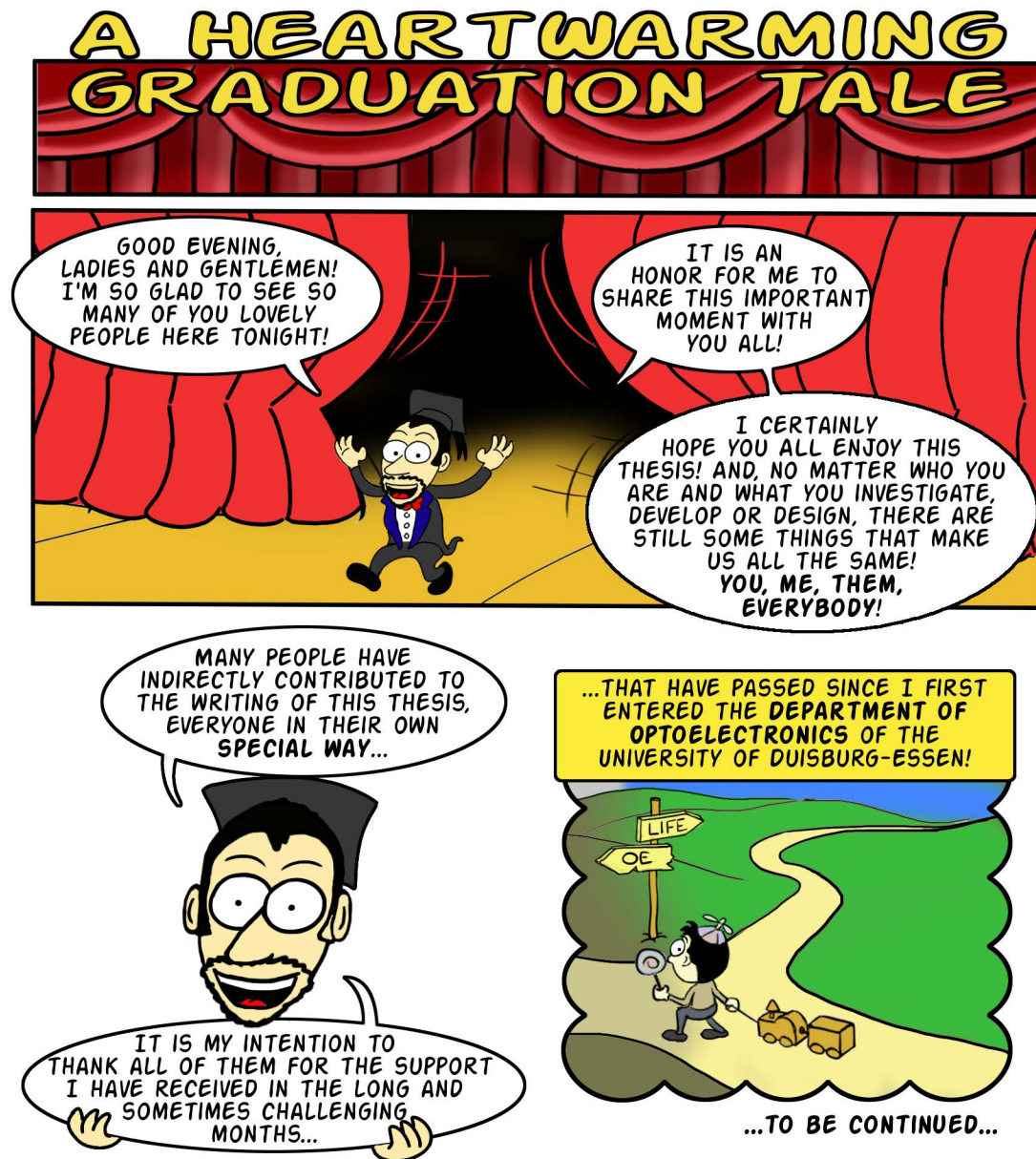
genehmigte Dissertation

von
Ivan Flammia
aus
Avellino

Gutachter: Prof. Dr.-Ing. Andreas Stöhr
Gutachter: Prof. Dr.-Ing. Klaus Solbach

Tag der mündlichen Prüfung: 31.03.2017

Acknowledgment



The writing of this thesis has been one of the most *inspiring* events in my life. The *very special* people who crossed my path sprinkled it with *academic*, *intercultural*, and *social epiphanies*, leading to an intense inner analysis and existential questions, such as:

Acknowledgment

How many mattresses per year does the average German buy?

Will I ever be able to integrate if I don't get a tattoo?

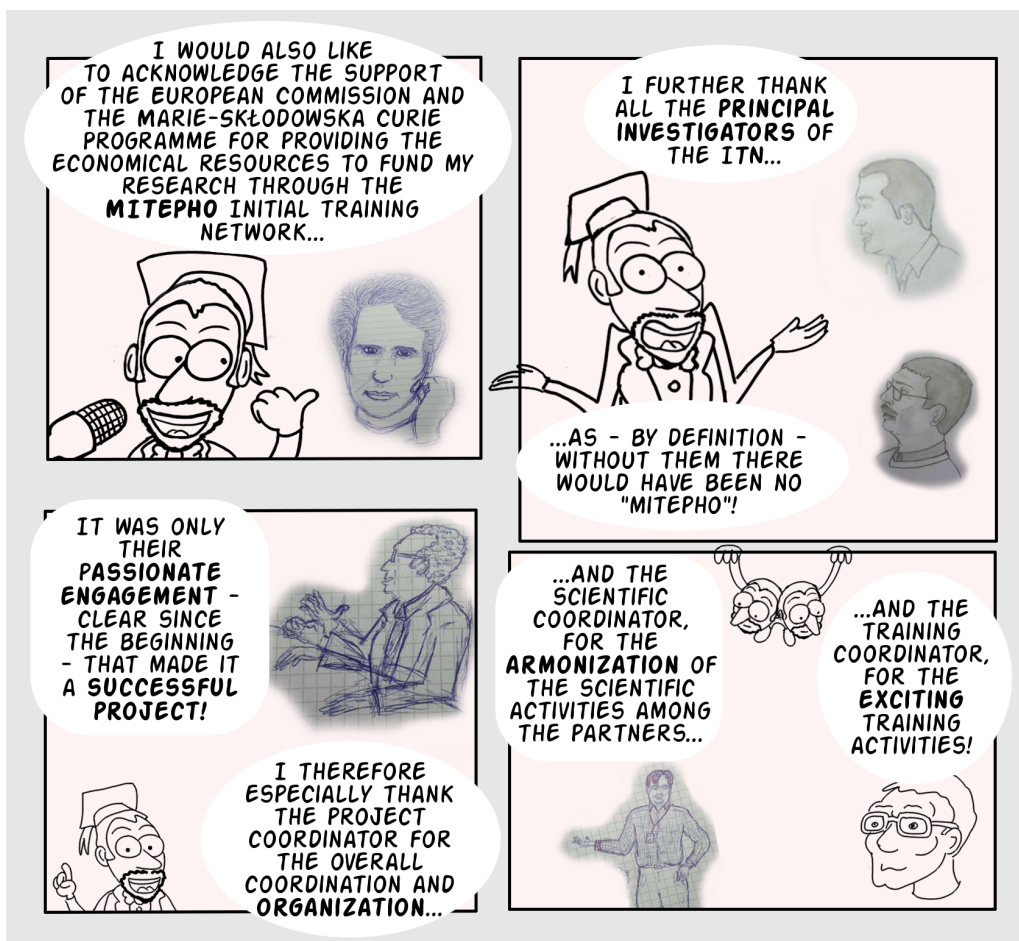
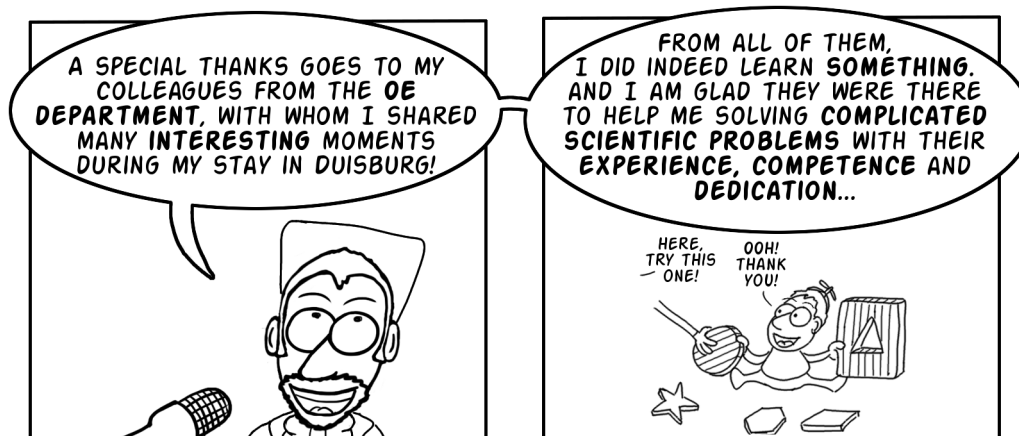
Should I buy an Audi to drive to the closest Lidl, so that I can save 10 cents off the bread?

Why didn't I choose sports science?

This surrealist melting pot of implausible events, disorienting discoveries, and pleasant surprises triggered a cathartic process culminated in the writing and drawing of a short comics story, which is my most heartfelt *creation* to date and whose first page opens this *Acknowledgment* section. Some other excerpts can be found at the bottom of this text. Hence, I wish to thank everyone who - to any extent - has been an inspirational source in these years:

Thank You for Your advice, obstacles, help, incitements, scoldings, entertainment, challenges, and support!





*Ivan Flammia
Duisburg, Germany
April 2017*

Abstract

This thesis investigates the potential offered by cost-effective printed circuit technology (PCT) for the packaging of mm-wave photodiode (PD) modules, as an alternative to the commonly used integration approaches based on thin or thick-film ceramic manufacture.

We will therefore analyze the limitations imposed by this technology, focusing on the loss mechanisms and the theoretical frequency limits due to the physical properties of the laminates, as well as limitations imposed by the achievable resolution, tolerances and manufacturing steps of printed circuit board (PCB) development processes.

We will then consider traditional planar transmission lines (PTL), in particular microstrips and grounded coplanar waveguides (GCPW), and the innovative substrate integrated waveguide (SIW), highlighting their characteristics and performance. We will show that via holes play a fundamental role, as they ultimately decide the highest possible frequency, independently of other parameters like conductor and dielectric loss, or etching inaccuracies. In fact, they are vital to guarantee a correct functioning of both GCPW and SIW, by avoiding board resonances and interferences between different lines. We will show that the current PCB via-hole technology allows the development of circuits working up to at least the upper limit of the W-band.

As microstrips are subject to higher radiation in the mm-wave region, GCPWs will be preferred for practical applications, also by virtue of their other practical advantages, such as easily accessible ground planes, increased design freedom, and extended impedance range. We will thus introduce the first concept of mm-wave PD modules with rectangular waveguide (WR) output for E-band Radio-over-Fiber (RoF) applications based on PCT integration boards. A particular feature of the proposed integration approach, is that a photonic transmitter can conveniently be assembled without any mechanical modifications of the WR, using standard off-the-shelf WR components, therefore simplifying the assembly process and reducing the cost of the module. We will also show that the availability of laminates with low moisture absorption as dielectric carrier furthermore opens up the possibility to develop quasi-hermetic packages without the need of dedicated radomes to seal the WR opening. The developed PD module will be used in mm-wave RoF demonstrators in order to prove the suitability of our approach for the development of commercial communication systems: We will be able to show a successful, *error-free*, 1-Gb/s, wireless connectivity in the 70-GHz communication band, with a power penalty limited to 1.5 dB.

We will also present several additional prototypes, which include dedicated, on-board biasing circuits, to allow integration of in-house-developed PDs and commercial amplifiers, and other solutions to reduce the loss of the signal power.

In order to overcome the shortcomings of microstrips and GCPWs, such as unwanted radiation and increased power dissipation due to high current densities, we will then intro-

duce for the first time the PCB SIW in the packaging of mm-wave photonic transmitters. The properties and advantages of this innovative transmission line in terms of low loss and high integration will be investigated and assessed, showing that its unique configuration allows a superior control of radiation and interferences, and drastically reduces losses. This suggests its use in all mm-wave systems where long on-board interconnects are required.

A new integration approach for the development of quasi-hermetic PD modules with in-package antennas based on PCB SIW will thus be presented, focusing in particular on non-directive data distribution systems. It will be shown that compact, low-loss, and quasi-hermetic packaging solutions can conveniently be designed making use of the SIW.

We will introduce and experimentally validate innovative GCPW-to-SIW transitions necessary for the integration of PD on SIW platforms, and specifically optimized for operation in the 60-GHz band. Design and optimization of mm-wave antennas for indoor RoF systems will be presented, testing their performance against PCB manufacture inaccuracies. Finally we will show an example of a fully characterized integration platform for PD modules, confirming the suitability of PCB SIW for the development of future, low-loss, and cost-effective RoF transmitters.

Contents

Acknowledgment	i
Abstract	v
1 Introduction	1
1.1 Broadband Wireless Access Demand	1
1.2 Millimeter-Wave Spectrum Allocation and Regulations	3
1.2.1 60-GHz Band	5
1.2.2 70/80-GHz Band	5
1.2.3 Other Bands	6
1.3 Radio-over-Fiber Technology for Millimeter-Wave Communication Systems	6
1.4 Photonic Transmitters	8
1.5 Aim and Organization of the Thesis	10
1.6 Projects	12
2 Constituents of Millimeter-Wave Photonic Transmitters	13
2.1 Guided Electromagnetic Propagation	13
2.1.1 General Loss Considerations	13
2.1.2 Rectangular Waveguide	16
2.1.3 Coaxial Cable	19
2.1.4 Microstrip Line	21
2.1.5 Grounded Coplanar Waveguide	28
2.1.6 Substrate Integrated Waveguide	30
2.1.7 Optical Fiber	35
2.2 Millimeter-Wave Photodiodes	38
2.2.1 pin-Photodiodes	40
2.2.2 Uni-Travelling Carrier Photodiodes	42
2.2.3 Travelling-Wave Photodiodes	42
2.3 Millimeter-Wave Amplifiers	42
2.4 Antennas	44
2.4.1 On-chip Antennas	44
2.4.2 In-Package Antennas	47
2.4.3 External Antennas	47
2.5 Conclusions	49
3 Hybrid Optoelectronic Integration Technologies	51
3.1 Optical Issues	52
3.2 Monolithic vs. Hybrid Integration	52

3.3	Dielectric Materials for Integration Platforms	53
3.3.1	Electrical Properties	53
3.3.2	Thermal Properties	54
3.3.3	Mechanical Properties	55
3.3.4	Hermeticity	55
3.3.5	Ceramics	55
3.3.6	Laminates	56
3.4	Processing Technologies	57
3.4.1	Thick-Film Technology	57
3.4.2	Thin-Film Technology	57
3.4.3	Co-Fired Ceramics	58
3.4.4	Printed Circuit Technology	59
3.4.5	Modeling PCT Lines for mm-Wave Applications	64
3.5	Bonding Technologies	67
3.5.1	Bond Wires and Bond Ribbons	67
3.5.2	Flip-Chip Bonding	69
3.5.3	Other Interconnecting Techniques	70
3.6	Module Housing	71
3.7	Conclusions	72
4	PCB Integration Platforms for mm-Wave Photodiodes Modules with Rectan- gular Waveguide Output	75
4.1	Photodiode Module with Rectangular Waveguide Output	75
4.2	Quasi-Hermetic GCPW-to-WR Transition	76
4.2.1	Transition with Built-In Planar Bias Network	86
4.3	Photonic Transmitters with Rectangular Waveguide Output	91
4.3.1	Integration of Commercial Photodiode	91
4.3.2	Integration of In-House-Developed Photodiodes	95
4.3.3	Concept for the Integration of On-Board Amplification	98
4.4	Conclusions	101
5	PCB Substrate Integrated Waveguide Technology for 60-GHz Optoelectronic Integration	105
5.1	60-GHz Indoor Data-Distribution System Concept	105
5.2	Technical Considerations for the Design of SIW Platforms	106
5.3	60 GHz GCPW-to-SIW Transitions	107
5.3.1	Transition with Integrated Planar Bias-Tee	109
5.4	60 GHz SIW H-Plane Horn Antennas	112
5.4.1	Standard SIW H-Plane Horn Antenna	112
5.4.2	Improved SIW H-Plane Horn Antenna	112
5.5	60 GHz SIW Integration Platform	122
5.6	Conclusions	124
6	Summary and Outlook	129

Bibliography	133
Appendix A Electromagnetic Theory	155
A.1 Maxwell's Equations	155
A.2 Electromagnetic Waves	157
A.3 Guided Electromagnetic Propagation	158
A.4 Microstrip Coupled Lines	161
A.5 Antennas	162
Appendix B Layouts of GCPW-to-WR Transitions	165
B.1 GCPW-to-WR-12 Transition	165
B.2 GCPW-to-WR-12 Transition with Bias Tee	166
Appendix C Layouts of SIW Designs	169
C.1 GCPW-to-SIW Transition with Tapered Line	169
C.2 GCPW-to-SIW Transition with Bias-Tee	169
C.3 Standard H-Plane SIW Horn Antenna	170
C.4 SIW H-Plane Horn Antennas with Matching Irises	171
C.4.1 SIW H-Plane Horn Antennas with External Iris	171
C.4.2 SIW H-Plane Horn Antennas with Internal Iris	172
Appendix D Calibration Sets	173
D.1 Calibration Set 1	173
D.2 Calibration Set 2	173
D.3 Calibration Set 3	174
Biography	175
List of Publications	177

List of Tables

2.1	Skin depth of several conductors at 50 GHz.	16
2.2	Critical frequencies of parasitic modes in microstrip lines.	28
2.3	Characteristic impedance Z_0 of several SIW configurations.	33
2.4	Energy band-gap and maximum absorbed wavelength of different semiconductor compounds.	38
4.1	Comparison of integration techniques for mm-wave PD modules.	102
5.1	Characteristics of the presented SIW antennas.	118

List of Figures

1.1	High-data-rate wireless scenario.	2
1.2	WLAN and WPAN data rates and ranges	3
1.3	Total propagation loss for different frequencies.	4
1.4	Typical RoF link.	7
1.5	Block diagramm of photonic transmitter.	8
2.1	Loss tangent.	14
2.2	Surface current density and skin depth.	15
2.3	Rectangular waveguide.	16
2.4	Electric and magnetic fields in a WR-12.	18
2.5	Propagation constant in WR-15.	18
2.6	Attenuation constant in WRs.	20
2.7	Impact of metal roughness on attenuation of WR-12.	20
2.8	Geometry of coaxial cable.	21
2.9	Model of microstrip line.	22
2.10	Effective permittivity and attenuation constant of microstrip lines.	23
2.11	Impact of surface roughness on conductor loss in microstrips.	25
2.12	Microstrip attenuation constant for different surface roughnesses.	25
2.13	GCPW model.	29
2.14	Effective permittivity and attenuation constant of GCPW.	30
2.15	SIW model.	31
2.16	Propagation and attenuation constant and S-parameters of SIW.	32
2.17	Field width modulation in SIW.	33
2.18	SIW attenuation constant for different substrate thickness and metal surface roughness.	34
2.19	SIW: Regions of operation.	36
2.20	Impact of via holes pitch on the SIW insertion loss.	36
2.21	Working principle of a PD.	39
2.22	Coplanar output contacts of PD.	40
2.23	pin PD.	41
2.24	Layer structure of HEMT amplifier.	43
2.25	Microstrip patch antenna.	45
2.26	Broadband planar antennas.	46
2.27	Horn antennas.	48
2.28	Feeding techniques for parabolic reflector antennas.	49
2.29	Gain of parabolic antennas.	50
3.1	Impact of line-width tolerance on characteristic impedance of GCPW.	61

3.2	Impact of substrate thickness on characteristic impedance of GPCW.	61
3.3	Configuration of via holes on the lateral ground plate of GCPW.	63
3.4	SIW for operation above 100 GHz.	64
3.5	Insertion loss of PCB GCPW at 70 GHz.	65
3.6	Insertion loss of PCB SIW at 60 GHz.	66
3.7	Bond wires and bond ribbons.	67
3.8	Maximum allowed length of mm-wave bonds.	68
3.9	Flip-chip interconnect.	69
3.10	MicroCoax interconnect.	71
4.1	Integration concept for a PD module with WR output.	76
4.2	GCPW-to-WR-12 transition.	77
4.3	GCPW-to-WR transition: Working principle.	78
4.4	GCPW-WR-12 transition: Model and simulation.	79
4.5	Propagation of the electric field in the GCPW-to-WR-12 transition.	80
4.6	Impact of misalignment on GCPW-to-WR-12 transition.	80
4.7	Manufactured GCPW-to-WR12 transition.	81
4.8	GCPW-to-WR-12 and to GCPW-to-WR-15 transitions: S-parameters.	81
4.9	GCPW-to-WR transition: Experimental validation.	82
4.10	Simulated and measured S-parameters of B2B GCPW-to-WR transition (setup 1).	83
4.11	Model of the B2B transition and measurement setup (setup 2).	84
4.12	Simulated and measured S-parameters of B2B transition (setup 2).	84
4.13	Impact of via holes on B2B transition (setup 2).	85
4.14	GCPW-to-WR transition with backshort.	86
4.15	GCPW-to-WR transition with metal lid.	87
4.16	B2B transition with metal lids: Measured S-parameters (setup 2).	87
4.17	Implementation of metal lid in packages.	88
4.18	GCPW-to-WR-12 transition with built-in planar bias tee.	89
4.19	Simulated and measured S-parameters of RF-choke.	90
4.20	B2B GCPW-to-WR-12 transition with bias tee: Measured S-parameters (setup 1).	91
4.21	PD module: Simulated S-parameters.	92
4.22	Pigtailed PT.	93
4.23	Experimental B2B RoF setup and BER measurements.	94
4.24	Experimental wireless RoF setup and BER measurements.	95
4.25	PD module based on in-house-developed PD: Model and simulations.	96
4.26	Prototype of PD module based on in-house-developed PD.	97
4.27	Measurement setup for PD module with integrated bias tee.	98
4.28	Integration concept for amplifiers.	99
4.29	Integration of MPA.	99
4.30	Integration of LNA.	100
4.31	PD module with integrated LNA.	100
4.32	Platforms for integration of LNA and MPA.	101

5.1	Concept for 60-GHz photonic transmitter based on SIW.	105
5.2	60-GHz indoor distribution system	106
5.3	GCPW-to-SIW transition with tapered line.	108
5.4	B2B tapered GCPW-to-SIW transition: Simulations and measurements. . .	108
5.5	GCPW-to-SIW transition with DC-block.	110
5.6	GCPW-to-SIW transition with fully planar bias tee.	111
5.7	GCPW-to-SIW transitions with bias tee: Measured S-parameters.	111
5.8	SIW integration platform: Block diagram.	112
5.9	Standard SIW H-plane horn antenna.	113
5.10	SIW antenna with two-block parallel-plate resonator.	114
5.11	SIW antenna with two-block parallel-plate resonator for optimum FTBR. .	115
5.12	SIW antenna with two-block transition for optimum FTBR: Simulated and measured S_{11}	115
5.13	SIW antenna with two-block parallel-plate resonator and inductive iris. . .	117
5.14	SIW antenna with two-block transition and inductive iris: Measurements. .	118
5.15	SIW antenna with grating transition.	119
5.16	SIW antenna with grating transition: Radiation patterns.	120
5.17	SIW Antenna with grating transition: S_{11} measurements.	121
5.18	SIW antenna with grating transition: Measured radiation pattern (60 GHz).	123
5.19	SIW integration platform: S_{11} measurements.	125
A.1	Loss tangent.	157
A.2	Transmission line concept.	159
A.3	Coupled-lines transformer.	161
A.4	Antenna concept.	162
B.1	Layout of GCPW-to-WR-12 transition.	165
B.2	Layout of GCPW-to-WR-12 transition with bias tee.	166
C.1	Layout of tapered GCPW-to-SIW transition.	169
C.2	Layout of GCPW-to-SIW transition with bias tee.	170
C.3	Layout of standard SIW H-plane horn antenna.	171
C.4	Layout of SIW H-plane horn antenna with external matching iris.	171
C.5	Layout of SIW H-plane horn antenna with internal matching iris.	172
D.1	Calibration set 1.	173
D.2	Calibration set 2.	174
D.3	Calibration set 3.	174

Acronyms and Symbols

Abbreviations

ASIG	Autocatalytic Silver Immersion Gold
ASE	Amplified Spontaneous Emission
B2B	Back-To-Back
BER	Bit-Error-Rate
BS	Base Station
BboF	Baseband-over-Fiber
CPW	Coplanar Waveguide
CTE	Coefficient of Thermal Expansion
DAS	Distributed Antenna System
DC	Direct Current
DF	Dissipation Factor
DSB-SC	Double-Sideband Suppressed-Carrier
E-Band	60-90 GHz Band
EDFA	Erbium-Doped Fiber Amplifier
EM	Electromagnetic, Electromagnetism
ENIG	Electroless Nickel Immersion Gold
ESA	Electrical Spectrum Analyzer
FSL	Free-Space Loss
FTBR	Front-To-Back Ratio
FTTH	Fiber-To-The-Home
G-S-G	Ground-Signal-Ground
GCPW	Grounded Coplanar Waveguide
GND	Chassis Ground
HBT	Heterojunction Bipolar Transistor
HD	High-Definition
HDTV	High-Definition Television
HE	Hybrid quasi-TE
HEMT	High-Electron-Mobility Transistor
HM	Hybrid quasi-TM
HPBW	Half-Power Beamwidth
HTCC	High-Temperature Co-fired Ceramic
IFoF	Intermediate-Frequency-over-Fiber
IL	Insertion Loss
IS	Isolation
LCP	Liquid Crystal Polymer

LNA	Low-Noise Amplifier
LO	Local Oscillator
LDI	Laser Direct Imaging
LTCC	Low-Temperature Co-fired Ceramic
MIMO	Multiple-Input/Multiple-Output
MMIC	Monolithic Microwave Integrated Circuit
MPA	Medium-Power Amplifier
MZM	Mach-Zehnder-Modulator
mm-wave	Millimeter-Wave
NRZ	Non-Return to Zero
O-H	Oxygen-Hydrogen
O/E	Optical-to-Electrical
OBPF	Optical Band-Pass Filter
OFDM	Orthogonal Frequency-division Multiplexing
OOK	On-Off Keying
OSA	Optical Spectrum Analyzer
PC	Polarization Controller
PCB	Printed Circuit Board
PCT	Printed Circuit Technology
PD	Photodiode
PTL	Planar Transmission Line
PTFE	Polytetrafluorethylene
pin	p-doped, intrinsic, n-doped
QAM	Quadrature Amplitude Modulation
RF	Radio-Frequency/mm-wave
RL	Return Loss
RoF	Radio-over-Fiber
rms	Root-mean-square
SA	Spectrum Analyzer
SIW	Substrate Integrated Waveguide
SMD	Surface-Mounted Device
SMF	Single Mode Fiber
SOLT	Short-Open-Load-Thru
TC	Thermal Conductivity
TE	Transverse Electric
TEM	Transverse Electromagnetic
TL	Transmission Line
TM	Transverse Magnetic
TRL	Thru-Reflect-Line
TW	Travelling Wave
UTC	Uni-Travelling Carrier
W-Band	90-120 GHz Band
WLAN	Wireless Local Area Network
WPAN	Wireless Personal Area network
WR	Rectangular Waveguide

WR-12	Rectangular Waveguide for 60-to-90-GHz Operation
WR-15	Rectangular Waveguide for 50-to-75-GHz Operation

Latin Symbols

B	Magnetic Induction vector
D	Antenna Directivity
D	Electric Displacement Vector
E	Electric Field Vector
E_g	Bandgap Energy of a Semiconductor
E_{photon}	Energy of a Photon
e_{ant}	Antenna Efficiency
f	Frequency
H	Magnetic Field Vector
I_{photon}	Photocurrent
J	Current Density Vector
j	Imaginary Unit
k	Wave Number
k	Propagation Vector
M	Magnetic Polarization Vector
P	Electric Polarization Vector
P_{opt}	Optical Power
R_{λ}	Responsivity of PD
R_s	Surface Resistance
T_d	Decomposition Temperature
T_g	Glass Transition Temperature
V_{π}	Quadrature Bias Voltage of MZM
Z_0	Characteristic Impedance of a Transmission Line
Z_{in}	Input Impedance of a Transmission Line
Z_L	Load Impedance of a Transmission Line

Greek Symbols

α	Attenuation Vector
α	Attenuation Constant
α_{abs}	Absorption Coefficient
β	Wavenumber
β	Phase Vector
Δ	rms Surface Roughness
Γ	Reflectivity
$\tan \delta$	Loss Tangent

δ_s	Skin Depth (Penetration Depth)
ε	Dielectric Permittivity
ε_{eff}	Effective Permittivity
ε_r	Relative Permittivity
ε_s	Strain
η	Intrinsic Impedance
η_q	Quantum Efficiency
λ_0	EM Wavelength in Vacuum
λ_r	EM Wavelength in a Medium
μ	Magnetic Permeability
μ_{eff}	Effective Permeability
μ_r	Relative Permeability
ρ	Electric Charge Density
σ	Electrical Conductivity
χ_e	Electric Susceptibility
χ_m	Magnetic Susceptibility
ω	Angular Frequency

Chemical Elements and Compounds

As	Arsenic
Al ₂ O ₃	Aluminium Oxide (Alumina)
AlN	Aluminium Nitride
BeO	Beryllium Oxide (Beryllia)
Ga	Gallium
GaAs	Gallium Arsenide
In	Indium
InP	Indium Phosphide
H	Hydrogen
NiCr	Nickel-Chromium
O	Oxygen
P	Phosphorus
SiO ₂	Silicon Dioxide (Silica)
WTi	Titanium-Tungsten

Constants

$h = 6.626 \times 10^{-34} \text{ kg} \cdot \text{m}^2/\text{s}$	Planck Constant
$k = 1.381 \times 10^{-23} \text{ kg} \cdot \text{m}^2/\text{s}^2 \cdot \text{K}^{-1}$	Boltzmann Constant
$q = 1.602 \text{ C}$	Elementary Charge
$c_0 = 299792458 \text{ m/s}$	Speed of Light in Vacuum

$$\varepsilon_0 = 8.854 \times 10^{-12} \text{ C}^2/\text{N} \cdot \text{m}^2$$

$$\eta_0 \approx 377 \Omega$$

$$\mu_0 = 4\pi \times 10^{-7} \text{ kg} \cdot \text{m}/\text{s}^2$$

Vacuum Permittivity

Intrinsic Impedance of Vacuum

Vacuum Permeability

1 Introduction

1.1 Broadband Wireless Access Demand

The *data tsunami* linked to the continuously growing demand for broadband connectivity and high-datarate communication is rapidly bringing to the saturation of the current networks' capacity [1]. Telecommunication providers are currently facing the problem of being able to deliver fixed broadband connectivity to corporate and private users at competitive prices: This is mostly due to the difficulties linked to the expansion of the existing optical fiber networks. In fact, the provided huge bandwidth together with the extremely low-loss properties made fiber a popular choice for broadband communication networks, being deployed across the world to serve as backbones and backhauls for the distribution of data. Unfortunately, the development of fiber-to-the-home (FTTH) networks is still limited by environmental factors, namely the difficulties (and therefore the costs) related to trenching in metropolitan areas. These costs are estimated to be in the order of ≈ 130000 \$ per km in the U.S. [2], which are obviously a prohibitive investment for small and medium enterprises, as well as for most domestic buildings. Furthermore, local regulations are becoming increasingly strict concerning the installation of fiber services, causing delays (months or years) in the actual implementation of new networks branches, because of the necessary impact studies and planning [3]. In other cases, e.g. in rural areas, where trenching costs would generally be lower, geological and natural factors (e.g. lakes, mountains, forests) do not always allow easy solutions to deploy the fiber.

All the above mentioned obstacles have generated a large effort from the industry and the international research community in the strive for the development of adequate wireless fiber extensions and/or replacements [4]. In particular, considerable work has been done in the past years to develop fixed point-to-point microwave links operating between 5 and 40 GHz, with typical applications in mobile backhaul and enterprise connectivity (link distance between some hundreds of meters and a several kilometers). The availability of sources, amplifiers and antennas, together with the relatively low atmospheric attenuation, allows the development of long-range (>5 km) carrier-class (99.999% availability per year) wireless connections in this frequency range. Unfortunately, because of the narrow channels established by the regulators, the connectivity of these systems is limited to a maximum of 350 Mb/s, achievable only with spectrally efficient modulation formats [5]. Data rates of 700 Mb/s or in excess of 1 Gb/s are eventually achievable only by additionally using techniques such as adjacent-channel transmission or dual channel polarization, which essentially require doubling the architecture of the system [6].

Fig. 1.1 illustrates how the use of millimeter-wave¹(mm-wave) solutions can be seen

¹The common definition of *millimeter-wave* usually comprises all frequencies with wavelength shorter than 1 cm (30 GHz) and longer than 1 mm (300 GHz). In this thesis the term will however be used to

as a panacea for the limited speed achieved by microwave links of spectrum, guaranteeing a connectivity of several Gb/s for short-range communication and at least 1 Gb/s for medium-range applications. Considerable work has been done in the last years for the regulation of the 60/70/80-GHz bands and for the development of suitable systems and components to profit of the possibilities offered by these bands. Details concerning the usage and the characteristics of the 70/80-GHz bands are given in Section 1.2.2.

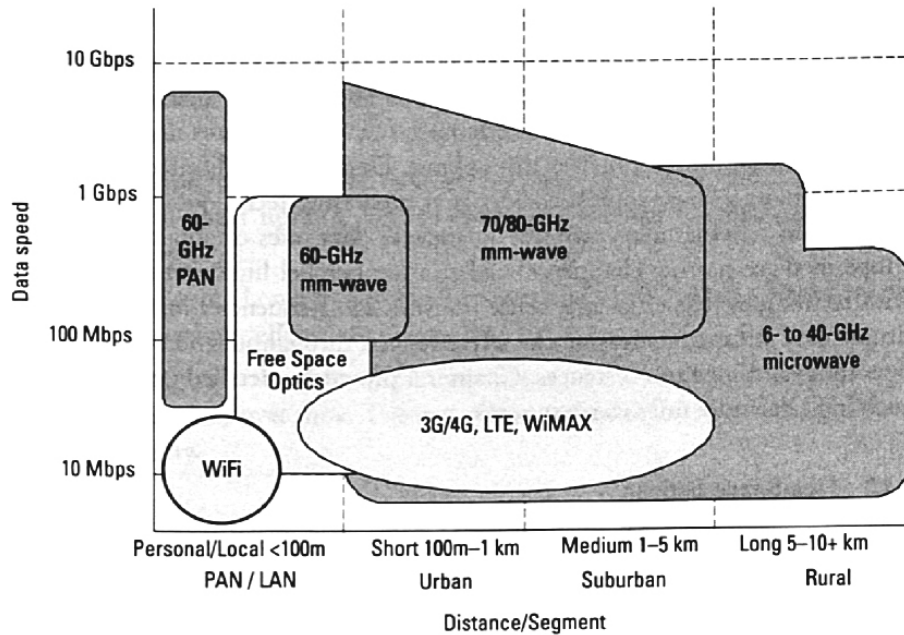


Figure 1.1: High-data-rate wireless scenario. Reproduced from [6] with permission of Artech House via Copyright Clearance Center.

From Fig. 1.1 it can be seen that, differently from the other mm-wave bands, the 60-GHz band is not only used for short range applications, but also for personal and local communication networks. In fact, where fiber connectivity is readily available, the market is further showing interest in the development of new wireless solutions, especially for indoor wireless personal area networks (WPANs) and wireless local area networks (WLANs), where a massive diffusion of *datarate-hungry* applications (such as uncompressed high-definition (HD) video streaming, online gaming, large file synchronization, and docking stations) is foreseen [7]. Fig. 1.2 depicts a more detailed view of the very-short-range wireless communication scenario, clearly showing that the data rate of up to a few Gb/s required by the above mentioned applications cannot be achieved using the relatively mature local-network wireless technologies currently available on the market [8]. In fact, even the latest WiFi technology, developed for short-distance multi-access connectivity, is

identify frequencies above 50 GHz, in order to comprise the recently regulated communication bands (60-GHz, 70-GHz, 80-GHz) and distinguish them from the gigahertz range (up to 50 GHz), that will be referred to as *microwave region*. This distinction is suggested by the general characteristics of the higher frequency bands and by the special approaches used by regulation bodies for the management of the different channels, as it will be explained in Section 1.2.

practically able to only guarantee a connectivity of a few Mb/s per user [6], in spite of the maximal 600 Mb/s data rate envisaged by the latest IEEE 802.11.n standard [9] and the ≈ 200 Mb/s achieved in laboratory demonstrations using multiple-input/multiple-output (MIMO) configurations in combination with orthogonal frequency-division multiplexing (OFDM) and high-order quadrature amplitude modulation (QAM) [10]. Similarly, ultra-wide band (UWB) systems can theoretically deliver connectivity in the Gb/s-range only using advanced modulations techniques and MIMO configurations [11,12], in spite of the large used bandwidth, essentially because of the strict regulations concerning the transmitted power². Once again, mm-wave technology can be used to overcome the current limitations posed by existing wireless technologies: The IEEE 802.15.3c standard has for the first time addressed data rates in excess of 1 Gb/s [13] introducing the use of 60-GHz technology into the saturated wireless scenario. More details concerning the 60-GHz band and its relevant regulations are given in Section 1.2.1.

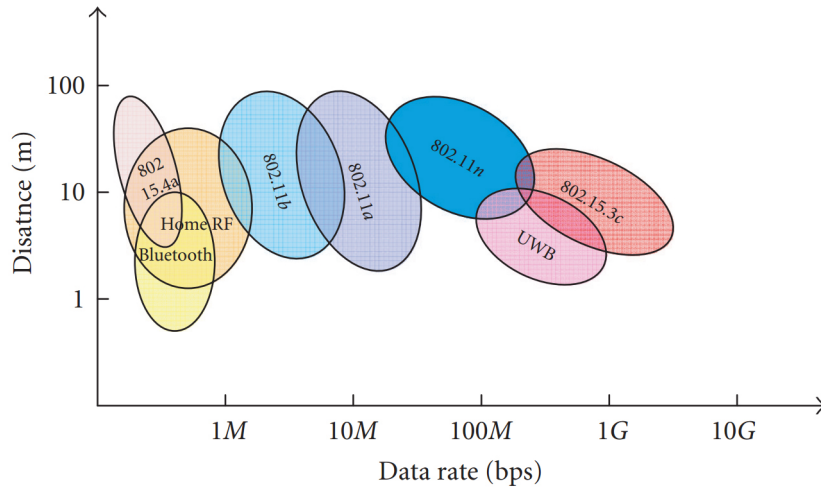


Figure 1.2: WLAN and WPAN data rates and ranges for different standards (after [8]).

1.2 Millimeter-Wave Spectrum Allocation and Regulations

As highlighted in the previous section, mm-wave technology is the key to high data rate wireless data transmission, as the usage of higher transmission frequencies allows the development of faster services with higher data rates, as reported, among others, in [6]. It is important to notice that mm-wave propagation suffers of higher free-space loss (FSL) than microwaves. FSL is the generally dominating form of attenuation in microwave and

²Due to their intrinsic nature, UWB systems are forced to operate with power levels located in the noise floor of other overlapping standards. The particular nature of UWB systems also makes international harmonization across the world challenging.

mm-wave radio links and is given by

$$FSL = \left(\frac{4\pi R}{\lambda} \right)^2 = \left(\frac{4\pi f R}{c} \right)^2 \quad (1.2.1)$$

where R is the propagation distance, λ is the wavelength, f is the frequency and c is the speed of light in air. As it can be seen, the FSL is directly proportional to the square of the transmission distance and to the frequency of the signal. Figure 1.3-left plots the FSL for different mm-wave carriers: It can be seen that there is an increase of 9-11 dB in comparison to the FSL of a microwave signal (23 GHz). However, as it will be discussed in section 2.4.3, this effect can be compensated by the fact that the reflector antennas used in the development of outdoor wireless systems have an increased gain, for a given antenna aperture, when used for mm-wave applications. Figure 1.3-right shows the effect of the atmospheric attenuation [14] in addition to the FSL and it is obvious that the 60 GHz band is the only one that is severely affected by the attenuation of atmospheric gases, due to resonance of oxygen at this frequency. However, this effect only becomes relevant for distances larger than a few hundreds meters. This clearly suggests that this band is suitable for short and very-short range communication, while its deployment for long-distance (> 1 km) links is not recommendable. In the recent years, regulation bodies

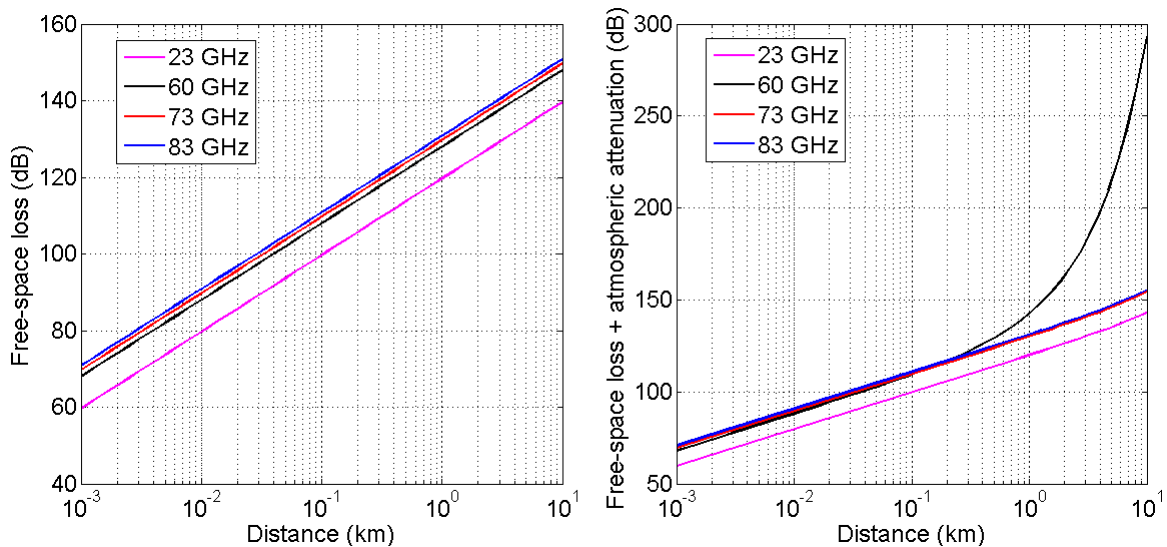


Figure 1.3: Free-space loss (left) and total propagation loss taking into account the atmospheric attenuation (dry air, sea-level, temperature = 15°C, pressure = 1.013 hPa, water vapor density = 7.5 g/m³) for different frequencies (right).

and research groups, as well as the commercial sector, have concentrated their work in high-speed communication applications taking into account the considerations mentioned above, trying to take advantage of the different characteristics offered by the different bands. Implications of these choices on the applications and the rules set by regulations entities will be discussed in the following sections.

1.2.1 60-GHz Band

The very peculiar characteristics of the 60-GHz band introduced in the previous section lead regulation authorities all over the world to allocate 5 to 7 GHz of spectrum for unlicensed telecommunication applications [15]. The allocated spectrum is either continuous or divided in large channels which can be joined together to achieve multi-GHz bands, which is a great advantage with respect to the crowded and parceled out lower-frequency communication bands [3]. The large frequency reuse guaranteed by atmospheric attenuation for distances above 1 km (see Fig. 1.3) and the costs saved on licenses (which can reach 4000 \$ a year for competitive microwave systems [5]) also contribute to increase the interest in the development of 60-GHz systems.

Two different markets are possible for wireless systems operating in this band: Point-to-point outdoor links and high-speed indoor wireless networks. Point-to-point outdoor links are of particular interest for enterprise connectivity, to achieve building-to-building extension of WLANs, and are regulated in different ways by authorities around the world [15]. However, minimum antenna gains of 20-50 dBi are considered mandatory in almost all countries, together with a number of other radiation requirements [3]. For the indoor scenario, which takes advantage of the intrinsic security and increased frequency reuse guaranteed by the attenuation of oxygen and walls on 60 GHz signals, a number of different applications are envisioned or currently being developed, among which: Cable replacement (e.g. for uncompressed HDTV streaming), Gb-wireless Ethernet, high-speed data transfer (wireless docking stations), and enhanced wireless gaming [7]. Accordingly, several private and public working groups (e.g. WirelessHD, ECMA-387, 802.15.3c, 802.11ad, WiGig) have been created with the aim of promoting standardization activities to support the development of the mentioned applications [16].

1.2.2 70/80-GHz Band

Recently, the E-band was opened up in several regions around the world, allocating the 71-76 GHz and 81-86 GHz ranges for communication applications. Additional frequencies above 90 GHz are allocated in the United States of America, achieving the extraordinary bandwidth of 12.9 GHz. The E-band is channelized, but paring (for simultaneous up-link and down-link) and aggregation of an unlimited number of adjacent channels are permitted [15].

Authorities around the world have chosen to manage E-band applications on the basis of different approaches, implementing *lightweight* license, license-exempt, or conventional license approaches [6]. The implementation of the simplified licensing systems, which implies very short acquisition time (hours or days) and low costs, has been partially made possible by the restrictive requirements on the antenna gain: In fact, minimum antenna gains are 38 dBi in Europe and 43 dBi in the USA, leading to *pencil beams* which increase the security, reduce the risk of interference, and allow sharing of mechanical infrastructures and intensive frequency reuse [5, 6, 17].

The high-gain requirements impose the usage of reflector antennas (see section 2.4.3), which requires E-band systems to be equipped with opportune rectangular waveguide con-

nectors (WR³), while the low atmospheric attenuation makes E-band systems a preferred solution for short/medium range (<5 km), with the actual maximum extension limited by local rain rates.

1.2.3 Other Bands

Besides the asymmetrical 92-94 GHz and 94.1-95 GHz channels⁴ allocated for communication in the United States of America, other mm-wave solutions are being considered worldwide in order to develop high-data-rate links.

Constrained by atmospheric attenuations peaks, two bands are foreseen to represent a new breakthrough in mobile communication: The 150-GHz band (extending from 125 to 165 GHz) and the 250-GHz band (spanning from 200 to 300 GHz), which sum up to an impressive total bandwidth of 140 GHz, suitable for at least 40 or 100 Gb/s transmission.

Although the atmospheric attenuation is slightly higher than in the 60/70/80-GHz band, considerations on the increased antenna gain similar to the ones introduced in section 1.2 apply and the impact of rain on transmission is comparable to the one occurring in the lower mm-wave range, making the upper mm-wave frequencies suitable for short-range and middle-range communication. No commercial systems are currently available, but several research groups are already showing interest in and experimental validation of 150-GHz [19, 20] and 250-GHz [21–23] wireless links.

1.3 Radio-over-Fiber Technology for Millimeter-Wave Communication Systems

Microwave photonics, i.e. the use of optical techniques for the generation, processing and distribution of microwave and mm-wave signals, has since a few decades attracted attention from industry and academia [24]. In fact, the optical generation and transmission of RF⁵ signals, in contrast to all-electronics techniques, not only guarantees low phase noise RF signal generation, ultra-wide frequency tunability and broadband modulation capabilities up to the THz range [15], but it further offers low-loss, low-cost and low-weight distribution possibilities thanks to the exceptional characteristics of optical fibers (see section 2.1.7).

Radio-over-Fiber (RoF) is a key technology for high-speed communications which combines electronics and optical techniques to achieve broadband signal and data distribution to remote locations. A typical RoF network for wireless distribution is depicted in Fig. 1.4: An RF signal carrying data packages is used to modulate an optical carrier in a central office (CO) and is then transported via an optical fiber to remote base stations (BSs), which extract the RF information signal and transmit it via an opportune antenna to the end user.

³The acronym chosen for the rectangular waveguide in this thesis will be “WR”, for association with the widely used nomenclature proposed in the EIA RS-261-B standard [18].

⁴The 94-94.1 GHz band is reserved for military applications.

⁵Here the expression *RF signal* is used to indicate any desired wireless signal (up to the mm-wave range), in juxtaposition with the auxiliary local oscillator (LO) and intermediate (IF) frequencies, which are linked by the following relation: $f_{\text{RF}} = f_{\text{IF}} + f_{\text{LO}}$.

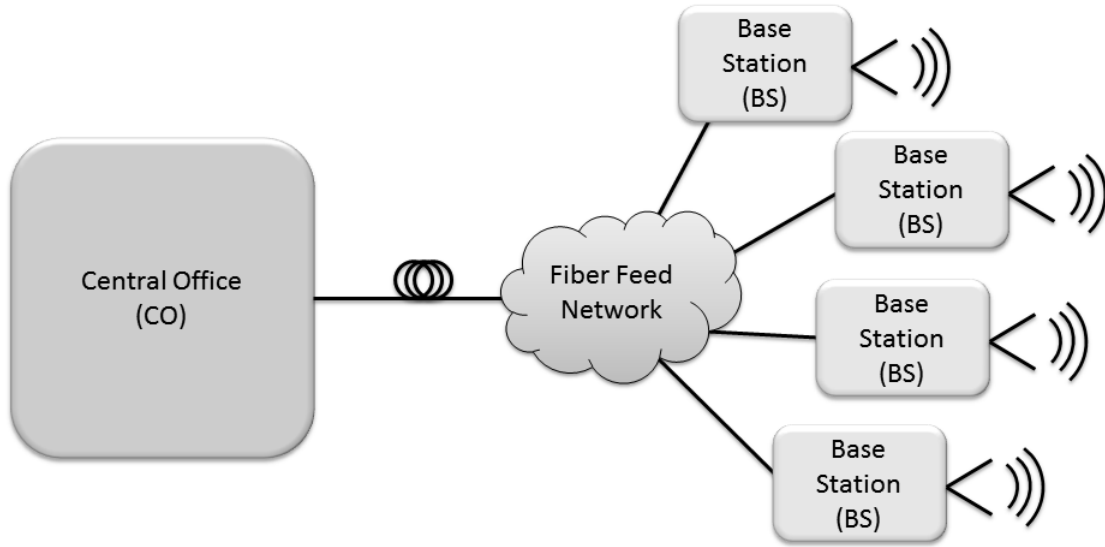


Figure 1.4: Typical RoF link.

In comparison to alternative techniques such as Baseband-over-Fiber (BboF) and Intermediate-Frequency-over-Fiber (IFoF), RoF has the important advantage of centralizing the signal processing and conditioning at the CO, reducing the BS architecture to essentially an optical-to-electrical (O/E) converter and a transmitting antenna. Eventually, RF amplification could be added in order to increase the wireless transmission distance. Besides reducing the overall cost of the system, this has several additional advantages. First of all, the BS is transparent to the actual RF modulation formats and protocols, thus enabling a simpler management of the network and an increased flexibility in terms of offered services, with any eventual upgrades carried out at the CO only. Furthermore, their simplified architecture reduces the overall power consumption of the BSs and makes the installation and maintenance processes easier.

In their simplest form, BSs are photodiode (PD) modules with a transmitting antenna, also called photonic transmitters, which perform the conversion of information from the optical to the electrical domain by means of the PD, possibly followed by an amplifier, and transmit the RF wireless signal⁶. Obviously, in order to achieve full-duplex communication, if this is required by the application, the BSs have to include additional hardware (circulator, amplifier, optical carrier generator) to process the wireless signal received from the users and transmit it via the optical fiber [25]. However, all the above mentioned considerations remain valid and represent crucial advantages in the current telecommunication scenario, where communication operators are reducing the extension of the cells, thus increasing the number of the required BSs, as well as in a number of emerging applications, such as indoor distributed antenna systems (DAS), extension of wireless coverage (e.g. in tunnels), and “last-mile connectivity” (where natural or administrative obstacles prevent the deployment of cables and fibers) [26].

While the implementation of RoF links at low frequencies is nowadays not particu-

⁶See section 1.4 and chapter 2 for further details.

larly challenging thanks to the availability of compact and reliable modulation techniques (direct laser modulation can be achieved up to ≈ 40 GHz in experimental setups [27] and up to ≈ 10 GHz for commercial devices) as well as of optical detectors for the O/E conversion (PDs), the setup of mm-wave RoF systems requires particular attention. In fact, besides the need for more complicated techniques (which require additional external modulators) are necessary to achieve appropriate optical modulation [25], a key issue is represented by the difficulty to develop fast PD modules for the BS, which have to be optimized for operation in the mm-wave range and have to be conveniently packaged in order to minimize loss, protect the chips from atmospheric agents and guarantee interconnectivity with external components, as it will be explained in section 1.4.

1.4 Photonic Transmitters

A schematic drawing of a photonic transmitter is shown in Fig.1.5, where optical interconnects (fibers) are depicted in red, mm-wave interconnects are depicted in blue, and bias lines for the active components are depicted in gray. The most important component of photonic transmitters is the PD⁷, which converts the optical signal to the electrical domain. The output of the PD is then generally amplified using mm-wave amplifiers⁸ and finally transmitted through appropriate antennas, whose topology depends on the actual application⁹.

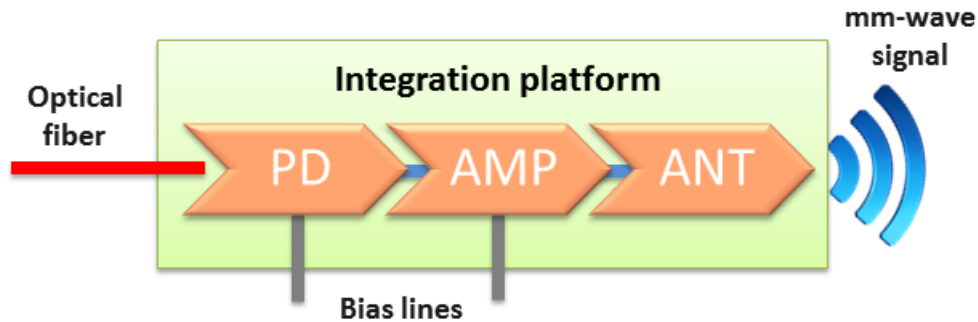


Figure 1.5: Block diagram of photonic transmitter. The PD is followed by an amplifier and by an antenna, respectively labeled *AMP* and *ANT* in the diagram.

The packaging of PD modules operating in the mm-wave range is not a trivial task as several requirements have to be satisfied, while taking into account multiple technological constraints. In particular, it is important to develop planar integration platforms that allow proper illumination of the PD and have a compact profile compatible with optoelectronic assembly processes. They must use interconnecting technologies which do not introduce excessive loss on the information signal and should be hermetically sealed

⁷Details concerning mm-wave PDs are given in section 2.2.

⁸See section 2.3.

⁹More details on the properties and choice of antennas are given in section 2.4.

in order to extend the lifetime of the devices. Finally, in order to support the widespread deployment of BSs, the integration technology must be cost-effective and should possibly rely on the usage of standard discrete components.

For outdoor mm-wave point-to-point applications, as described in sections 1.2.1 and 1.2.2, the integration of the chip with WR connectors is crucial, as they are commonly used as input connectors for the high-gain antennas necessary to achieve the required high-directivity, as well as for filters and amplifiers, because of their high power handling capabilities, low attenuation and high quality factor¹⁰. While commercial PD modules are usually equipped with a coaxial output, the research community has shown an increasing interest in the past years in designing mm-wave PD modules with WR connectors. The approaches proposed in literature to couple the output of the PD chip to a WR are usually based on thin probes placed across the WR opening [28–31] or inserted into the WR [32–36]. The adopted assembly processes involve sophisticated manufacturing technologies, such as split-block and waveguide machining [28, 34, 35] in order to overcome assembly issues and realize non-standard elements required by the design (e.g. reduced-height waveguides), while the circuitry is realized using expensive thin-film manufacturing technology in order to increase the achievable resolution of the circuit elements (see section 3.4.2). As a result, the development of the PD modules incurs high costs (due to the expensive equipment) and their efficiency is limited by the low yield due to the used circuit technology and the necessity of non-standard elements. It should also be noticed that all presented approaches require dedicated alignment procedures and do not provide a mechanical enclosure of the WR opening, thus moisture and particles can penetrate into the module through the WR: This is recognized as a serious issue for optoelectronic devices, therefore additional components are sometimes required in order to solve the hermetic shortcoming of the listed integration approaches (such as the special sealing window proposed in [37]), which unfortunately increase the loss, the cost, and the complexity of the assembly.

For short-range mm-wave applications where a high directivity of the antenna is not required (such as scientific environments or specific indoor consumer systems), a simple and compact approach for the antenna integration is represented by the development of on-chip or in-package antennas. For narrow-band applications, simple patch [38] or slot [39] antennas are used, while improved patch antenna configurations [40, 41], bow-tie, log-periodic or log-spiral antennas (e.g. as reported in [42–44]) are used to achieve wider operating bandwidth. Often a silicon lens is added to the module to improve the directivity of the antennas [39, 43, 44], thus reducing the amount of power radiated in unwanted directions. The antennas are either developed on dedicated substrates using thin-film [40] or micromachining techniques [39], either developed on the same chip of the PD to avoid the usage of discrete interconnects [43, 44]: The main drawback of these approaches, is that the antennas require a relatively large area of expensive semiconductor wafer. As the size of the antenna increases with decreasing frequency, this solution is preferable only for applications in the higher mm-wave and terahertz range.

¹⁰Rectangular waveguides are discussed in section 2.1.2.

1.5 Aim and Organization of the Thesis

The aim of this thesis is to investigate the potential offered by cost-effective printed circuit technology (PCT) for the packaging of mm-wave PD modules, as an alternative to the packaging solutions introduced in section 1.4.

In recent years, some mm-wave printed circuit board (PCB) designs have been proposed for all-electronics applications, such as pure antenna concepts (e.g. in [45, 46]), packaging of amplifiers [47] or radar front-ends [48]. We first proposed the possibility of using laminates¹¹ and PCT for the development of mm-wave optoelectronics modules with WR output for E-band point-to-point applications in [51]. The peculiarities of our integration approach are the use of a cost-effective circuit development technology and the lack of any mechanical modifications of the WR, allowing therefore a simplified assembly and the usage of standard WR components: This eliminates the need for split-block manufacture and therefore reduces the overall cost of the module. The availability of laminates with low-moisture absorption as dielectric carrier furthermore opens up the possibility to develop quasi-hermetic¹² packages without the need of additional radomes, provided that a hermetic housing is connected to the top side of the assembly, as shown in Fig. 4.1.

However, using PCT for the development of mm-wave platforms requires careful design and comprehension of the limitations imposed by this technology. For this reason, it is important to analyze the loss mechanisms and the theoretical frequency limits due to the physical properties of the laminates. Furthermore it is necessary to identify the limits imposed by the achievable resolution, the tolerances and the manufacturing steps of the printed-circuit development process. A detailed analysis of the microstrip - probably the most common planar transmission line (PTL) - will lay the foundations to introduce important aspects concerning laminates and the design of PCB transmission lines. However, as microstrips can be subject to high undesired radiation in the mm-wave region, different transmission lines will be introduced: In particular the grounded coplanar waveguide (GCPW) will be considered, as it has several practical advantages when compared to the microstrip, and, if properly designed, helps to reduce interconnecting loss. We will thus show that several prototypes of mm-wave photonic transmitters and modules, featuring either a commercial PD or a chip developed in house, with or without integrated amplification, can be conveniently assembled using PCT and traditional PTL. The developed devices will be successfully used in mm-wave RoF demonstrators, in order to prove the suitability of our approach for the development of commercial communication systems.

Although GCPWs are intrinsically more suitable than microstrip to control radiation, they still suffer of relatively high loss in the mm-wave region: In fact, radiation can occur at any discontinuities and the high current density at the edges of the signal line increases conductor loss. Therefore we will introduce for the first time the PCB substrate integrated waveguide (SIW) in the packaging of mm-wave photonic transmitters [52], in

¹¹Note that, although all examples presented in this thesis will be based on laminates produced by the Rogers Corporation, there are equivalent products offered by several competitors. Non-comprehensive surveys of laminate suppliers are given, among others, in [49, 50].

¹²Although generally not accepted in harsh environments (e.g. in space or underwater locations), quasi-hermetic packages are accepted in non-critical situations where this is sufficient to extend the lifetime of the packaged devices, as discussed in section 3.3.4.

order to overcome the shortcomings of traditional PCB transmission lines in the mm-wave range. The properties of this innovative line in terms of low loss and high integration will be investigated and assessed, showing that the PCB SIW is an excellent candidate for the development of high-performance packaging solutions: In fact, its unique configuration allows a superior control of radiation and interferences, and drastically reduces losses. This will be demonstrated by introducing a new integration platform for PD modules with in-package antennas based on PCB SIW, focusing in particular on non-directive distribution systems: It will be shown that compact, low-loss and quasi-hermetic packaging solutions for 60-GHz operation can conveniently be designed making use of the SIW.

Organization of the Thesis

Besides the current chapter, which presents general introductory topics, additional concepts necessary for the correct understanding of the functioning of PD modules will be presented in chapter 2: They include fundamentals of applied electromagnetism (EM) (propagation, guiding structures), of passive and active electronics (antennas, amplifiers), as well as of optoelectronics technology (PDs). In particular, the factors limiting the performance of traditional transmission lines (WR, coaxial cable, microstrip and GCPW) in the mm-wave region will be analyzed. Special attention will be given to the properties of the SIW and its suitability for the development of compact and low-loss mm-wave optoelectronic packages will be assessed.

Chapter 3 will focus on optoelectronic integration technologies, exploring the challenges related to the different aspects of packaging. Particular emphasis will be given to the usage of organic substrates and PCT to develop reliable mm-wave hybrid assemblies suitable for large-scale photonic-electronic integration. Theoretical and practical frequency limits for the usage of laminates will be studied and assessed. Experimental investigation of the attenuation properties of mm-wave PCB interconnects will be presented and convenient modeling techniques will be introduced. Guidelines and alternative solutions to overcome limitations of classical hybrid integration will also be considered.

Chapter 4 will introduce the first experimental, quasi-hermetic, integration concept for E-band PD modules based on laminates. The presented device features a WR output, a fundamental requirement for mm-wave transmitters designed for point-to-point RoF links (see section 1.4). The manufactured module has the advantage of being quasi-hermetic without the need of additional sealing windows or radomes and it is based on a commercial PD with integrated bias network. It will be shown that it can be successfully employed in 70-GHz RoF systems to achieve *error-free* 1 Gb/s data transmission. Further improvements concerning the integration of PDs without integrated bias network, as well as on-board amplification will also be discussed, proving the flexibility of the developed assembly approach.

Chapter 5 will focus on the usage of the SIW in the development of quasi-hermetic 60-GHz RoF transmitters for indoor applications, presenting the design of a SIW integration platform for PDs. We will introduce innovative planar GCPW-to-SIW transitions developed to allow the integration of PDs with SIW structures. Furthermore, we will present a feasibility study for 60-GHz PCB sector antennas systems fed by SIWs and suitable for data distribution systems. Different techniques will be used to improve the

matching of the antennas and their radiation properties, in order to verify and overcome the intrinsic accuracy limitations of PCB processes. Experimental characterization of the designed mm-wave interconnects and antennas will be shown, which highlight the superior performance of the SIW technology and its suitability for low-loss mm-wave circuits.

Finally, in chapter 6 a summary of the presented results will be given, discussing the achievements and the learned lessons. The identified limitations and possible solutions to improve and further develop the presented designs will also be considered.

1.6 Projects

The work presented in this thesis was mostly carried out within two projects (*MITEPHO* and *iPHOS*) funded by the European Commission under the Seventh Research Framework Programme (FP7). In this perspective, this thesis supported the development of cost-effective, high-speed photonic transmitters for the systems and applications envisaged by the projects.

MITEPHO Initial Training Network

The main scientific objective of the *MI*crowave and *TE*rahertz *PHO*tonics (MITEPHO) initial training network (grant agreement: 238393) is “to design and develop efficient and reliable sources for the photonic generation of microwave and terahertz, providing sufficient power to be useful in selected areas of application” [53]. The focus is on the development of compact and cost-effective photonic solutions to support the deployment of future RoF infrastructure.

iPHOS

The *Integrated PHO*tonic transceivers at sub-terahertz wave range for ultra-wideband wireless communication*S* (iPHOS) project (grant agreement: 257539) targets “the development of compact and low power transceivers that enable wireless data transfer at sub-terahertz carrier frequencies and their application to future high data-rate short-distance communication links” [54].

2 Constituents of Millimeter-Wave Photonic Transmitters

This chapter contains introductory concepts useful to understand and appreciate the role of all fundamental parts of a photonic transmitter, which have been introduced in section 1.4 (see Fig. 1.5). Additional theoretical concepts and definitions used in this chapter are given in Appendix A.

2.1 Guided Electromagnetic Propagation

Transmission lines (TLs) are structures used to carry and guide EM signals. In order to describe how the fields propagate within them, we can model them as generic cylindrical structures, with a constant cross section along the linear axial coordinate of propagation (the z axis in the Cartesian coordinates system shown in Fig. A.2, in appendix A.3).

2.1.1 General Loss Considerations

The attenuation¹ due to the physical properties of a guiding structure in which an EM wave propagates can generally be expressed as the sum of

$$\alpha = \alpha_c + \alpha_d + \alpha_l + \alpha_r \quad (2.1.1)$$

where α_c is the conductor loss (due to the limited conductivity of the metallic structures), α_d is the dielectric loss (directly related to the $\tan \delta$ of the dielectric present in the transmission line), α_l the leakage loss (due to leakage through dielectrics with finite resistivity), and α_r is the radiation loss (related to unwanted radiation from open configurations and particularly sensitive to discontinuities). While the conductor, leakage and radiation losses assume specific formulations for every transmission line, it is possible to express the dielectric loss (in Np/m) of any guiding structures filled with homogeneous dielectric² as [55]:

$$\alpha_d = \frac{\pi \sqrt{\epsilon_r} \tan \delta}{\lambda_0} \quad (2.1.2)$$

where λ_0 is the free-space wavelength of the EM wave, ϵ_r is the relative dielectric constant, and $\tan \delta$ is the *loss tangent* of the dielectric medium, described in the following.

¹See appendix A.2 for a formal definition of the *attenuation constant* α .

²For lines which are only partially filled with dielectric an effective permittivity ϵ_{eff} can be defined and a specific filling factor Q can be introduced into the formula to take into account the reduced attenuation due to the presence of air [55].

Loss Tangent

A wave travelling within a dielectric medium incurs in loss due to several physical phenomena, which are described by the imaginary parts of μ and ε (accounting for the loss in the material due to damping effects in the oscillation of the dipoles), and by the finite conductivity σ of the medium. A practical quantity to describe the loss in common media is the *loss tangent*, which can be conveniently defined as follows³:

$$\tan \delta \stackrel{\text{def}}{=} \frac{\omega \varepsilon'' + \sigma}{\omega \varepsilon'} \quad (2.1.3)$$

It is important to notice that the contribution of dipole oscillation damping and conductivity cannot be distinguished by external measurements of power dissipation, therefore the dielectric permittivity is often redefined as:

$$\varepsilon \stackrel{\text{def}}{=} \varepsilon'(1 - j \tan \delta) = \varepsilon_r \varepsilon_0 (1 - j \tan \delta) \quad (2.1.4)$$

where $\varepsilon_r = \varepsilon'_r$ (relative permittivity) is now a real number. From (2.1.3) and (2.1.4) it can be seen that the $\tan \delta$ expresses the ratio of the the imaginary and real parts of ε , as shown in Fig. 2.1:

$$\tan \delta = \frac{\varepsilon''}{\varepsilon'} \quad (2.1.5)$$

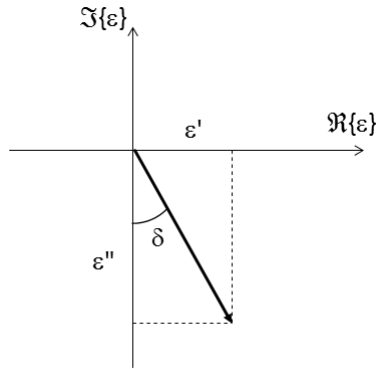


Figure 2.1: Loss tangent ($\tan \delta$).

The loss tangent is an important parameter for substrates commonly used for high-frequency applications and is usually included in the data sheets by the manufacturers, together with the relative permittivity ε_r . The complex dielectric permittivity can thus be calculated using equation (2.1.4). The effect of these parameters on EM waves and signals traveling in a transmission line are analyzed in section 2.1.1. An extensive collection of loss tangent and dielectric permittivity of common substrates from different manufacturers can be found in [50].

³A more detailed derivation of the loss tangent is proposed in appendix A.1.

Skin Depth

The *skin depth* (or *penetration depth*) δ_s is parameter that describes the confinement properties of a medium with respect to the penetration of EM radiation and it is defined as the distance from the material's surface at which the magnitudes of propagating EM fields are reduced to $e^{-1} \approx 0.368$ with respect to their amplitudes. A widely used approximated expression of δ_s for good conductors is [56]:

$$\delta_s = \sqrt{\frac{2}{\omega\mu\sigma}} \quad (2.1.6)$$

The skin depth has a direct influence on the current flow on a metal surface, which shows an exponential decay (with respect to the penetration into the metal) given by $J(z) = J_0 e^{-z/\delta}$, as shown in Fig. 2.2-left. It is therefore often used in microwave and mm-wave applications to describe the ability of conductors (metals) to confine and guide the EM energy, rather than transmitting it through their interior. As a rule of thumb, it can be considered that the fields are extinguished after travelling a distance of $5\delta_s$ into a material, which corresponds to an attenuation of more than 99%. As shown in Fig. 2.2-right, the skin depth in copper ($\sigma = 5.96107 \text{ S/m}$, $\mu_r = 0.999991$) for frequencies above 60 GHz is $\approx 0.25 \mu\text{m}$: This means that a copper layer of a few micrometers is sufficient to shield and prevent leakages of EM fields at this frequency. Furthermore, this example shows that in the mm-wave range only the coating of the guiding structure is important, as a thin layer of good conductor such as gold or silver is sufficient to improve the conductor loss of the structure or to prevent uncontrolled radiation of the EM fields, when used as shielding layer. Plating an adhesion layer of poor conducting metal or a native metal layer with a metal with better electrical and/or chemical properties is a largely used approach in several circuit manufacturing technologies, as described in section 3.4. Table 2.1 summarizes the skin depth of commonly used metals in PCB manufacture.

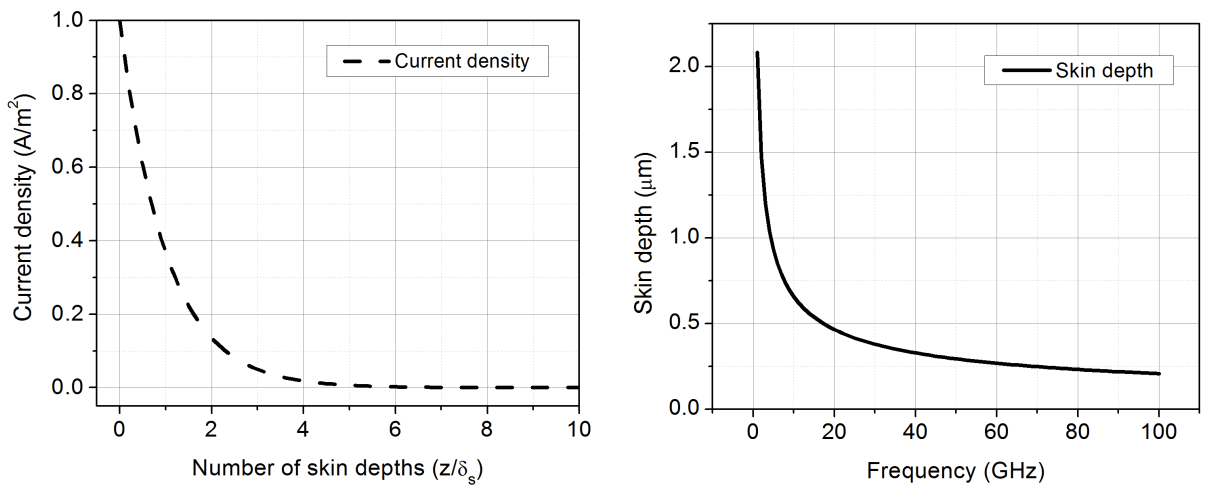


Figure 2.2: Normalized surface current density as a function of the skin depth (left) and skin depth of copper as a function of frequency (right).

Because of the concentration of EM fields in a thin superficial layer of conductors in the mm-wave range, it is useful to define a *surface impedance* as [57]:

$$Z_s = R_s + jX_s = \frac{E_t}{H_t} = (1 + j)\sqrt{\frac{\mu\omega}{2\sigma}} \quad (2.1.7)$$

with E_t and H_t being the tangential electric and magnetic field components and the *surface resistance* R_s being expressed by

$$R_s = \sqrt{\frac{\mu\omega}{2\sigma}} \quad (2.1.8)$$

Table 2.1: Skin depth of several conductors at 50 GHz.

Material	Conductivity (S/m)	Skin Depth (μm)
Brass	1.5×10^7	≈ 0.6
Gold	4.1×10^7	≈ 0.4
Copper	5.8×10^7	≈ 0.3
Silver	6.2×10^7	≈ 0.3

2.1.2 Rectangular Waveguide

Rectangular waveguides are among the most common guiding structures used in EM systems. They are basically metallic tubes (usually air-filled, although fully or partially dielectric-filled waveguides can be developed and used) with rectangular cross sections (see Fig. 2.3) and are suited for high-power and low-loss applications. Among their

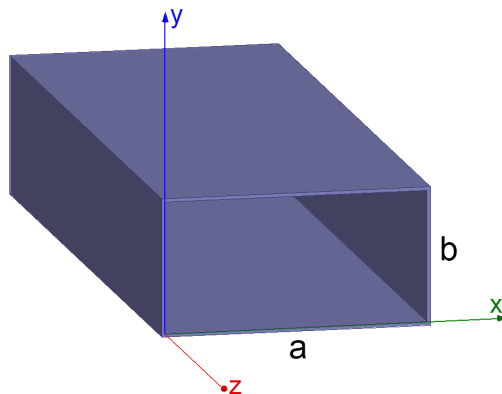


Figure 2.3: Rectangular waveguide.

advantages there are also the high isolation from external interference and the absence of

unwanted emission of energy, intrinsically originated by the closed metallic structure. The WR allows the transmission of EM waves in forms of TE and TM modes, and therefore exhibits a high-pass behavior. The transversal components of the propagation vector, obtained from boundary conditions imposed by the metallic rectangular geometry are expressed as:

$$k_{t,mn} = \sqrt{\left(\frac{m\pi}{a}\right)^2 + \left(\frac{n\pi}{b}\right)^2} \quad (2.1.9)$$

where m and n are the modes indexes associated with each TE_{mn} and TM_{mn} mode and a and b are the dimensions of the waveguide, as indicated in Fig. 2.3. Hence, from equation A.3.11, the cut-off frequencies of the different modes can be calculated to be:

$$f_c = \frac{1}{2\sqrt{\mu\varepsilon}} \sqrt{\left(\frac{m}{a}\right)^2 + \left(\frac{n}{b}\right)^2} \quad (2.1.10)$$

It should be noted that for TE modes the indexes m and n cannot be simultaneously zero (to avoid trivial solutions), while for TM modes they cannot be zero at all (this means that the TM_{10} and TM_{01} modes cannot propagate, thus leaving the TM_{11} as the first TM propagating mode) [58]. Being $a > b$ by construction, the first propagating mode in a WR is always the TE_{10} mode, which is therefore called *fundamental mode*, and its cut-off frequency is given by:

$$f_{c,TE_{10}} = \frac{1}{2a\sqrt{\mu\varepsilon}} \quad (2.1.11)$$

The TE_{10} mode is characterized by having $E_x = E_z = H_y = 0$, while the other components of the EM field are given by:

$$E_y = -j\frac{\omega\mu a}{\pi} A \sin \frac{\pi x}{a} e^{-jk_{z,10} z} \quad (2.1.12)$$

$$H_x = -j\frac{k_{z,10} a}{\pi} A \sin \frac{\pi x}{a} e^{-jk_{z,10} z} \quad (2.1.13)$$

$$H_z = A \cos \frac{\pi x}{a} e^{-jk_{z,10} z} \quad (2.1.14)$$

Figure 2.4 shows the electric and magnetic field vectors propagating within a WR-12 waveguide at a frequency of 70 GHz.

The maximum operating frequency of a WR is usually assumed to be the cut-off frequency of the second propagating mode, in order to allow a single-mode operation. For standard commercial WRs the condition $a = 2b$ is generally assumed⁴, thus leading to:

$$f_{c,TE_{20}} = f_{c,TE_{01}} = 2f_{c,TE_{10}} \quad (2.1.15)$$

which indicates that WRs have a maximum operational bandwidth of one octave (although usually reduced to 1.2-1.9 of $f_{c,TE_{10}}$ to account for fabrication tolerances). Figure 2.5 shows an example of the propagation constants of the first two modes of a standard

⁴The width b should be as large as possible in order to minimize conductor loss (see equation 2.1.16). However choosing $b > a/2$ would lead to a reduction of the operational bandwidth, as indicated by equation 2.1.10, which leads to the optimum value of $b = a/2$.

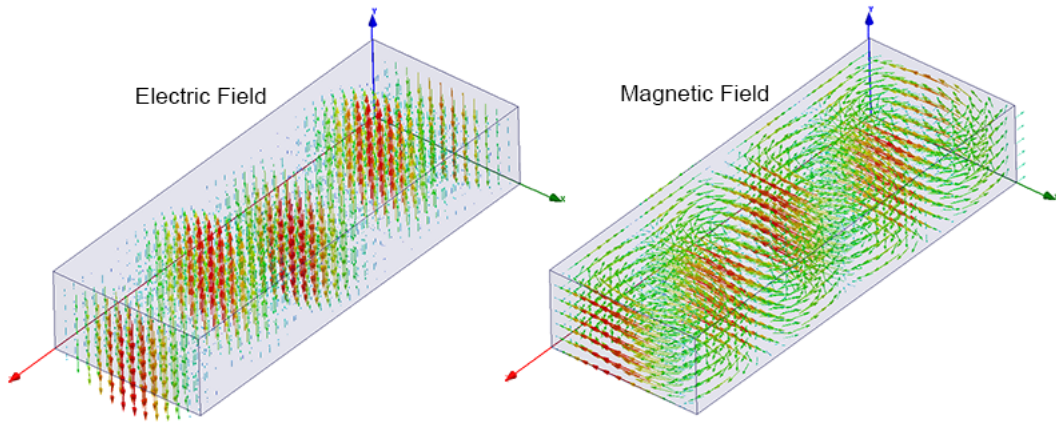


Figure 2.4: Electric and magnetic field vectors of the fundamental mode (70 GHz) propagating in a WR-12.

WR-15 waveguide ($a = 3.76$ mm, $b = 1.88$ mm): It can be seen that the theoretical monomodal bandwidth extends from 40 to 80 GHz, where the second mode starts to propagate, although it is commercially considered for applications limited to the 50-75 GHz range, in order to have some safeguard margins to take into account manufacture tolerances.

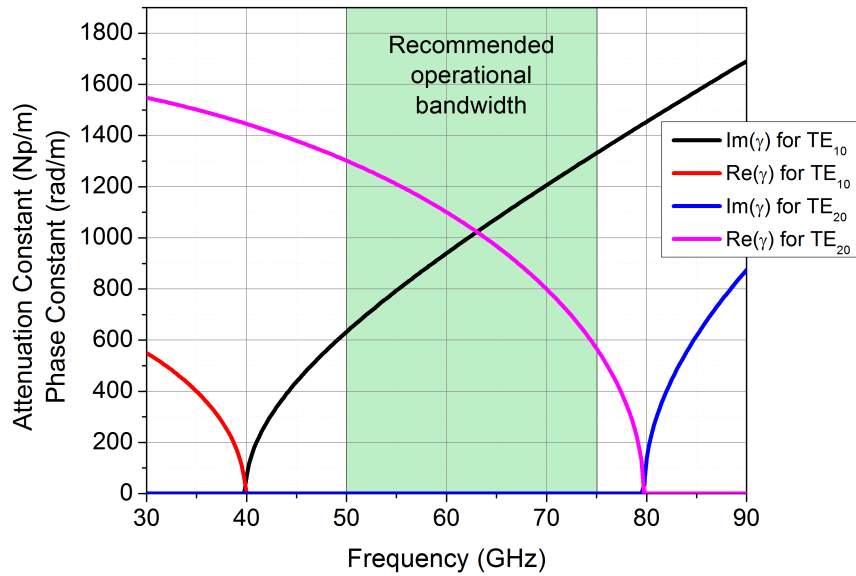


Figure 2.5: Propagation constant for the TE₁₀ and TE₂₀ field in WR-15.

The attenuation of a wave travelling in a WR can be expressed as the sum of the dielectric loss α_d (given by equation 2.1.2 and negligible for air-filled waveguides) and the

conductor loss α_c which can be expressed as [57]:

$$\alpha_{c, \text{TE}_{10}} = \frac{R_s}{b\eta_0\sqrt{1 - \left(\frac{f_c}{f}\right)^2}} \left[1 + \frac{2b}{a} \left(\frac{f_c}{f}\right)^2 \right] \quad (2.1.16)$$

with R_s given by equation 2.1.8. Figure 2.6 shows the attenuation constant of standard WR-12 and WR-15 waveguides made of brass and silver, extracted from full-wave analysis (HFSS). As it can be seen, the over-all attenuation constant decreases as frequency increases, and it is therefore preferable, in order to reduce loss, to use the waveguides at frequencies sufficiently higher than their cut-off frequency f_c . Furthermore, it can be seen that the conductivity of the used metal plays an important role, as the attenuation in brass waveguides can be twice as high as the one in silver, or other comparable good conductors such as copper or gold. From the depicted plots, the maximum theoretical loss, for a brass waveguide, can be computed to be always lower than 5 dB/m in the 50-90 GHz range. In practice, the loss due to waveguides will be higher, as the internal surface roughness⁵ affects the attenuation constant. Using a simplified *Groiss model*⁶ [59] to account for this effect in HFSS allows us to estimate that the attenuation constant of a WR-12 waveguide might be doubled even for a rms value of the roughness $\Delta = 0.5 \mu\text{m}$ (see Fig. 2.7). Note that real-life loss might be even higher, as discussed in section 2.1.4.

One of the main disadvantages of WR is that even the ones suited for mm-wave applications, although their internal dimensions shrink to fit with the requirements of the operational bandwidth, remain bulky and heavy components. In particular, the standardized interface of commercially available components remains very large: The diameter of the flange is ≈ 2 cm, even for those designed to operate in the mm-wave range. Another difficulty that has to be overcome when adopting WRs is the need of special transitions from planar circuits and devices, in order to efficiently couple the signal into the waveguide. One example of such transitions, used to achieve integration of photonic receivers with a WR output port, will be presented in Chapter 4.

2.1.3 Coaxial Cable

Coaxial cables (Fig. 2.8) are very common and versatile guiding structures, based on an internal cylindrical signal conductor (of radius a) and an external ground layer with circular cross section (of radius b), separated by a dielectric layer, which can also be air.

Similarly to the case of the WR, the external metal conductor guarantees a radiation-free operation. Due to the two separate metal conductors, a fundamental TEM mode can propagate, with zero cut-off frequency, which potentially makes coaxial cables very broadband lines. The upper frequency limit is approximately set by the cut-off frequency of the first higher-order TE or TM mode, which can be computed as [60]:

$$f_c = \frac{1}{\lambda_c \sqrt{\mu\varepsilon}} = \frac{1}{\pi(a+b)\sqrt{\mu\varepsilon}} \quad (2.1.17)$$

⁵The surface roughness is usually described as a root-mean-square (rms) value of the deviation of the metal's profile from a perfectly smooth surface.

⁶The Groiss model implemented in HFSS offers results close to the ones described by the experimental *Hammerstad-Jensen formula* introduced in equation 2.1.23.

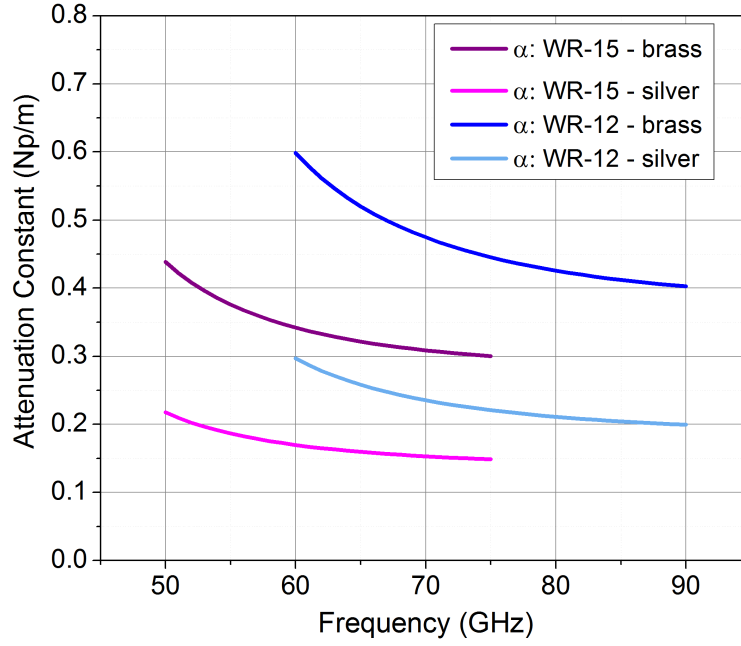


Figure 2.6: Attenuation constant of the TE_{10} mode in standard WR-15 (50-75 GHz) and WR-12 (60-90 GHz) waveguides made of brass and silver.

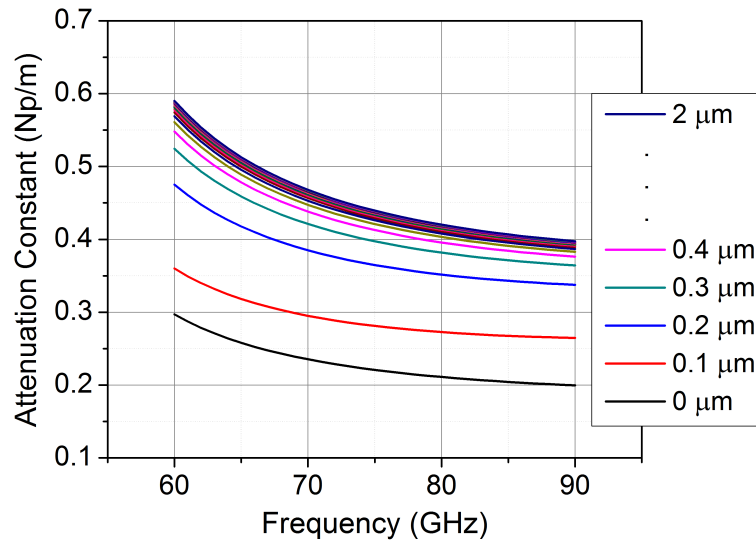


Figure 2.7: Impact of metal roughness (expressed as rms-value of its surface deviation) on attenuation of silver WR-12.



Figure 2.8: Geometry of coaxial cable.

where λ_c is the corresponding cut-off wavelength. From equation 2.1.17 follows that, in order to guarantee a broadband operation, the geometrical dimensions of the line (radii) have to be shrunk, which can constitute manufacturing problems for the upper mm-wave range (above 100 GHz) and dielectrics with low ε_r should be used. From static analysis it is possible to derive closed form equations for the characteristic impedance⁷ of coaxial transmission lines as a function of its geometrical parameters:

$$Z_0 = \frac{\eta}{2\pi} \ln \left(\frac{b}{a} \right) \quad (2.1.18)$$

where η is the wave impedance within the insulating dielectric. The expression of Z_0 can then be used to calculate the conductor attenuation constant as:

$$\alpha_c = \frac{R_s}{4\pi Z_0} \left(\frac{1}{a} + \frac{1}{b} \right) \quad (2.1.19)$$

with R_s given by equation 2.1.8, while the dielectric attenuation constant can be calculated by equation 2.1.2.

In spite of their important advantages (excellent isolation, low dispersion and wide-band operation), coaxial cables suffer of integration difficulties similar to those of WRs, as they have a complex, non-planar cross section and are generally much larger than chips or equivalent planar lines. Furthermore, access to the signal line is not straightforward because of the shielding ground layer.

2.1.4 Microstrip Line

Differently from the WR and the coaxial cable, the microstrip is a PTL, i.e. it can be created on a dielectric substrate using any of the techniques described in chapter 3⁸: It is therefore very compact and easily integrated with chips and devices. It is based on a conductive strip (signal line) with a ground metal layer, separated by a dielectric substrate, as shown in Fig. 2.9. Microstrips are physically small in comparison to the previously

⁷The common value for the characteristic impedance of commercial coaxial cables and connectors is 50 Ω (which is also a standard reference value for measurement equipment). This value is an average value between 75 Ω (the value of impedance that minimizes the propagation loss for air-filled coaxial cables) and the value of 30 Ω that guarantees the maximum power capacity [58].

⁸The research community is also engaged in the development of *planar versions* of coaxial lines and WRs. One example of the latter is the *substrate integrated waveguide* that will be discussed in section 2.1.6.

analyzed guiding structures and offer a very easy access to the signal line, although the connection to ground requires via holes or other techniques, such as lateral metallization. However, the open and inhomogeneous structure of microstrips exposes the circuits to other drawbacks, such as dispersion and risks of cross-talk, as it will be described in the following sections.

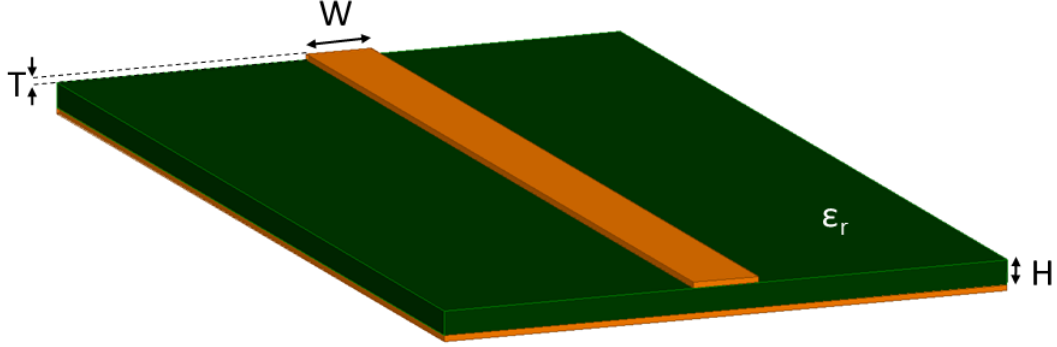


Figure 2.9: Model of microstrip line with width W and thickness T on a dielectric substrate of thickness H and permittivity ϵ_r .

Dispersion

The presence of two different dielectric materials (air and substrate) prevents a pure TEM propagation. However, the propagation along a microstrip can be described as a *quasi-TEM mode*, by considering an effective permeability μ_{eff} (although μ_{eff} is generally 1) and an effective permittivity, which is defined as the ratio of the capacitance of the line to the capacitance of the line in case the dielectric substrate is completely replaced by air [61]:

$$\epsilon_{\text{eff}} = \frac{C_{\text{actual}}}{C_{\text{air}}} \approx \frac{\epsilon_r + 1}{2} + \frac{\epsilon_r - 1}{2} G\left(\frac{W}{H}\right) \quad (2.1.20)$$

where $G(W/H)$ is a factor depending on the width W and substrate's thickness H , given in [62], together with formulas for the characteristic impedance of the line, also taking into account the impact of the metallization thickness T . The formulas are accurate within a 2% margin on a very large range of physical parameters.

In order to take into account the effect of dispersion at higher frequencies, that might be detrimental for broadband operation, corrections have been presented by several researchers, e.g. in [63–65]. However, the negative impact of dispersion can be neglected if [66]:

$$\frac{H}{\lambda_r} = \frac{Hf\sqrt{\epsilon_r}}{c_0} \leq 0.05 \quad (2.1.21)$$

with c_0 being the light speed in vacuum. Equation 2.1.21 is a rather strict rule and clearly shows that in order to achieve higher frequency operation, the substrate thickness H has to be kept to a minimum. If the substrate has a high dielectric constant, the restrictions on H are even stricter, as from a physical point of view, a larger dielectric layer with a

higher dielectric constant increases the inhomogeneity of the structure. As an example, it can be computed that to achieve 100 GHz operation on an alumina substrate ($\epsilon_r = 9.9$) the layer should not be thicker than 50 μm , while on a common polytetrafluoroethylene (PTFE) laminate (e.g. the Rogers RT/duroid 5880 [67], with $\epsilon_r = 2.2$) the maximum allowed thickness would be 100 μm . However the condition set by equation 2.1.21 can be relaxed, allowing the ratio H/λ to achieve values up to 0.2, if the line length is not excessively long [66].

Figure 2.10 shows the effective permittivity and the attenuation constant of microstrip lines as a function of frequency, for different values of impedance⁹. The plots assume a substrate with $\epsilon_r = 2.2$ and thickness $H = 127 \mu\text{m}$ and a metal thickness $T = 17 \mu\text{m}$.

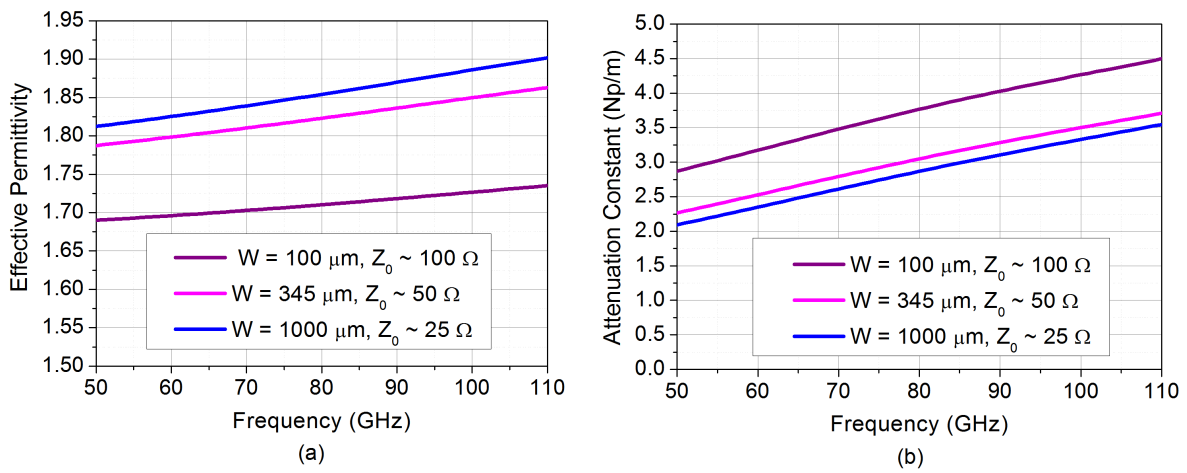


Figure 2.10: Effective permittivity and attenuation constant of microstrip lines for several line widths.

Losses

The microstrip tends to behave similarly to a “wire on a ground plate” [68], therefore radiating if the thickness of the substrate is too large. Formulas for radiation loss depend on the microstrip structure under analysis but show, as a general trend, that the radiated-to-incident power ratio is given by

$$\frac{P_{\text{rad}}}{P_{\text{in}}} = 2\pi \frac{\eta}{Z_0} \left(\frac{H}{\lambda_r} \right)^2 S(\epsilon_{\text{eff}}) \quad (2.1.22)$$

where the factor $S(\epsilon_{\text{eff}})$ depends on the actual microstrip configuration [69]. It is clear from equation 2.1.22 that thicker substrates increase the radiation loss and that the effect

⁹These results are obtained by HFSS solving a bidimensional problem based on the cross section of the transmission line, therefore essentially account for ohmic and dielectric losses only. All other propagation constants reported in following sections are based on the same simulation method, unless otherwise stated.

is stronger at higher frequencies (smaller wavelengths), eventually dominating other forms of power loss, as experimentally shown in [70, 71]. Using a dielectric with higher relative permittivity can mitigate this effect, by concentrating the field within the substrate and therefore decreasing unwanted radiation¹⁰ ($S(\epsilon_{\text{eff}})$ is always inversely proportional to the effective permittivity for any of the analyzed configurations), but could lead to higher dielectric and conductor loss, as discussed in the following.

For conductor and dielectric losses in microstrips, closed form formulas are reported in [72]. Dielectric loss can be reduced by using dielectrics with lower ϵ_r (for a given $\tan \delta$), which in turn might increase radiation loss. However, conductor loss is generally dominant in the mm-wave range (with the exception of particularly lossy dielectrics). Conductor loss can be decreased by using wider lines, as shown in Fig. 2.10, although the width W cannot be arbitrarily large, in order to prevent unwanted resonances¹¹, besides the constraints set by the required characteristic impedance of the line. Of particular interest is the effect of surface roughness on the conductor loss: The irregular surface of the metallization layers increases the path followed by the currents induced by the guided EM wave, therefore increasing the resistance and thus loss. Fitting of experimental data has lead to the derivation of formulas which allow to estimate the impact of the metallization roughness on the component of the attenuation constant due to metal as [61]:

$$\alpha_{c, \text{rough}} = \alpha_{c, \text{smooth}} \left\{ 1 + \frac{2}{\pi} \arctan \left[1.4 \left(\frac{\Delta}{\delta_s} \right)^2 \right] \right\} \stackrel{\text{def}}{=} \alpha_{c, \text{smooth}} F \left(\frac{\Delta}{\delta_s} \right) \quad (2.1.23)$$

As shown in Fig. 2.11, the factor $F(\Delta/\delta_s)$ in equation 2.1.23 can reach values of up to 2, thus doubling the α_c . As an example, it can be considered that a rms surface roughness of $2.5 \mu\text{m}$ is 10 times larger than the penetration depth of a 60 GHz signal in a copper-based microstrip ($\delta_s \approx 2.5 \mu\text{m}$), thus essentially doubling α_c . However, the phenomenon is not linear and even a roughness of $1 \mu\text{m}$ is enough to cause a 98% increase in α_c for the case considered above. This is clearly expressed by Fig. 2.11, which plots the attenuation constant of a $50\text{-}\Omega$ microstrip for different values of the rms surface roughness Δ : The *saturation* in the increase of loss is already visible for $\Delta = 0.5 \mu\text{m}$.

It should be noticed that, as the frequency increases, the penetration depth decreases (see Fig. 2.2), therefore the surface roughness plays a more critical role in the mm-wave range than in the lower microwave spectrum. Equation 2.1.23 was derived by fitting of a limited set of experimental data and might not perfectly model the effects of conductor loss on every structure or at very high frequencies. Recently, several models have been presented, which show that a factor of 3 or even 5 are possible in some cases [73, 74]. Those models take into account 3D features of the metal's profile, which might be subject to large variability due to manufacturing practices and repeatability, and require accurate profile measurements which are generally not made available by manufacturers. Therefore

¹⁰Obviously the considerations made here have to be seen in a different way in microstrip antenna applications: In fact, in that case it is desirable to use substrates which are thicker and have lower ϵ_r , in order to improve the overall radiation efficiency. Trade-offs are then required to prevent excessive loss on interconnecting lines, to avoid the excitation of higher-order modes, or if the area available for the antenna is a limiting factor.

¹¹See the following section for details on higher-order modes in microstrip lines.

equation 2.1.23 can be used to estimate the *minimum detrimental effect* due to surface roughness.

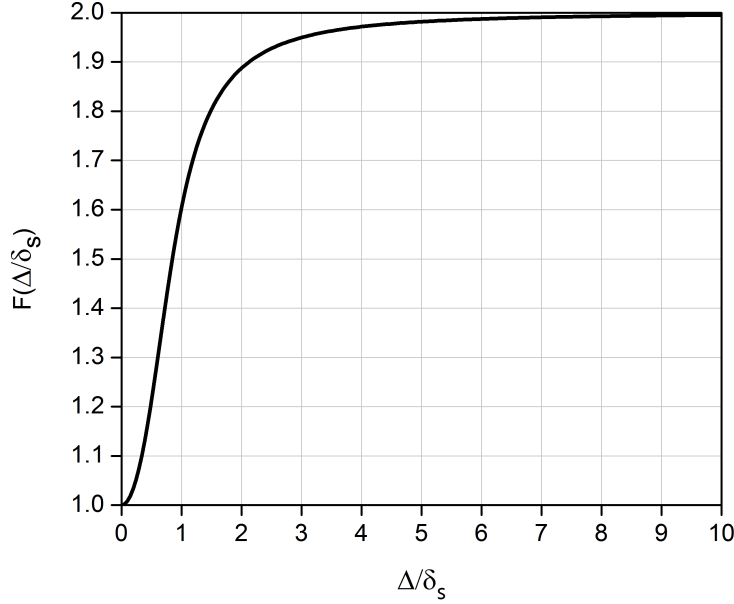


Figure 2.11: Multiplication factor for α_c due to surface roughness in microstrips.

Other Modes in Microstrip Structures

Energy leakage for microstrip can also occur with coupling to higher-order modes. In fact, several other modes, besides the fundamental quasi-TEM mode, can propagate in a microstrip circuit and they have to be taken into account in order to guarantee a proper functioning of the design.

Surface Waves Surface waves can exist at the air/dielectric interface of the microstrip substrate. They can be supported in form of TM or TE modes, and several modes can coexist, depending on the operation frequency. The lowest surface mode is the TM_0 mode, which has a zero cut-off frequency, i.e. it is intrinsically present in microstrip lines together with the fundamental quasi-TEM mode. However, its field's strength is negligible for low frequencies and it only becomes an actual source of leakage above the *critical frequency* [58]:

$$f_{TM_0} \approx \frac{c_0}{2\pi H} \sqrt{\frac{2}{\epsilon_r - 1}} \arctan(\epsilon_r) \quad (2.1.24)$$

Higher-order TM_n modes have cut-off frequencies given by:

$$f_{c, TM_n} = \frac{n c_0}{2H \sqrt{\epsilon_r - 1}} \quad (2.1.25)$$

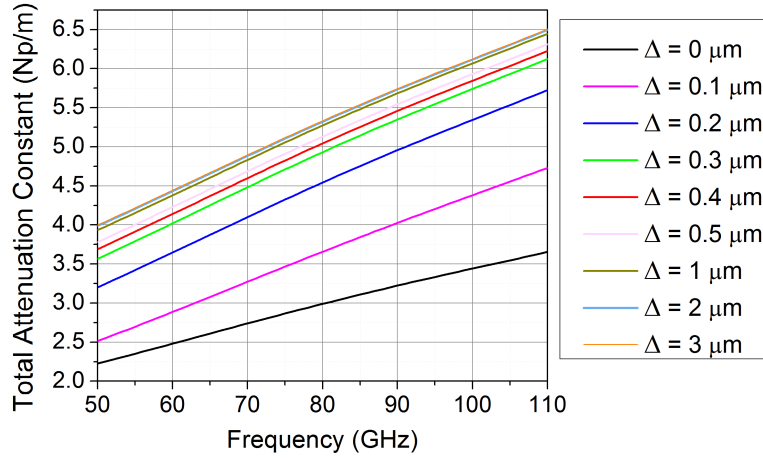


Figure 2.12: Total microstrip attenuation constant for different values of the rms surface roughness Δ .

where $n = 1, 2, 3, \dots$ is the mode index. However, the TE_1 mode starts propagating before the TM_1 and tends to be excited by any transverse discontinuities of the line. The cut-off frequencies for TE_n modes (with $n = 0, 1, 2, \dots$) are given by:

$$f_{c, TE_n} = \frac{(2n - 1) c_0}{4H\sqrt{\epsilon_r - 1}} \quad (2.1.26)$$

Transverse Resonance The transverse section of a microstrip can be considered as a possible transverse resonator if its width approaches $\lambda_r/2$. Although this field is generally orthogonal to the fundamental quasi-TEM mode of the microstrip, any discontinuity might allow a coupling and hence loss into this parasitic mode. This problem is particularly evident for wide lines as the first resonance frequency can be estimated to be [75]:

$$f_{c, Tr} \approx \frac{c_0}{2\sqrt{\epsilon_r}(W + H)} \quad (2.1.27)$$

One way to prevent transverse resonances is to use narrow longitudinal slots in the microstrip signal line; however it might be difficult to implement this solution in PCB technology in the mm-wave range, as the slot might have a non-negligible minimum dimension (e.g. $100 \mu m$) in comparison to the wavelength within the dielectric.

Parallel-Plate Mode Parallel-plate modes can propagate between the signal line and the ground when the thickness of the dielectric layer is close to $\lambda/2$ in the dielectric material, with the cut-off frequency given by [58]:

$$f_{c, PP} = \frac{c_0}{2H\sqrt{\epsilon_r}} \quad (2.1.28)$$

Table 2.2 summarizes the critical frequencies discussed above for two exemplifying commercial laminates, chosen taking into account their suitability for mm-wave applications (low $\tan\delta$) and their respectively low and high ε_r . The configurations considered in table 2.2 are:

1. Rogers RT/duroid 5880, $\varepsilon_r = 2.2$
 - a) $H = 127 \mu\text{m}$, $W = 383 \mu\text{m}$
 - b) $H = 254 \mu\text{m}$, $W = 805 \mu\text{m}$
 - c) $H = 381 \mu\text{m}$, $W = 1284 \mu\text{m}$
 - d) $H = 508 \mu\text{m}$, $W = 1813 \mu\text{m}$
2. Rogers RT/duroid 6010 [76], $\varepsilon_r = 10.2$
 - a) $H = 127 \mu\text{m}$, $W = 110 \mu\text{m}$
 - b) $H = 254 \mu\text{m}$, $W = 227 \mu\text{m}$
 - c) $H = 381 \mu\text{m}$, $W = 346 \mu\text{m}$
 - d) $H = 508 \mu\text{m}$, $W = 467 \mu\text{m}$

Note that the substrate thicknesses are chosen from the ones made available by the manufacturer and the line width has to be chosen, for every configuration, in order to achieve a characteristic impedance of 50Ω (assuming a metallization thickness of $10 \mu\text{m}$), which can be considered to be as a must-have value in any design. However, lower impedance values might be necessary for specific applications, which would require a wider W and therefore would decrease the $f_{c, \text{Tr}}$ of the transverse resonance mode. From the values listed in table 2.2, it can be seen that using very thin laminates ($H = 127 \mu\text{m}$) does not set restrictions on the choice of ε_r (all critical frequencies are above 195 GHz ¹²). However, if thicker laminates are necessary (for mechanical reasons or for antenna requirements), using substrates with low ε_r is necessary, as critical frequencies appear already below 100 GHz for a $250\text{-}\mu\text{m}$ -thick Rogers RT/duroid 6010.

Another reason to prefer low values of ε_r in the mm-wave range is that this reduces the impact of manufacturing tolerances on the final design, differently from the lower microwave spectrum where high effective permittivity is a precious resource used to shrink the otherwise unpractically large design, as it will be discussed in chapter 3.

Obviously, similar conclusions can be drawn for ceramic substrates, as the range of available relative permittivity is similar (see chapter 3 for more details), or semiconductor-based designs (although in this case the choice is generally limited to higher values of ε_r); in these cases, however, thinner substrates can be considered thanks to different manufacturing technologies or to the usage of *thinning techniques*.

¹²We are limiting this analysis to the upper limit of the W-band (120 GHz).

Table 2.2: Critical frequencies of parasitic modes in microstrip lines.

Config.	f_{TM_0} (GHz)	f_{c, TM_1} (GHz)	f_{c, TE_1} (GHz)	$f_{c, \text{Tr}}$ (GHz)	$f_{c, \text{PP}}$ (GHz)
1-a	555	1078	539	227	796
1-b	277	539	269	108	398
1-c	185	359	180	69	265
1-d	139	270	135	49	199
2-a	258	389	195	271	370
2-b	129	195	97	132	185
2-c	86	130	65	88	123
2-d	65	97	49	65	82

2.1.5 Grounded Coplanar Waveguide

Grounded coplanar waveguides, also called *conductor-backed coplanar waveguides*, can be considered as an extension of the microstrip concept, where ground layers have been added on the top side of the substrate, using the same metal layer of the signal line (see Fig. 2.13). This overcomes one of the main practical drawbacks of microstrips (i.e. the difficulty in accessing ground layers for short-circuiting purposes or grounding of surface-mount components and chips) and additionally establishes grounding paths between different lines, thus improving isolation.

With or without lower ground plane, coplanar waveguides are common lines for integrated circuits, especially in the mm-wave range, and they are a natural choice for several electronics and optoelectronic devices with coplanar output pads (e.g. modulators and PDs¹³), and they are particularly suitable for flip-chip integration, a technique often used in mm-wave assemblies (see section 3.5.2). Grounded coplanar waveguides generally offer better isolation and dispersion properties than microstrips [77], and tend to radiate less, reducing power loss [71] and EM interference [78].

Grounded coplanar waveguides can support several modes, with the fundamental one being a quasi-TEM *coplanar waveguide mode*, for which an effective dielectric constant and a characteristic impedance can be defined and calculated using formulas derived by means of conformal mapping techniques and experimentally validated [79], similarly to the microstrip's case. Here, however, the thickness of the top metal layer plays a stronger role for the actual field distribution, as strong capacitive coupling can occur between the edge of the signal lines and those of the top metal layers. Therefore corrections for the dimensioning of the signal line have been developed, in order to include the impact of the metallization into the formulas for the characteristic parameters of GCPW [80]. The additional top ground plates add a degree of freedom for the designer, as they not only

¹³See Fig. 2.22 and 4.31.

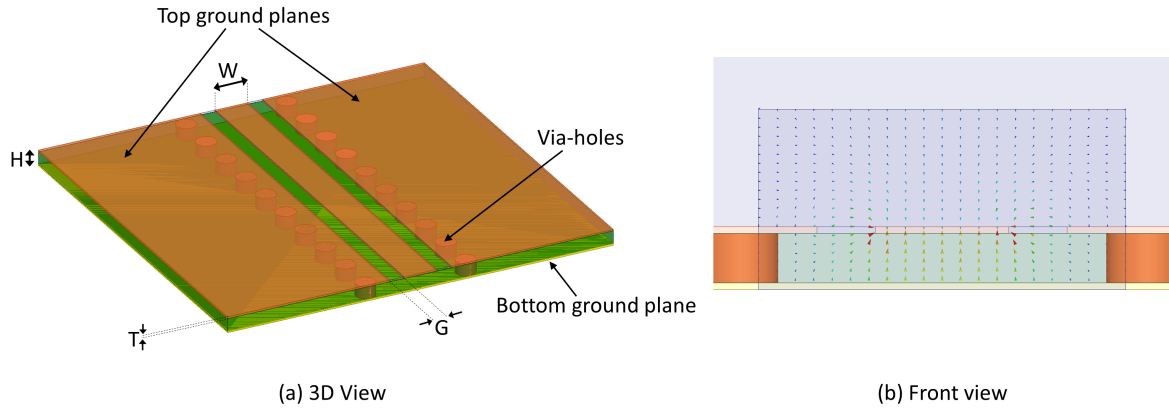


Figure 2.13: (a) Model of GCPW, with highlighted fundamental parameters (line with width W , line gaps G , metal thickness T , dielectric thickness H) and (b) front view of the line, showing the electric-field distribution of the fundamental mode.

expand the range of achievable characteristic impedances for a given substrate thickness H , but also allow a required characteristic impedance to be obtained by several combinations of line width W and slot width G .

Additional modes can be carried by the GCPW (or generated at discontinuities). In particular, if a voltage difference is established across the lateral ground planes, a *slotline mode* can be excited and propagate. Its excitation can be avoided by using air-bridges or metallized via holes to guarantee that the ground plates have similar potential at key points of the circuit. Furthermore, the parallel plate mode, whose cut-off frequency can be calculated by equation 2.1.28, can obviously be excited between the top and bottom metal layer. Conductive via holes short-circuiting the top and bottom ground layers are an effective solution in this case too, especially if they are drilled close to the internal border of the top ground plates, next to the signal lines. Besides the transverse resonance, which can be calculated by equation 2.1.27, an additional radiation problem, which can be very detrimental for the transmission properties of the line, can occur in GCPW circuits due to the large top ground planes: They can give rise to patch-antenna resonances at frequencies identified by¹⁴:

$$f_{mn} = \frac{c_0}{2\sqrt{\varepsilon_r}} \sqrt{\left(\frac{m}{W_g}\right)^2 + \left(\frac{n}{L_g}\right)^2} \quad (2.1.29)$$

where m and n are the resonance indices, c_0 the speed of light in vacuum, ε_r is the dielectric constant of the substrate, L_g is the length of the substrate and W_g its width. For circuits larger than a few millimeters, such as multi-chip modules that are usually in the centimeter scale, these resonances are well within the mm-wave frequency range and must be avoided, as they can dramatically increase the loss due to radiation. The usage of closely spaced via holes can prevent these resonances from appearing within the working range of the circuits: As a rule of the thumb, it can be considered that the maximum via-to-via pitch

¹⁴Note that equation 2.1.29 is a specialized case of equation 2.4.3, introduced in section 2.4.1.

should be less than a half wavelength [77,81] in the dielectric, preferably approaching a quarter of wavelength [82]. This helps reducing the overall loss of GCPWs in comparison to microstrips at high frequencies [71,78], but also sets a limit on the highest operational frequency of the line, for a chosen substrate thickness, as it will be discussed in section 3.4.4. It is also important to highlight that metal-plated or, preferably, metal-filled via holes have additional value for the design, as they can be used to convey heat generated by active components (diode, amplifiers) to the bottom ground plane.

Figure 2.14 shows the effective permittivity and the attenuation constant of a 50- Ω GCPW based on the Rogers RT/duroid 5880, with the following geometrical parameters: $W = 340 \mu\text{m}$, $H = 127 \mu\text{m}$, $G = 150 \mu\text{m}$, $T = 17 \mu\text{m}$ and $\varepsilon_r = 2.2$.

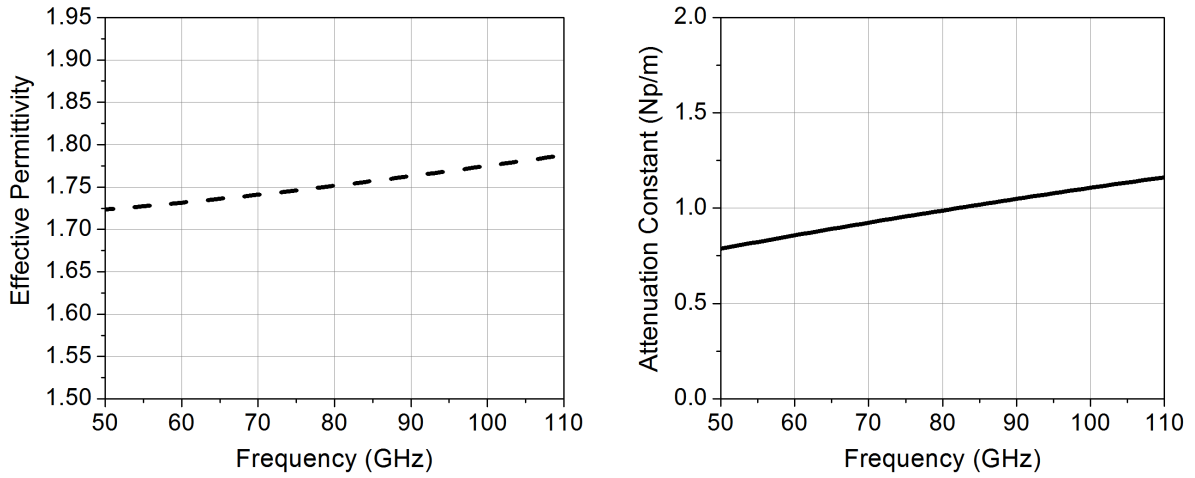


Figure 2.14: Effective permittivity and attenuation constant of GCPW.

2.1.6 Substrate Integrated Waveguide

As described in the previous sections, planar configurations are very practical and allow the development of a large range of compact and light structures, but they generally suffer of interferences and cross-talks, undesired radiation, and cannot support a large amount of RF power. Normally, for applications where high power, low loss, or a high quality factor are demanded, the bulky and expensive metallic WR are the mandatory choice for the designer.

Recently, an innovative guiding structure has been introduced in order to cover the gap between planar technologies and WRs. The structure, called substrate integrated waveguide (SIW), post-wall waveguide [83] or laminated waveguide [84], is a replica of the WR, built by using top and bottom metal layers on a dielectric substrate, connected by vertical metalization (in form of metallic walls or a fence of metalized slots or via holes). It has a high quality factor, a characteristic which makes it suitable for low-loss filters [85,86] and resonators [87], but also high-power handling possibilities, which suggest its application for the development of compact power dividers [88] and directional couplers [89,90]. Several antennas based on SIW have also been proposed: In particular, the nature of the SIW makes it particularly convenient for the development of slot arrays

(as shown by [91–94], among others) and H-plane horn antennas (e.g. in [95–97]), but more complex multi-layer configurations have also been reported (e.g. in [45, 98, 99]).

Several techniques can be used to create SIWs, such as advanced thin-film and thick-film technology or co-fired ceramics, however their advantages are especially interesting when developed using PCB technology on traditional RF substrates.

Figure 2.15 shows an example of SIW modeled in HFSS. The model is based on a Rogers RT/duroid 5880 with $381\ \mu\text{m}$ thickness (H) and metallized copper layers. The other parameters are: $W = 2.5\ \text{mm}$, via-hole diameter $d = 200\ \mu\text{m}$ and pitch $p = 400\ \mu\text{m}$. The via holes are assumed to be plated with $10\ \mu\text{m}$ copper (this value is large enough to prevent any transmission of mm-wave signals through the metallization layer, as discussed in section 2.1.1).

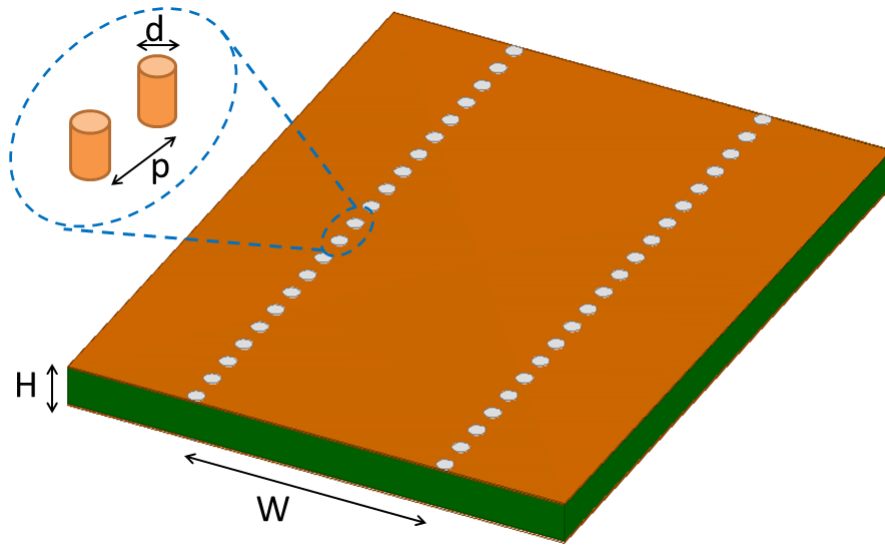


Figure 2.15: Model of SIW, with highlighted fundamental parameters (d = diameter of via holes, p = pitch between via holes, H = thickness of substrate, W = width, or distance between the lateral walls.)

Due to their nature, SIWs share most of WRs characteristics, although not all propagation modes can be supported. In particular, the discontinuous side walls prevent the propagation of all modes that require the current to flow in the direction of propagation (i.e. all TM_{mn} and TE_{mp} with $p \neq 0$), while TE_{m0} modes are supported. The electric-field distribution of the first two modes (TE_{10} and TE_{20}) is shown in Fig. 2.16-left, together with their attenuation and phase constants (clearly similar to the ones of the TE_{10} and TE_{20} of WR): It can be seen that, to achieve single mode operation, the usable bandwidth of the SIW is limited to about 50%, like in the case of standard WRs. The simulated S-parameters of the structure for a length $L = 5\ \text{mm}$ are shown in Fig. 2.16-right.

Furthermore, they are very thin in comparison to traditional WRs and, similarly to dielectric-filled metallic waveguides, the adopted substrates have $\epsilon_r > 1$: Both factors contribute to lower the characteristic impedance when compared to WR operating in the

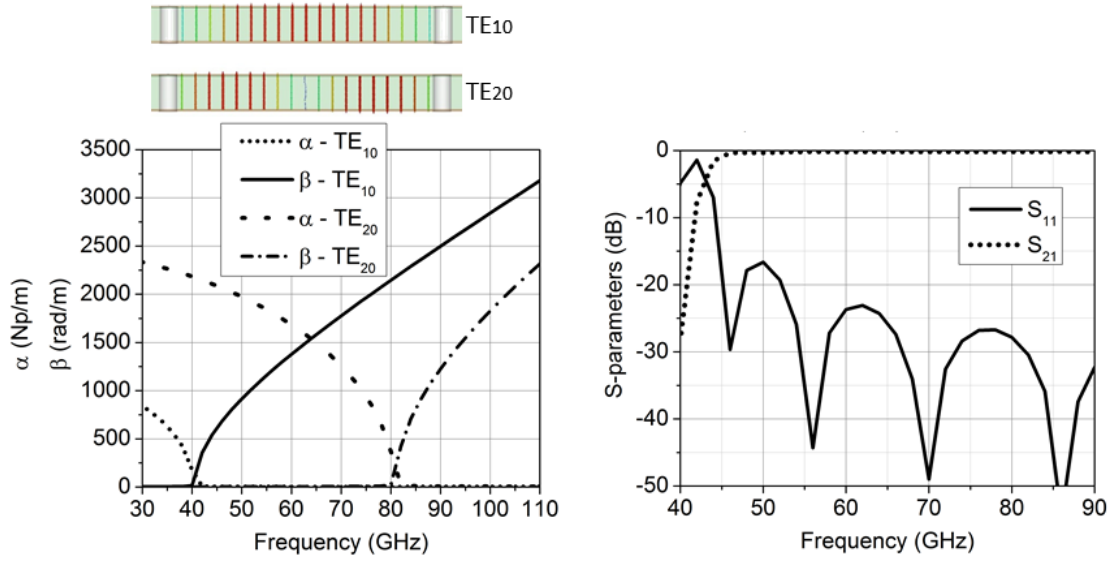


Figure 2.16: Left: Electric field distribution, attenuation and phase constants of the TE₁₀ and TE₂₀ modes mode in the SIW. Right: S-parameters of the SIW obtained by monomodal simulation (HFSS).

same frequency range. The characteristic impedance¹⁵ of the SIW depicted in Fig. 2.15 is $\approx 75 \Omega$ at 60 GHz, whereby the impedance of a common WR-15 would be $\approx 500 \Omega$. Other values of impedances for several configurations (substrate thickness and line width) are given in table 2.3.

Several simple formulas (empirical and semi-analytical) have been proposed in order to establish an equivalence between SIW and WR [101–103]. The correspondence can easily be achieved by observing that, due to the spacing between the via holes, the *width* of the EM field is *modulated* along the transmission line (see Fig. 2.17); this must be considered when modelling the SIW as a WR. In particular, the following relation can be taken into account [103]:

$$W_{\text{eff}} = W - 1.08 \frac{d^2}{p} + 0.1 \frac{d^2}{W} \quad (2.1.30)$$

where W_{eff} is the effective width of the WR corresponding to a SIW of width W , thus establishing a cut-off frequency for the fundamental mode: $f_c = c_0/\lambda_c = c_0/(2\sqrt{\epsilon_r} W_{\text{eff}})$. Note that equation 2.1.30 is an empirical formulation and it is valid for $p < 3d$ and $d < W/5$.

¹⁵Note that, as it is indicated by equations A.3.9–A.3.12 in appendix A.3, the characteristic impedance of TE₁₀ waves is a function of frequency. The values reported here are estimations calculated by HFSS at 60 GHz [100], based on the transmitted power and the excited current within the waveport, and are only intended to describe the influence of the substrate thickness on the characteristics of the SIW.

Table 2.3: Characteristic impedance Z_0 of a SIW for different values of the substrate thickness H and width W). The dielectric constant of the substrate is $\varepsilon_r = 2.2$.

H (μm)	W (mm)	Z_0 (Ω)
127	2	60
	2.3	41
	2.7	31
254	2	120
	2.3	86
	2.7	61
508	2.3	165
	2.7	123
	3	104

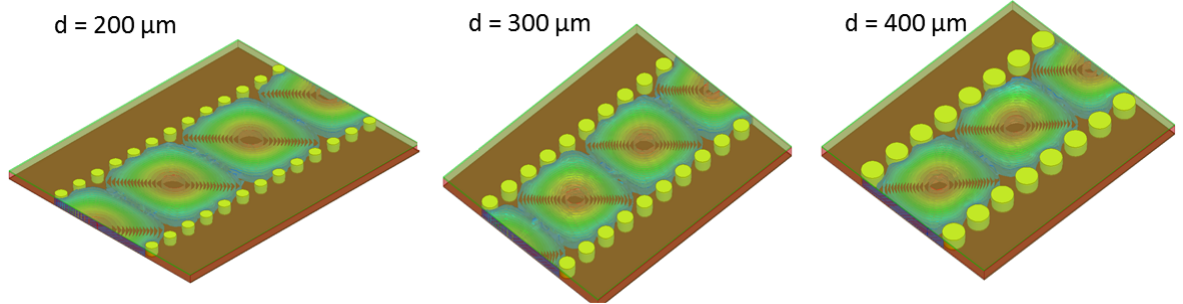


Figure 2.17: Modulation of the SIW field for several values of the via holes diameter d .

Loss in SIWs

The SIW is subject to three main mechanisms of loss, due to conductor, dielectric and leakage/radiation [104]. The conductor (α_c) and dielectric (α_d) components of the attenuation constant can easily be calculated by considering the corresponding formulas for traditional dielectric-filled WR (see equations 2.1.16 and 2.1.2), which can be rewritten here as:

$$\alpha_c = \frac{\sqrt{\pi f \varepsilon_0 \varepsilon_r}}{H \sqrt{\sigma_c}} \frac{1 + 2(f_c/f)^2 H/W_{\text{eff}}}{\sqrt{1 - (f_c/f)^2}} \quad (2.1.31)$$

$$\alpha_d = \frac{\pi f \sqrt{\varepsilon_r}}{c \sqrt{1 - (f_c/f)^2}} \tan \delta \quad (2.1.32)$$

Equation 2.1.31 clearly shows that, as in the case of the WR, the conductor loss, for a given width W_{eff} (usually fixed by the required operating bandwidth), can be reduced by increasing the thickness H of the substrate, up to $W_{\text{eff}}/2$, although in SIW technology lower limits might be imposed by the manufacturing constraints (e.g. the allowed via-holes aspect ratio) or other design requirements¹⁶. Figure 2.18-left shows the simulated attenuation constant¹⁷ in SIW lines of width $W = 2.5$ mm for different substrate thicknesses, confirming the considerations made above. Furthermore, in Fig. 2.18-right the impact of the rms surface roughness Δ is analyzed for the same SIW, in the case of $H = 127 \mu\text{m}$.

From equation 2.1.32 it can be seen that the usage of low-loss laminates (with minimal $\tan \delta$) is necessary to minimize the dielectric loss.

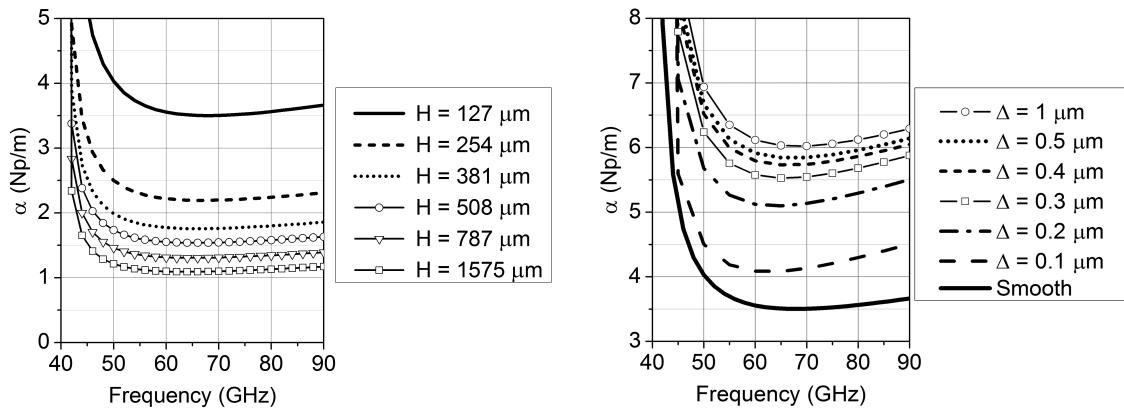


Figure 2.18: Attenuation constant of SIW: Impact of substrate thickness (left) and impact of metal surface roughness (right).

¹⁶In particular, this is in contrast with the need for reducing the substrates thickness in order to increase the operational bandwidth of other planar transmission lines, as discussed in section 2.1.4.

¹⁷It must be noted that, for the SIW, the attenuation constant estimated by two-dimensional simulation will be close to the actual one, as radiation loss is essentially absent from the SIW if the via holes are dimensioned according to the guidelines given in the following section (*Regions of Operation*).

While the dimensioning of the via holes does not play a direct role for conductor and dielectric loss (except for its influence on the W_{eff}), it becomes critical when analyzing radiation loss in SIWs. The pitch between two via holes regulates the amount of leaking field and it can be shown that negligible loss can be achieved when $p < 2.5d$ [105], although other restrictions might be necessary, in particular with respect to the wavelength of the operating frequency, as it will be introduced in the next section.

Regions of Operation

SIWs working in their fundamental mode have a cut-off wavelength given by $\lambda_c = 2\sqrt{\varepsilon_r} W_{\text{eff}}$ and the radiation loss is negligible when the spacing between the via holes is kept small enough. However, SIWs might also be considered for operation as leaky-wave structures/antennas, with the leakage rate regulated by the geometry of the via hole fence. Some assumptions can be made in order to establish working regions regulated by the relative dimensions of the via-hole diameter and pitch [104]. Considering a maximum acceptable value of 10^{-4} Np/rad for the attenuation due to radiation when operating as guiding structure and a minimum radiation *attenuation* of 10^{-3} Np/rad for leakage wave antenna, three regions (leakage, forbidden and guided-wave) can be found in the D - P plane. Furthermore, the intrinsic periodicity of the SIW can lead to band-gap effects, with the first band-gap resonance appearing for $\beta p = \pi$. As band-gap effects can have very detrimental effects on the transmission properties of the guiding structure [103], the dimensioning of the SIW should guarantee that band-gap phenomena are external to the operating bandwidth of the line, i.e. they should occur at $f \geq 2f_c$. Hence [106]:

$$\beta = \frac{\pi}{p} \implies \sqrt{k^2 - k_c^2} = \frac{\pi}{p} \implies \sqrt{4k_c^2 - k_c^2} = \frac{\pi}{p} \implies \sqrt{3}k_c = \frac{\pi}{p} = \frac{2\sqrt{3}\pi}{\lambda_c} = \frac{\pi}{p} \quad (2.1.33)$$

which results in the following constraint:

$$\frac{p}{\lambda_c} \leq \frac{1}{2\sqrt{3}} \approx 0.25 \quad (2.1.34)$$

where the limit has been reduced to 0.25 in order to account for tolerances. The limits identified by the phenomena discussed above are summarized in Fig. 2.19 and must be taken into account when designing SIW circuits¹⁸.

To illustrate the impact of the pitch on the characteristics of the line, Fig. 2.20 shows the simulation of a 5-mm-long SIW for different values of the via hole separation: While passing from 400 to 800 μm only causes minor leakage and has a minor impact on the S_{21} , using a pitch of 1600 μm adds up to 3 dB of loss.

¹⁸Note that Fig. 2.19 identifies an additional *over-perforated region*, which is defined by assuming that $s < \lambda_c/20$. This condition sets a lower limit for the operating frequency, which is less important for applications in the mm-wave range.

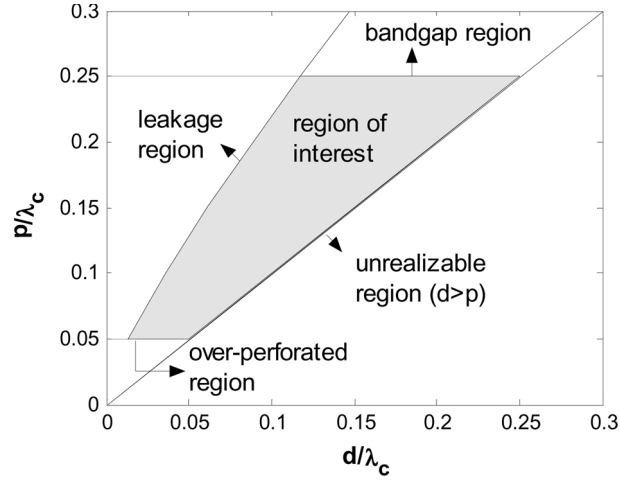


Figure 2.19: SIW: Regions of operation. © 2006, IEEE. Reprinted, with permission, from [106].

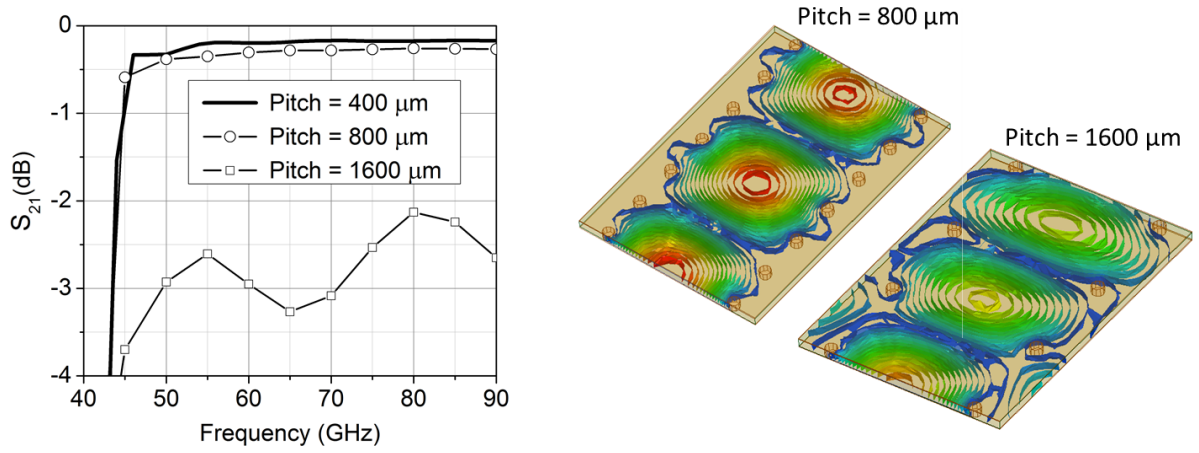


Figure 2.20: Simulated S_{21} of SIW for different values of the pitch (left) and corresponding electric field distributions (right).

2.1.7 Optical Fiber

An optical fiber is essentially a cylindric dielectric waveguide which guides EM waves thanks to total internal reflection, with the propagation taking place in form of TM, TE, quasi-TE (HE), and quasi-TM (EH) modes [107]. They are used to collect the optical signal generated by a laser source and to guide it, together with the carried information, to a PD. The actual structure of an optical fiber consists of a glass core (although quartz or plastic fibers are used too), surrounded by a cladding layer whose refractive index $n = \sqrt{\epsilon_r}$ is lower than the one used for the core. They are extremely important to achieve wired long-distance communication, as signals transmitted via optical fiber undergo an attenuation which can be several orders of magnitude smaller than the one that would take place in metallic guiding structures. They furthermore are immune to EM interference, are not sources of undesired radiation, are generally not expensive (the average cost is only a few dollars per meter [2]) and offer a bandwidth of several dozens of THz, which makes possible the transmission of signals even in the frequency ranges above the mm-wave bands.

The common range of applicability of optical fibers comprises wavelengths between 0.6 and 1.7 μm , although special *windows* are preferred for communication applications. The minimum achievable loss profile in glass fibers is essentially due to Rayleigh scattering occurring because of the amorphous nature of glass and the irregular distribution of its SiO_2 molecules. Being the Rayleigh scattering inversely correlated with the fourth power of the wavelength, systems operating at higher wavelength are generally preferable. However, fibers contain a considerable amount of O-H compounds (originated by the penetration of hydrogen atoms within their structure), which show resonances similar to those of water, with a large absorption peak at 2730 nm, as well as additional absorption occurring at several other wavelengths. As a result, some wavelengths are not favorable for long-distance communication, leaving two main bands¹⁹ to the interest of researchers. In particular, the window centered at 1550 nm, which offers the lowest attenuation (only 0.2 dB/km), and the window centered at 1300 nm, with a slightly higher attenuation (0.5 dB/km). The interest in the latter is due to the fact that at ≈ 1300 nm SiO_2 exhibits almost no chromatic dispersion M , i.e. the dispersion due to changes of the refractive index with the wavelength, which is often expressed in ps/nm-km and is given by [107]:

$$M = \frac{1}{c\lambda} \left(\lambda^2 \frac{d^2 n}{d\lambda_0^2} \right) \quad (2.1.35)$$

On the contrary, the 1550 nm band can show values of chromatic dispersion as high as 20 ps/nm-km, but its superior low-loss profile and the fact that all-optical amplifiers essentially work in the same band make it the preferred choice for high-end applications [108]. Depending on the size of the core, fibers can be classified as single-mode and multi-mode. Single-mode fibers have a core's diameter of less than 10 μm , allowing the propagation of only one mode (the fundamental HE_{11} mode), with a radial field amplitude

¹⁹A traditional bandwidth, centered at a wavelength of 850 nm, is also used (although its attenuation and dispersion characteristics are worse than the other two bands) as its wavelength fits with the one of the first generation of laser diodes and because it is particularly suitable for monolithic integration of electrical and optical GaAs devices [108].

that can be approximated as a gaussian beam [107]:

$$I(r) = I_0 e^{-\frac{2r^2}{r_0^2}} \quad (2.1.36)$$

Multi-mode fibers have cores which are larger than 50 μm (whose main advantage is the easier coupling of light from a source), which allows a very large number of modes to propagate at the same time. Multi-mode fibers suffer of rather significant modal dispersion (generally higher than the intrinsic chromal dispersion of the material), which generally makes them not suitable for high-end applications [108].

Optical fibers suffer of several other non-idealities (waveguide dispersion, polarization-mode dispersion, unperfect field confinement, as well as other linear and nonlinear effects) which can reduce the practical bandwidth and length of the interconnects. A detailed treatise of these phenomena is given in [109].

2.2 Millimeter-Wave Photodiodes

Photodiodes are among the most common used *photodetectors*, thanks to their compatibility with semiconductor manufacture technology, their small size and overall good performance. The working principle of PDs is based on the fact that any incident photon whose energy E_{photon} exceeds that of the band-gap energy of the PD material can be absorbed and used to generate a *photocurrent* I_{photo} [107], i.e.:

$$E_{\text{photon}} = hf \geq E_g \quad (2.2.1)$$

where h is the Plank's constant, f the frequency of the light wave and E_g is the band-gap of the PD material, as shown in Fig. 2.21. This corresponds to a maximum wavelength given by:

$$\lambda_{\text{max}} \approx \frac{1.24}{E_g} \quad (2.2.2)$$

where λ is expressed in μm and E_g in eV ²⁰. Typical values of λ_{max} for common semiconductor substrates and compounds can be found in table 2.4: It can be seen that more advanced compounds are needed in order to develop materials with a band-gap and absorption properties suitable for operation at the standard optical communication wavelengths²¹ [110, 111].

The ability of the PD to generate a photocurrent under illumination is generally expressed via its *responsivity* R_λ :

$$R_\lambda \stackrel{\text{def}}{=} \frac{I_{\text{photo}}}{P_{\text{opt}}} = \frac{\eta_q q \lambda}{hc_0} \quad (A/W) \quad (2.2.3)$$

²⁰1 eV = 1.60218×10^{-19} J.

²¹Optical communication systems have mostly been developed at 1300 and 1550 nm because of the particular properties of optical fibers at these wavelengths, as discussed in section 2.1.7.

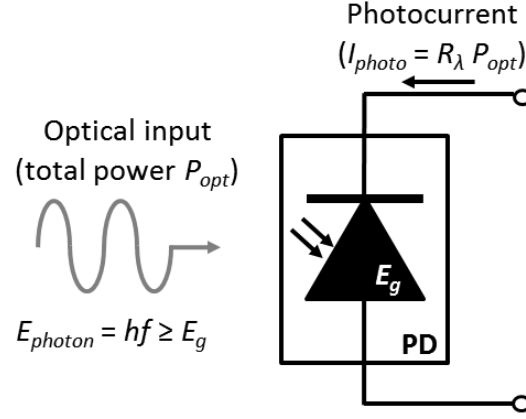


Figure 2.21: Working principle of a PD.

Table 2.4: Energy band-gap and maximum absorbed wavelength of different semiconductor compounds.

Semiconductor	E_g (eV)	λ_{max} (μm)
Si	1.12	1.107
GaAs	1.42	0.873
InP	1.35	0.916
$In_{0.7}Ga_{0.3}As_{0.64}P_{0.36}$	0.89	1.393
$In_{0.53}Ga_{0.47}As$	0.75	1.653

where P_{opt} is the incident optical power, q is the elementary charge of one electron, λ is the wavelength of the light beam, c_0 is the speed of light in vacuum, and η_q is the *quantum efficiency*, defined as the ratio of the number of generated electrons per second to the number of impinging photons per second. For a standard pin PD (see section 2.2.1) the quantum efficiency is related to the *absorption coefficient* α_{abs} and the width W of the absorption layer by:

$$\eta_q = \frac{P_{\text{abs}}}{P_{\text{opt}}} = (1 - \Gamma) (1 - e^{-\alpha_{\text{abs}}W}) \quad (2.2.4)$$

where P_{abs} is the total absorbed optical power and Γ is the reflectivity of the air/semiconductor interface, which reduces the amount of light actually penetrating into the absorbing layers. The responsivity can be regarded as a transfer function of the PD and its values are generally in the range of 0.2-0.8 A/W. Difficulties to achieve values approaching 1 A/W are mostly due to and recombination of electron-holes pairs before they can actually contribute to the photocurrent. The first problem can be addressed by either artificially roughening the external surface of the diodes or applying an *anti-reflection layer* with an intermediate refractive index between the one of air ($n = 1$) and that of the semiconductor. This solution also mitigates recombination occurring at the air/semiconductor interface, although further recombination might occur within the PD itself, due to fabrication imperfections of the wafers. The total current flowing through a PD is the sum of the photocurrent and the so-called *dark current*, which can be expressed as the current of a classical p-n junction:

$$I_{\text{tot}} = I_{\text{dark}} - I_{\text{photo}} = I_s e^{\left(\frac{qV}{nkT} - 1\right)} - I_{\text{photo}} \quad (2.2.5)$$

where I_s is the reverse saturation current, V is the voltage applied across the junction, T is the absolute temperature, k is the Boltzmann constant and n is the ideality factor of the pn-junction. Note that in case of positive bias, the dark current will largely dominate the photocurrent, while with a moderate reverse bias it will essentially result in a nonzero current level in absence of illumination, that must be taken into account at circuit level. Typical values of dark current are in the μA -nA range.

The minimum detectable power P_{min} for a PD is established by the current noise floor, to which dark current, thermal noise, and shot noise contribute, and by the reponsivity, i.e.:

$$P_{\text{min}} = \frac{I_{\text{noise}}}{R_\lambda} \quad (2.2.6)$$

As an example, for a current noise floor of 1 nA and a responsivity of 0.5 A/W, the minimum power that the PD can detect is in the order of 2 nW.

Photodiodes, independently of their internal structure, are either equipped with on-chip antennas used for direct radiation of the mm-wave signal extracted from the light carrier (see section 2.4.1 and reference [112] for an example), or have electrical interconnects (generally in form of coplanar or grounded coplanar waveguide as shown in Fig. 2.22 and in references [110, 112, 113], among others) from which the signal can be extracted,

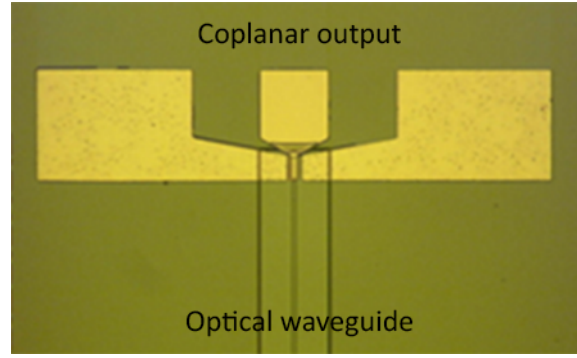


Figure 2.22: Typical coplanar output contacts of laterally illuminated PDs.

eventually conditioned, and guided to transitions to in-package or external antennas (see sections 2.4.2 and 2.4.3).

In the following sections, an overview of the most common PD configurations used in the mm-wave range will be given. For a more comprehensive treatise and for additional alternative configurations, the reader can refer to [26, 108, 114, 115].

2.2.1 pin-Photodiodes

The pin-PD is an improvement of the basic pn-junction diode, where a large intrinsic layer is included between the external p/n doped layers. The electron-hole generation occurs in this region, with light being forced to pass through one of the two external layers in traditional vertically illuminated PDs²². The electric field established by the positively and negatively doped layers can thus easily push the carriers, whose movement will be parallel to the direction of propagation of the light wave, towards the electrical contacts at the output of the PD.

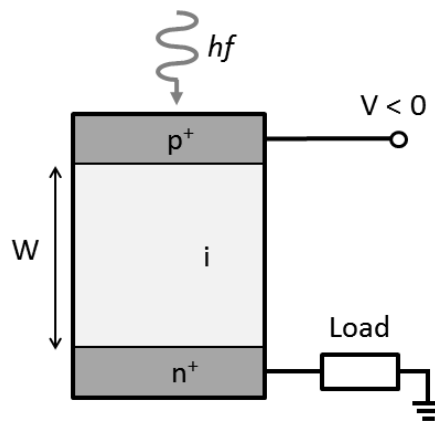


Figure 2.23: Schematic representation of a pin-PD.

²²Note that carriers generated in the doped layers mostly recombine without contributing to the photocurrent and will not be considered in this analysis.

The major mechanisms that limit the speed of pin-PD can be identified as the total diode capacitance (i.e. the diode capacitance of the depleted region plus any other external parasitic capacitance) and the transit time required by the carriers to cross the depletion layer. Unfortunately, the two issues cannot be addressed separately and require a trade-off in the design phase. In fact, the transit time can be decreased by decreasing the width of the intrinsic layer, but this would in turn both increase the capacitance of the junction (therefore increasing the RC-constant of the electrical model of the PD) and decrease the responsivity of the PD (which is proportional to the volume of the depletion region, i.e. to both its width and area). This limits the usage of traditional pin-PD to the lower mm-wave spectrum, with 3-dB bandwidth in the order of 40-50 GHz [116, 117].

In order to achieve higher operational frequencies, laterally illuminated pin-PD have been developed, where a narrow (thinner than $1\ \mu\text{m}$) undoped layer, sandwiched between the doped layers, guides the photons within the substrate. In this configuration, the transit time of the carriers is greatly reduced, as the width of the transit region is now essentially limited to the thickness of the guiding layer, from which they vertically move to the top and bottom doped layers. As the light is now traveling in a *horizontal* direction (i.e. along the layers' interfaces), the absorption region can be made long enough to essentially absorb all crossing photons²³ without impacting on the transit time. The width of the absorption region can also be reduced, as it is not anymore important for the absorption and thus the built-in capacitance can be reduced. This configuration greatly helps increasing the 3-dB bandwidth of the PD above 100 GHz [118, 119], although the augmented difficulty to achieve a good coupling between the light-feeding optical fiber and the thin integrated waveguide might cause a drop in the overall efficiency [114].

2.2.2 Uni-Travelling Carrier Photodiodes

Uni-travelling carrier (UTC) PD have been developed in order to extend the 3-dB bandwidth of pin PDs. In UTC PDs, photons are absorbed in a thin p layer, where the generated holes are collected by the close p-contact, while electrons quickly move towards the n-electrode. This way, the lower drift velocity of holes does not affect the response of the PD, as only electrons cross the intrinsic layer, following a fast, quasi-ballistic motion (no scattering occurs) [114]. The intrinsic layer can therefore be extended in order to reduce its capacitance, and therefore increasing the maximum working frequency of the PD. The main drawback of UTC PDs is that the thin absorbing layer (the thickness can be in the order of 100 nm) drastically reduces the responsivity, although its 3-dB bandwidth can be extended to the limits of the mm-wave range [120] and well into the THz range, if resonant improvements are exploited [121]. UTC PDs can deliver a considerable higher current than pin PD without incurring saturation thanks to the reduced *space charge effect*: In the standard pin configuration, the generated carriers tend to accumulate in the absorption layer, as the current density increases, thus generating an additional electric field (which reduces the internal field due to the p-n layers and therefore slows down the carriers) and eventually leading to saturation of the current. A similar phenomenon hap-

²³In this case the quantum efficiency can be calculated by equation 2.2.4, in which the *length* of the absorption layer is substituted to the width.

pens in UTC structures, although obviously only based on electrons: The reduced amount of accumulated charge, together with the higher velocity of carriers, makes the saturation effect appear at current levels which are one or two orders of magnitude higher than that of pin PDs [122, 123].

2.2.3 Travelling-Wave Photodiodes

A different approach to overcome the limitation due to the RC-cutoff is based on using long RF electrodes, creating a mm-wave coplanar transmission line which runs in parallel with the optical waveguide (in this case the optical signal is fed laterally, similarly to the approach described in the second part of section 2.2.1) and that is continuously loaded by the internal diode capacitance [124]. If the speed of the group velocity of the optical wave and the phase velocity of the mm-wave signal traveling in the coplanar line (from which the *traveling-wave (TW) PD* denomination) are the same, it is theoretically possible to achieve infinite operating bandwidth, with the photocurrent being at the constant value of half of the DC photocurrent of the standard pin diode (this is due to an external matching load required by the TW configuration). Practically, TW PDs operating in the THz range have been demonstrated [125].

2.3 Millimeter-Wave Amplifiers

Generally, the output signal of a PD has to be amplified before transmission. The integration of amplifiers can be monolithic or hybrid (advantages and disadvantages of the two approaches are discussed in section 3.2).

The most common amplifier configurations employed in mm-wave optoelectronics modules are heterojunctions bipolar transistors (HBT) and high-electron-mobility transistors (HEMT), based on GaAs or InP technologies. While InP has better performance in the upper mm-wave band and shows gain cut-off frequencies well in the lower THz-range, its intrinsic fragility and smaller processable wafers make this choice more expensive and favours the usage of GaAs for applications in which cost is particularly important.

For modules working at frequencies higher than 30 or 40 GHz, the HEMT is the preferred transistor configuration [126, 127] and thus a popular choice for E-band applications. Its simplified layer structure is shown in Fig. 2.24. The HEMT is based on a heterojunction between semiconductor layers with different bandgaps (the top layer is also used to achieve a Schottky contact with the capping layer and the amplifier's electrodes), which creates a potential well in order to accumulate electrons in the channel layer, in form of a *two-dimensional electron gas*. The concentration of the electrons depends on the difference between the energy bandgaps of the two materials and can be modulated by the voltage applied to the gate pad. Being confined in the undoped channel layer prevents the electrons from having interaction with dopants, while the additional spacer layer is used to prevent Coulomb scattering. As a result, carriers can move rapidly and the operating frequency of the amplifier can considerably be increased. The underlying buffer layer is used to reduce mechanical strain by achieving a better lattice match with the substrate (not shown in Fig. 2.24): This relaxes constraints on the choice of the channel layers and

gives more freedom to the designer for the optimization of the transistor.

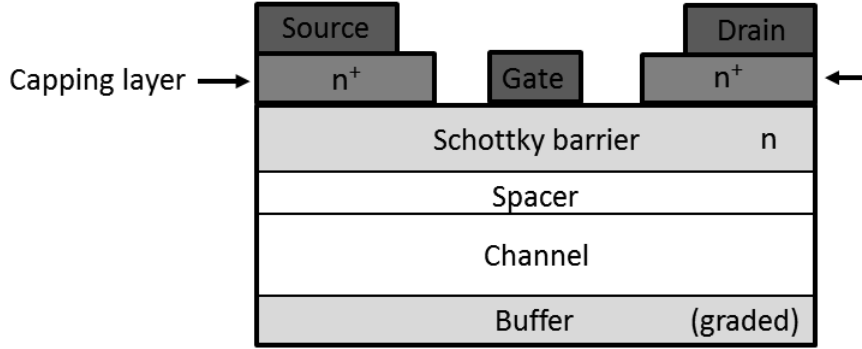


Figure 2.24: Layer structure of HEMT amplifier.

A HEMT is characterized by several characteristic frequencies [128], that will be now shortly introduced. The *cut-off frequency* can be calculated as

$$f_c = \frac{g_m}{2\pi C_{gs}} \quad (2.3.1)$$

where g_m is the transconductance of the device and C_{gs} is the gate-to-source capacitance. The *extrinsic cut-off frequency* is given by

$$f_T = \frac{g_m}{2\pi \{(C_{gs} + C_{gd})[1 + g_d(R_s + R_d)] + C_{gd}g_m(R_s + R_d)\}} \quad (2.3.2)$$

with C_{gd} being the gate-drain capacitance, R_s and R_d being the source and drain resistance, respectively. Finally the *maximum oscillation frequency* can be calculated as

$$f_{max} = \frac{f_c}{\sqrt{4R_0g_d + 4\pi f_c R_g C_{gd}}} \quad (2.3.3)$$

where R_0 is the sum of the channel, source and gate resistances. It appears obvious that some compromises are necessary in order to increase the working frequency, as most of the parasitic capacitances and resistances depend with different laws on the physical parameters of the devices, in particular on the transistor's aspect ratio (channel length over spacer width), the output pads shape and the quality of the achieved ohmic contacts. HEMTs can be optimized to achieve high-power outputs, although, thanks to their high transimpedance, they naturally perform at their best in low-noise operation, which is particularly important for direct integration with PDs, in order to improve the overall noise performance of the optical receiver. Improvement of the noise figure is achieved by minimizing the channel length and by reducing the parasitic gate and source resistances. Higher output power can be achieved by increasing the band-gap difference at the heterojunction (thus increasing the density of the two-dimensional electron gas) as well as the single band-gaps (in order to allow higher breakdown voltages), by introducing an additional doped layer, and by increasing the number of gate fingers.

The integration of commercial low-noise and middle-power HEMTs in PD modules will be discussed in section 4.3.3.

2.4 Antennas

Differently from transmission lines, where radiation (intended as a phenomenon happening every time electrons are accelerated or decelerated due to a time-varying field) is generally an undesired effect, antennas are structures that are specifically designed in order to radiate (or collect) an EM signal (see Fig. A.4).

They can be realized in different forms and size (taking into account constraints given by the required working frequency, the available space and other mechanical issues), and using different technologies and materials.

Antennas can be located in different parts of a communication module and can be found in different forms and size, from the monolithically integrated on-chip antennas to antennas integrated in packages (which help to relax requirements for the design of the single elements of the system) [129], to externally mounted antennas (generally bulky elements imposed by restrictive requirements). In the following sections, a short overview of the different antenna choices for PD modules will be given, analyzing the key aspects of each technology, while more theoretical concepts and definitions useful to understand the properties of antennas can be found in Appendix A.5.

2.4.1 On-chip Antennas

On-chip antennas are used in order to avoid external interconnects between the PD and the radiating structure, thus eliminating assembly steps and reducing power loss and other parasitic effects. Although three-dimensional radiating structures can be created for on-chip applications, we only consider here antennas in planar form, as their integration level is the highest and they can be fabricated at no (or very small) additional cost.

Patch Antenna

The most common planar antenna is the microstrip patch antenna²⁴. Although only rarely used for mm-wave optoelectronics applications [41, 131], this antenna is an important reference for on-chip, in-package and even external antennas (in form of array to form a flat panel reflector), therefore this section will shortly analyze its properties and layout, which is shown in Fig. 2.25, where the antenna is etched on a substrate with relative dielectric permittivity ϵ_r (it is assumed that the magnetic permeability is $\mu_r \approx 1$) and the substrate and ground plane are assumed to be infinite.

Different feeding techniques (the most common ones being the microstrip line feed and the coaxial probe) can be used to excite the antenna, depending on technological requirements, and they will not be considered here. To achieve optimum radiation at a

²⁴Our analysis will be limited to traditional rectangular patch antennas, although different shapes and modifications have been proposed in literature to improve bandwidth, gain and polarization of patch antennas. The interested reader can find a detailed treatise in [130].

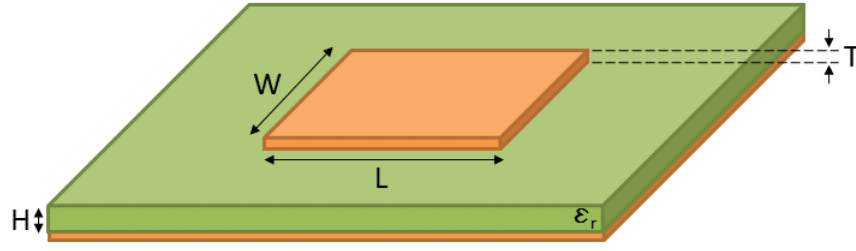


Figure 2.25: Model of microstrip patch antenna, with width W , length L , and metal thickness T , on a dielectric substrate of thickness H and permittivity ϵ_r .

given frequency f_R , the patch's dimensions should be chosen to be [132]:

$$L = \frac{c_0}{2f_R\sqrt{\epsilon_r}} - 2\Delta L \quad (2.4.1)$$

$$W = \frac{c_0}{2f_R} \sqrt{\frac{2}{\epsilon_r + 1}} \quad (2.4.2)$$

where c_0 is the speed of light in free space, and the factor ΔL takes into account the fringing fields at the edges of the patch²⁵. As introduced in section 2.1.4, the radiation from microstrip structures is improved if the height of the substrate is increased (although this is only valid until the height becomes large enough to allow surface wave propagation) and if the ϵ_r of the dielectric is low. As a guideline, it can be assumed that the gain of patch antennas is generally lower than 10 dBi. By considering that a patch antenna and its ground plate actually form a possible resonator, it is obvious that multiple resonances - besides the fundamental one identified by equations 2.4.1 and 2.4.2 - can arise and the corresponding frequencies ($f_{m,n}$, where m and n correspond to the resonating modes) can be calculated as [132]:

$$f_{m,n} = \frac{c_0}{2\sqrt{\epsilon_r}} \sqrt{\left(\frac{m}{W}\right)^2 + \left(\frac{n}{L}\right)^2} \quad (2.4.3)$$

This could be a problem for unwanted radiation - hence loss - or interference even in circuits that are not designed to operate as antennas, as already discussed in section 2.1.5.

Broadband Antennas

Microstrip patch antennas are largely used antennas but their radiation properties are not suitable for all applications. Other on-chip antennas are generally considered in order to achieve broadband operation in the mm-wave range. Among them, the most common designs used in PD modules are the bow-tie and log-periodic antennas, shown in Fig. 2.26. These antennas are truncated versions of infinite structures whose geometry is described by angles rather than by actual physical, that makes their radiation properties virtually independent from frequency. Due to their truncated nature, they will have a lower cut-off frequency, as well as a higher-frequency limit, identified by the wavelength

²⁵Several expressions are available in literature to estimate the actual value of ΔL , e.g. in [132, 133].

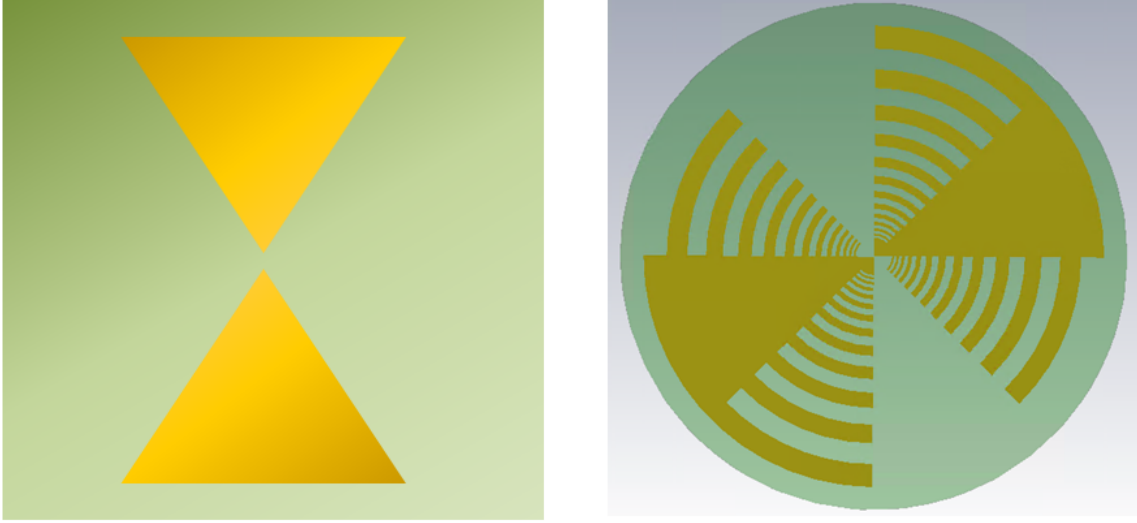


Figure 2.26: Broadband planar antennas: Bow-tie (left) and log-periodic (right) designs.

$\lambda_{\max} \approx 8F$, where F is the size of the feeding structure [132]. Detailed design guidelines as well as historical information about the development of these antennas and the description of similar radiators can be found in references [132] and [134]. Note that the antennas discussed here are not supposed to be backed by a ground plate, thus their radiation is bidirectional, with broad main beams perpendicular to the plane of the antenna. In practical applications, where the antenna is located on a substrate, the preferred direction of radiation will actually be through the substrate, due to the higher ε_r in comparison to the one of air. In order to improve the gain of the antennas used in photonic transmitters, dielectric lenses²⁶ (for instance made of silicon or quartz) can be used to focus the beam at the bottom of the substrate, as demonstrated in [19, 136–138].

2.4.2 In-Package Antennas

One disadvantage of on-chip antennas is that they can occupy a large area of expensive semiconductor substrate, vastly greater than that required by the PD itself. In order to reduce the amount of semiconductor material required by a single device, in-package antennas can be developed, where cheaper substrates (ceramics or laminates) are used to develop interconnects and host the optical chip and other components. The antenna might be integrated by either creating it on a dedicated chip or by directly designing it as part of a platform. The latter approach gives the designer more freedom in the choice of materials and configurations, as well as a considerably larger area than the one offered by integration on the PD chip. The usage of in-package antennas based on different assembly techniques is diffused in mm-wave electronics [139–141] in order to create compact and cost-effective designs. The substrate integrated waveguide introduced in section 2.1.6 is a

²⁶An overview of the most common lens antennas used in the mm-wave range can be found in [135].

perfect candidate for in-package antenna development, as it permits the creation of single antennas and arrays [91, 142–144], together with high-quality-factor filters and matching elements, while allowing an easier development of hermetical housings. The design and integration of in-package antennas based on SIW technology for 60-GHz PD modules are discussed in chapter 5.

2.4.3 External Antennas

Sometimes the gain of on-chip or in-package antennas is not sufficient for the intended application and the designer needs to feed the signal generated by the module to bulky external antennas, through dedicated 3D transitions, as external antennas are connected to PD modules through mm-wave connectors (coaxial connectors or, especially in the mm-wave range, WRs).

Horn Antennas

The most common antennas used for laboratory experiments, as well as feed for highly directional reflector antennas, are horn antennas. There are several possible designs of these *aperture antennas*, and a number of expedients have been developed by researchers in order to improve their bandwidth or radiation. The following paragraphs will introduce the basic principles of horn antennas and shortly discuss their properties.

H-Plane Horn Antennas The simplest horn antenna is the H-plane horn antenna (Fig. 2.27-a), which essentially is a WR whose opening is flared in order to achieve confinement of the field. They have to be designed taking into account a trade-off between the necessity to keep the phase error at their aperture at a minimum level and the need to increase the size of the final aperture in order to achieve a high gain G , the latter being estimated by [145]:

$$G = e_{\text{ant}} D \approx D = 10.2 \frac{a'b'}{\lambda_0^2} \quad (2.4.4)$$

where a' and b respectively are the width and height of the horn aperture, D is the directivity of the antenna, and the antenna efficiency has been assumed to be $e_{\text{ant}} \approx 1$, in this case. The radiation properties of H-plane horn antennas are well understood: From the radiation plots reported, among others, in [132], it can be seen that the antenna is suitable as sector antenna, because of the ability to control the radiation in the H-plane. However the E-plane pattern has a wider half-power beam width (HPBW) due the fixed height b , and could lead to excessively high front-to-back ratio (FTBR) and impedance mismatch, in case $b \ll \lambda$, as it will be discussed in section 5.4. H-plane horn antennas have originally been developed as external metallic components, but their shape makes them particularly suitable for integration on chips and modules using several manufacturing techniques [146, 147]; one example of in-package 60-GHz SIW H-plane horn antenna based on PCT will be presented in chapter 5.

Pyramidal Horn Antennas As it can be seen from equation 2.4.4, flaring the aperture also in the E-plane leads to a larger gain, as this helps to control the radiation in the

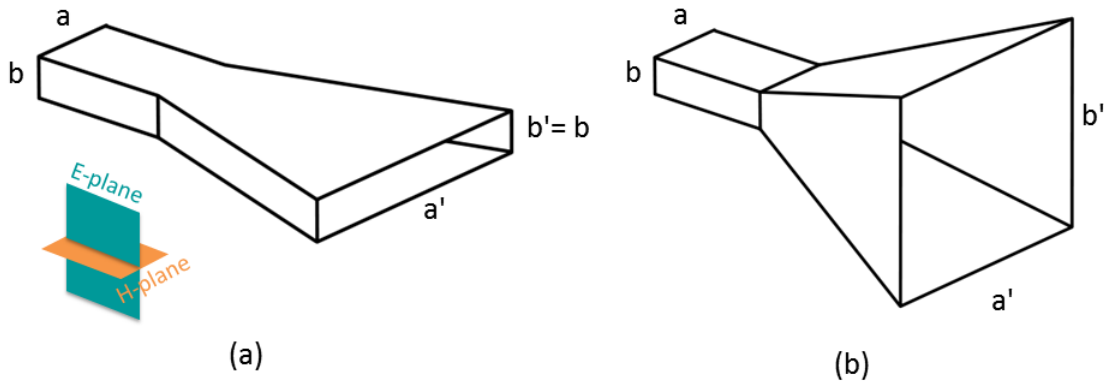


Figure 2.27: Horn antennas: H-plane horn antenna (a) and pyramidal horn antenna (b). The inset in (a) shows the H-plane and E-plane.

E-plane too. This approach leads to a *pyramidal horn*, shown in Fig. 2.27-b. Several trade-offs are again required, in order to guarantee a minimal phase error in spite of the double-direction flare [132, 145]. The common gain of off-the-shelf pyramidal horn antennas ranges from 20 to 25 dBi. Horn antennas are often used as feed for reflector antennas, that will be introduced in the next section.

Reflector Antennas

For demanding point-to-point communication, very high antenna gains are required (see section 1.2), which can be achieved only by designing very large arrays (whose operation is generally resonant rather than broadband) or by employing broadband reflector antennas. The most common antennas employed to achieve high gain are *parabolic reflectors*²⁷ where a horn antenna is used to feed a parabolic metal shield (see Fig. 2.28-a) which has the property of reflecting power originated from its focus in form of parallel rays²⁸, which leads to very directive antenna patterns. The maximum achievable gain can be estimated as [132]:

$$G = \left(\frac{\pi L}{\lambda_0} \right)^2 e_{\text{ap}} \quad (2.4.5)$$

where e_{ap} and L are the *aperture efficiency*²⁹ and the diameter of the reflector respectively. The maximum gains of parabolic reflectors with different diameters are shown in Fig. 2.29, which show that even small dishes (diameters of 20 cm or slightly larger) are sufficient to satisfy the requirements for mm-wave point-to-point links introduced in chapter 1. Note

²⁷Other reflector shapes are possible, from the simple plane reflector to the corner reflector, although their ability to collimate the reflected wave is lower than the parabolic reflector. The simpler shapes are however sometimes used in consumer applications where low-weight and low-cost are an important feature of the system.

²⁸Ray-optics approximation is used in analyzing parabolic reflectors, as their size is usually several order of magnitude larger than the operational wavelengths.

²⁹Values of e_{ap} between 60% and 85% are possible using different reflectors and illumination techniques [132].

that for this plot the efficiency has been assumed to be 70%: This is a typical value for a *Cassegrain antenna*, which uses the alternative feeding technique shown in Fig. 2.28-b, originally introduced to avoid the detection of thermal noise from the Earth's ground in astronomy applications and generally preferred for the more convenient location of the feed, which does not require cables, waveguides or other front-end electronics to be placed in front of the main reflector and thus relaxes constraints on the size of the feeding element.

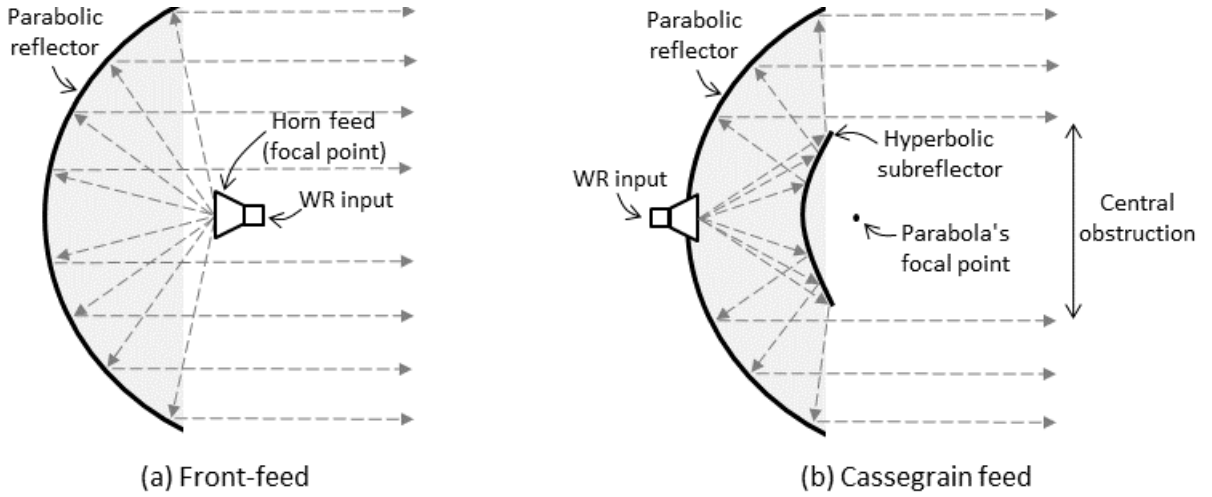


Figure 2.28: Feeding techniques for parabolic reflector antennas. Adapted from [132].

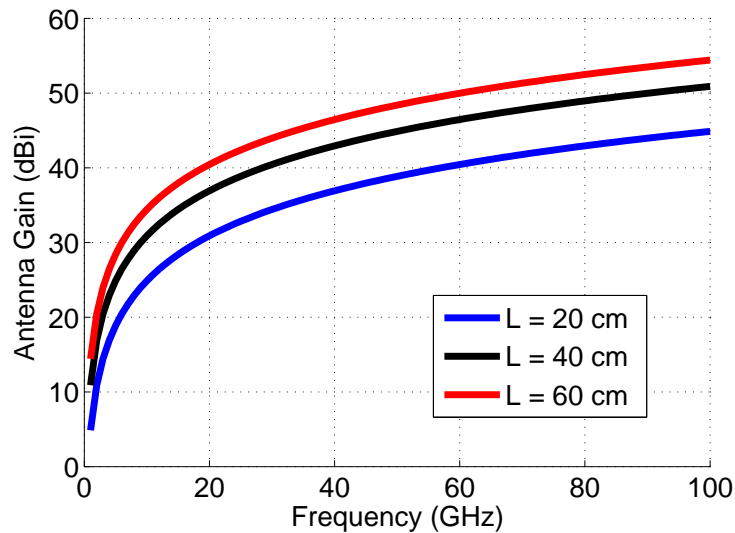


Figure 2.29: Gain of parabolic antennas with different diameter (L) as a function of frequency.

2.5 Conclusions

In this chapter the fundamental components of PD modules and their working principles have been introduced, together with an analysis of the special requirements imposed on the manufacturing technology of optical and electronic chips by the strive for achieving better performance, in particular higher working frequencies and output power, in the mm-wave range.

We have applied EM principles to describe and characterize the behavior of typical topologies used for on-chip and intra-board interconnects, whose loss and wave-guiding characteristics are critical for the successful development of integration platforms.

Special emphasis has been given to the analysis of the limiting factors of three-dimensional guiding structures (WR, coaxial cable), as well as traditional (microstrip, GCPW) and innovative (SIW) planar PCB interconnects. We have highlighted that radiation loss can make microstrips unpractical in the mm-wave range. This explains the preference accorded to GCPWs in applications above 50 GHz: With some compromises on their characteristics, GCPWs are suitable for operation up to 100 GHz and beyond, especially if thin dielectric substrates with low dielectric constant are used. As loss can nevertheless still be an issue for GCPWs, we have finally suggested that PCB SIWs could be used as alternative low-loss interconnects for mm-wave applications. We have thus identified guidelines for the proper dimensioning of GCPW and SIW circuits, especially addressing the requirement for closely spaced via holes. A more detailed analysis on the maximum operating frequencies and other critical aspects of planar technologies will be given in chapter 3.

Finally, the most common on-chip, in-package, and external antennas used in mm-wave applications and RoF systems have been introduced. It has been highlighted that only external Cassegrain or parabolic-reflector antennas can meet the current requirements for mm-wave point-to-point communication: An approach to develop PD modules suitable for the integration of external antennas and based on PCT integration platforms will be introduced in chapter 4. For 60-GHz indoor communication, the antenna requirements are different and sector antennas can be considered for some applications: A study of the feasibility of in-package antennas for RoF modules based on PCT SIW will be presented in chapter 5.

3 Hybrid Optoelectronic Integration Technologies

Optoelectronic packaging can be defined as “working on the connection of opto-electronic integrated circuits to optical and electrical transmission lines and bias supply combined in a environmental stable housing” [148]. In this regard, it can be seen as an “outgrowth of electronic packaging” [149], as it shares and expands most of the properties and principles of the latter, by including requirements concerning the optical inputs and/or outputs, which will be introduced in section 3.1.

Essentially, any optoelectronic package has to provide environmental and EM protection to its housed components, as well as detachable mechanical, optical and electrical contacts, in order to provide a “functional product for the end user” [150]. Essential requirements for a good package are the appropriate removal of the produced heat and prevention of unwanted EM radiation from the internal circuitry, as well as the resistance to mechanical and thermal shocks, without influencing the functioning of the internal devices [151].

It is possible to define several levels of optoelectronic packaging, namely [152]:

- **Level 0:** Uncased device (e.g., laser diode, PD) with its integrated optical and electrical interconnects;
- **Level 1:** Single or multiple optical and electrical integrated-circuit components (e.g. lenses, PDs, electrical amplifier, passive surface mount components) assembled into a case with electrical and optical input and outputs; additional passive structures (such as surface-mount bias components) can be included in the package, exploiting the possibilities of creating electrical interconnects offered by the supporting substrate;
- **Level 2:** Modules and product boards (e.g. transponder on a daughter card); this level of packaging is similar in nature to level 1 and therefore shares with it analogous assembly techniques and issues;
- **Level 3:** Mother board with product boards or cabling (e.g. transponder mounted on a mother board).

In this chapter, several integration approaches for hybrid optoelectronic modules will be introduced, with particular emphasis on the development of PD modules (optoelectronic packaging level 1) based on PCT. The interest in this approach can be easily understood by the increasing drive for low-cost packaging, necessary to the development of accessible consumer applications [153], particularly in the 60-90 GHz range [66]. However limits due to manufacture constraints and additional EM issues need to be carefully addressed when using such technology in the mm-wave range, as it will be discussed in section 3.4.4.

3.1 Optical Issues

Independently of the chosen mechanical and electronic integration approach, any PD module requires an optical input, in order to deliver a light signal to the chip: In fact, a fundamental requirement for the usage of optical receivers in actual systems, is the development of pigtailed PD modules, i.e. modules which can be easily connected to light sources via standard optical connectors.

In literature, several approaches are available to achieve optical connectivity, depending on the PD type (top or lateral illumination) and the requirements of the package. Besides free-space interconnections, in which the light beam is controlled by a number of mirrors, prisms and lenses and that finds its application mostly in transferring the signal between multiple optical boards, guided-wave interconnections based on fibers and/or waveguides are widespread for on-chip and on-board signal steering and thus for the development of pigtailed devices [154].

The majority of the alignment processes in optoelectronic interconnects is done by *active alignment*, i.e. driving the device, such as a PD, in its normal operation status and monitoring the output while refining the alignment of the fiber using advanced positioning tools which allow translation along and rotation around the three axis (x-y-z). Position accuracies in the order of 0.5-1 μm can be achieved by using multiple steps, but this approach is very time-consuming and expensive.

In order to speed-up the assembly process, several *passive alignment* approaches have also been developed. The most common is based on using a silicon substrate where grooves and cavities are used to guide the alignment of fibers and lenses, whereas exploiting the self-alignment properties of flip-chip connectivity, using mechanical alignment features etched on the chips or the carriers and the registration based on fiducial marks have also shown to be a valid alternatives. The accuracy of passive alignment is in the order of 1-5 μm , approaching that of active alignment [154].

The development of faster and more accurate alignment processes will be fundamental for the future improvement and further diffusion of optical RoF systems.

3.2 Monolithic vs. Hybrid Integration

When working on the integration of several optical and/or electrical chips, it is possible to consider either monolithic or hybrid integration.

Monolithic integration is based on the principle that all required active and passive components, including their interconnects, are designed and manufactured on the same semiconductor substrate (e.g. silicon, gallium arsenide or indium phosphide) as a large single chip, working at level 0 of the optoelectronic packaging hierarchy. This elegant approach offers advantages, such as the reduction of parasitic effects due to discrete interconnections between components and the simplification of the required macroscopic optical assemblies [126, 155–157]. However, it requires a larger amount of semiconductor substrate's area, and reduces the choice of the elements to those compatible with the adopted substrate and processing technique. Achieving a complete monolithic integration is often impossible, due to the lack of substrates suitable for all required optical and

electrical elements, or interconnects. When monolithic integration is possible, the integrated components would be unoptimized, as the requirements on the layers' structure to achieve optimal performances are different for different devices and require several time-consuming manufacturing iterations. While the monolithic approach might allow higher yield and better reproducibility, the high density of neighboring elements might also raise concerns for unwanted EM interference between the devices. An additional issue is also that, in case of failure of one of the constituents, it is impossible to perform maintenance or reparations on the module [158].

As a matter of fact, *hybrid integration* – where an external carrier, generally less expensive than a semiconductor wafer, is used as integration platform for singularly optimized and manufactured devices [41, 137, 159] – is currently a necessity. This technique might lead to larger assemblies and requires additional design effort to minimize mechanical instabilities and non-ideal behavior of electrical interconnects. However, besides being more suitable for fast prototyping, it offers great freedom to the designer, thanks to the large choice of available components, in terms of variety as well as property range. The hybrid integration additionally offers the possibility of tuning and repairing the circuits after manufacture.

When used in practical systems, even monolithically integrated components require a further connection to a level 1 or 2 platform, thus making necessary the usage of hybrid methodologies. Therefore the following sections will analyze in details the most common substrates and manufacturing technologies available for the development of hybrid integration platforms and will explore some of the specific issues arising when working on mm-wave modules.

3.3 Dielectric Materials for Integration Platforms

The choice of the appropriate material to be used for integration platforms is dictated by several factors related to thermal, mechanical and electrical properties.

3.3.1 Electrical Properties

The most important electrical parameters of mm-wave substrates are their dielectric constant and the dielectric loss tangent, whose impact on wave propagation and attenuation has been analyzed in sections 2.1-2.1.1.

A low dielectric constant is generally desired for applications above 50 GHz, in order to reduce uncertainty on the line properties and extend the operational range of the circuits by shifting the appearance of high order modes at higher frequencies (see section 2.1.4). Commercially available substrates have dielectric constants ranging from 2 to 12.

The loss tangent must be chosen to be as small as possible, as dielectric loss tangent is directly proportional to both this parameter and frequency, as indicated by equation 2.1.2). Substrates for mm-wave applications have a dielectric loss tangent ranging from 0.0001 to 0.001.

3.3.2 Thermal Properties

Thermal issues are particularly important in the mm-wave range, as high-power devices tend to concentrate the active elements in relatively small areas, in order to reduce loss due to long interconnects.

Thermal Conductivity The thermal conductivity (TC) of substrates have to be considered when they are used in high-power applications or to host active devices. The total TC is the result of several physical mechanisms allowing heat transmission related to electron, EM wave propagation and phonon transportation, with the latter being the most important term for heat removal in dielectrics [153]. The TC depends on the actual composition of the substrate and is generally indicated by the manufacturer in W/K. If the TC of the substrates is not sufficient for the envisaged application, several techniques can be adopted in order to reduce the temperature of high-power modules. The most common way is to exploit metal-filled via holes, taking advantage of the large thermal conductivity of metals in comparison to common ceramic and organic dielectrics. As optoelectronics modules contain temperature sensitive devices such as PDs, lasers and modulators, active cooling elements, such as *Peltier cells*, might also be included in the packaged devices.

Thermal Expansion The thermal expansion of materials describes their change in volume due to temperature variations. The thermal expansion coefficient (CTE) is defined as:

$$CTE \stackrel{\text{def}}{=} \frac{\Delta L}{L \Delta T} \quad (3.3.1)$$

where L is the material extension (length or thickness), ΔL is the change of the extension due to a temperature change ΔT .

Different CTEs can be an issue for complex rigid assemblies, as the different amount of expansion or contraction of materials attached to each other can induce stress and deformations in the package. It is therefore important that the CTEs of the different materials used in packages are comparable in order to avoid damages and extend the temperature working range of the module. Most ceramic materials show rather low CTEs (less than 10 ppm/°C) which is suitable for integration with semiconductor. On the other hand, organic *composites* used in PCT processes have a rather high CTE, which can be engineered to match that of copper (17 ppm/°C), to prevent delamination effects. It must be noted that most of the PCT composites nevertheless show a higher CTE (more than 100 ppm/°C) in the z-direction (the direction perpendicular to the laminate's plane) than in the x-y plane (the plane of the laminate): Although this is not a real issue for the thin substrates used in the mm-wave range, manufacturers have developed tailored materials with reduced z-CTE to suit the needs of applications in which tight control is required, e.g. for via holes requirements in multi-layer boards.

The CTE is not constant and can change with temperature, therefore it is generally defined as an average value over a specific temperature range, e.g. 1-100°C.

3.3.3 Mechanical Properties

External conditions such as temperature changes or mechanical stimuli can induce forces on packages. Mechanical stability is fundamental in order to offer a reliable base for hybrid integration of components, but also to protect the module from environmental stress.

Young's Modulus The Young's modulus E is an important parameter for packaging materials, usually provided by manufacturers. It is defined as the ratio of the internal forces (stress, σ) induced by external stimuli to the overall deformation (strain, ε_s) due the same stimuli, and it is a measure of the "resistance of a material to deformation in the direction of forces applied to it" [153]:

$$E = \frac{\sigma}{\varepsilon_s} \quad (3.3.2)$$

Ductile materials, such as organic laminates, exhibit a *plastic* behavior, showing very little change in stress for high level of strains, whereas *brittle materials*, such as InP, do not experience this saturation effect.

3.3.4 Hermeticity

Hermeticity is an important issue in optoelectronics packaging, as moisture, water, gases and particles might interfere or compromise the functioning of electronic interconnects, chips and optical assemblies, by either changing the dielectric properties substrates and increasing the risk of delamination during the processing, or by affecting internal circuitry (e.g. through oxidation).

The materials that offer the lowest permeability to water are, in order, metals, ceramics and glass [135]. However, laminates based on liquid crystal polymer (LCP) and PTFE also show very low water absorption (0.02-0.04%) and are therefore referred to as *quasi-hermetic* materials, which has triggered their usage in packaging applications where insulation must be achieved under humid conditions [160]. In particular, experimental validation of LCP modules has shown conformity with military requirements on the leak rates of substrates [66].

3.3.5 Ceramics

Ceramics are a common choice for high-end electronics applications as they allow the development of high-resolution lines and their mechanical properties (such as stiffness) make them suitable for the development of thin substrates. There are multiple processes used to manufacture circuits and integration platforms on ceramics, as discussed in sections 3.4.1-3.4.3. Ceramic materials have the advantages of offering a higher thermal conductivity than laminates (which is particularly important in high-power applications) and of being hermetic, which can simplify the packaging process, although they are brittle and therefore difficult to machine.

Several ceramics are used as a substrate for mm-wave circuits [151], the most common being alumina (Al_2O_3). It is used in an almost pure form (99.6% alumina) for thin-film

applications and in 96%-form for thick-film circuits, the latter being more robust but showing a coarser surface and higher dielectric loss. For high power applications, beryllia (BeO) can be used, thanks to its high thermal conductivity, but its higher surface roughness and the potential damage for human health during its processing can make manufacture more complicated and expensive. Aluminum nitride (AlN), is particularly suitable for integration of silicon devices, thanks to their similar thermal expansion, although it can require additional processing steps in order to improve the quality of its metallization. Thanks to their low-cost, glass and fused silica (quartz/SiO₂) are sometimes used for thin-film development, with the latter being preferred because of its smoother surface and lower $\tan\delta$; it is sometimes preferred for mm-wave applications, also because of its lower dielectric constant, in comparison to alumina and other ceramics.

3.3.6 Laminates

As discussed in section 3.4.4, laminates are used for PCT processes and consist of a dielectric core clad with metal layers. The dielectric layer is a *composite* material, consisting of a *resin* and a *fabric*, used to achieve a higher degree of mechanical stiffness (which simplifies machining) and to extend the range of available dielectric constant and improve other characteristics, such as the CTE.

PTFE is the preferred resin for high-end applications. PTFE is a *thermoplastic*, i.e. it does not undergo multiple melting due to heating after the first curing, but it can become softer if the temperature is increased above the *glass transition* temperature T_g , which should always be higher than the maximum processing temperature used in the adopted PCT process. The T_g of laminates depends on the actual fabric-resin combination used and can be engineered to be higher than 300 °C. In the same range (above 300 °C) should lay the *decomposition temperature* T_d , i.e. the temperature at which permanent degradation of the substrate occurs, defined as the point at which the decomposition of the resin induced by the heat causes a weight loss of 5%.

Glass, quartz and ceramics can be used as fabric for laminates. One problem arising from using traditional woven fiberglass fabrics is that this introduces dielectric anisotropy, because of the patterned dielectrics structure. Therefore manufacturers have developed *nonwoven substrates* based on randomly distributed glass microfibers and ceramic particles, in order to minimize the impact of anisotropy on the design. Aiming at reducing the loss of the laminate and increasing their dielectric constant, ceramic fillers were introduced in the 1970's; as a result, laminates with ϵ_r ranging from approximately 2 to 10 are currently available on the market.

As an alternative to classical laminates, LCPs have proven to be suitable for the development of multi-layer mm-wave PCBs and packages [161, 162]. LCP is a flexible organic substrate, available in form of laminated boards from several suppliers, which offers some advantages in comparison to PTFE laminates. In fact, it is particularly suitable to multi-layer assembly, as its melting temperature can be engineered, producing layers that melt below 300 °C and thus can be used as bonding layers, while the ones used as circuit carrier are not affected due to their higher T_g . Furthermore, its CTE matches the one of copper, which reduces delamination due to the multiple thermal cycles necessary to PCT development, and is readily available from manufacturers in very thin (25 μm) to

thick (1 mm) layers. However its dielectric constant is only available in a restricted range ($2 \leq \epsilon_r \leq 5$), while its nominal loss tangent is generally two-to-three times higher than that of high-end PTFE laminates.

3.4 Processing Technologies

There are several technologies which are suitable for the production of integration platforms, based on a number of different substrate manufacturing techniques, metallization approaches, machining possibilities and integration capabilities. Sections 3.4.1 to 3.4.4 will explore the crucial aspects of the different manufacturing techniques, with particular emphasis on the integration based on printed circuit technology, as this is attractive for consumer applications, thanks to the fact that its *cost per circuit* is 6 to 10 times lower than that of concurrent technologies [163].

3.4.1 Thick-Film Technology

Thick-film technology makes use of relatively low-cost screen printing techniques¹ to create conductive structures on ceramic substrates, usually alumina, beryllia or aluminum nitride. Typical thickness of substrates are in the 0.1-1 mm range, while the area can extend to 20 by 20 cm. Multi-layer structures are possible, with every layer being fired independently.

The resolution of conductive structures is in the order of 25-120 μm [72], with tolerances of 10-25 μm , with thickness of the metal layers of 7-15 μm [66]. Metal pastes, which are applied to the substrate through a wire frame (screen) can be based on gold, copper, silver or mixed solutions (gold-palladium, silver-palladium), however subsequent hybrid integration possibilities might be hindered if gold is not used (e.g. due to soldering issues) [151].

Laser machining can be used to create different substrate shapes and drill via holes, as well as to trim integrated resistors. Via holes can also be filled with metal pastes, in order to achieve multi-layer interconnectivity or EM shielding, or to improve the heat-sinking capability of the structure. Thick-film structures undergo processing temperatures of up to 1000 °C.

3.4.2 Thin-Film Technology

Thin-film technology is used to overcome the limitations of thick-film technology for higher frequency ranges. Substrates are generally ceramic, in particular alumina and quartz, but other materials such as aluminum nitride, beryllium oxide, sapphire, glass, ferrite, silicon, InP and GaAs are suitable to be processed with thin-film techniques. The substrate's thickness and area depend on the characteristics of the adopted wafers and the available technology, therefore areas larger than 200 cm² are difficult to process.

Conductive structures are produced by vapor deposition or sputtering, in combination with photolithographic techniques, requiring operation in vacuum, and can achieve

¹Thick-layer etching techniques are also possible, achieving higher line resolution, but they require equipment and steps typical of the thin-film technology, which is treated in section 3.4.2.

resolutions on the micrometer scale [153]. In order to facilitate adhesion to the substrate, a very thin layer of titanium-tungsten (WTi) or nickel-chromium (NiCr) is usually deposited at first, followed by a nickel barrier layer and finally by a thicker (1-4 μm) layer of gold. For lower frequency applications, the gold layer can sometimes be galvanically thickened up to 10 μm , in order to improve the conductive properties of the metallization [151, 153]. Laser drilling is used for shaping and to drill via-holes, which can be metal-plated during the metallization phase. Thin-film processes allow for the integration of resistive, inductive, and capacitive elements, and can be used to develop multi-layer assemblies.

Thin-film on aluminum nitride, silicon, and quartz is the most common manufacturing technology used for mm-wave optoelectronics modules [28, 33, 164, 165], mostly because of the achievable high resolutions and the smoothness of the metallization, which helps minimizing EM loss. However, its limited manufacturing yield and the high cost of the required equipment might not be suitable for supporting the consumer-application market.

3.4.3 Co-Fired Ceramics

Co-fired ceramics offer a very high-level of integration thanks to the possibilities provided by their intrinsic multi-layer nature, which allows the development of complex three-dimensional structures, buried elements and cavities. The particularity of this technique, based on ceramic substrates, is that all layers are pressed together and then fired, after the creation of the required metallization. Two different approaches can be identified, with respect to the firing temperature (low/high).

High-Temperature Co-fired Ceramic (HTCC)

High-Temperature Co-fired Ceramic circuits are usually based on alumina or aluminum nitride (the latter particularly suitable for high-power applications thanks to its higher thermal conductivity). The dielectric layers (with thickness of 100 to 500 μm) are created from a slurry based on ceramic, glass, binding materials and solvent, with the ceramic particles having sub-micrometer diameters.

Because of the high temperature (up to 2000 °C) at which the final structures are fired, HTCC modules have to use metals with high melting temperature but poor electric properties for their metal circuits (e.g. Molybdenum or Tungsten), which increase the conductor loss. External metal interconnects can be plated with metal with higher electrical conductivity after the firing, in an attempt to improve the overall loss.

Via holes usually have an aspect ratio of 1:1 with minimum diameter and pitch of approximately 75 μm and 150 μm , respectively [66, 153].

As a result of the firing, the material volume shrinks of about 20%, mostly because of the evaporation of solvents, which has to be taken into account in the design phase [153].

Low-Temperature Co-fired Ceramic (LTCC)

Low-Temperature Co-fired Ceramic are manufactured from *green tapes* and can produce structures of up to 100 layers [135], allowing the development of highly integrated systems. The fact that the firing temperatures are in the 850-900 °C range allows the usage of gold,

silver or even copper for interconnects, thus reducing the conductors loss in comparison to HTCC. Resolutions of 25-100 μm are achievable on the top metallization layers by using photo-image techniques [166]. Another advantage of low firing temperatures is the possibility of creating buried or surface resistors, which increases the integration capability of LTCC systems. LTCC materials are also subject to 10-15% shrinkage after firing, although new formulations allow to reduce this inconvenience to negligible values (less than 1%) [167].

Via holes can be manufactured by punching or laser drilling, with a diameter of 100-200 μm and an accuracy which is in the order of 5-20 μm , and are filled using thick-film paste, which also enables their usage as thermal vias [66].

LTCC manufacturers make use of dielectric green tapes that, although mechanically less robust than ceramics used in HTCC, have a lower dielectric loss; together with the low-loss metallization, this makes LTCC circuits more suitable for mm-wave applications [168, 169], in spite of their cost, that can be up to 30% higher than that of similar HTCC technology [163].

3.4.4 Printed Circuit Technology

Printed circuit technology is a well-established manufacturing technology, based on standard low-cost processing steps, which can be employed in the development of electronics system from very-low frequency up to the mm-wave range. However the resolution requirements of circuits working at frequencies above 50 GHz need particular attention in order to achieve good performance.

Printed circuit boards are developed from dielectric layers, whose top and bottom sides are generally laminated with copper. The most common ways to achieve this sandwiched metallization is based on either rolled or electrodeposited copper foils [170]. Rolled copper is generally more flexible and shows a RMS surface roughness (Δ) value of 0.4 μm at the dielectric side and 0.3 μm at the top side. Electrodeposited copper foils for high-frequency applications are generally rougher ($\Delta \leq 2\mu\text{m}$), but with special refining steps - in which treatment layers are added to improve the adhesion to the dielectric - can achieve surface roughness of 0.5 and 0.3 μm at the dielectric and top side, respectively [171]. The surface roughness increases the overall loss of the circuits, as discussed in section 2.1.4, and must be therefore carefully taken into account in the design phase: Assuming the optimistic average roughness value of 0.4 μm already increases the theoretical conductor loss of printed circuits by a factor $\alpha_{c, \text{rough}} = 1.8$, considering a skin depth of $\approx 2.5\mu\text{m}$ at frequencies above 50 GHz and using equation 2.1.23. The metal layers are processed using a photoresist covered by a mask generated with high-precision camera and subsequently illuminated with ultraviolet light. For higher frequencies applications a laser direct imaging (LDI) might be employed, in order to achieve a better resolution. After the exposition, the substrate is immersed in a developer which removes the exposed parts of the photoresist to allow etching of the copper. The boards are finally freed from the remaining photoresist, rinsed in water and dried. The final processing step consist of the milling of the panel to separate the single circuits, which can have any arbitrary shape compatible with the size of the tip used in the cutting process. Each panel can have dimensions approaching 0.5 square meters, which allows the development of hundreds or even thousands

of circuits at the same time. Double-side circuits can be created and multi-layer designs (with up to 50 layers [172]) are made possible by using adhesive layers or other assembly techniques. Elements such as resistors can be mounted on the external sides or buried within multi-layer boards and metallized (plated or filled) via holes can be created for grounding purposes, heat-removal or to create three-dimensional interconnects. Several surface finishes based on silver, metal, tin, gold and lead are available to the designers: In particular, an *electroless nickel immersion gold* (ENIG) metallization is generally preferred in order to avoid oxidation and corrosion and to simplify the wire-bonding and other assembly processes [170]. PCT boards have to withstand temperatures of up to 150 °C, as several bake-outs might be performed in order to remove volatile substances. For multi-layer assembly and soldering purposes, temperature higher than to 300 °C might be necessary in order to melt the adhesion layers.

Process Tolerances

Resolution and Etching Tolerances Tolerances on the line width can be estimated in the order of 10% of the width, with the actual accuracy depending on the quality of the process, the size of the panel and the thickness of the metallization layers. As rule of the thumb, it can be assumed that minimum realizable strip width PCT metal is twice the thickness of the metallization [173], although for very thin metallizations (eg. 9 μm thickness) this might exceed the limits of state-of-the art photolithographic systems, whose minimum achievable line/gap width is in the order of 50-100 μm .

The impact of etching tolerances on the impedance of a GCPW has been analyzed using HFSS and the results have been summarized in Fig. 3.1. The nominal model, designed to have an impedance of $\approx 50 \Omega$ in the 60-85 GHz range and shown on the left side of Fig. 3.1-a, is based on a substrate thickness $H = 127 \mu\text{m}$, a metallization thickness $T = 17 \mu\text{m}$, a line width $W = 340 \mu\text{m}$, a gap width $G = 150 \mu\text{m}$, and a perfectly vertical etching profile. It can be seen from Fig. 3.1-b that for a line width tolerance of $\pm 10\%$ ($W = 374 \mu\text{m}$ and $306 \mu\text{m}$, respectively) an impedance change of up to 5Ω (10%) can occur, which corresponds to a RL of at least 25 dB, a value that is not of concern in most applications. Figure 3.1-c additionally shows the impact non-vertical etching profile, for both acute and obtuse etching angles, as shown on the right side of Fig. 3.1-a: It can be seen that for the configuration under consideration, this is a less critical issue than the absolute inaccuracy on the width of the signal line.

Substrate Thickness The thickness of the dielectric layers of commercial laminates can exhibit tolerances of $\approx 10\%$. This obviously affects the characteristic impedance of the lines, as shown in Fig. 3.2, with an impact which is comparable to the one of etching inaccuracies: In fact, a change of the characteristic impedance in the order of 10% is seen in this case too. The same configuration depicted on the left side of Fig. 3.1-a has been used for this simulation.

Via Holes Drilling of via holes encounters several limitations, connected with the substrate thickness and the accuracy of the equipment. A general rule of the thumb is that

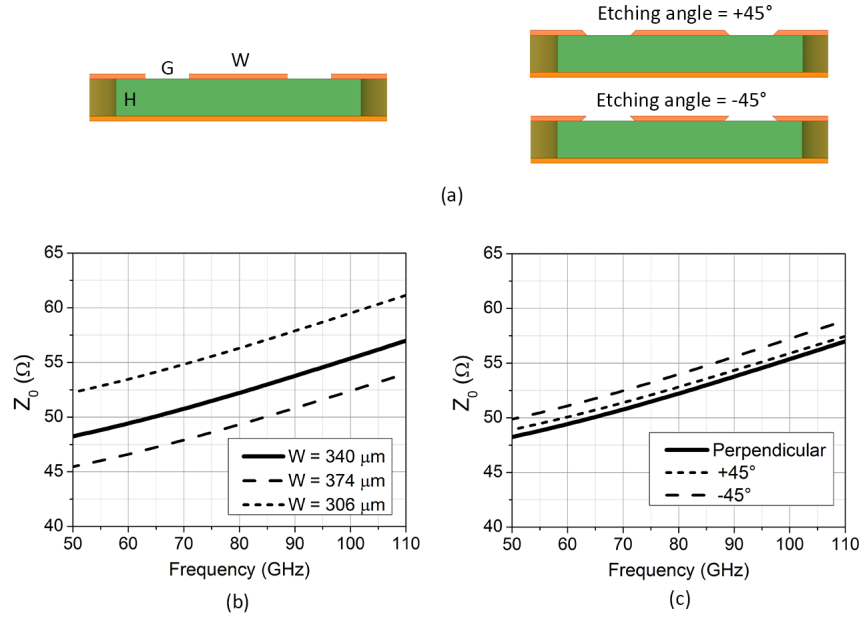


Figure 3.1: Front view of GCPW based on RT/duroid 5880 laminate (a) and impact of the line width (W) tolerance (b) and of the etching angle (c) on its characteristic impedance of a GPCPW. The solid thick line represents the results obtained with the nominal values.

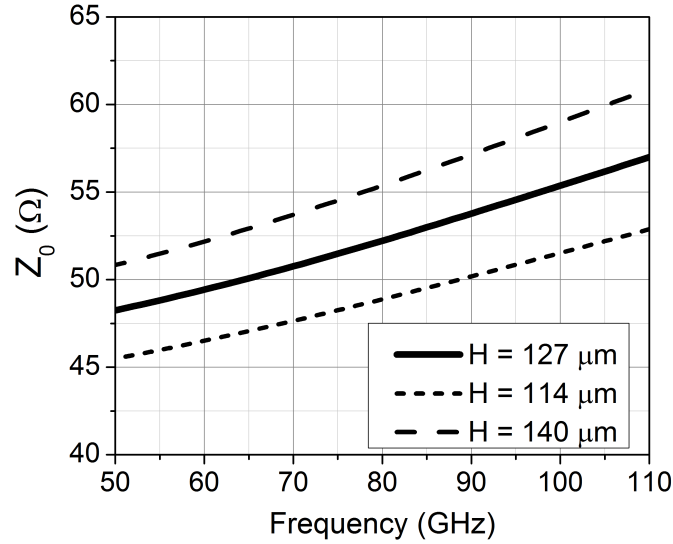


Figure 3.2: Impact of substrate-thickness (H) tolerance on the characteristic impedance of a GCPW based on RT/duroid 5880 laminate. The solid thick line represents the results obtained with the nominal value.

the aspect ratio (height to diameter) of via holes cannot exceed 6 to 1², therefore thinner laminates are preferred in order to achieve thin via holes³. The thinnest laminates have a thickness in the order of 130 μm , which would allow a diameter limit ($\approx 20 \mu\text{m}$) that cannot be reached because of the size of the mechanical drilling systems: In fact, the minimum via holes diameter (D_{via}) achievable by standard manufacturing processes is in the order of 100-200 μm , with the 100 μm achievable only employing special laser drilling machines and not always practical on all laminates because of mechanical instability. The aspect-ratio limit identified above plays a more important role in multi-layer boards, in particular for *through-hole vias*, i.e. via holes crossing all layers⁴, thus limiting the maximum number of layers to 5 or 6, if thin diameters are required.

The minimum distance (pitch) between two adjacent via holes is limited by the drilling positioning tolerance, which makes necessary to create *rims* (or catch-pads) around the nominal drilling position of each via hole center, as shown in Fig. 3.3. The typical drilling positioning accuracy is currently in the order of 100 μm , thus imposing a diameter of the rim contour given by: $D_{\text{rim}} = 2 \times 100 \mu\text{m} + D_{\text{via}}$. The minimum pitch p_{min} coincides with the rim diameter and it can be therefore calculated that using first-class equipment allows pitches in the order of 350-400 μm .

In GCPW circuits, where the via holes help prevent loss due to parasitic modes, the pitch between via holes plays a crucial role for the correct functioning of the design: In fact, it has been introduced in section 2.1.5 that the pitch should not exceed one quarter of wavelength within the substrate ($\lambda_r = \lambda/\sqrt{\epsilon_r}$). Therefore the maximum operational frequency of GCPW circuits is given by:

$$f_{\text{max}} = \frac{c_0}{\lambda_{\text{min}}} = \frac{c_0}{\sqrt{\epsilon_r} \lambda_{r, \text{min}}} = \frac{c_0}{\sqrt{\epsilon_r} p_{\text{min}}/0.25} \quad (3.4.1)$$

where c_0 is the speed of light in vacuum. Assuming a dielectric constant of 2.2 and minimum via diameter of 100 μm , the maximum working frequency can reach 160 GHz, while a more common via diameter of 200 μm lowers it to 126 GHz. A smaller rim diameter also reduces the minimum distance of the via holes from the edges of the ground plates (Fig. 3.3), which has to be minimized to improve the suppression of high-order modes and resonances, as explained in section 2.1.5. It is important to notice that the calculated limits are based on empirical rules for the dimensioning of the via-holes pitch. Therefore higher operational frequencies might be acceptable, if some trade-offs on power leakage are accepted.

In SIWs, the pitch of the via holes should not be larger than one quarter of the in-substrate wavelength corresponding to the highest intended frequency of operation (usually $1.9 f_{c, \text{TE}_{10}}$), nor larger than twice the via diameter, in order to exclude band-gap resonances and reduce radiation loss (see section 2.1.6). Considering a pitch of 400 μm and a diameter of the via holes of 200 μm , simulations have been performed in order to verify the

²Note that special techniques, such as *peck drilling* and *pulse drilling*, can be used to achieve aspect ratios larger than 10 [172].

³This is not always the aim of the designer, as large metal-filled via holes are also used to remove heat from the layers hosting active elements.

⁴Other via holes types are *blind vias* (connecting internal layers to the top or bottom plates) and *buried vias* (crossing one or more internal layers)

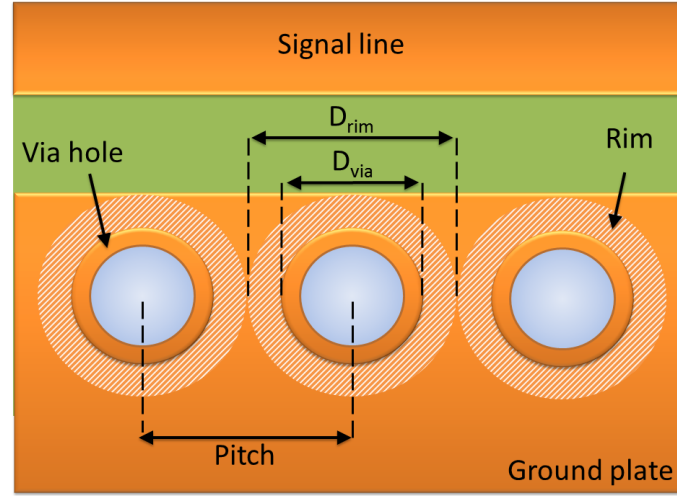


Figure 3.3: Configuration of via holes on the lateral ground plate of GCPW.

suitability of PCT SIW in the W-band and above, as shown in Fig. 3.4. A RT/duroid 5880 substrate with nominal $\tan\delta$ and smooth metallization is assumed in the simulated model: The nominal width of the SIW is 1.3 mm, while the substrate thickness is 127 μm . It can be seen that the line is perfectly able to confine the EM field up to 150 GHz and no signs of degradation are visible from the simulated S-parameters.

Dielectric Constant and Loss Tangent The dielectric constant of the substrates changes as a function of frequency. Manufacturers provide values measured at specific frequencies to be used as design reference. However, changes in the ϵ_r can lead to resonance shifts in filters, resonators and antennas, as well as to changes of the lines' impedance, thus compromising the functionality of the circuit. For mm-wave applications it is therefore important to use materials whose dielectric constant has a low value, as this reduces the impact on the circuit features, and that is relatively stable over frequency. As an example, the RT-duroid 5880 (with a nominal $\epsilon_r = 2.2$) which has been used as candidate for mm-wave design in most of the examples presented so far, has been proven to have a stable dielectric constant in the mm-wave range ($\epsilon_r = 2.24$ at 60 GHz) [174]. Comparable results have been found for other mm-wave laminates [174, 175]. Similarly, LCP substrates have been demonstrated to have stable dielectric constant (less than 5% variation) up to 110 GHz [176].

The $\tan\delta$ has a direct impact on the overall loss of the lines, therefore it is required that its value remains low in the mm-wave range. PTFE-based and LCP laminates are generally characterized by manufacturers only up to the lower GHz range. Experimental studies available in literature show that low-loss organic substrates can be used at frequencies above 100 GHz, although their dielectric loss might be higher than the nominal one: The $\tan\delta$ of LCPs has been found to have an increase of 30% [174] in the low-mm-wave range, and is expected to increase at higher frequencies (a peak of 90% increase has been found at 90 GHz in [176]). Similarly, the $\tan\delta$ of the RT/duroid 5880 has been measured

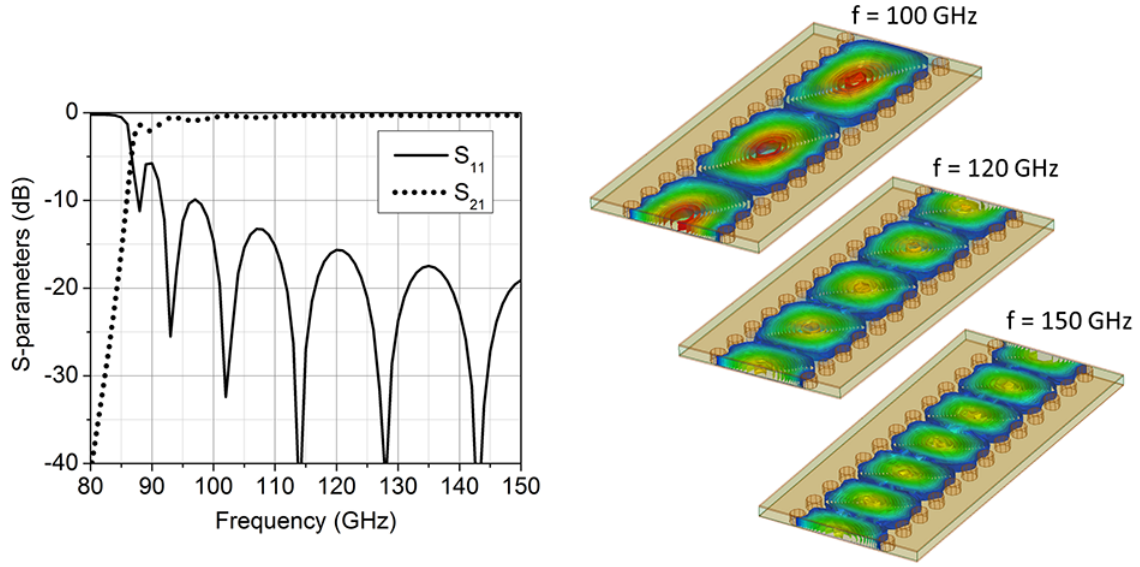


Figure 3.4: SIW for operation above 100 GHz: S-parameters (left) and electric field distribution for different frequencies (right).

to reach levels of 0.02 at frequencies above 100 GHz [177], a value which is 20 times larger than the nominal 0.0009.

3.4.5 Modeling PCT Lines for mm-Wave Applications

Predicting the actual characteristics of a designed transmission line can be challenging, as these depend on the accuracy of the manufacture, on the surface finish, on the tolerances of the metal and dielectric layers, and on the measurement environment. To produce accurate estimations during the design phase, prior knowledge should be acquired in order to set correct values for the parameters of EM simulations.

Rather than trying to model all phenomena separately, it is convenient to model all losses through an increased fictive $\tan\delta$, which has the advantage of not increasing the computational time required by the simulations. It is particularly appropriate to actually consider a 1-cm line for this kind of comparative study, as this allows the straightforward calculation of the attenuation constant (in dB per centimeter) of the PTL, as it will be shown in the following.

1-cm GCPW

Figure 3.5-a shows a 50- Ω 1-cm GCPW line built on a 127- μm -thick Rogers RT/duroid 5880, with a final metallization thickness⁵ of ≈ 35 μm . It can be seen in Fig. 3.5-b that

⁵The laminate has rolled copper metal layers with a thickness of 18 μm , which is then increased by the plating of the via holes and finally treated with an ENIG process.

HFSS simulations of this line predict less than 0.5 dB/cm in the 70-75 GHz range⁶, if the nominal $\tan\delta$ is adopted in the model and no surface roughness or other non-idealities are considered (black dashed line). On the other hand, the measurement of the attenuation of the same structure (obtained after subtracting the measured S_{21} of the same *thru* used for the calibration, also shown in Fig. 3.5-a⁷, from the measured S_{21} of the line) show that an attenuation of more than ≈ 1.5 dB/cm occurs in actual prototypes (orange solid line)⁸. It is however sufficient to consider a $\tan\delta_{\text{GCPW}} = 0.015$ in the simulation in order to have a correct estimation of the average loss, as clearly shown by the blue dotted line in Fig. 3.5-b.

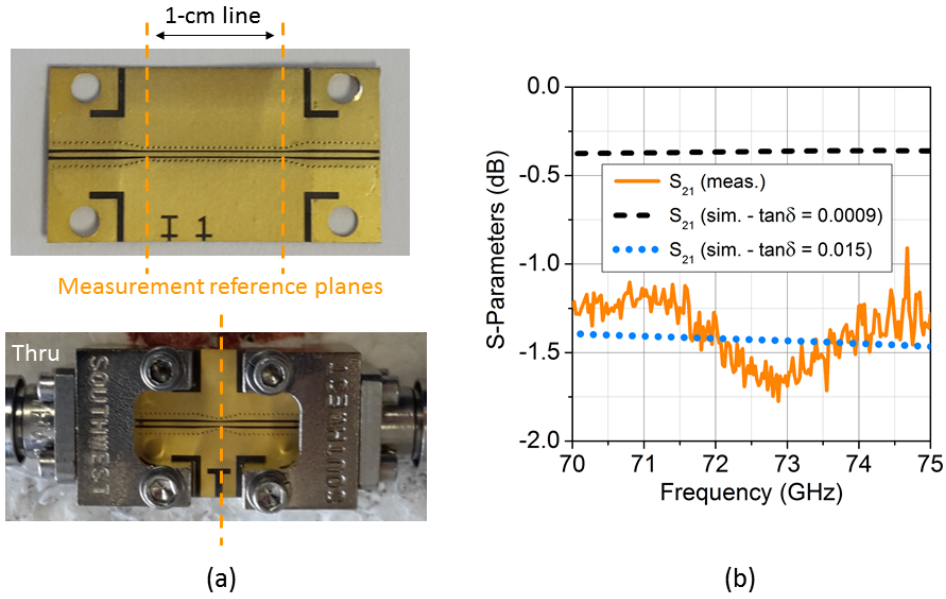


Figure 3.5: 1-cm GCPW line and thru (a) and the measured and simulated S-parameters of 1-cm-long PCB GCPW (b).

1-cm SIW

A similar characterization has been performed for SIWs designed to have an operational bandwidth of 35-70 GHz on a 381- μm -thick Rogers RT/duroid 5880 with an overall thickness metallization⁹ of ≈ 35 μm . This experiment focuses on the 57-64 GHz range, as its results will be used to model the 60-GHz integration platforms introduced in chapter 5.

⁶This frequency range has been considered in order to fit with the available measurement equipment and the target frequency of the designs introduced in chapter 4.

⁷The full calibration kit used for this measurement is shown in appendix D.1.

⁸The oscillations visible in the measurements are probably due to minor impedance mismatch caused by over-etching.

⁹Also in this case, the laminate has rolled copper metal layers with a thickness of 18 μm , which is then increased by the plating of the via holes, and an ENIG surface finish.

In this case, two GCPW-to-SIW transitions¹⁰ have been used to connect the coaxial connectors used to launch the signal into the laminate with the SIW. Two SIWs with different lengths have been inserted between the GCPW-to-SIW transitions, resulting in the two prototypes shown in Fig. 3.6-a. Thus the attenuation for 1-cm SIW has been calculated using the formula:

$$\alpha = -S_{21,1\text{-cm-SIW}} = \frac{S_{21,long} - S_{21,short}}{L_2 - L_1} \quad (3.4.2)$$

where α is expressed in dB/cm, the measured S-parameters of the *short* and *long* prototypes are expressed in dB, and the lengths L_1 and L_2 in cm. It can be noticed in Fig. 3.6-b that, while simulations of the SIW line based on the nominal $\tan\delta = 0.0009$ suggest an attenuation of 0.17 dB/cm (black dashed line), the actual measured loss is approximately 0.23 dB/cm, as indicated by the S_{21} extracted using equation 3.4.2 (orange solid line)¹¹. This situation can be recreated in simulations using a $\tan\delta_{\text{(SIW)}} = 0.0015$, as shown by the blue dotted line, which clearly suggests that SIW are intrinsically less prone than traditional PTL to undesired loss, if the design rules introduced in section 2.1.6 are respected, and their usage in mm-wave applications is strongly recommended, whenever possible.

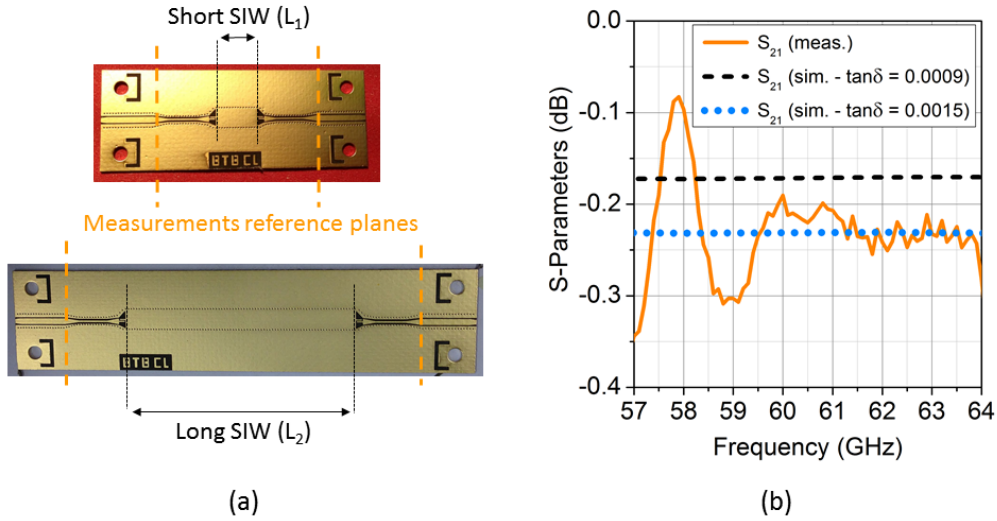


Figure 3.6: Prototypes of GCPW-to-SIW transition with short and long SIW (a) and the measured and simulated S-parameters of 1-cm-long PCB SIW (b).

Note that, as it will be shown in section 5.3, when simulating circuits based on a combination of traditional PTL and SIW, it is fundamental to model the different sections of the substrate with the appropriate fictive $\tan\delta$ (one to account for the minor increases loss in SIWs and one for the more critical loss introduced by GCPW). For instance,

¹⁰The model of the used GCPW-to-SIW transition will be introduced in section 5.3.1 and in particular in Fig. 5.5.

¹¹The larger ripples visible in the 57-59 GHz range are due to difficulties in the alignment of the coaxial connectors to the GCPW lines and should therefore be considered as artifacts [178].

for the circuit and substrate configuration presented in Fig. 3.6-a, the combination of $\tan\delta_{\text{(SIW)}} = 0.0015$ and $\tan\delta_{\text{(GCPW)}} = 0.01$ gives the best matching between simulations and measurements. In this case the $\tan\delta_{\text{(GCPW)}}$ is lower than the one calculated in the previous section ($\tan\delta_{\text{(GCPW)}} = 0.015$), as the substrate thickness is larger and therefore more field of the wave travelling along the GCPW is actually confined in air: Excessively increasing the $\tan\delta$ of the substrates would therefore lead to an over-estimation of the loss, as the fictive $\tan\delta_{\text{(GCPW)}}$ includes the impact of surface roughness and other non-idealities and has been derived considering a specific line cross-section. Furthermore, the considered frequency is lower in this case, and the loss tangent calculated for applications above 70-GHz would have an excessive impact on a 60-GHz circuit, even if built on the same laminate, as the theoretical dielectric loss is proportional to the frequency of the propagating signal (see equation 2.1.2).

3.5 Bonding Technologies

Bonding technologies are used to establish electrical connections between chips and packages or carriers.

3.5.1 Bond Wires and Bond Ribbons

Bond wires are the most common type of first-level interconnect. They are thin cylindrical wires (common diameters are 17 and 25 μm) which extend between two metal contact pads (Fig. 3.7-a). The preferred material for bond wires is gold, although aluminum and copper bondwires might be used in order to reduce cost in high-volume applications.

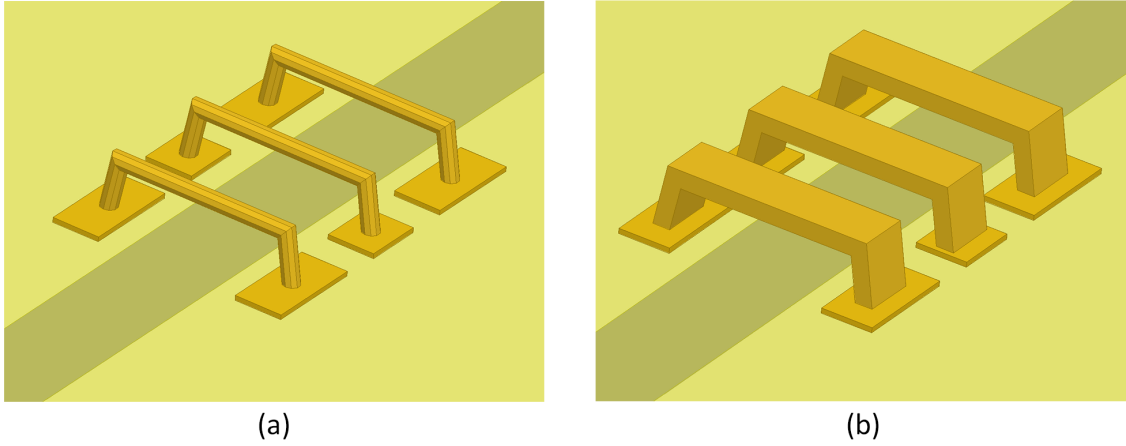


Figure 3.7: Simplified model of bond wires (a) and bond ribbons (b) connecting coplanar pads on two different substrates.

There are several techniques to attach the bond wires to the metal pads (ultrasonic bonding, thermocompression bonding, and thermosonic bonding), as well as multiple contact shapes, namely the ball-and-stitch and the wedge contacts. Wedge bond wires are usually preferred for higher-frequency applications because this approach allows a reduced overall

length of the bond [153], although thermosonic ball bonding is preferred for the integration of brittle optoelectronic chips, as this reduces the risk of chip damages [179].

The actual shape of the bond wires depends on the initial chip-substrate configuration and the bonding process. Accurate modeling can be performed for all segments of the wire and resonant-circuit or transmission-line models can be constructed in order to predict their performances [72, 153]. Nevertheless, a first estimation of the impact of the bond wire on the signals can be performed by modeling its self-inductance L_{bond} as that of a wire in free space [180]:

$$L_{\text{bond}} = 2 \left[l \ln \left(\frac{2l}{r} \right) - 1 \right] \quad [nH] \quad (3.5.1)$$

where l is the total length of the bond wire and r is the radius of the wire, both given in cm. It has been shown that the maximum allowed bond wire length (for a RL higher than 10 dB) is $0.033 \lambda_0$ (the wavelength in air of the operating frequency) [181]: This means that the maximum bond wire length is $100 \mu\text{m}$ already at 100 GHz, as shown in Fig. 3.8. Considering that the thickness of optical chips is generally in the order of 100-200 μm , this is impossible to achieve in chip-on-substrate configurations. Even considering additional aligning techniques, such as a cavity in order to place the chip and align its metal contact to the ones of the board (side-by-side bonding)¹², it can be challenging to draw such short interconnects because of the excess of dielectric which might extend out of the chip contact pads or the laminate transmission line¹³, as well as because of the intrinsic elevation of the bond wire from the chip.

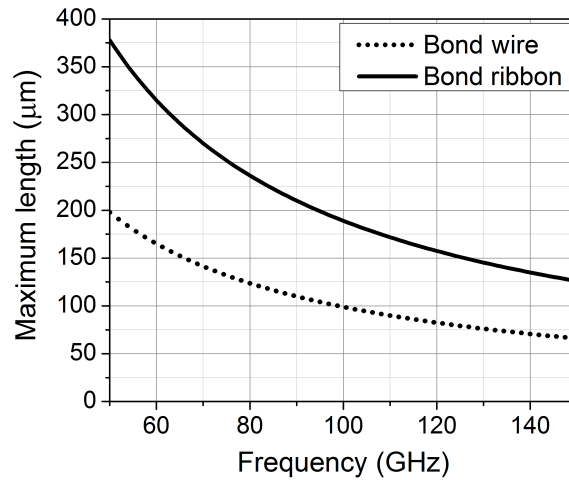


Figure 3.8: Maximum allowed length of mm-wave bond wires and ribbons to achieve a RL of at least 10 dB.

Using bond ribbons (Fig. 3.7-b) rather than bond wires considerably reduces the inductance of the interconnect [181] and therefore opens up the possibility of using longer bonds, with the maximum length for 10-dB RL given by $0.063 \lambda_0$, as shown in Fig. 3.8.

¹²See Fig. 4.32 for an example.

¹³Examples of alignment techniques are shown in Fig. 4.26.

Unfortunately the bond ribbon technology is less developed and flexible: Ribbons can be drawn in one direction only and at specific point, therefore requiring rotation and mechanical translation of the modules, thus slowing down the assembly operation.

For both wire and ribbon bonds, compensations techniques aimed at reducing the wire inductance or cancelling at a specific frequency can be used to improve the performance of the bonds: They can be based on matching stubs [182, 183], on using several wires in parallel configuration¹⁴, or on choosing a capacitive bonding point on unmatched circuits.

3.5.2 Flip-Chip Bonding

Flip-chip bonding is an excellent technique suitable for mm-wave applications because it drastically reduces the length of the interconnect, by attaching the chip output pads directly to the substrate metallization using bonding bumps, as depicted in Fig. 3.9.

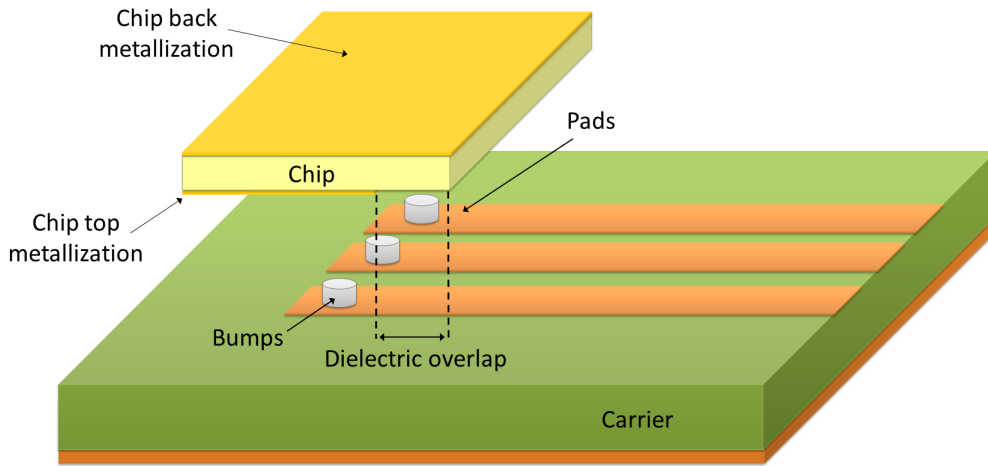


Figure 3.9: Flip-chip interconnect.

Flip-chip transitions depend on a number of physical parameters, although a simplified model essentially features a shunt capacitance [185] and their performance can be improved by minimizing the size of pads and bumps and increasing the pitch of the ground bumps, in the common case that flip-chip is based on coplanar-like structures. Flip-chip is particularly suitable for mm-wave interconnects, as it not only shows lower insertion loss and higher return loss than wire bonds and ribbons, but also have a non-resonant behavior thanks to their relatively compact dimensions [186]. Nevertheless, problems might arise from the interaction of the chip with the carrier metallization (*dielectric overlap*) or with the epoxy underfill that is sometimes used in order to facilitate the bonding process and make it more stable, as this will affect the properties of the transmission lines and other

¹⁴Using more than two wires per pad does not further improve the performance because of the increased mutual inductance [184]. Furthermore, it can be very challenging to bond more than two wires on the same chip pad.

resonant structures on the chip (*detuning*), as well as cause additional dielectric attenuation. These problems should be addressed in the design phase, when possible, but this is not feasible for general-purpose chips.

The usage of the flip-chip approach to integrate chips on PCB laminates can have additional drawbacks due to the generally large-sized pads (the minimum resolution of PCT technology is in the order of 50-100 μm) and the low- ε_r substrates, which are the preferred choice for mm-wave applications: This requires larger pads on the chip and therefore uses a large amount of semiconductor area. Thin dielectric substrates¹⁵ are preferred for flip-chip integration, as they help achieving the desired impedance of the pads, in spite of the size constraints [187].

Similarly to the case of bond wires and ribbons, matching circuits aiming at canceling the capacitive behaviour of the structure can also be used to locally improve the performance of flip-chip interconnects, if this is required by the specific application [182, 185].

3.5.3 Other Interconnecting Techniques

Besides the above mentioned well-established techniques, other approaches have been considered by the research community in order to transfer signals from chip to chip or from chip to motherboard.

Electromagnetic Coupling

In order to avoid the assembly issues due to long wires and tight control of the bump size, EM coupling between quarter-wave coupled lines can be used. This approach is relatively simple and does not show the low-pass characteristic of wires, ribbons and flip-chips, but it is resonant in nature and is generally not used for broadband interconnects [188].

MicroCoax

An evolution of the classic bond-wire interconnect is the microCoax [66]. It is essentially a very compact coaxial transmission line, that is grown around a bondwire, which thus becomes the internal conductor: At first a plastic layer is deposited around it in order to serve as dielectric spacer, then a second metallization is used to create the coaxial ground layer, as shown in Fig. 3.10. This means that an actual transmission line with controlled impedance and guiding characteristic is used to connect the chip and the board pads and therefore no mismatch nor radiation occur. The bandwidth of microCoax bonds is only limited by the appearance of higher-order modes of coaxial structures: The corresponding cut-off frequencies are inversely proportional to the physical dimensions of the line (see equation 2.1.17), therefore the operation of microCoax bonds can be considered monomodal up to the limits of the W-band. MicroCoax connections have been proven to introduce less than 1 dB of attenuation and to have a RL of at least 20 dB in the whole 0-115 GHz, even for the exceptional bond length of 2.2 mm [66].

¹⁵Laminates based on LCP are therefore particularly useful, as the suppliers provide LCP substrates with a thickness smaller than 100 μm .

Unfortunately, this technology is very expensive, as it requires a number of processing steps (creating the bond wire, adding the dielectric coating, laser drilling to create the connecting via hole to which the the coaxial is connected to the board, and the final selective metallization) and is therefore currently only suitable for demanding high-end applications (military and space modules).

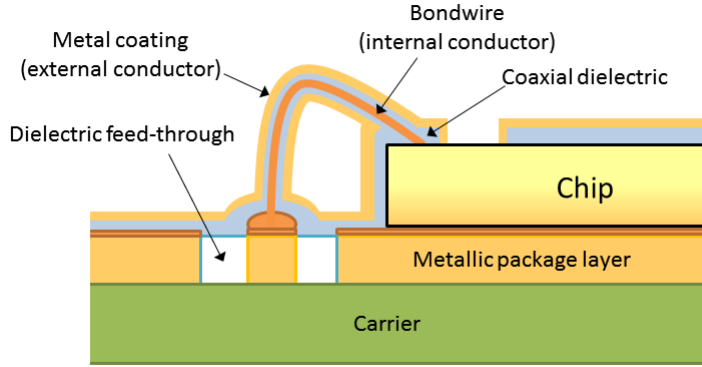


Figure 3.10: MicroCoax interconnect between a carrier (board) and a chip. Adapted from [66].

3.6 Module Housing

A fully packaged module is often fully or partially enclosed in an approximately rectangular metallic box, which reduces its susceptibility to interferences and protects the circuitry from electrical and mechanical shocks. This could lead to the excitation of cavity resonances, which form standing waves within the package and can compromise the isolation between circuits and the functioning of the module above the cut-off frequency f_{101} of the first resonant mode, which can be estimated from [58]:

$$f_{mnp} = \frac{c}{2\pi} \sqrt{\left(\frac{m\pi}{A}\right)^2 + \left(\frac{n\pi}{B}\right)^2 + \left(\frac{p\pi}{C}\right)^2} \quad (3.6.1)$$

where c is the speed of light and $B < A < C$ are the dimensions of the package and n , m , and p are the corresponding modal indices. Packaged modules actually are partially loaded cavity resonators with complex geometry due to the substrate, the chips and the surface-mount components; the effect of substrates can be neglected for thin dielectric carriers with low ϵ_r , therefore, if the chips are small in comparison to the package, the simple metallic resonator offers a good approximation for the estimation of the first resonant frequency. In the mm-wave range it is usually impossible to keep the dimensions of the package below half of the wavelength corresponding to the maximum frequency of interest, i.e. $C < \lambda_{\max}/2$, as this corresponds, for instance, to 3 mm at 50 GHz and 1.4 mm at 110 GHz, which are comparable to the dimensions of a single chip. Therefore additional techniques have to be used to suppress or weaken the resonances, such as absorbing foams

injected into the package [189] or lossy dielectrics and resistive coatings deposited on the walls of the housing [190, 191]. The partitioning of the package in cabinets and the usage of metal diaphragms [192] as well as additional planar circuits [193] can also be used to alter or dampen the resonant modes.

3.7 Conclusions

In this chapter the issues related to integration of PD modules for mm-wave operation have been addressed.

Both monolithic and hybrid integration have been considered and their advantages and disadvantages have been compared. Although monolithic integration has a potential for reducing losses and developing more compact devices, it is more expensive and sometimes even impossible due to incompatibility of materials and processes required for different elements (lasers, amplifiers, PD, low-loss lines). Hybrid integration is therefore currently necessary to the development of new modules with more functionalities, and additionally has the advantage of being particularly suitable for prototyping and fast time-to-the market applications.

We have thus introduced the different processing technologies available for the development of hybrid integration platforms (thin-film, thick-film, LTCC, HTCC, PCT), analyzing their properties and resolution possibilities. Thin-film circuit development is the process that currently guarantees the highest line resolution and accuracy, therefore its use is widespread for mm-wave optoelectronic applications. However, the very expensive equipment, the lengthy manufacturing process, and the low yield of the process make the use of more efficient technologies, such as PCT, desirable in order to support consumer-driven applications. We have considered sources of uncertainty and tolerances (e.g. etching inaccuracy, substrate thickness, and other electrical and mechanical parameters of PCBs), and we have discussed their impact on mm-wave boards. Although each parameter only introduces tolerable deviations on the characteristics of the transmission lines, their combination could impact particularly sensitive structures, such as resonant lines and filters. However, this phenomenon can be kept under control with preliminary investigations and simulations, as it will be shown by the examples introduced in chapters 4 and 5.

Measurements of SIW and GCPW lines in the 60-GHz and 70-GHz bands have shown that the signal attenuation due to radiation, surface roughness and dielectric loss can be effectively estimated by using opportune values of artificial $\tan\delta$. We have demonstrated that the intrinsic radiation-free nature of the SIW makes it more reliable in comparison to traditional planar technology, proving an excellent correlation between experimental and ideal simulated results. The demonstrated low-loss property of the SIW makes it particularly desirable for applications in the mm-wave, especially in cases in which long on-board signal traveling paths are required.

We have highlighted that via holes play a fundamental role, as they ultimately decide the highest possible frequency, independently of other parameters like conductor and dielectric loss, or etching inaccuracies. Via holes are vital to guarantee a correct functioning of both GCPW and SIW, by avoiding board resonances and interferences between

different lines. We have estimated that the current via hole technology clearly allows the development of PCB up to at least the upper limit of the W-band, although higher operational frequencies might be achieved, as far as the increased radiation loss does not compromise the functionality of the circuit. Some recent examples of PCB integration in the 80-120 GHz range can be found in [187, 194].

We have furthermore analyzed well-established bonding technologies (bond wires and ribbons) used to connect the chips to the carrier, showing that their usage at mm-wave frequencies is appropriate. Although flip-chip interconnects generally offer better performance above 100 GHz, their usage on low- ϵ_r laminates might not be feasible because of the required pads spacing. Alternative solutions aiming at simplifying the assembly or reducing the loss of the interconnect have also been considered and their benefits highlighted, although their usage is limited to specific conditions and applications.

Finally, the impact of metal housings on the circuit performance has been analyzed, highlighting that special countermeasures are necessary in the mm-wave range in order to avoid the excitation of cavity resonances within the packaged module, which would compromise the functionality of the system.

4 PCB Integration Platforms for mm-Wave Photodiodes Modules with Rectangular Waveguide Output

As introduced in chapter 1, the E-band has very peculiar characteristics that make it attractive for high-speed wireless communication, which led the worldwide allocation of the 70/80 GHz bands for point-to-point wireless communication. In order to minimize the risk of interference between adjacent systems/links and increase frequency reuse, regulation bodies request the usage of very high-gain antennas with WR input connectors (see section 1.2). Consequently, commercially competitive RoF systems require the development of integrated PD modules featuring a WR port, as the attention given to this topic by the research community in the last years proves. In fact, several approaches have been suggested to couple the output of the PD chip to a WR, generally making use of probes placed across the WR opening [28–31] or inserted into the WR [32–36]. The circuit manufacturing technique required for the proposed designs (thin-film) makes the packaging of PD modules rather expensive, due the high cost of the equipment and the low yield of the assembly processes, which is limited by the small size of the processed substrates and the split-block and waveguide machining (e.g. in [28, 34, 35]) necessary to manufacture and assemble non-standard elements, such as reduced-height waveguides. None of the mentioned approaches provide a mechanical enclosure of the WR opening, thus allowing moisture and particles to penetrate into the module, which can cause malfunctioning and failure of the system. Therefore additional sealing components are required in order to provide an enclosure without excessively compromising the transmission [37].

On the basis of the results introduced in chapter 3, where it has been asserted that PCB technology can theoretically be used for the development of mm-wave modules up to the W-band, and where the actual losses of PCB PTLs have been verified experimentally in the 60/70-GHz bands, this chapter will introduce several integration platforms entirely based on PCT: We aim to develop compact, cost-effective, E-band PD modules with WR output, as an alternative to the integration concepts mentioned above.

4.1 Photodiode Module with Rectangular Waveguide Output

The proposed integration concept [51] is depicted in Figure 4.1. It is based on the integration of an E-band PD featuring a GCPW output with a GCPW-to-WR-12 transition created on a PCB laminate, which couples the field into the WR through slots etched

in the ground plane. The usage of laminates with low moisture absorption as dielectric carrier allows therefore the development of quasi-hermetic packages without the need of additional radomes, provided that a hermetic housing is connected to the top side of the assembly. All designs and experimental validations presented in this chapter are based on a 127- μm -thick Rogers RT/duroid 5880. The choice of a thin laminate was dictated by the need to reduce radiation loss, as some design elements represent sensitive discontinuities prone to radiation. Furthermore, using thinner substrates help excluding the excitation of unwanted parasitic modes and having a more uniform field in GCPWs, reducing the current density at the lateral edges of the signal trace.

The PD chip and the laminate are connected via bonding wires or ribbons and share a metallic submount for mechanical and grounding purposes. The laminate can be aligned and secured to the WR using the conventional pins and screws of standard WR flanges (the alignment holes are visible in Fig. 4.7), thus dramatically simplifying the assembly procedure in comparison to previously reported alignment concepts, as discussed in section 1.4.

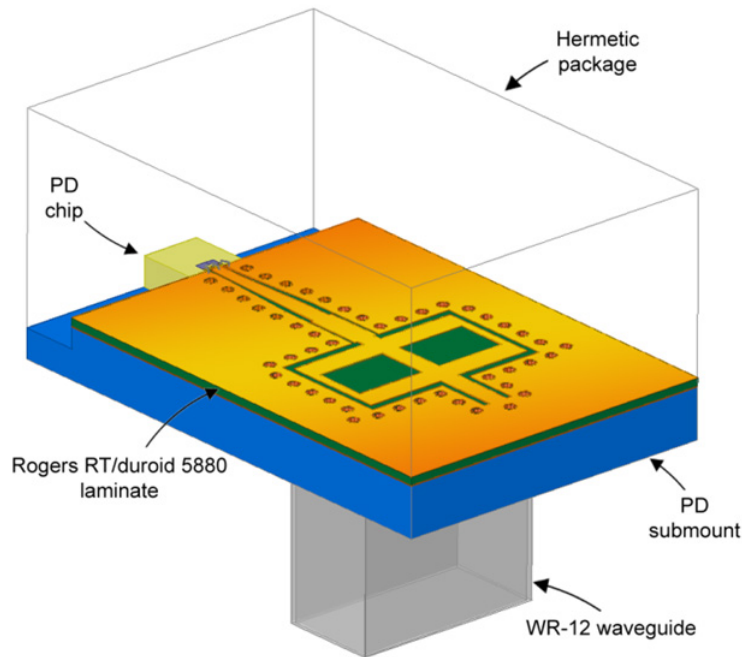


Figure 4.1: Integration concept for a PD module with WR output.

4.2 Quasi-Hermetic GCPW-to-WR Transition

Millimeter-wave PDs generally have a 50- Ω CPW or GCPW output line that can be easily connected to similar transmission lines. We have therefore chosen to develop a 50- Ω GCPW transmission line etched on the mm-wave laminate, to which the output of the PD is bonded. The additional ground layer of the GCPW and the metal-plated via holes used

to suppress high order modes within the substrate enable a more efficient heat removal from the PD chip or other active elements, such as amplifiers, that could be included in the design (see section 4.3.3). It also helps to confine the majority of the EM field into the laminate, leading to an improved coupling efficiency into the WR and reduced undesired radiation. In the design phase, special attention has been given not only to the theoretical optimization of the individual sub-blocks, but also to the analysis of practical construction constraints and design rules, in order to develop an integration concept that can actually be manufactured using commercially available PCT.

Based upon the guidelines reported in [195], a double-slot antenna has been designed for operation in the 71-76 GHz wireless communication bandwidth in order to couple the signal from a 50- Ω GCPW to the WR, as using a double-slot coupling rather than a single slot allows an extended frequency range [196, 197]. In fact, as it will be shown in the following, the transition exhibits a broadband behaviour and it would be possible to use it for systems working in both 70/80 GHz bands (e.g. for transceiver or for dual-channel applications); however, for practical purposes (characterization, experimental system validation) the design process has been carried out focusing on the optimization for operation in the 71-76 GHz band. The two slots are etched on the bottom ground (see Fig. 4.2-b), while a matching structure is used on the top side (see Fig. 4.2-a) of the laminate in order to reduce the radiation into free space and improve the coupling. The best way to analyze the behaviour of the transition is by considering a signal coming from the WR that has to be coupled to the GCPW [198]. The two waves excited by the two slots into the substrate are in opposition of phase (as shown in Fig. 4.3-a) and cancel each other in the center of the transition, while they are free to propagate away from the transition along the central GCPW lines, as shown in Fig. 4.3-b. On one side, the GCPW is short-circuited, therefore the wave is reflected back and is allowed to join the other wave by traveling along the guiding lines that encircle the coupling point (see Fig. 4.3-b). A similar coupling mechanism occurs when a wave coming from the GCPW input has to be coupled into the WR.

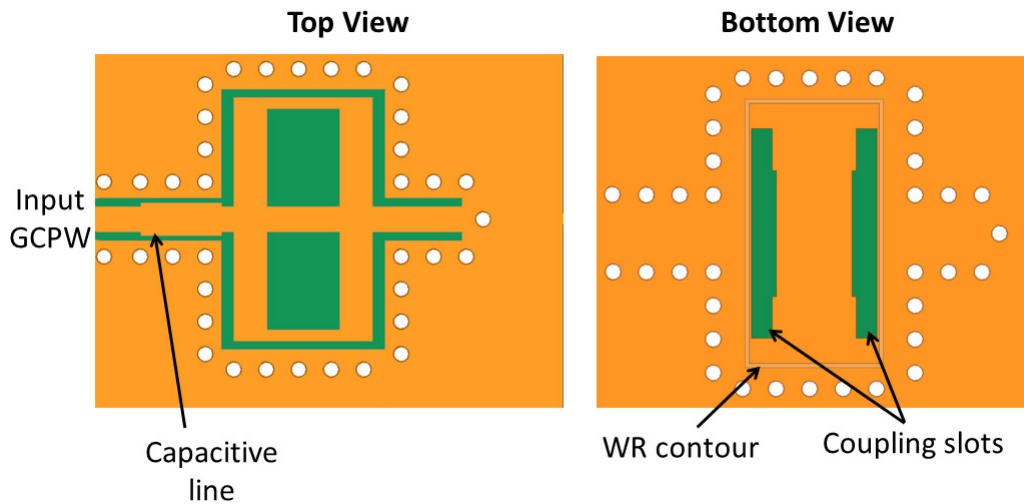


Figure 4.2: Detailed view (top and bottom) of the GCPW-to-WR-12 transition.

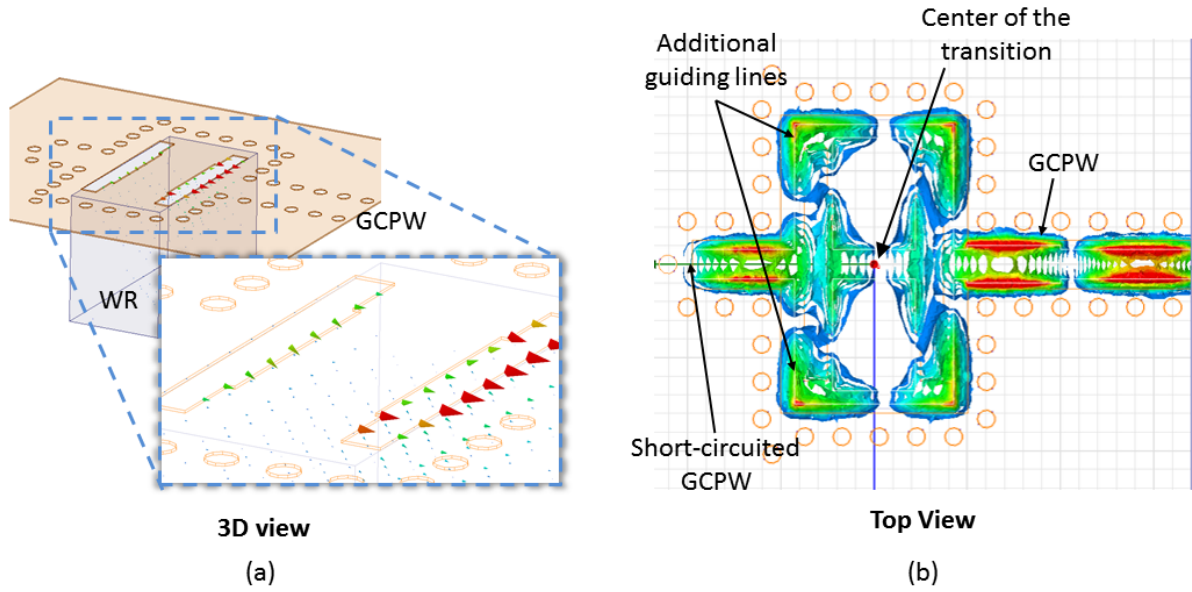


Figure 4.3: Working principle of the GCPW-to-WR transition: (a) View of the waves excited by the two slots (only the bottom ground of the laminate is shown); (b) view of the waves traveling along the transmission lines and matching structures on the top side of the laminate.

In order to achieve a perfect match at 73 GHz, the shape of the coupling slots has been modified by adding a shorter notch in the internal side (see Fig. 4.2-b) and by inserting a 1-mm-long capacitive line ($Z_0=45 \Omega$) between the GCPW port and the transition (see Fig. 4.2-a).

To prevent the excitation of higher-order modes, and in particular to suppress the patch-antenna resonances that can be established between the two metal layers of the substrate (see section 2.1.5), an EM wall has been created in proximity to the GCPW signal line, connecting the bottom and top ground layers with a fence of metal-plated via holes. Figure 4.4-a shows an exploded view of the transition optimized for the 71-76 GHz range. As it can be seen, the via holes have been placed as close as possible to the transmission lines and the coupling slots, respecting the guidelines for commercially available PCB manufacturing techniques.

The GCPW-to-WR-12 transition has been modeled and optimized using the commercial software tool Ansoft HFSS. The dimensions of the optimized design are given in Appendix B.1. The simulated performance of the transition is shown in Fig. 4.4-b. It can be seen that the simulated IL is less than 2 dB from 62 to 82 GHz (black line), with ≈ 1.5 dB in the 71-76 GHz range. These results are based on a dielectric with nominal $\tan\delta = 0.0009$ and perfectly smooth conductors. A more reliable estimation of the measurable loss of the transition, which takes into account the modeling considerations suggested in section 3.4.5 ($\tan\delta = 0.015$), is given in the same plot (red line) and shows that up to ≈ 1 dB of additional loss can be expected to be found during experimental characterization. Within the mentioned 62-82 GHz range, the RL at the WR port is higher than 12 dB (pink line), while the RL at the GCPW port is higher than 18 dB (blue line). The

transition has been designed in order to achieve the best performance in the 71-76 GHz, where the expected maximum IL is ≈ 2.5 dB and the RL is higher than 25 dB. Figure 4.5 further shows the propagation of the 73-GHz electric field in the structure: Due to the thin substrate, the electric field is concentrated within the substrate and in proximity of the GCPW gaps, and is then conveyed into the WR.

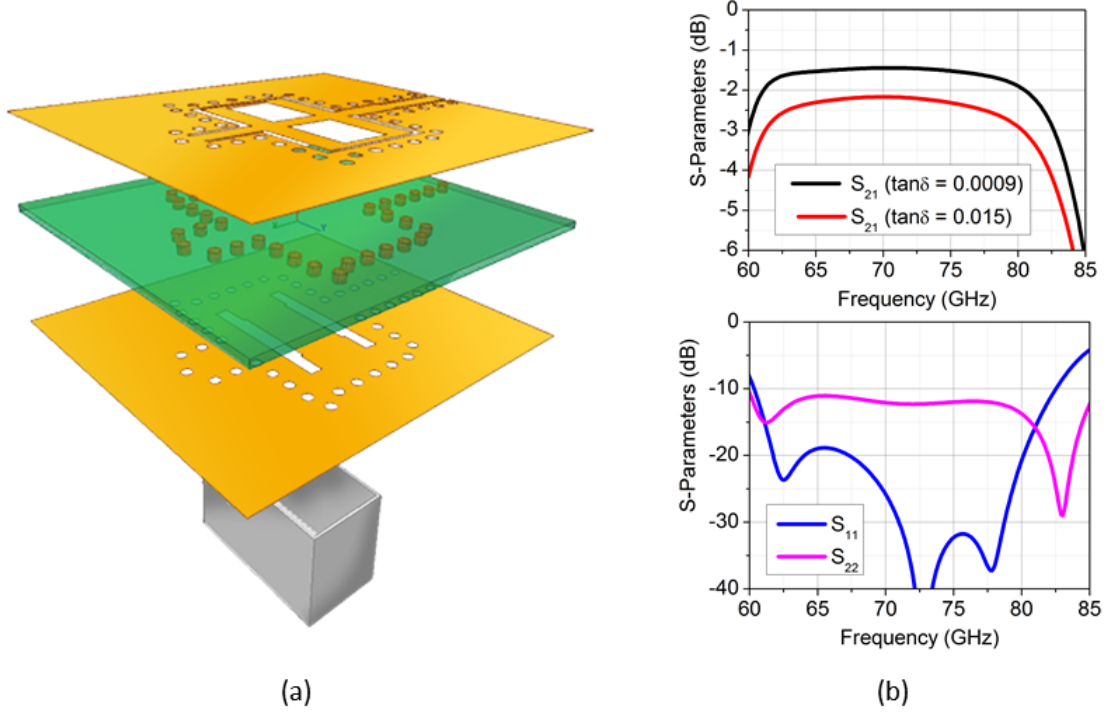


Figure 4.4: Exploded view of GCPW-to-WR-12 transition (a) and its simulated S-parameters (b). Port 1 is located at the GCPW input and port 2 is located at the WR-12 output.

One of the most challenging assembly issues may derive from the alignment of the WR. Therefore, alignment holes have been included in the prototype laminates (see Fig. 4.7), in order to profit of the pins of a standard WR flange to achieve a correct positioning of the transition. The accuracy of this solution is limited by the drilling alignment precision of the PCB manufacturer, which is estimated to be in the order of 100-200 μm , depending on the accuracy of the adopted equipment (see section 3.4.4). The impact of the misalignment on the assembly has been analyzed by means of HFSS simulations¹. Figure 4.6 shows that a misplacement of the WR away from the GCPW port is more severe than one in the opposite direction. However, in both cases, even a displacement of 200 μm can still be accepted, as the RL at the GCPW port would still be higher than 10 dB; at the same conditions, the RL at the WR port can decrease down to 7 dB, although this parameter

¹Only *longitudinal misalignment* (i.e. along the direction of the GCPW line) has been considered here, as *lateral misalignment* is less crucial thanks to larger distance from the slot edges to the WR contour in this direction.

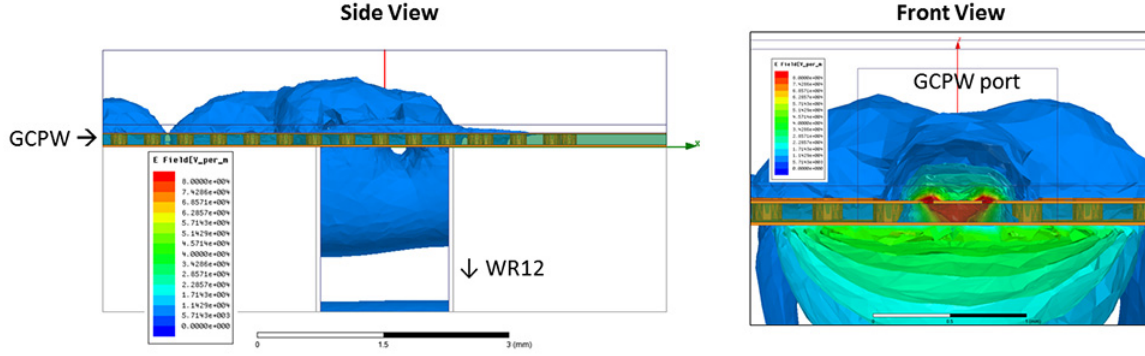


Figure 4.5: Propagation of electric field (73 GHz) from the GCPW to the WR-12 output.

is not crucial for the application considered here, where the feeding port is at the GCPW. The impact on the IL is negligible and has not been reported here.

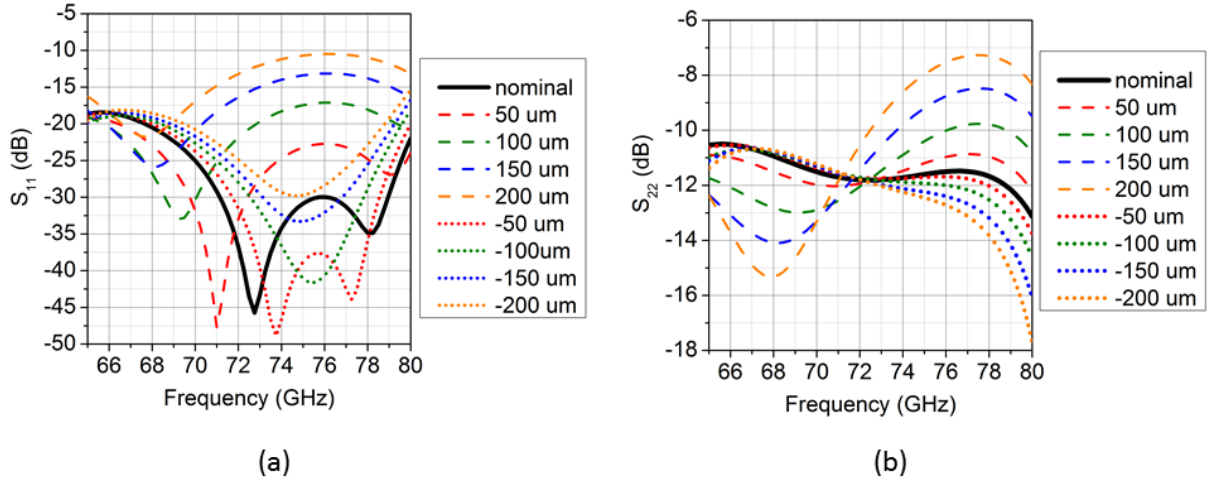


Figure 4.6: Impact of the misalignment of the WR on the RL at the GCPW port (a) and at the WR port (b). A shift away from the GCPW port is indicated with positive numbers, while a shift towards the GCPW is indicated with negative numbers. The thick black lines, given as a reference, represent the nominal case (perfect alignment).

In order to facilitate the bonding process and use bond wires of acceptable length when connecting the PD chip to the laminate, a smaller GCPW configuration is needed, therefore a linear GCPW taper, visible in the transition shown in Fig. 4.7) has been designed. Its geometry has been optimized optimized for achieving a low IL and to allow optimum coupling (bonding) to the PD as well as to the antenna structure, while always keeping the impedance of GCPW close to 50 Ω .

Before proceeding to experimental validation, as the equipment available for the measurements was equipped with WR-15 ports, the performance of the transition has been simulated with both WR-12 and WR-15 outputs. A comparison of the two simulations,

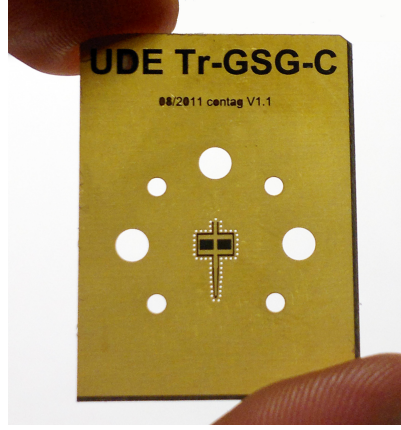


Figure 4.7: Manufactured GCPW-to-WR12 transition

which assume a dielectric with nominal $\tan\delta = 0.0009$, is shown in Fig. 4.8-a: Clearly, the IL is only slightly affected by the different size of the WR while the RL is reduced from 18 dB to 15 dB at the GCPW port and from 12 dB to 9 dB at the WR port. The negligible impact on the IL and the relatively small changes in the transition's RL when being used with a WR-15 port confirm the appropriateness of the adopted measurement equipment.

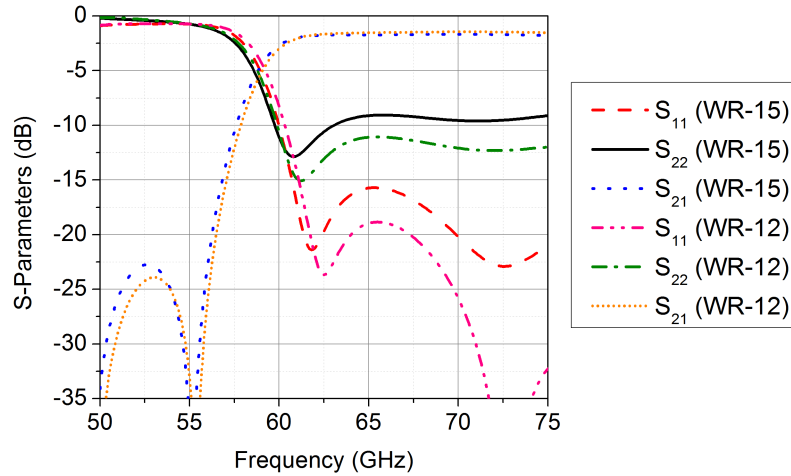


Figure 4.8: Simulated S-parameters of the transitions from GCPW to WR-12 and to WR-15.

The first experimental validation of the transition was carried out exciting a mm-wave signal on the GCPW probe through a G-S-G probe² and measuring the signal delivered to a mixer with WR-15 input port by means of a spectrum analyzer (SA), as shown in Fig. 4.9-a. Measurements of the S_{21} of several fabricated transitions³ are depicted in

²An additional small taper has been added to the end of the GCPW in order to allow the placement of the G-S-G contacts and launch the signal into the laminate.

³The metal layers of the laminate used in for these prototypes are 9- μm rolled-copper layer, with addi-

Fig. 4.9-b⁴ [199]. Although this approach has some uncertainty (due to the placing of the G-S-G fingers and the estimated loss of the required interconnects, such as the probe and the coaxial connector), the measured average IL is ≈ 2.5 dB, which is in excellent agreement with the expected value mentioned above (see Fig. 4.4). Of further interest is that the measurements clearly show that, if no metallized via holes are added along the GCPW, the leakage of the EM power can introduce up to 6 dB of additional loss. The use of metal-filled rather than metal-plated via-holes has no influence on the RF performance (see section 2.1.1) and will not be considered in the following.

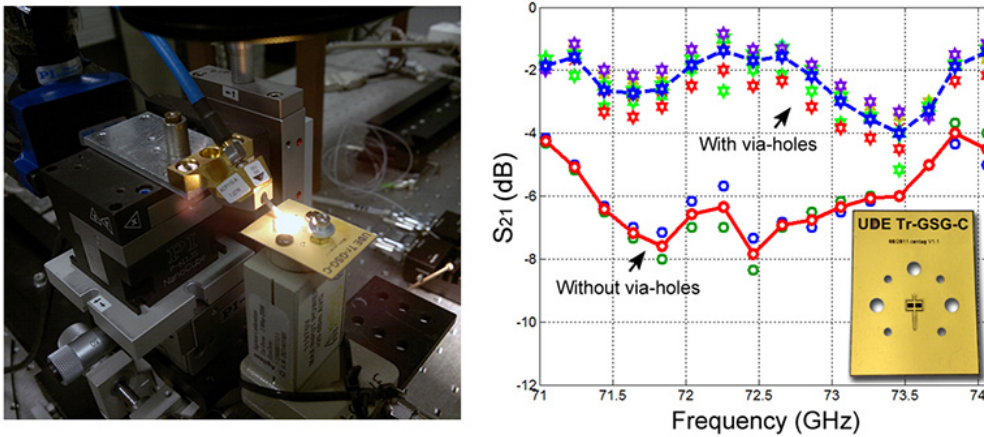


Figure 4.9: Experimental validation of the GCPW-to-WR transition: (a) Measurement setup and (b) measured S_{21} of the transition with (blue dashed line) and without (solid red line) via holes; the values have been obtained averaging measurements of several transitions with via holes (stars) and several transitions without via holes (circles). The inset shows one of the measured transitions.

For a second experimental characterization, the back-to-back (B2B) setup shown in Fig. 4.10-a has been used: End-launch connectors connected to VNA ports are used to launch the signal into the GCPW of one transition, which is then coupled to a WR-12 E-plane bend (bending radius = 2.5 cm; total length of the waveguide ≈ 13 cm), which finally guides the wave to the second transition, connected in a similar configuration. In order to improve the accuracy of the calibration and reduce the impact of connectors from the measured results, a narrowband TRL calibration based on standards designed on the same laminate board of the transitions has been used (see Appendix D.1). Two measurements based on four different prototypes⁵ are shown in Fig. 4.10-b, together with

tional copper plating and galvanic nickel-gold surface finish. The total metal thickness is $\approx 20\mu\text{m}$. The same configuration is used for the prototypes shown in Fig. 4.11 and 4.16.

⁴A calibration has been performed in order to preventively remove the loss of mixer and cables connecting its output to the spectrum analyzer.

⁵Due to limited material availability, the metal layers of the laminate used for these prototypes are $18\text{-}\mu\text{m}$ rolled-copper layers, with additional copper plating and ENIG surface finish. The total metal thickness is $\approx 35\mu\text{m}$.

simulated S-parameters: It can be noticed that the measurements show some variability due to the accuracy in placing the end-launch connectors and to the tension generated by the coaxial cables attached to the connectors. Nevertheless, the average IL measured with this setup in the 70-75 GHz range can be estimated to be 9.5 dB, which includes the loss of the 1-cm GCPW line added at the input of each transition (shown in the inset in Fig. 4.10-b) in order to allow the connection of the coaxial connectors, and the loss introduced by the WR-12 bend, which can be estimated from simulations to be at least 0.5 dB. The measurements show a good agreement with the simulated behaviour of the same configuration, as reported in the same plot.

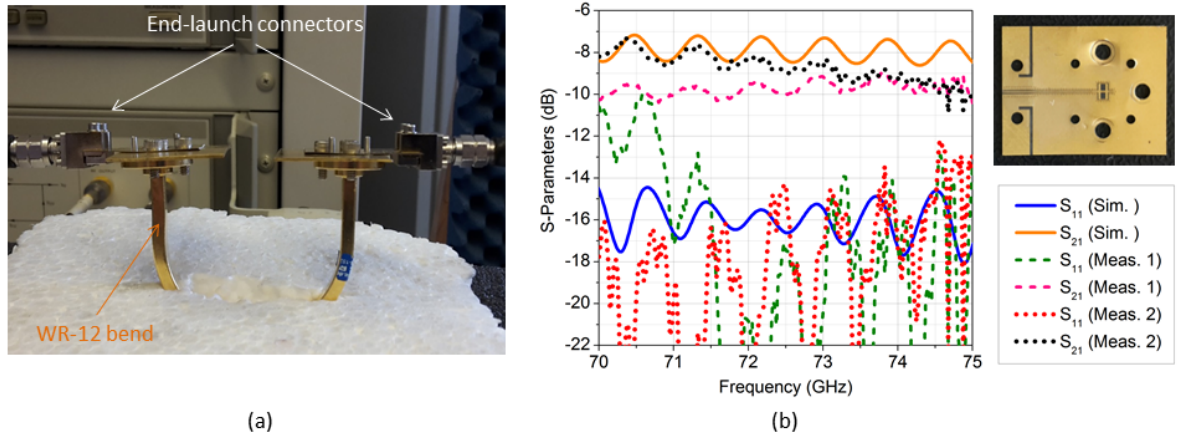


Figure 4.10: Measurement setup (a) and S-parameters of the B2B transition (b).

For a more a broadband characterization, a second B2B setup has been considered as it is shown in Fig. 4.11. In this case, using the WRs as input ports allows the usage of a commercial SOLT calibration kit and a mechanically stable connection to the VNA ports. The two transitions⁶ are connected by a 2-cm GCPW. A comparison of the measured and simulated results for this configuration is given in Fig. 4.12-a, from which a good overall agreement can be noticed. In particular, in the band of interest (71-76 GHz) the RL settles around the value of 9 dB for both measured and simulated B2B transitions. The measured IL is ≈ 7.5 dB, whereas the corresponding simulated value is below 5 dB, when the nominal $\tan\delta$ is used; using an increased $\tan\delta = 0.015 - 0.018$ for the simulation provides an excellent agreement between measurements and simulations, as shown in Fig. 4.12-b. Considering the ≈ 2.5 dB of loss ascribable to the 2-cm GCPW line that is used to connect the two transitions, it is possible to estimate an IL ≈ 2.7 dB for a single transition in the 71-75 GHz range, which suggests that the higher loss - when compared to simulations - reported in Fig. 4.10 are actually due to the non-idealities of the setup. It is important to notice that the B2B configuration shows a flat measured IL in the wide 60-75 GHz range, with fluctuations smaller than 2 dB.

The importance of using via holes has also been verified with this setup: A comparison of the measured S-parameters of the B2B transition with and without via holes

⁶The metal layers of the laminate used in for these prototypes are 9- μm rolled-copper layer, with additional copper plating and galvanic nickel-gold surface finish. The total metal thickness is $\approx 20\mu\text{m}$.

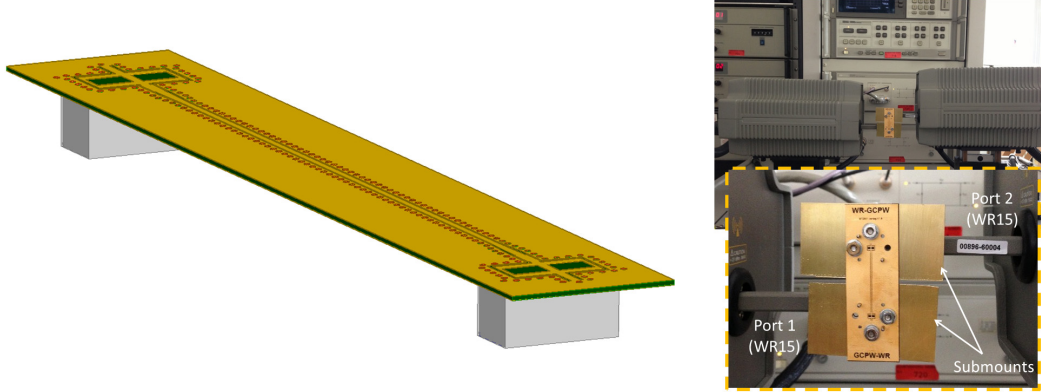


Figure 4.11: Left: Model of the B2B transition. Right: Setup for VNA measurements (setup 2).

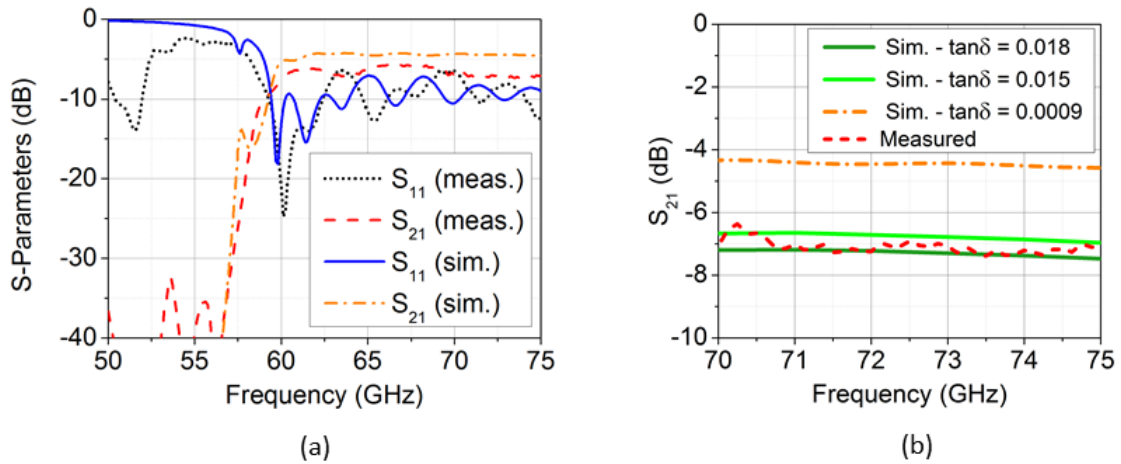


Figure 4.12: Simulated and measured S-parameters of the B2B transition (setup 2) (a) and impact of the $\tan\delta$ on the IL (b).

is given in Fig. 4.13. As expected, the RL is not strongly affected by the removal of the via holes but the IL is highly degraded, due to parasitic modes that are excited between the top and bottom ground planes, forming standing-wave patterns and eventually being radiated from the edges of the laminate. These measurements are in good agreement with the results obtained with the measurement setup shown in Fig. 4.9 and confirm that via holes are crucial for a proper behavior of the transition in the E-band and cannot be omitted from the final design.

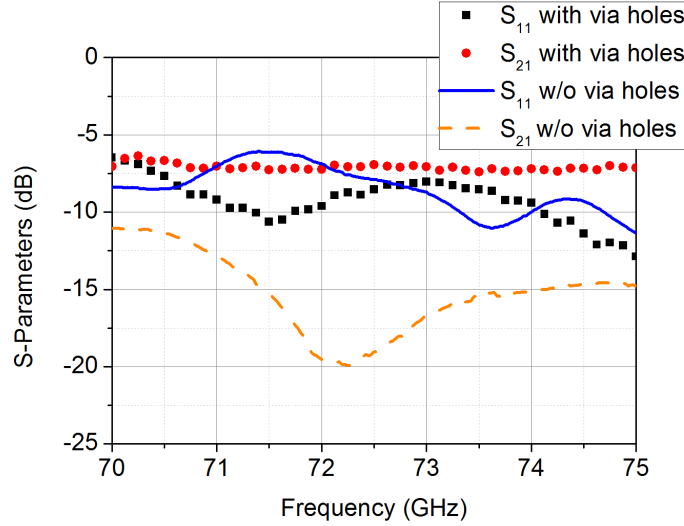


Figure 4.13: Measured S-parameters of the B2B transition with and without via holes.

Although the matching structures on the top side of the laminate reduce the undesired radiation to the open air, energy is still radiated in correspondence to the coupling point. As shown in Fig. 4.14, it is possible to reduce the loss of more than 1 dB by using a quarter-wave waveguide backshort⁷. However backshorts are additional components, that would even require special machining in order to avoid short-circuiting of the GCPW line, and would make the package bulkier and more expensive. Therefore the possibility of using a simple metal lid to emulate the effect of the backshort on the transition has been investigated, as shown in Fig. 4.15. The results clearly indicate that this simple solution allows reducing the simulated loss of up to 1 dB and would therefore be preferred to the conventional backshort for its unproblematic implementation in packages.

This improved transition has been experimentally tested⁸ and the measurements have confirmed the expected ≈ 2 dB reduction of the IL of the B2B configuration in comparison to the B2B structure without metal lids, as shown in Fig. 4.16. For this experiment, the metal lids have been realized with conductive tape positioned with the help of a spacer at a height of ≈ 1.5 mm (the value suggested by simulation-based optimization) above the transitions. For a packaged device, a more stable realization is preferable, which can be

⁷Note that this simulation assumes a nominal $\tan\delta = 0.0009$, as we are only interested in estimating the net improvement introduced by the backshort rather than in the overall loss.

⁸The prototypes have been manufactured on the same laminate and with the same process of the transitions shown in Fig. 4.11.

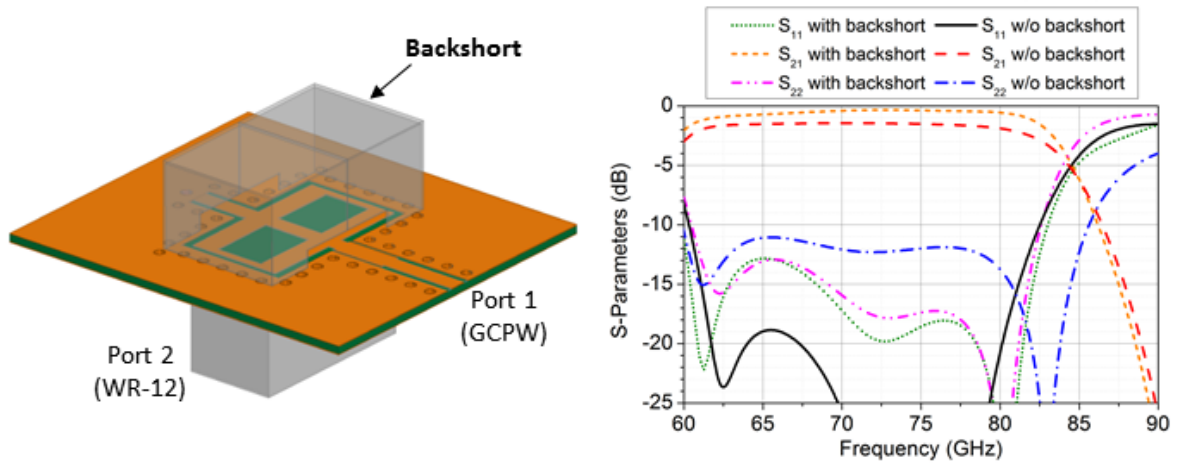


Figure 4.14: Model of transition with backshort (left) and comparison of simulated S-parameters of the transition with and without backshort (right). A WR-12 waveguide is used for these simulations.

achieved by placing a metal cover on the spacer used to secure the screws of the WR flange (Fig. 4.17-a) or by using a low-profile package, e.g. gluing a metallized spacer at the internal side of the package cover (Fig. 4.17-b).

4.2.1 Transition with Built-In Planar Bias Network

One of the advantages of using laminates for the integration of PDs is the relatively low cost of the substrate, which gives more freedom to the designer when integrating additional circuitry, at essentially no increased manufacturing cost.

In the transition introduced in section 4.2, there is a large area of unused laminate due to the size of standard WR flanges. Therefore it can be useful to dedicate this space to the implementation of a bias network, thus allowing the integration of PD lacking an internal bias circuit [200].

The first required component is a planar RF-choke that allows the DC current to reach the PD, while preventing loss of the mm-wave signal through the DC path. This can be achieved by means of two open-circuited stubs in a parallel configuration providing an RF short-circuit which is then transformed into an RF open-circuit by a quarter-wave transformer, as illustrated in Fig. 4.18-a. The length of the transformer, ideally set to be a quarter of the wavelength corresponding to the central frequency (73.5 GHz), had to be increased to allow the drilling of the via holes. The effects of this modification on the performance of the RF-choke have been compensated by additional optimization of the dimensions (length and width) of the transformer and the stubs [201, 202].

Narrow-band (blue lines) and broadband (red lines) measurements of the S-parameters of the RF-choke⁹ are shown in Fig. 4.19, together with the simulated response (thick

⁹The metal layers of the laminate used in for these prototypes are 9- μm rolled-copper layer, with additional copper plating and autocatalytic silver immersion gold (ASIG) surface finish. The total metal thickness is $\approx 35\mu\text{m}$. The same configuration is used for the prototypes shown in Fig. 4.26–4.32 .

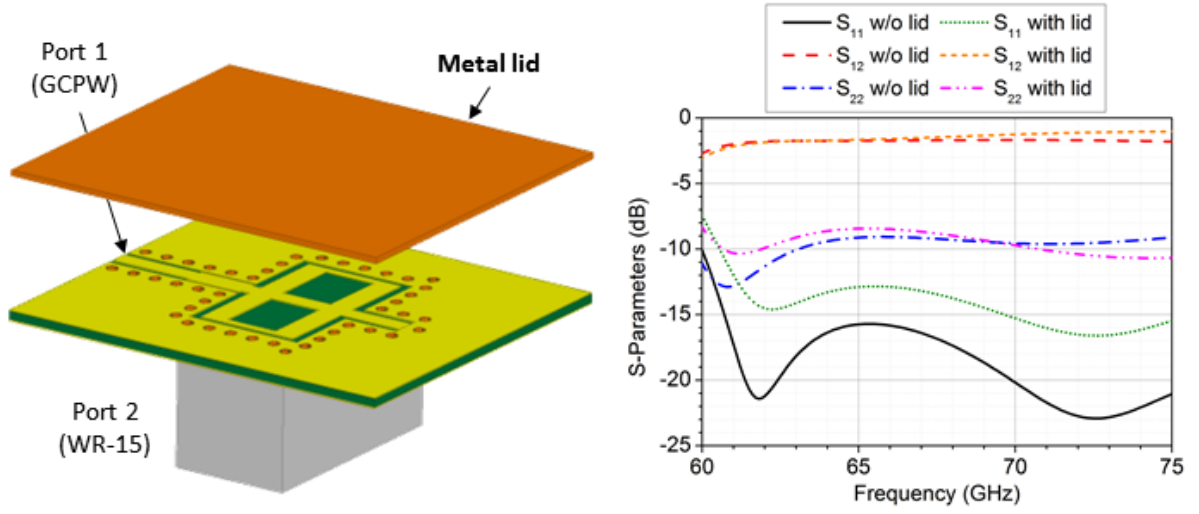


Figure 4.15: Model of transition with metal lid (left) and comparison of simulated S-parameters of the transition with and without lid (right). A WR-15 waveguide is used for these simulations.

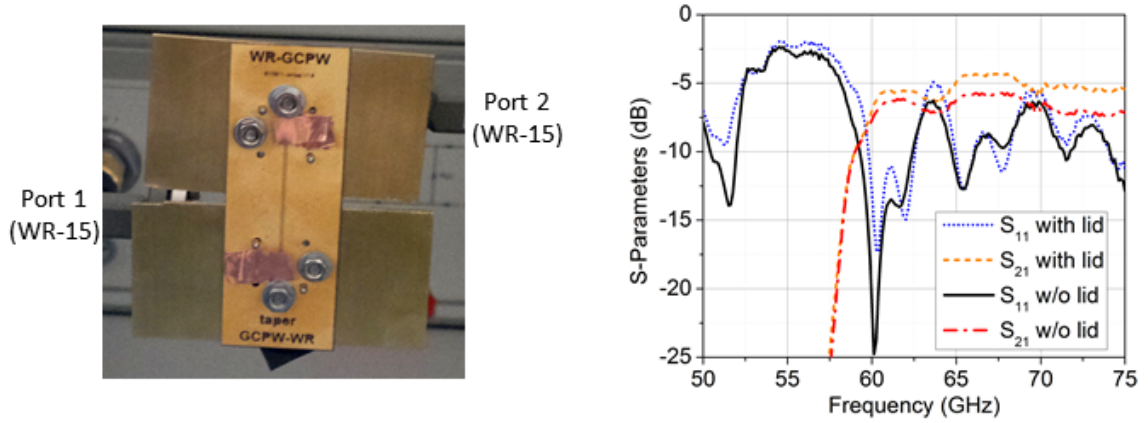


Figure 4.16: Left: Measurement setup of the B2B transition with metal lids. Right: Measured S-parameters with and without metal lids (the latter is depicted in Fig. 4.11).

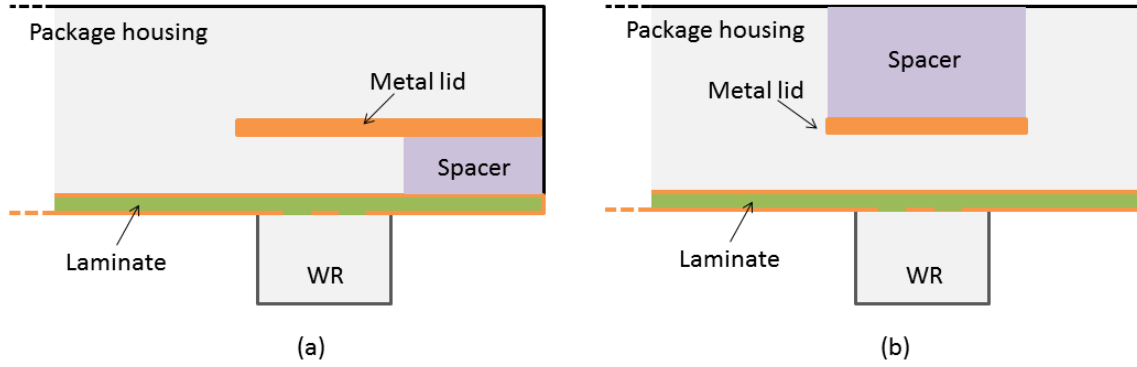


Figure 4.17: Possible implementations of metal-lid reflector in packages.

black lines). The narrow-band measurements make use of end-launch coaxial connectors with TLR calibration set designed on the same laminate of the measurements (see appendix D.1), while the broadband measurements make use of ground-signal-ground (G-S-G) probes and are calibrated using an on-substrate SOLT calibration kit¹⁰. The measurements show a good agreement with the simulations, as depicted in Fig. 4.19-a and 4.19-c: In the 71-76 GHz range the IL is ≤ 0.6 dB¹¹, the RL is at least 15 dB, while the RF-to-DC isolation (IS) is at least 27 dB, making the structure virtually invisible to the RF signal generated by the PD. The broadband measurements, shown in the full 60-90 GHz range in Fig. 4.19-b and 4.19-d, demonstrate that the RF-choke can be used for systems working in the full E-band, if an IL of 1.5 dB is accepted.

Another issue that has to be solved in the previously reported transition is the short-circuited $\lambda/2$ stub used to achieve a constructive wave interference at the coupling point: This stub would short-circuit the DC feed to the ground layer, thus making it impossible to apply a DC bias to the PD. A successful solution to this problem is shown in Fig. 4.18-b, where the short-circuited stub is substituted by a $\lambda/4$ open-circuited stub. In the ideal case, the two stub configurations are fully equivalent for the RF field. As the result of the numerical optimization process, the stub's length, originally dimensioned accordingly to the wavelength of the central frequency (73.5 GHz) of the band of interest, has finally been reduced and a rounded shape has been preferred to a straight rectangular ending.

The final optimized layout of the transition is shown in Fig. 4.18-c and the corresponding dimensions are reported in appendix B.2. Figure 4.18-d shows the current density distribution of a 73.5 GHz signal excited at the GCPW port: It can be noticed that the EM energy propagates from the RF input (GCPW port) to the RF output (WR port) and no RF field reaches the DC feed point. From the simulated S-parameters shown in Fig. 4.18-e, it is possible to see that the IL is less than 2 dB (1.7 dB at the central frequency 73 GHz), the RL at the GCPW port is at least 25 dB, and the RF-to-DC IS is

¹⁰The impact of probe-to-line contact and of the thin taper used to launch the signal into the GCPW line has been de-embedded by removing the measurements of *thru*-lines using the Advanced Design System software.

¹¹The spikes seen in the narrow-band measurements are obviously due to calibration errors and are therefore not considered in this analysis.

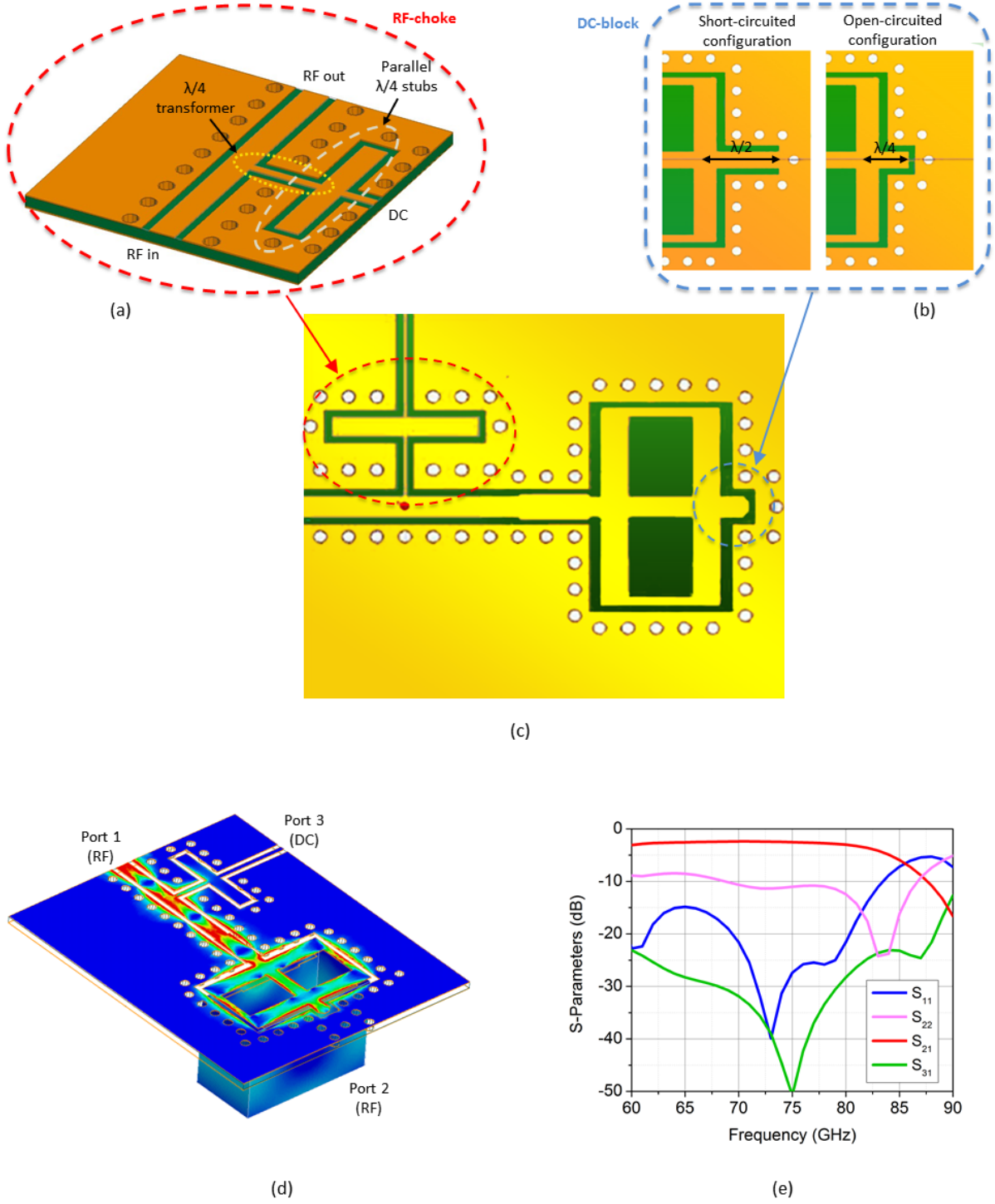


Figure 4.18: Transition with built-in planar bias tee: Design of RF-choke (a), design of DC-block (b), layout of the complete transition (c), current density distribution of a 73.5 GHz signal excited at the GCPW input (d), simulated S-parameters of the transition (e).

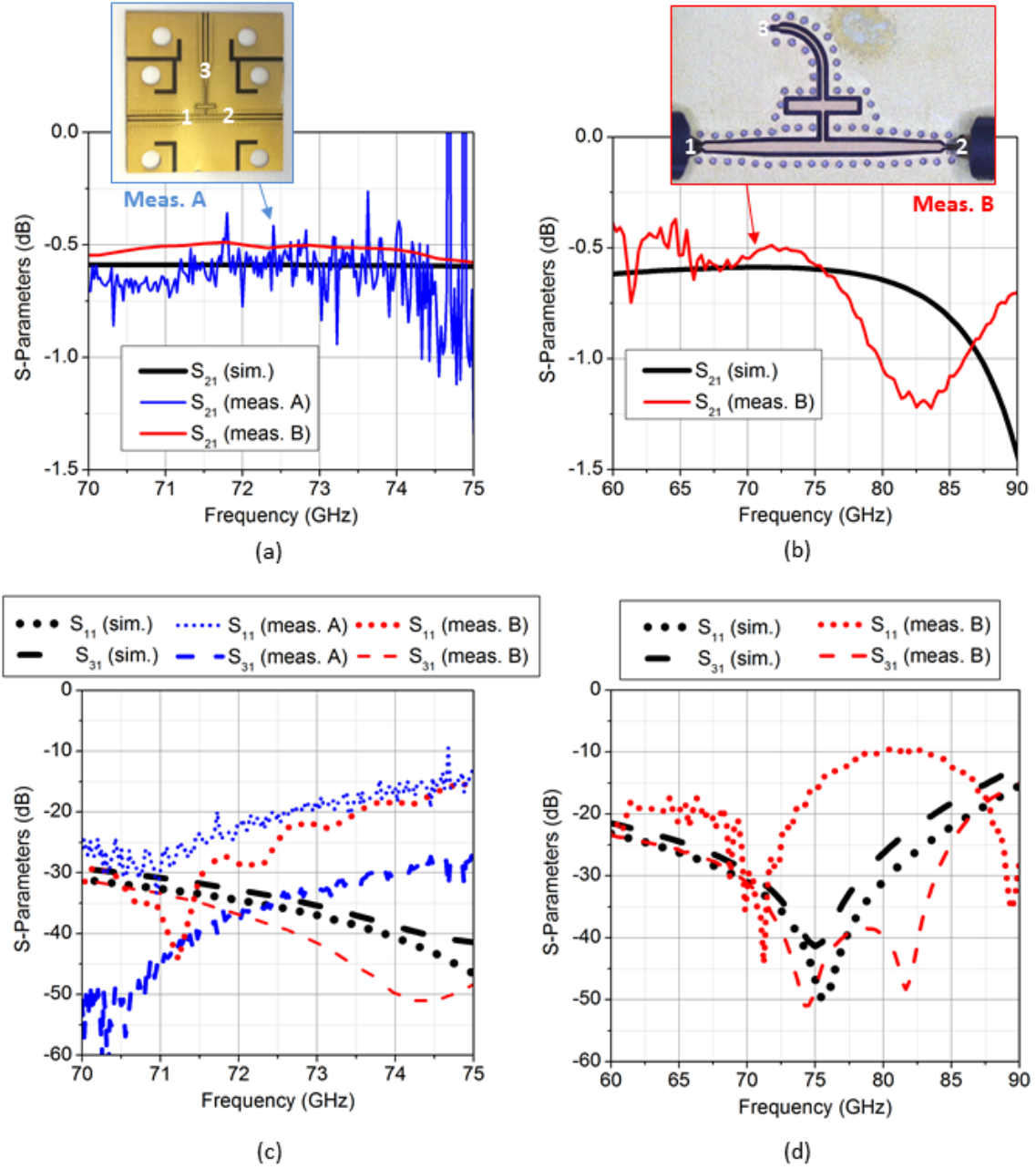


Figure 4.19: Narrow-band (a and c) and broad-band (b and d) measurements of the S-parameters of the RF-choke, compared with simulations. The insets in (a) and (b) shows the prototypes used in the respective experiments (*Meas. A*, *Meas. B*).

better than 34 dB in the 71-76 GHz range.

In order to experimentally validate the new design, the same B2B setup introduced in Fig. 4.10-a has been used, as shown in Fig. 4.20-a, where two sets of two transitions¹² with full bias network have been employed (one of the prototypes is shown in the inset of Fig. 4.20-b). It can be seen that the measured RL at the GCPW ports is generally higher than 10 dB¹³, while the measured IL has an average value of ≈ 9.5 dB and is comparable with the one measured for the transition without bias network (see Fig. 4.10-b), which confirms the equivalence of the designs.

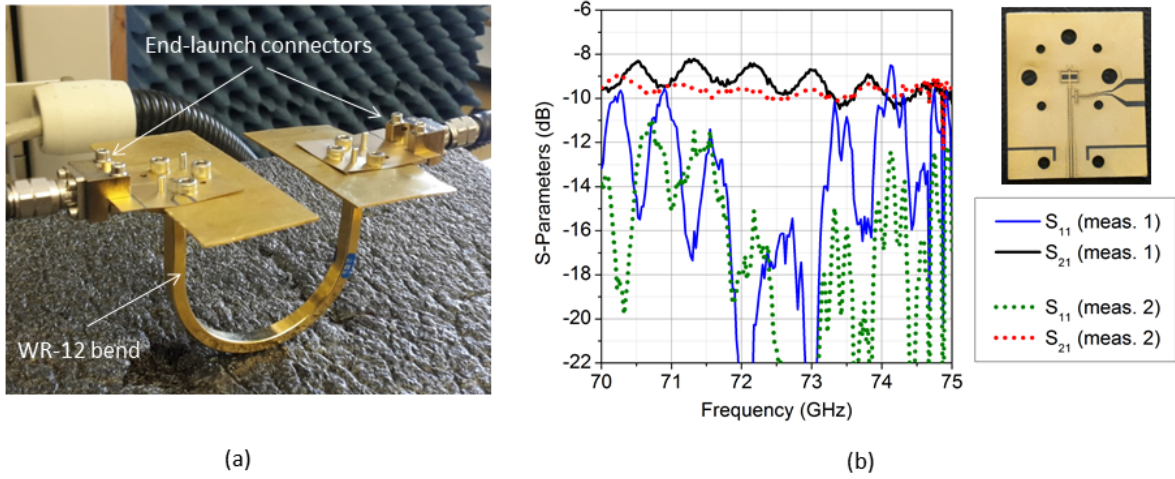


Figure 4.20: B2B measurement setup for GCPW-to-WR-12 transition with built-in bias tee (a) and measured S-parameters (b). The inset in (b) shows one of the prototypes used for the measurements.

4.3 Photonic Transmitters with Rectangular Waveguide Output

4.3.1 Integration of Commercial Photodiode

The transition presented in section 4.2 has been used to design a PD module, whose 3D model has already been presented in Fig. 4.1. The bonding ribbons connecting the PD to the laminate have been designed to be have a total length of 170 μm , as this allows minimal impact on the transmission of the 70 GHz signal, as discussed in section 3.5. The resulting simulated S-parameters of the assembly are shown in Fig. 4.21 (solid lines). In the whole 71-76 GHz range, the IL is ≈ 3 dB, while the RL at the PD-chip port is higher than 9 dB.

¹²These prototypes have been manufactured on the same laminate and with the same process of the transitions shown in Fig. 4.10

¹³One single point above 74 GHz reaches 8.5 dB: This is probably due to incorrect alignment of the end-launch connectors, as suggested by the minor ripples of the measured curves.

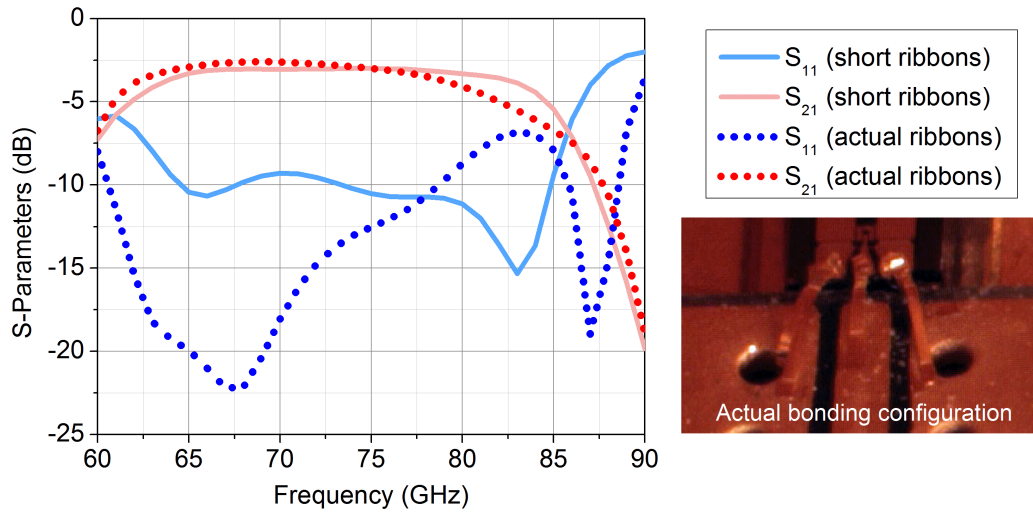


Figure 4.21: Simulated S-parameters of the PD module. Port 1 is at located at the PD pads, port 2 is at the WR output.

Figure 4.22-a shows a picture of a pigtailed PD module prototype based on the presented design, featuring a commercial InGaAs/InP PD with integrated bias network [203] and a standard WR-12 output with UG-387/U flange. A mechanical submount is used to sustain the chip and its integrated biasing network. A standard single-mode fiber (SMF) is glued at the backside of the PD to provide the necessary optical input. The optical and electrical assembly steps have been performed by u2t Photonics A.G. (now Finisar Corporation).

Due to difficulties occurred during the integration phase, a bonding ribbon longer than $300 \mu\text{m}$ has been used for the signal line and ribbons of $\approx 600 \mu\text{m}$ have been implemented on the ground connections, as shown in the inset of Fig. 4.21. However, thanks to the low inductance of the ribbons, the impact on the performance of the assembly is negligible in the 71-76 GHz, as reported in Fig. 4.21 (dotted lines).

The measured RF output power delivered by the prototype in the 71-75 GHz range for several DC photo-current levels is shown in Fig. 4.22-c: It can be seen that it exhibits a very flat response within the band of interest with a power fluctuation of only ± 0.5 dB around the maximum (-12.5 dBm), achieved at a DC photocurrent of 10 mA. The 1-dB compression point of the module is found to be at ≈ 9 mA, with a corresponding RF output power of -13.5 dBm as shown in Fig. 4.22-d. The prototype has been characterized using the setup shown in the inset of Fig. 4.22-d. In Fig. 4.22-b, a horn antenna is connected to the module, in order to build a photonic transmitter that can be used for laboratory wireless transmission experiments, as it will be introduced in the following sections.

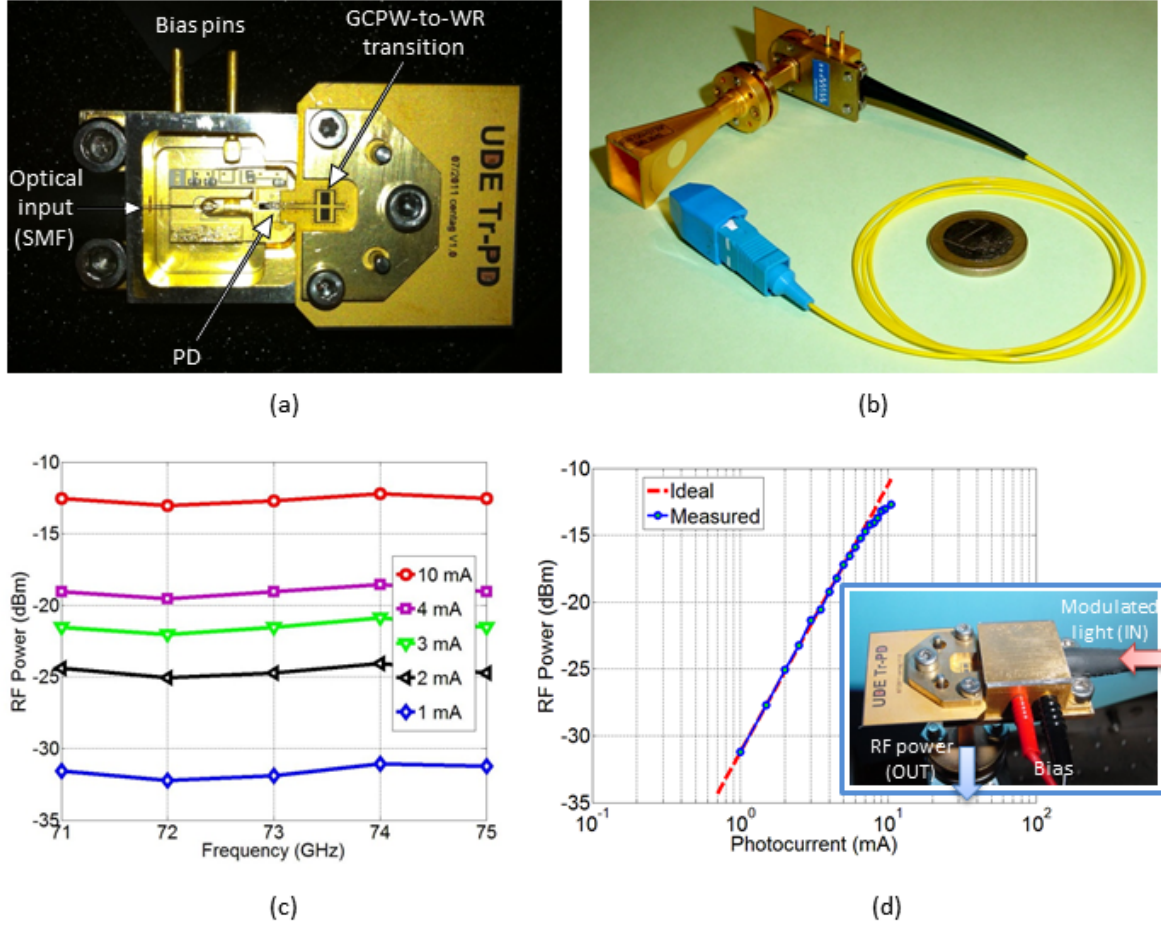


Figure 4.22: Pigtailed PD module (a) and photonic transmitter with horn antenna (b); RF output power of the module as a function of frequency, for several photocurrent levels (c) and output power at 73 GHz plotted as a function of the photocurrent (the red dashed line represents the ideal square-law characteristic $P_{RF} \propto I_{photo}^2$) (d). The inset in (d) shows the setup used for the characterization of the module.

1 Gb/s Back-to-Back Transmission Demonstration

The first experimental B2B¹⁴ RoF link setup used to demonstrate the capability of the developed module is shown in Fig. 4.23-a [204].

A 1550 nm laser source, followed by a polarization controller (PC), generates the optical carrier and a Mach-Zehnder modulator (MZM) biased at V_π is used to generate a double-sideband suppressed-carrier signal (DSB-SC). The optical signal is then amplified by an erbium-doped fiber amplifier (EDFA) followed by an optical band-pass filter (OBPF) and a second PC. The signal is then modulated by a second MZM biased at quadrature point. The data (a 1 Gb/s non-return-to-zero on-off-keying (NRZ-OOK) signal with a word length of $24^{31}-1$) is generated by a pseudo-random bit sequence generator (PRBS). A final optical amplification stage is used to compensate for the losses due to the MZM and an additional OBPF is used to eliminate amplified spontaneous emission (ASE) noise from the EDFA. Finally, the modulated RoF signal is delivered to the PD module, whose output is connected to a Schottky envelope detector by a WR-12 waveguide. The Schottky envelope detector, whose average responsivity is ≈ 3200 V/W in the frequency range of 71-76 GHz, down-converts the signal to baseband. The baseband signal is then amplified and launched to an error detector to perform bit-error-rate (BER) measurements.

The measured B2B BER characteristics for 1 Gb/s transmission are shown in Fig. 4.23-b, where it can be seen that error-free¹⁵ ($\text{BER} < 10^{-9}$) transmission has been achieved in the whole 71-76 GHz range. As a result of the flat reponse of the PD module, as well as of the used MZM and detector, the power penalty associated with a variation of the RF carrier frequency that was necessary to achieve this result is less than 1.5 dB.

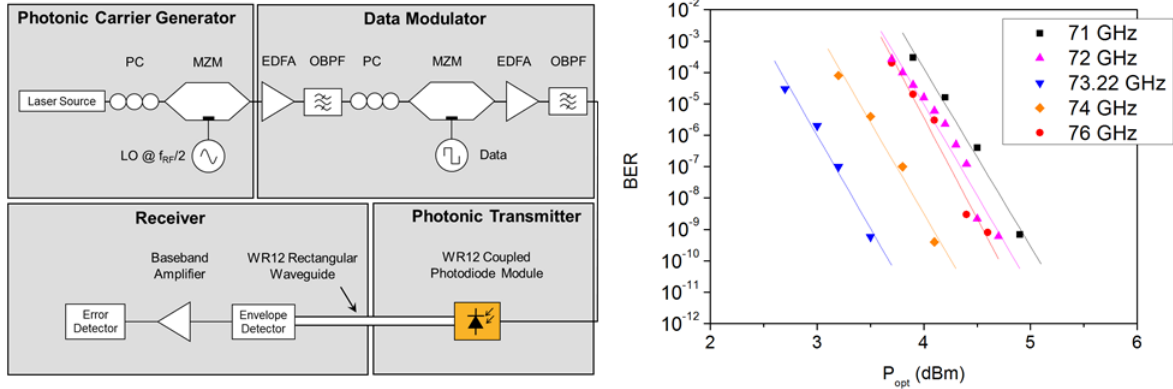


Figure 4.23: (a) Experimental B2B RoF system setup featuring a photonic carrier generator, a data modulator, the developed photonic transmitter and a receiver; (b) measured BER characteristics.

¹⁴Here, *back-to-back* is used to identify a RoF link without wireless path.

¹⁵The actual definition of *error-free system* is not unique. The typical requirement in most lightwave systems is a BER of 10^{-9} , although even a BER of 10^{-14} might be considered in some cases [109].

1 Gb/s Wireless Transmission Demonstration

The setup introduced in the previous section has been modified as shown in Fig. 4.24-a in order to establish a test wireless link between the PD module and the receiver [205]: A 21-dBi-gain horn antenna is now connected to the photonic module to radiate the signal generated by the PD towards the receiving antenna, and a WR-12 LNA with 25-dB gain is used to increase the power of the mm-wave signal before delivering it to the antenna.

For the receiver, a teflon lens with 6 dBi gain is used to focus the main lobe onto the receiver module, which collects the signal through a log-periodic antenna, photolithographically fabricated on a silicon substrate connected to a hemispherical high-resistivity silicon lens. A planar zero-biased Schottky barrier diode (SBD) with a responsivity reaching 1278 V/W at 72 GHz is used for direct envelope detection. After the down-conversion operated by the SBD, two baseband amplifiers (with a total gain of 40 dB) boost the signal before it reaches the BER detector. The measured BER characteristics for 1 Gb/s transmission on a link distance of 2.5 m (laboratory setup) are shown in Fig. 4.24-b. It can be seen that error-free ($\text{BER} < 10^{-9}$) wireless transmission has been achieved at all measured frequencies, with a power penalty of 1.2 dB.

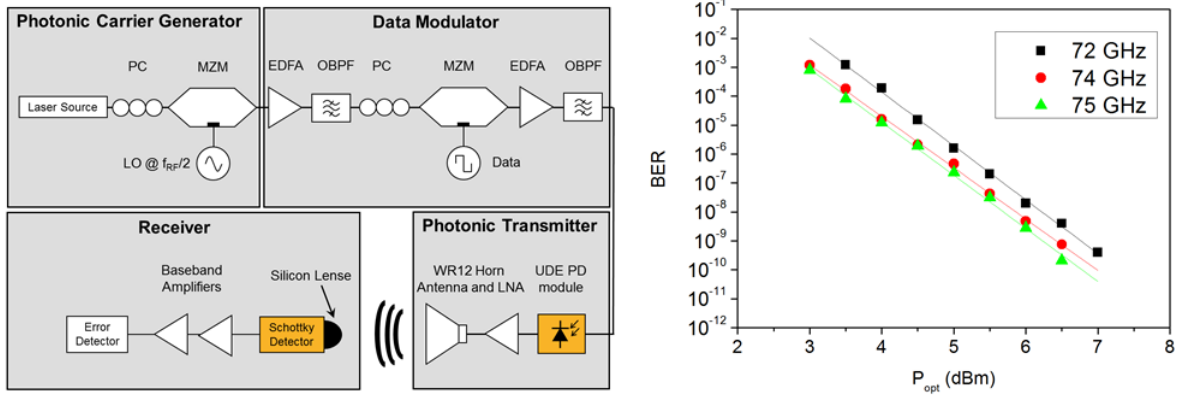


Figure 4.24: Experimental system setup of the high-speed wireless link featuring a photonic carrier generator, a data modulator, the developed photonic transmitter and a receiver (a) and the measured BER characteristics (b).

4.3.2 Integration of In-House-Developed Photodiodes

In order to couple the output of PDs developed *in-house* into a WR, the transition presented in section 4.2.1 has been used to design an E-band module with a built-in bias tee, as shown in Fig. 4.25-a.

Due to equipment limitations, in this case bond wires have been considered for the integration. Simulations have shown that even a length of 230 μm would not cause excessive loss in assembly: It can be seen from Fig. 4.25-b that the overall IL from the PD output to the WR is less than 3.5 dB, while the RL at the PD chip is at least 12.5 dB and the RF-to-DC isolation is at least 33 dB.

The PD used for the integration is a high-speed waveguide-type 1.55 μm photodetector, based on III-V semiconductor technology with a 50- Ω GCPW output [206]. The

PD and the transition are sustained by a brass submount, a common material for optoelectronics packages [207], which is shaped in order to accommodate the boss of the WR's flange, as shown in 4.26-a; the PD and the laminate are glued to the submount using conductive paste [208].

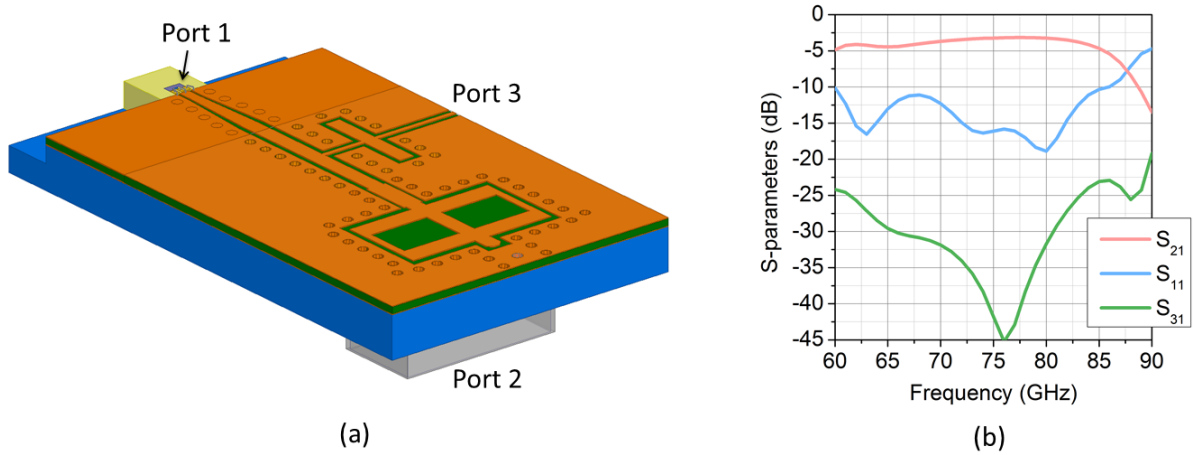


Figure 4.25: HFSS model and simulated S-parameters of the module based on in-house-developed PD.

A picture of the assembled PD module is shown in Fig. 4.26-b. It can be seen that, because of technological limits, very long¹⁶ bond wires have been created during the assembly. This is due to the additional InP substrate that extends out of the PD's output contacts (a by-product of the cleaving process) and to the excess dielectric core of the laminate, due to manufacturing challenges of the PCB. The long bond wires introduce inductive mismatch (thus decreasing the RL) and cause undesired radiation, thus increasing the IL. To verify the effect of these anomalies, the S-parameters of the full module have been simulated using the realistic model shown in Fig. 4.26-c [208]. It can be observed that the total IL from the PD to the WR output is increased to ≈ 7.5 dB and the RL at the PD port is very low (less than 2 dB): This can be very detrimental for the PD, as the reflected power would be directly fed to its output.

The PD module has been tested according to the setup shown in Fig. 4.27 and it has been successfully employed to extract a 73 GHz signal generated using a photonic approach based on external modulation of the laser output: A 1550-nm laser followed by a polarization controller generates the optical carrier and a MZM is used to generate a DSB-SC signal, using a local oscillator source of frequency $f_{RF/2}$. After optical amplification and filtering (not shown in Fig. 4.27), the signal is delivered to the PD module where the PD extracts the RF signal, that is then guided into the WR and detected by a mixer connected to a SA. The total loss, from the PD output contacts to the SA has been measured to be ≈ 9.5 dB at 73 GHz. The measured and estimated values are thus in good agreement, with the 2 dB difference likely due to the uncertainty of the conversion loss of the mixer used to detect the RF signal and its interconnecting cables, as well as to

¹⁶The total length is in the order of 700-800 μm .

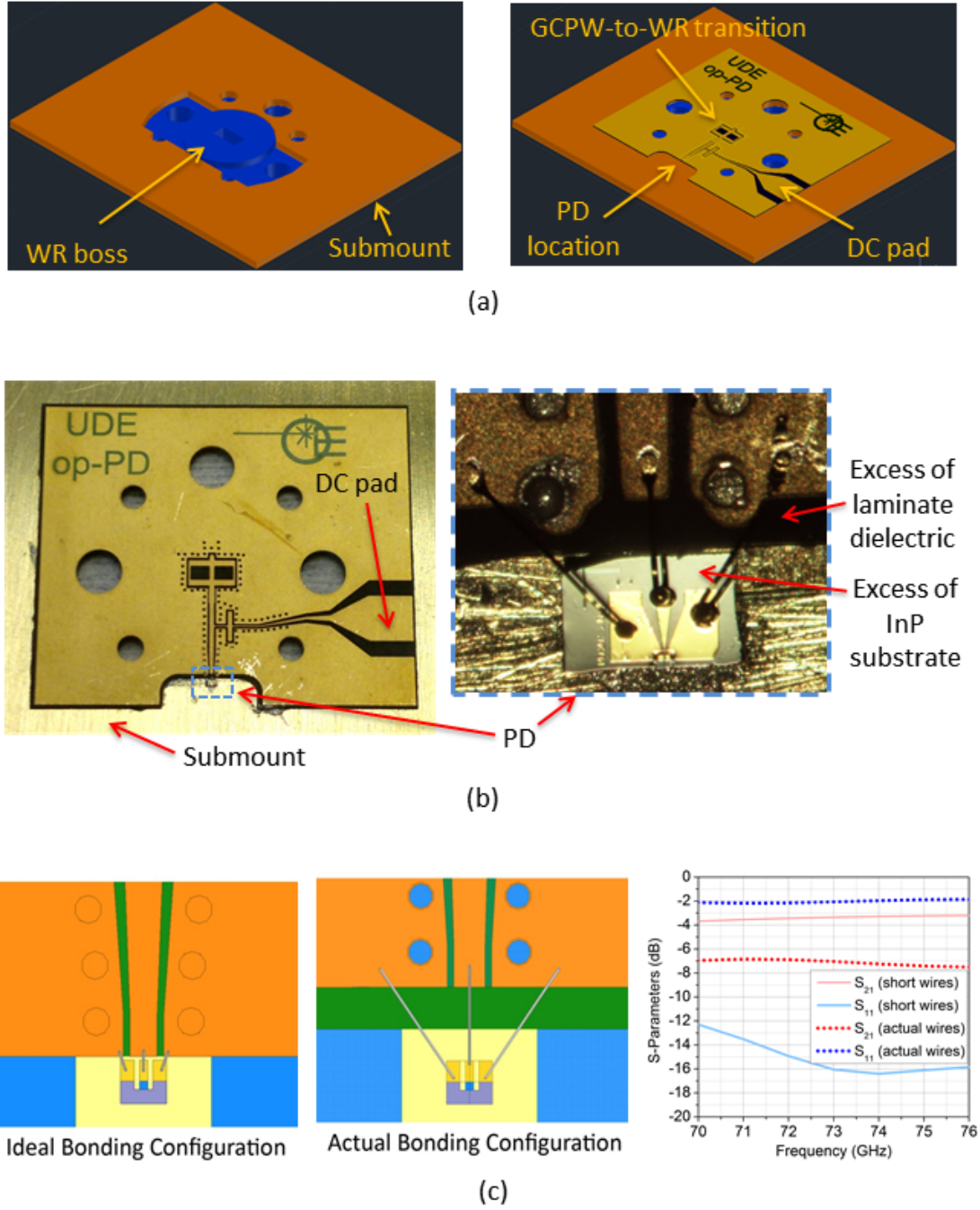


Figure 4.26: Concept for integration of in-house-developed PD (a); assembled prototype of the module and magnified view of the chip/laminate interface (b); ideal (designed) and actual (implemented) bonding configuration and their simulated S-parameters (c).

possible damages to the chip metallization occurred during the bonding process¹⁷. Further characterization of the frequency response of the module has not been possible, due to failure of the PD, which was presumably caused by the high level of power that has been reflected to its output contact. The successful extraction of the mm-wave signal from the WR nevertheless proved the validity of the integration concept, which was only limited by technological shortcomings.

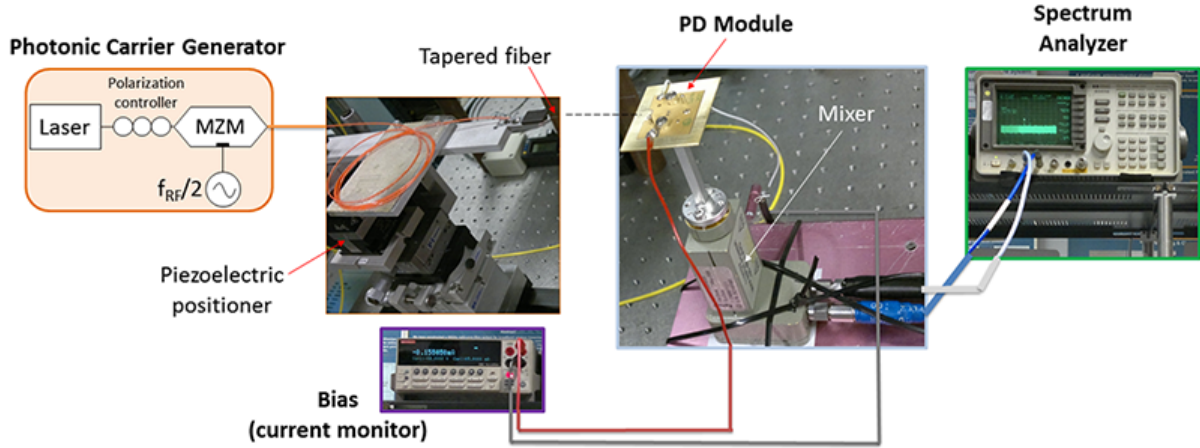


Figure 4.27: Measurement setup for the PD module with integrated bias tee.

4.3.3 Concept for the Integration of On-Board Amplification

When the mm-wave power delivered by the PD is not high enough for the required application or transmission distance, amplifiers have to be used in order to boost the signal before the transmission. In section 4.3.1, an external bulky amplifier has been connected to the WR output of the PD module to increase the transmitted power. An alternative to this approach is to use the laminate hosting the transition to allow hybrid integration of MMIC amplifiers.

The integration concept, shown in Fig. 4.28 [208], is based on the fact that the RF laminate used for the GCPW-to-WR transition and for the bias of the PD can also be used as substrate to host the SMD components necessary to the bias of the amplifiers as well as the MMIC chip [209]. Starting from the design shown in Fig. 4.26-a, the necessary circuit traces for the DC supplies of the amplifiers have been drawn on an extended laminate, glued on a larger brass submount. Two commercial amplifiers manufactured by Hittite Microwave¹⁸ with integrated input and output DC-block have been considered for the design of the platforms, as it will be introduced in the following.

¹⁷When the metallization of the InP does not have a good adherence to the substrate, *peeling-off* phenomena can occur, leading to the complete removal of the metal layer, as well as to unstable contacts or minor damages.

¹⁸Now Analog Devices.

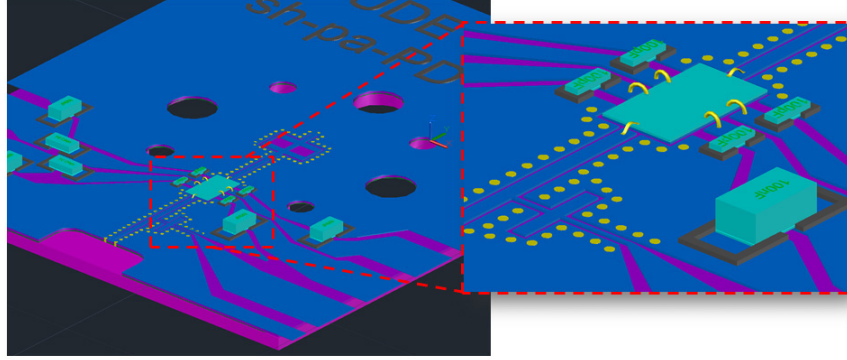


Figure 4.28: Integration concept for amplifiers. The transition's laminates also hosts the SMD components necessary to bias the amplifier.

Integration of Middle Power Amplifier (MPA)

At first, because of its simpler biasing circuit, the integration of a GaAs HEMT MPA [210] with a gain of 24-25 dB in the 71-76 GHz range has been considered as a proof of concept, with the assembled prototype shown in Fig. 4.29. The module has been tested by launching a mm-wave signal directly at the input pads of the amplifier chip using a G-S-G probe: Because of damages to the chip occurred during the bonding process (see the inset in Fig. 4.29), the final stage of amplification has been compromised, therefore the maximum measured gain was 16 dB.

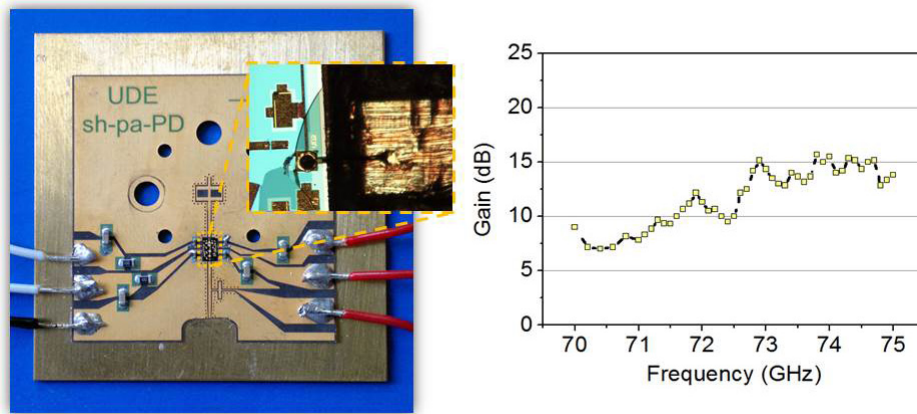


Figure 4.29: Experimental MPA integration (left) and measured gain (right). The inset shows the cracked chip substrate in correspondence to the final amplification stage.

Integration of Low Noise Amplifier (LNA)

Besides the the MPA, the integration of a GaAs HEMT LNA [211] has also been considered, as LNAs are generally the preferred choice as first amplification stage, in order to

reduce the overall noise figure of the system. The module featuring the integrated LNA is visible in Fig. 4.30, together with its measured gain. The maximum measured gain is 13 dB at 73 GHz. The oscillating pattern of the measured curve (essentially similar to the one of the measured MPA gain) can be attributed to deviation in the calibration of the setup.

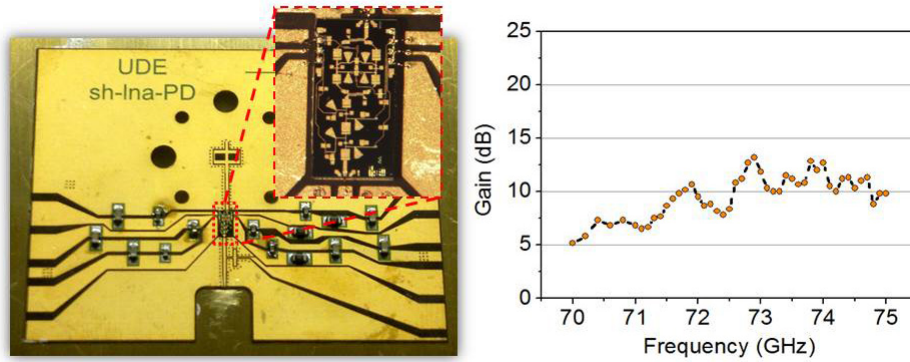


Figure 4.30: Experimental LNA integration (left) and measured gain (right).

A PD was then integrated in the same module, and used in a setup similar to the one introduced in Fig. 4.27, with additional DC sources necessary to bias the amplifier, as shown in Fig. 4.31. It has nevertheless been impossible to employ the module in RoF transmission tests, as during the biasing operations the amplifier has been damaged by the bias voltage applied to the PD. The cause of the failure has been identified in the decoupling capacitor integrated at the input of the amplifier, which seems to be unable to withstand the high voltage (-8 V) required by the PD. For further development of modules with integrated amplifiers it is therefore necessary to add an additional decoupling structure on the laminate, such as a CL section (see Appendix A.4), as described in [212–214].

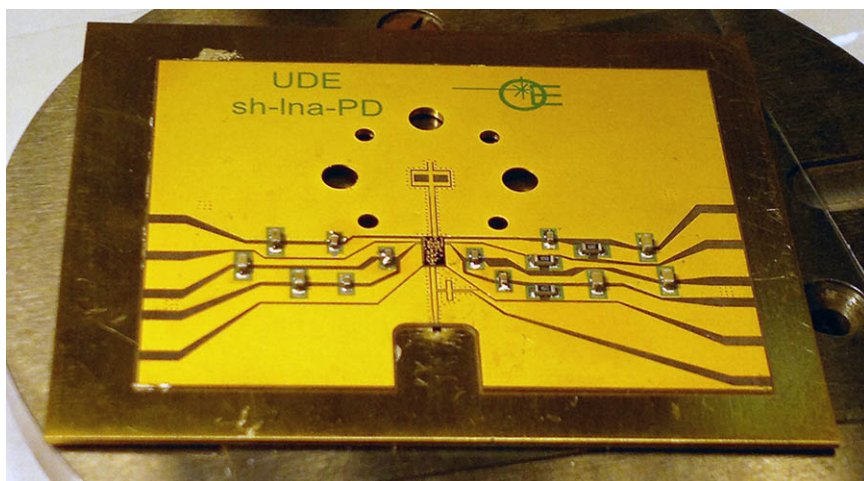


Figure 4.31: PD module with integrated LNA.

Integration of LNA and MPA

It is common to use a chain of amplifiers in order to further increase the output power. Normally a LNA is used as first element in order to reduce the overall noise figure of the system. With the two amplifiers considered in the previous sections a theoretical total gain of more than 38 dB could be achieved. Two different solutions (based on the fact that the LNA has a thickness of $100\ \mu\text{m}$ while the MPA has a thickness of only $50\ \mu\text{m}$) can be considered, in order to minimize the parasitic effects due to the bonding. Figure 4.32-right depicts an approach in which the two amplifiers share a common ground area on the laminate and the output of the LNA and the input of the MPA are connected directly by one bond wire (side-by-side configuration). Another alternative is the milling of a cavity into the laminate to host the LNA, so that its output pads are almost at the same level of the laminate top metallization, while the MPA can be bonded from the standard chip-on-substrate position, as shown in Fig. 4.32-left.

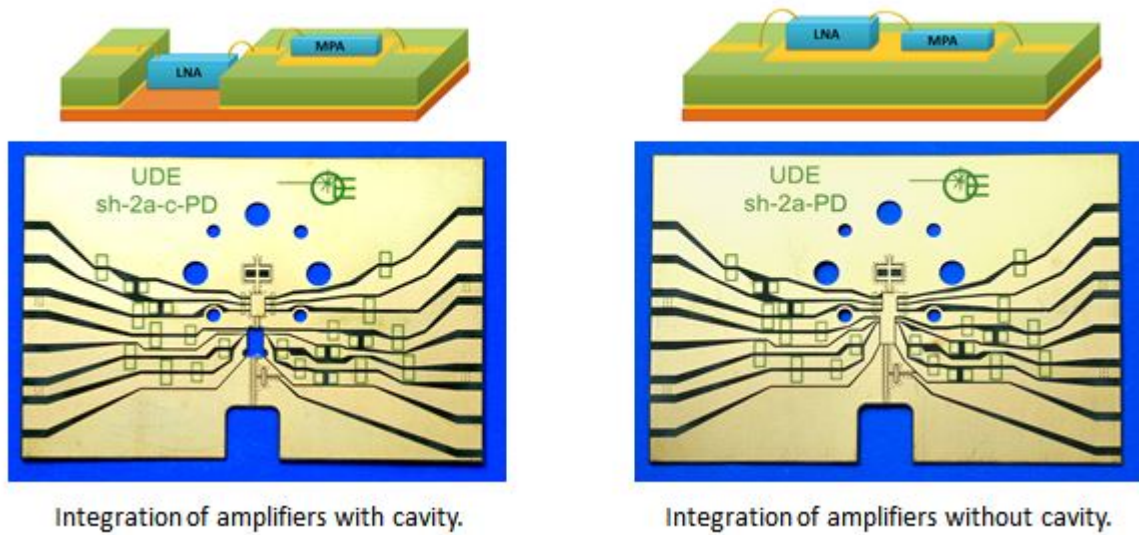


Figure 4.32: Platforms for integration of LNA and MPA.

4.4 Conclusions

In this chapter, a novel integration concept for mm-wave PD modules with WR output has been introduced. The proposed method assumes the PD chip being bonded to a GCPW line created on a laminate: Thus the signal extracted from the PD can be guided by the GCPW to a vertical transition based on a double-slot coupling structure etched on the bottom side of the laminate, which couples it to the WR output. The whole integration platform can be manufactured using PCB technologies and the alignment to the WR is achieved by using the pins of a standard WR flange, greatly simplifying the assembly procedure when compared to previously reported solutions. Furthermore, the proposed integration technique does not require any mechanical modifications of the WR. Using

quasi-hermetic PCB materials as substrate, our approach enables near-hermetic enclosing of the WR aperture, eliminating the need for sealing elements at the WR output. Table 4.1 summarizes the characteristics of the proposed integration concept and offers a comparison with other available solutions for mm-wave PD modules operating at frequencies below 100 GHz.

Table 4.1: Comparison of integration techniques for mm-wave PD modules.

Reference ⁽¹⁾	UDE (this work)	RAL [34]	NTT [29, 30]	YZU/NCU [33]	TUB [32]
Hermeticity	Quasi-hermetic	No	No	No	No
Machining/ Non-standard components	No	Yes	Yes	No	No
Use of PCB materials and techniques	Yes	No	No	No	Yes ⁽²⁾
Difficultly of as- sembly	Low ⁽³⁾	High	High	Middle	Middle

⁽¹⁾ University of Duisburg-Essen (UDE), Rutherford Appleton Lab (RAL), Nippon Telegraph and Telephone Corporation (NTT), Yuan Ze University (YZU), National Central University (NCU), Berlin Institute of Technology (TUB).

⁽²⁾ TUB firstly proposed an approach based on a thin-film silicon integration platform, later introducing an alternative PCB design in an attempt to simplify the assembly and reduce the loss.

⁽³⁾ The approach proposed in this work requires no alignment blocks or procedures, as the laminate lays on the central boss of the WR and its position is set by the pins of a standard flange.

The GCPW-to-WR transition has been tailored to work in the 70-GHz band, with a measured IL of only 3.2 dB in the large 60-75 GHz band. Using the modeling techniques introduced in section 3.4.5, the response of the prototypes can be accurately predicted by EM simulations and therefore the design procedure and the proposed concept are suitable for the development of PD modules in the mm-wave range.

The work presented in this chapter has triggered interest from the industry in using PCT for mm-wave optoelectronic packaging [215] and a prototype PD module has been assembled using a commercially-available PD, which is able to deliver a maximum of -13.5 dBm of output power before reaching the 1-dB compression point. The module has been successfully employed in demonstrative back-to-back and wireless RoF communication links: Thanks to the flat frequency response of the transition and to the linearity of the used active components, error-free transmission has been achieved in the whole 71-76-GHz range with a power penalty of less than 1.5 dB.

Further improvement of the design has led to the integration of a fully planar, broadband, on-board bias tee, that enables the usage of in-house developed PDs - which are not

equipped with an integrated bias network in order to reduce the chip size and simplify their design. The impact of the bias tee on the performance of the transition has been carefully minimized (the additional introduced IL is less than 0.6 dB) and it has been proved that the design of the improved integration platform is fully equivalent to the one discussed above. It should be noticed that the transition with integrated bias tee is particularly interesting for the development of other mm-wave modules, too: Although this topic has not been directly addressed in this thesis, we have reported in [216] about the development of a zero-biased SBD module¹⁹ with WR-12 input, based on a slightly modified version of the transition, and successfully used in wireless, 70-GHz RoF demonstrations.

Additionally, extended platforms for the integration of on-board electrical amplification have been introduced: Several assemblies featuring commercial LNAs and MPAs have been realized and tested, demonstrating the flexibility and feasibility of the suggested approach. However, experimental work has highlighted that the integrated DC-blocks of the used amplifier chips are not sufficient to protect the amplifiers' inputs from the bias voltage of the PD and therefore additional on-laminate protection circuits are needed for the successful development of future modules, as shown in [212].

Suggestions on the possibilities to further improve the coupling of the signal into the WR have also been presented, showing that a metal lid can conveniently be introduced in packaged modules to emulate the constructively interfering effect of a WR backshort and thus reduce the residual radiation at the coupling point: This simple solution allows a 1-dB decrease of the overall IL of the transition in the 71-75 GHz range.

The results presented in this chapter laid the foundations for the development of commercially competitive PD modules with WR output. The optimization of the bonding technology and the integration of amplifiers will allow the development of fully functional photonic transmitters suitable for E-Band RoF applications. Redesigning the electrical interconnects together with the use of automated integration techniques for SMD components will open up the possibility of integration within standard butterfly packages [217], while the integration of a reflecting metal lid - easily built into the package - can be used to further increase the output power.

It should be noticed that, if complex systems with an increased number of interconnects are required, it could be advisable to introduce in the design different TLs that allow an overall reduced loss and better manufacture control, such as the SIW. Practical examples of novel SIW-based integration platforms for PD modules for 60-GHz RoF applications will be proposed in chapter 5.

¹⁹Industrial partner for this application has been ACST GmbH.

5 PCB Substrate Integrated Waveguide Technology for 60-GHz Optoelectronic Integration

In this chapter, we will investigate the potential of PCB technology to manufacture SIW circuits and their application in the development of integration platform for mm-wave indoor RoF systems. The interest in the SIW arises in particular from their proven low-loss characteristic (see section 3.4.5), as this can facilitate the employment of PCB technologies well above the 100 GHz limit, where GCPWs might suffer of excessive loss, as suggested by the experimental results achieved in the E-band (see chapter 4). However, other advantages can be considered when SIW are used: As suggested in Fig. 5.1, a SIW platform would facilitate the quasi-hermetic packaging of PDs, thanks to its ability to completely confine the guided signal within the laminate dielectric. Thus, no short-circuits of the lines delivering the signal to the antenna would arise from the contact with the housing walls, independently of the actual antenna configuration.

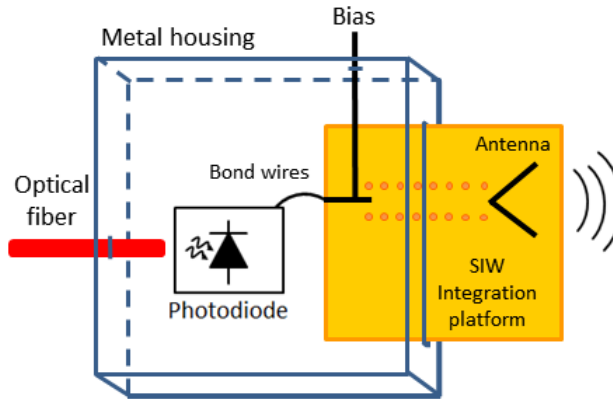


Figure 5.1: Simplified concept of 60-GHz photonic transmitter module based on a SIW integration platform. The SIW exits the metal housing through a dedicated hermetically-sealed slot.

5.1 60-GHz Indoor Data-Distribution System Concept

As introduced in section 1.2.1, the 60 GHz band has been allocated worldwide for high-speed communication applications. Although regulations in different countries are different

(channelization, total frequency range, and so on) there is, in general, a 7-GHz bandwidth available to develop mm-wave communication systems. Besides outdoor applications (mm-wave links), a large market for 60-GHz systems will be for indoor consumer applications such as data distribution or uncompressed HD video streaming. The intrinsic possibility of antenna remoting supported by RoF can foster the development of 60 GHz high-data rate indoor broadcasting systems by facilitating the positioning of the transmitting unit, as shown in Fig. 5.2 [218]. In the depicted concept, the photonic transmitter is located in the top-left edge of the room and is equipped with a sector antenna in order to focus the radiated power only into a predefined area, thus increasing the energy efficiency of the system. The radiation pattern of the antenna has to be focused in the vertical plane to prevent unwanted radiation toward the ceiling or the floor, but should have a wider beam in the horizontal plane, in order to extend the covered area (ideally 180° to cover the whole room). For the room dimensions given in Fig. 5.2, vertical and horizontal beam-widths of 40° and 180° respectively guarantee an efficient coverage of the three walls opposite to the antenna installation. By considering the radiation property of an H-plane horn antenna, introduced in section 2.4.3, it is obvious that its sector radiation pattern is suitable for this application. The relatively simple integration of H-plane horn antennas with SIW technology and the demonstrated low-loss properties of the latter¹ suggest that the SIW can be used to develop a complete integration platform for a photonic transmitter, equipped with an opportune in-package antenna [100], as it will be shown in section 5.4.

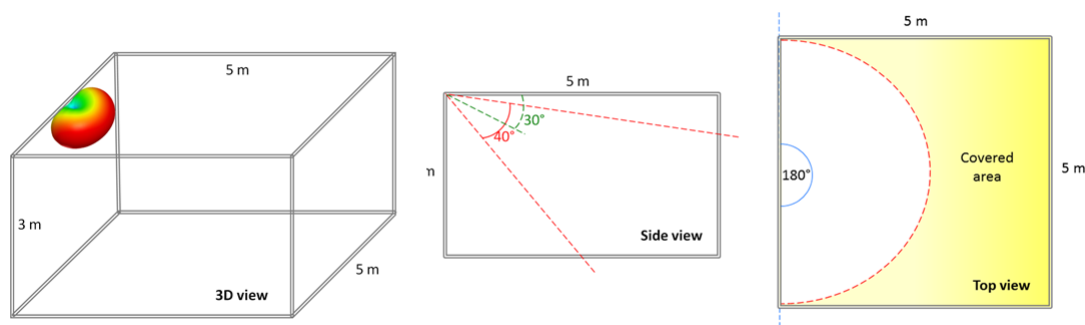


Figure 5.2: Indoor distribution of uncompressed HD video signal: 3D-view of the room, with the required antenna's radiation pattern (left), side-view (center) and top-view (right) of the room.

5.2 Technical Considerations for the Design of SIW Platforms

In designing mixed PTL and SIW structures, several considerations have to be taken into account when choosing the characteristic of the adopted substrate. In particular, a trade-off is required in choosing the thickness of the dielectric core. Specific problems in the

¹See section 3.4.5.

mm-wave range are represented by the fact that thick substrates might require wide signal conductors (for microstrips or GCPWs) to achieve 50- Ω impedance. This could have some advantages, such as the reduction of conductor loss, but for mm-wave frequencies it could lead to signal conductors which are comparable with a quarter of wavelength, which might allow the excitation of transverse resonance modes and make more difficult the design of T-junctions and other distributed components (e.g. stubs). As a common drawback of non-homogeneous guiding structures, large substrate thickness additionally increases the dispersion of the wave traveling across the line. For the SIW, a large dielectric core would reduce the conductor loss, but it could lead to a large width (distance between the via-holes fences) in order to achieve low impedances (less than 100 Ω) for an easier matching to PTL circuits; being the width of the SIW primarily responsible for the operational bandwidth too, it would reduce the cut-off frequency and thus eventually make it impossible to work in the desired frequency range. Because of the above mentioned considerations on the signal propagation, thin substrates are therefore preferred at high frequencies; however, as part of the system is based on an in-package sector antenna, considerations on the radiation properties of the antenna have to be taken into account (see section 5.4). As a result of the trade-off between several constraints a Rogers RT/duroid 5880 laminate with $\epsilon_r=2.2$ and thickness $H=381\text{ }\mu\text{m}$ has been chosen for all the designs presented in this chapter. Due to limited availability of the material, a metal thickness of $18\text{ }\mu\text{m}$ has been used for the manufacture of the prototypes². According to the considerations suggested in section 3.4.5, two different $\tan\delta$ have been used to model the substrate for GCPW lines and for SIW structures, within the same designs: A $\tan\delta_{\text{(GCPW)}} = 0.01$ has been used for traditional PTLs, while a $\tan\delta_{\text{(SIW)}} = 0.0015$ has been used for SIW lines.

5.3 60 GHz GCPW-to-SIW Transitions

A prerequisite for the integration of PDs with SIW is the development of GCPW-to-SIW transitions when using bonding wires or ribbons to lead the signal from a PD chip to an RF laminate, as discussed in section 4.3.1.

Several transitions from traditional PTLs to SIW are available in literature. For instance, via holes can be used to connect the central track of the PTL to the SIW's bottom ground layer, as in [219], while a more common approach is based on tapering the signal trace of the planar transmission line to fit with the SIW's width and is described in literature with several variations or improvements [220–222]. An example of such transition, based on the guidelines given in [223] and optimized for the 60 GHz range, is shown in Fig. 5.3-a. The transition relies on the progressive tapering of the GCPW's signal line into the SIW³, while gradually extending the GCPW's gaps to form triangular stubs within the top metal layer of the SIW. The actual dimensions of the elements of the transition are listed in Appendix C.1. It can be seen in Fig. 5.3-b that this simple approach allows the development of relatively broadband transitions, with a RL > 15 dB from 50 to more than 70 GHz, and a corresponding IL of less than 0.5 dB [100].

²The final metal thickness due to the plating of via holes is expected to be $\approx 35\text{ }\mu\text{m}$, therefore this value has been used in the simulations.

³The length of the taper should be approximately $\lambda/4$ at the central frequency of interest.

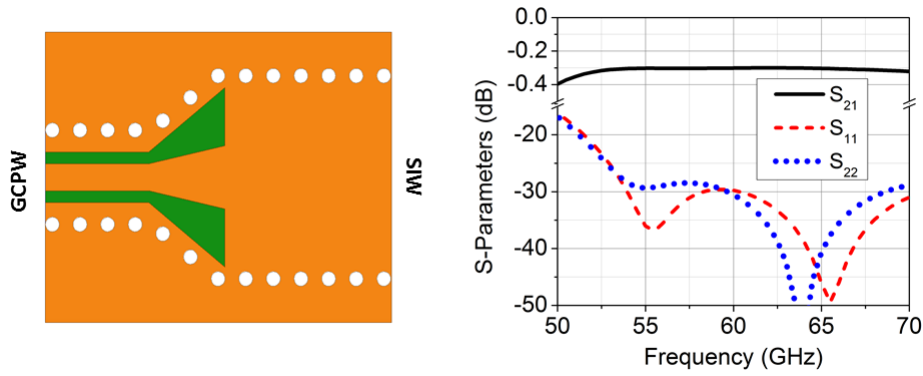


Figure 5.3: GCPW-to-SIW transition with tapered line (left) and its simulated S-parameters (right). *Port 1* identifies the GCPW input, while *port 2* is located at the SIW output.

Both methods mentioned above are not suitable for the integration of PDs as they create show a DC short-circuit between the GCPW signal and the ground layer. However, the relatively simple design of the transition presented in Fig. 5.3 makes it suitable for the characterization of SIW antennas, as it will be shown in section 5.4.2, therefore a calibration set based on this transition has been designed, as described in Appendix D.3. The transition has been tested by means of VNA measurements, using high-frequency coaxial connectors and coaxial-to-WR adapters for the connection to a VNA with WR ports. The calibration kit shown in Fig. D.2 (see appendix D) has been used to calibrate the setup. The results of the measurements of two B2B configurations (depicted in Fig. 5.4-a) are compared with simulations in Fig. 5.4-b, proving that the modeling method based on the dual $\tan\delta$ (see section 3.4.5) allows a good estimation of the properties of mixed SIW/PTL circuits and that the transition actually has a large operating bandwidth and low loss (≤ 1 dB in the 50-70 GHz range). The increased RL is probably due to minor overetching of the lines and small misalignment of the coaxial connectors, but is nevertheless higher than 12 dB in the whole 50-70 GHz range.

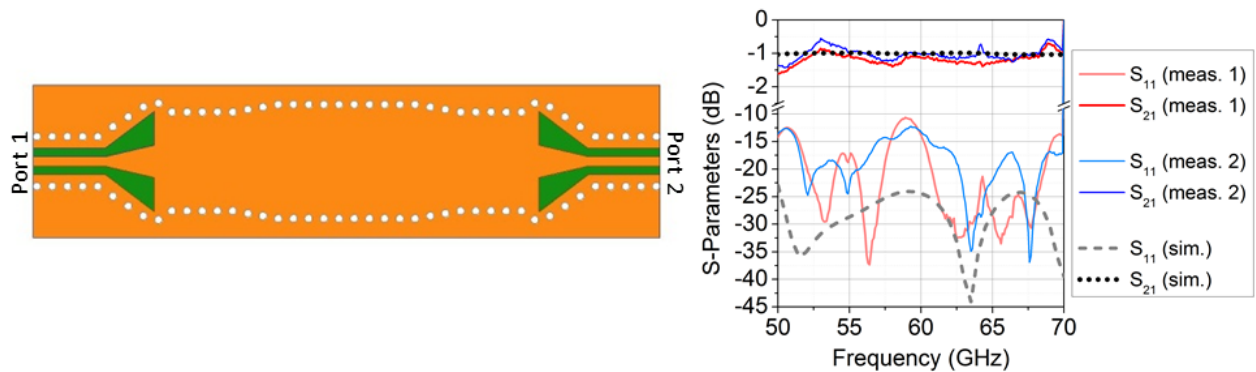


Figure 5.4: B2B tapered GCPW-to-SIW transition: Simulations and measurements.

To overcome the short-circuit problem, a transition based on slot coupling could be

used, which has the drawback of requiring at least two PCB layers [224]. A more convenient, single-layer approach has been suggested in [225], where an interdigitated structure is used to transfer the signal from a microstrip to a SIW in the Ku-band. The main drawback of this solution is that it requires 4-6 fingers to achieve a satisfying matching: Although possible at lower frequencies, that is a challenging problem for very high frequencies where the SIW dimensions shrink and they might not be able to host the large interdigitated transition. In the next section, a new GCPW-to-SIW transition based on a single coupled-line section will be introduced, specifically designed for the development of 60-GHz PD modules.

5.3.1 Transition with Integrated Planar Bias-Tee

In order to allow the biasing of the PD, the transition from GCPW to SIW should be equipped with a bias tee, featuring a DC-block and an RF-choke [226]. The DC-block functionality can be achieved by using a coupled-line (CL) section: In order to guarantee the impedance matching condition between the GCPW and the SIW, the CL section has to be connected to input/output transmission lines whose characteristic impedances $Z_{\text{in}} = Z_{\text{GCPW}}$ and $Z_{\text{out}} = Z_{\text{SIW}}$ satisfy equation A.4.3, which has been used as starting point for the optimization of the design, performed with the help of HFSS. The model of the transition featuring the DC-block is shown in Fig. 5.5.

Several iterations have been performed to achieve a trade-off between SIW propagation and impedance characteristic, GCPW properties and actual manufacturability of the CL section, due to PCB etching constraints (the limit on the minimum width of gaps and lines has been set to 100 μm). The optimization resulted in the layout shown in Fig. 5.5-a⁴, corresponding to the following impedance values: $Z_{0e} = 187\ \Omega$, $Z_{0o} = 76\ \Omega$, $Z_{\text{in}} = 46\ \Omega$, $Z_{\text{out}} = 78\ \Omega$. Note that at the GCPW side an additional taper is used to reduce the width of the line, as this is more convenient for the realization of the necessary RF-choke, presented in the next section. The taper has been designed in order to not compromise the properties of the transmission. The length of the coupled section is slightly shorter than the nominal quarter-wave length (at 60.5 GHz) because of the additional end-coupling effect of the CL with the GCPW and the SIW. The lateral grounds of the GCPW have been prolonged and merged to the SIW top metal, thus allowing the creation of an interrupted fence of via holes, which prevents the excitation of parasitic modes into the substrate. Similarly to the transitions based on tapering, proper dimensioning of the slots created around the coupled-line section is important to achieve an appropriate flow of current (in-phase with the signal line) and thus achieving low coupling loss and high RL. Figure 5.5-b demonstrates how the signal coming from the GCPW is transferred into the TE_{10} mode of the SIW, while Fig. 5.5-c shows that a RL of at least 17 dB is guaranteed in the 57-64 GHz range and the IL is ≈ 0.5 dB.

An RF-choke is further required to prevent the loss of RF power through the DC circuitry. An RF-choke based on the same principle as the one presented in section 4.2.1 has been therefore designed and included in the transition, obtaining the layout shown in

⁴The dimensions are listed in appendix C.2. Note that the layout reported in the appendix includes the RF-choke introduced in the following (see Fig. 5.6).

Fig. 5.6-a⁵ [100]. The numerical results of full-wave simulation of the complete transition are reported in 5.6-b. As it can be seen, the IL is less than 1 dB and the IS is better than 27 dB in the full 57-64 GHz range, while the RL is larger than 18 dB and 15 dB at the GCPW and SIW ports, respectively.

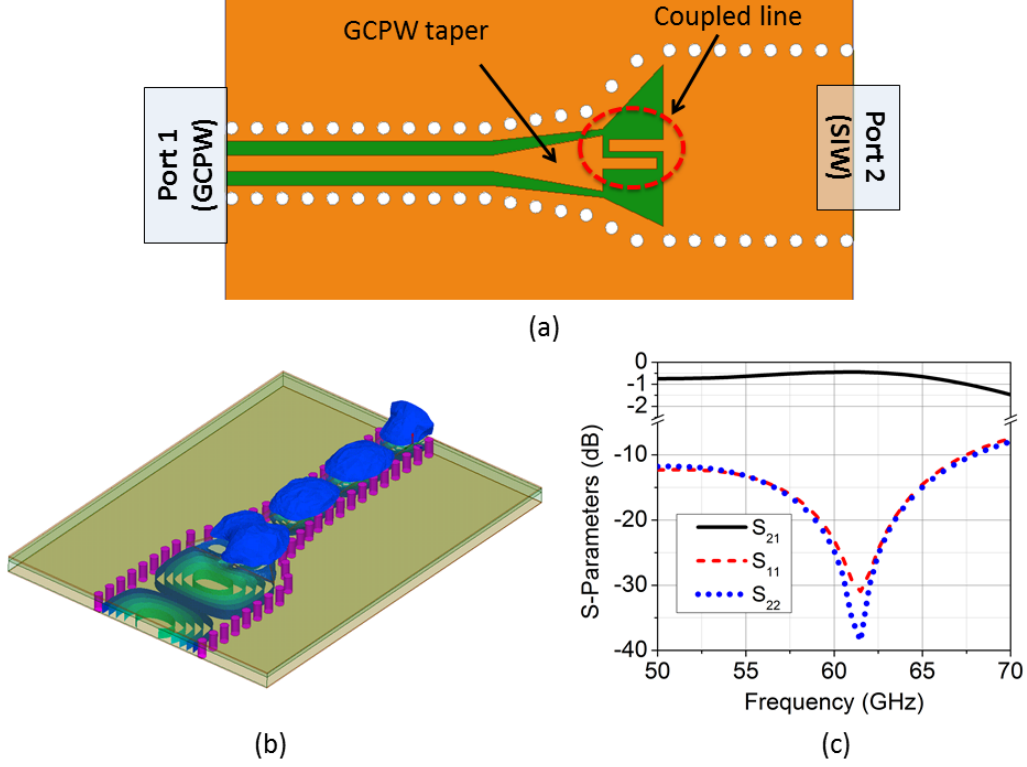


Figure 5.5: GCPW-to-SIW transition with DC-block: Model (a), propagation of the electric field from the GCPW to the SIW port (b), and simulated S-parameters (c).

In order to experimentally verify the proposed designs, B2B versions of the transitions (with and without RF-choke) have been manufactured and measured.

A comparison between simulated and measured performance of all back-to-back transitions is shown in Fig. 5.7. An excellent agreement is found between the simulated and measured IL, whose maximum values for the transitions without and with RF-choke are 1.8 dB and 2.2 dB, respectively. From the measured data, it can further be estimated that the RF choke only introduces 0.2 dB of loss for a single GCPW-to-SIW transition and it does not affect the matching between the two RF ports, as the measured RL for both ports is larger than 12 dB in the whole 57-64 GHz range (in good agreement with the values suggested by the simulations) [227].

The experimental validation of the designed transition with RF-choke opens the possibility to the development of 60 GHz photonic transmitters based on SIW technology, as shown in Fig. 5.8. Several antenna designs, which can be used to radiate the signal

⁵The corresponding optimized dimensions are listed in appendix C.2.

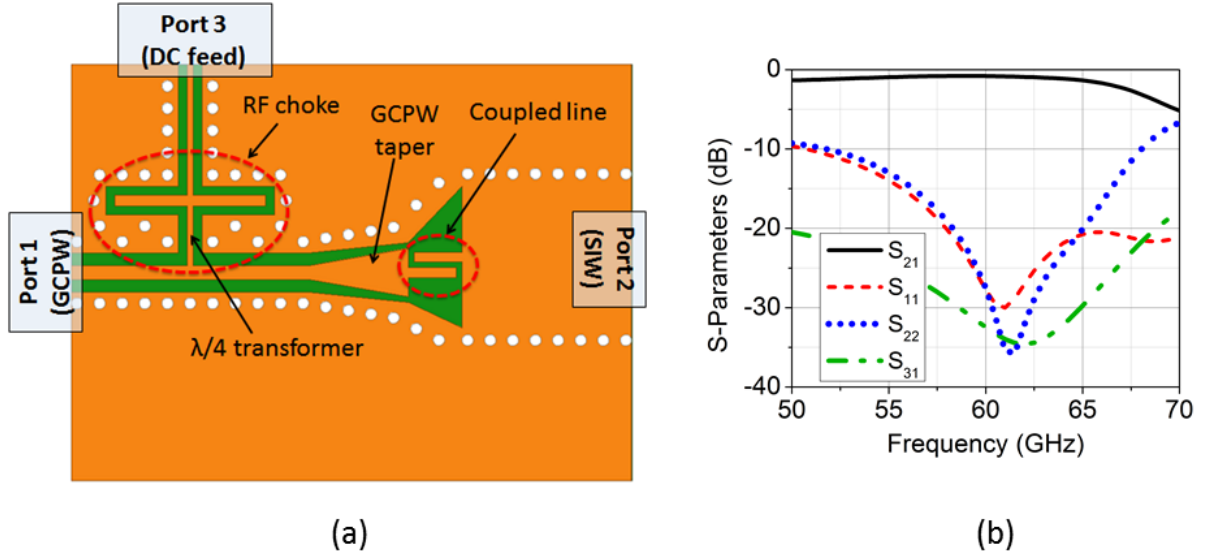


Figure 5.6: GCPW-to-SIW transition with fully planar bias tee: Model (a) and simulated S-parameters (b).

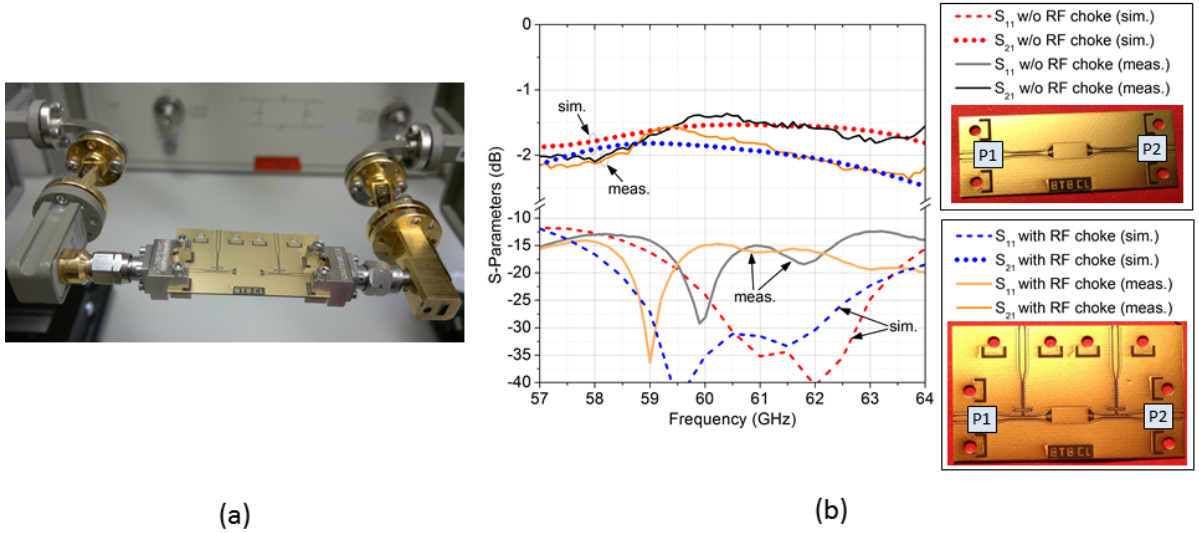


Figure 5.7: Measurement setup of the B2B GCPW-to-SIW transition with fully planar bias tee (denominated *with RF-choke*) (a) and comparison of simulated and measured S-parameters, for the same transition and the one featuring only a DC-block (denominated *w/o RF-choke*) (b).

coupled from the PD to the SIW, will be considered in the following section.

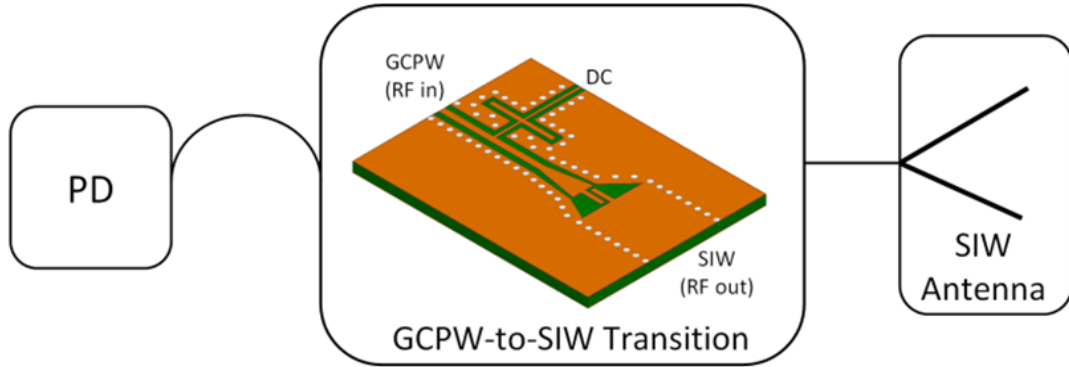


Figure 5.8: SIW integration platform: Block diagram.

5.4 60 GHz SIW H-Plane Horn Antennas

5.4.1 Standard SIW H-Plane Horn Antenna

Based on the information summarized in section 2.4.3, a SIW H-plane horn antenna is a perfect candidate for the applications described in section 5.1. However additionally considerations are required, due to the special nature of SIW, whose dimensions are bound to the thickness of the adopted substrate. Designing a traditional H-plane horn antenna⁶ (Fig. 5.9) would result in a very poor match ($RL < 2$ dB), as a result of the very low impedance of the antenna aperture, and an omni-directional radiation pattern in the E-plane, with a FTBR of 1.6 dB (see Fig. 5.9-b) and a maximum gain of 3.5 dBi (see Fig. 5.9-c). Therefore, improvement of the antenna is required in order to achieve the radiation properties desired for 60-GHz indoor data-distribution systems suggested in Fig. 5.2.

5.4.2 Improved SIW H-Plane Horn Antenna

Several approaches have been suggested in literature in order to improve the radiation characteristics and/or the RL of SIW H-plane horn antennas manufactured on thin substrates. For fully planar solutions, mostly impedance matching and wave focusing techniques based on dielectric extensions [96,97] or lens [98,228] extending out of the top and bottom metallization are used. These techniques work relatively well with substrate thicknesses in the order of $\lambda/6$. An additional way is based on loading the SIW antenna aperture with parallel-plate resonators in order to establish resonances in the RL [229]. This technique is particularly suitable for very thin laminates (with thickness less than $\lambda/6$) and can be used to achieve impedance matching, radiation pattern improvements, or both. Due to the versatility of the latter approach, its characteristics will be analyzed in details in the following.

⁶The dimensions of the design are reported in appendix C.3.

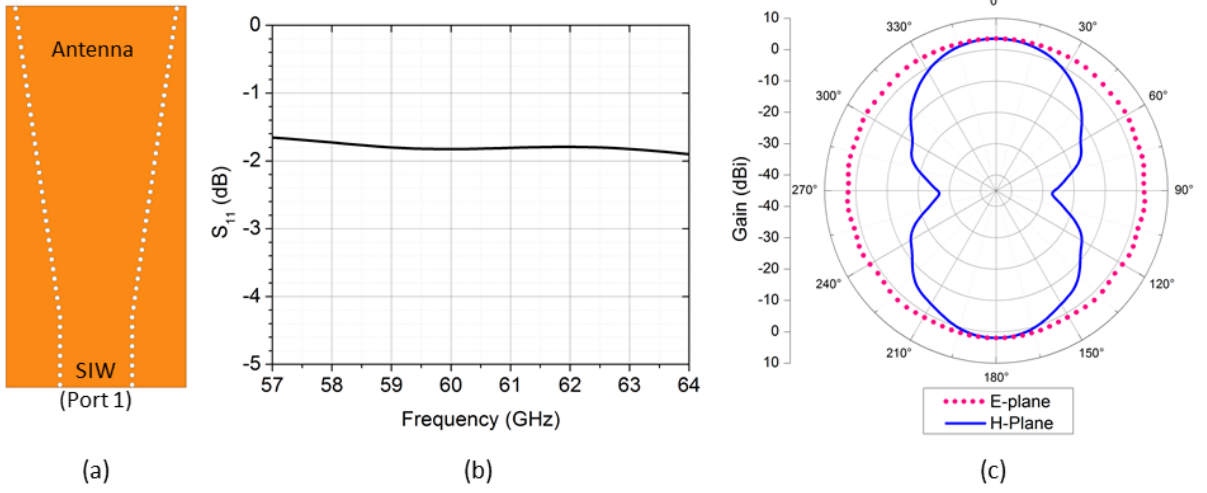


Figure 5.9: Standard SIW H-plane horn antenna: Model (a), simulated S_{11} (b) and 60-GHz radiation pattern (c).

SIW Antenna with Two-Block Parallel-Plate Resonator Transition

Using parallel-plate resonators as shown in Fig. 5.10, can have a positive effect on the matching of SIW H-plane antennas, as well as on their radiation properties.

The impact on the radiation can be understood by considering the spacing between the parallel plates as radiating elements (slots) that, together with the final aperture of the antenna, can create a linear array. It has been shown in [230] that an approximate expression for the array factor of two radiating elements, under the assumptions that all resonators have the same length L and that the signals *feeding* the radiating elements have similar amplitudes⁷, is given by:

$$AF(\phi) \propto \left(1 + e^{-j\left(\frac{2\pi L}{\lambda_0} \sin \phi - \gamma\right)} \right) \quad (5.4.1)$$

where $\gamma = \beta_{pp} L$ is the phase difference between the signal feeding the different slots, with $\beta_{pp} = \frac{2\pi}{\lambda_0} \sqrt{\epsilon_{r,pp}}$ being the propagation constant of the parallel plate waveguide established by the top and bottom resonator's plates, and $\epsilon_{r,pp}$ being its effective permittivity, defined taking into account the fringing fields. In order to achieve a high FTBR, the radiation must show destructive interference at $\phi = -\pi/2$, hence:

$$\frac{2\pi}{\lambda_0} \sqrt{\epsilon_{r,pp}} L + \frac{2\pi L}{\lambda_0} = \pi \quad (5.4.2)$$

Therefore, in order to minimize the FTBR at a given frequency f_{FTBR} , the length L_{FTBR} of the parallel-plate resonators should be chosen to be:

⁷Obviously the radiating elements (slots) have different feeding amplitudes, as part of the energy is radiated by the preceding slot. As a result of the approximation, the FTBR obtained using the L_{FTBR} given by equation 5.4.3 will not be infinite, and some radiation in the backward direction will still take place [229].

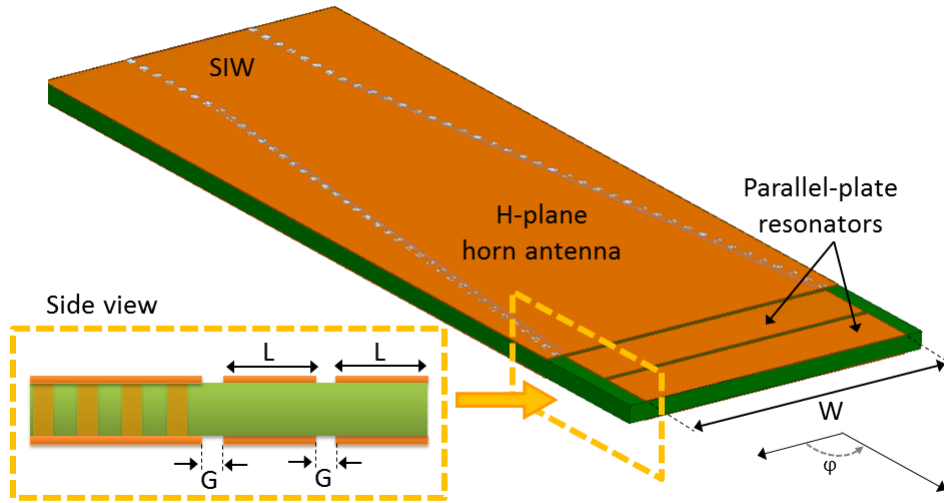


Figure 5.10: SIW antenna with two-block parallel-plate resonator.

$$L_{\text{FTBR}} = \frac{c_0}{2f_{\text{FTBR}}(1 + \sqrt{\epsilon_{r, \text{pp}}})} \quad (5.4.3)$$

Based on the given guidelines, the antenna has been optimized for 60 GHz operation. With $\epsilon_{r, \text{pp}}$ evaluated to be 1.83 for the configuration in use [231], the optimum length of the parallel plates has been estimated to be $L_{\text{FTBR}} \approx 1.1$ mm. From optimization performed with HFSS, an actual optimum length $L_{\text{FTBR}} = 1.21$ mm with gaps⁸ $G = 100 \mu\text{m}$ has been found⁹, achieving a value of FTBR of 21 dB and a maximum gain of 7 dBi, as shown in Fig. 5.11-c [100].

In order to experimentally verify the design, the prototype shown in Fig. 5.12, in which the presented antenna is fed through the GCPW-to-SIW transition with CL¹⁰, has been built and its RL has been measured¹¹. The concatenation of parallel-plate resonators used to improve the radiation properties of the antenna, can also be considered as a load *connected* to the SIW antenna aperture, that affects its matching. However, their length is not optimized to achieve perfect match at 60 GHz. It can be seen in Fig. 5.12-b that simulations predict a RL of at least 4 dB for the 57-64 GHz range. This minimum value has been confirmed by the two reported measurements, in spite of minor deviations from the ideal simulated results.

⁸Note that the gaps should be much smaller than the operational wavelength and that it would be better to keep the first gap smaller than the others, in order to guarantee a more balanced amplitude of the feeding signal. However, the limits of PCB design do not allow to have gaps smaller than $\approx 100 \mu\text{m}$, therefore in this case it has been decided to constrain all gaps to be $100 \mu\text{m}$.

⁹The width W has been set to be equal to the final aperture of the horn antenna. All other dimensions of the design are identical to the ones of the standard H-plane antenna shown in Fig. 5.9, and can be found in appendix C.3.

¹⁰As shown in Fig. 5.7, the RF-choke does not affect the RL of the transition, therefore it has been omitted from this prototype.

¹¹The calibration kit described in section D.2 has been used to calibrate the VNA.

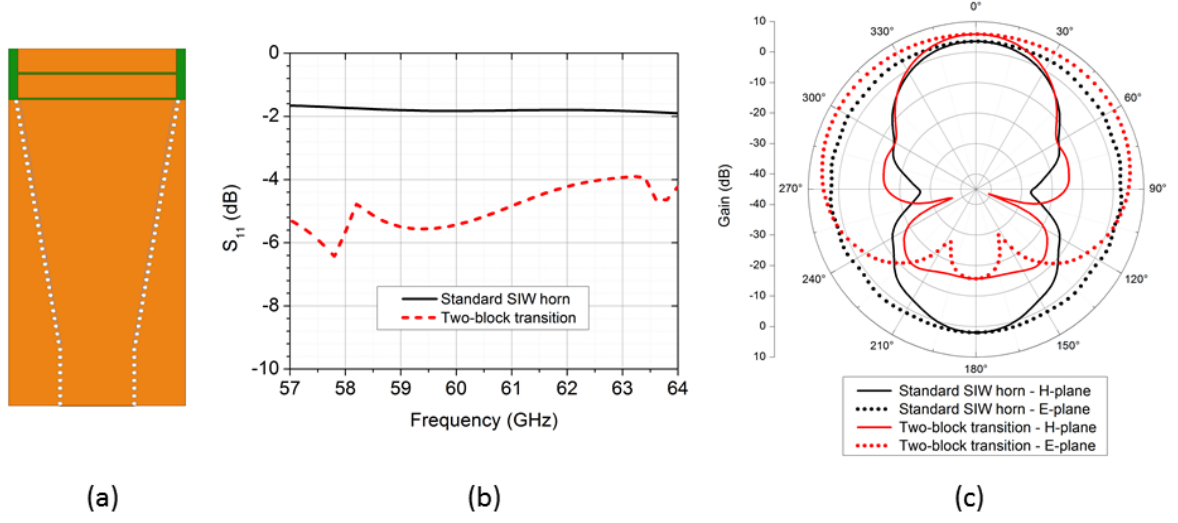


Figure 5.11: SIW antenna with two-block parallel-plate resonator for optimum FTBR: Model (a), simulated S_{11} (b), and 60-GHz radiation pattern (c). A comparison with the standard antenna shown in Fig. 5.9 is given in the same plots.

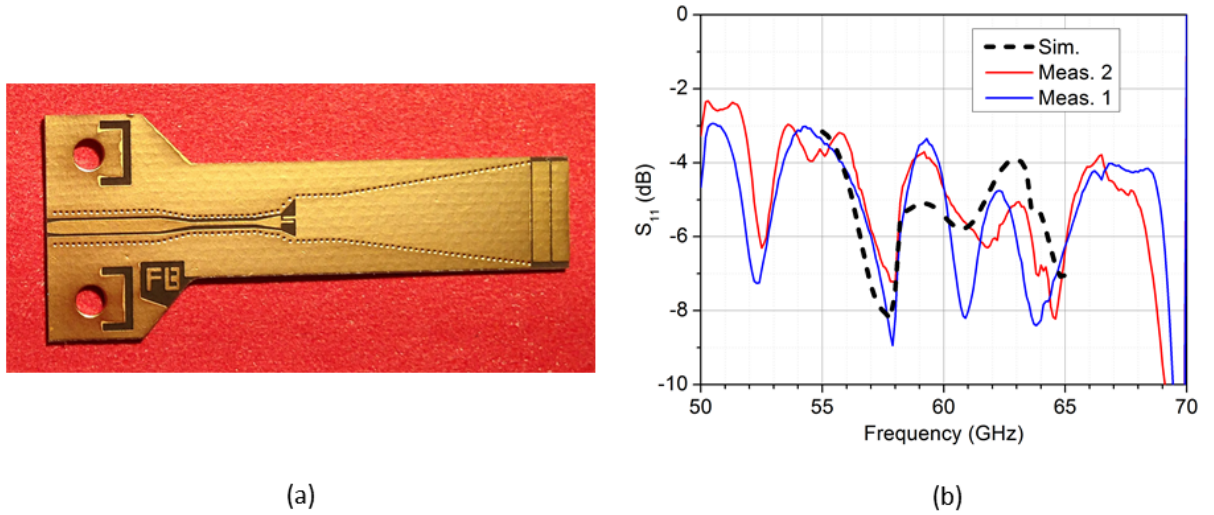


Figure 5.12: SIW antenna with two-block transition for optimum FTBR: Prototype (a) and its simulated and measured S_{11} (b). The antenna is fed through the GCPW-to-SIW transition shown in Fig. 5.5.

The frequency f_{RL} at which the resonators improve the RL of the antenna can be calculated as [229]:

$$f_{\text{RL}} = \frac{c}{2L(1 + 0.7\frac{H}{L})\sqrt{\epsilon_r}\sqrt{1-K}} \quad (5.4.4)$$

with H being the thickness of the substrate and K being the coupling factor between two resonators [232]. It has been shown in [230] that f_{RL} is always larger than f_{FTBR} for a given L , thus the two requirements are not compatible. In fact, L_{RL} must be larger than L_{FTBR} to achieve matching at 60 GHz: Using HFSS for the optimization, it has been found that in our case the length of the resonators should be $L_{\text{RL}} = 1.45$ mm to achieve an optimum RL at 60 GHz [100].

A compromise that simultaneously improves RL and FTBR can be found by introducing a grating of the parallel-plate resonators [229], which has the effect of decreasing the $\epsilon_{\text{r,pp}}$ of the structure. This solution will be presented in section *SIW Antenna with Grating Transition*, on page 117.

SIW Antenna with Matching Irises

If the antenna is not required to operate in the whole 57-64 GHz band, it is possible to use alternative resonant matching techniques, like the inductive iris shown in Fig. 5.13-a, to improve its RL at a specific frequency [233]. The position of the iris is chosen based on the impedance position on the Smith chart: While moving away from the point at which the SIW fence starts flaring, a point at which a $50\ \Omega$ with capacitive load is achieved and then the inductive load of the iris is used to compensate the capacitive reactance. Obviously, the matching iris does not affect the radiation properties of the antenna, therefore the radiation pattern of the antenna shown in 5.13 is identical to the one of the antenna without iris (Fig. 5.11). Therefore, using this approach in combination with the two-block transition allows the development of an antenna with the same excellent radiation properties (FTBR = 21 dB) and an operating bandwidth of 1 and 2 GHz for a tolerated RL of 10 and 5 dB, respectively. Further improvement can be achieved by extending this approach using an *internal* iris (with respect to the antenna), as depicted in 5.13-b. Moving towards the discontinuity point (the antenna/air interface) by multiples of $\approx \lambda/2$ will guarantee a broader matching, centered at the same frequency. As the propagation of the EM field inside the antenna is influenced by phase delays, the exact positioning and dimensioning of the iris can be found by numerical optimization. The final iris guarantees a RL of at least 5 dB from 57 to 62.5 GHz, while a RL of 10 dB or even 15 dB are achieved in the ≈ 58.5 to 61.5 GHz and 59.5 to 61 GHz, respectively, allowing the development of multi-channel systems.

This technique has the advantage of being only dependent on the via-to-via positioning, whose relative accuracy is generally higher than etching precision. Therefore it can be expected that in the mm-wave this matching method is particularly accurate in comparison to printed techniques. Several prototypes of the antenna, combined with the GCPW-to-SIW transition with CL (as shown in Fig. 5.14-a), have been manufactured and measured to verify the accuracy of the matching technique¹². The comparison of

¹²The calibration of the VNA has been performed using the calibration kit described in appendix D.2.

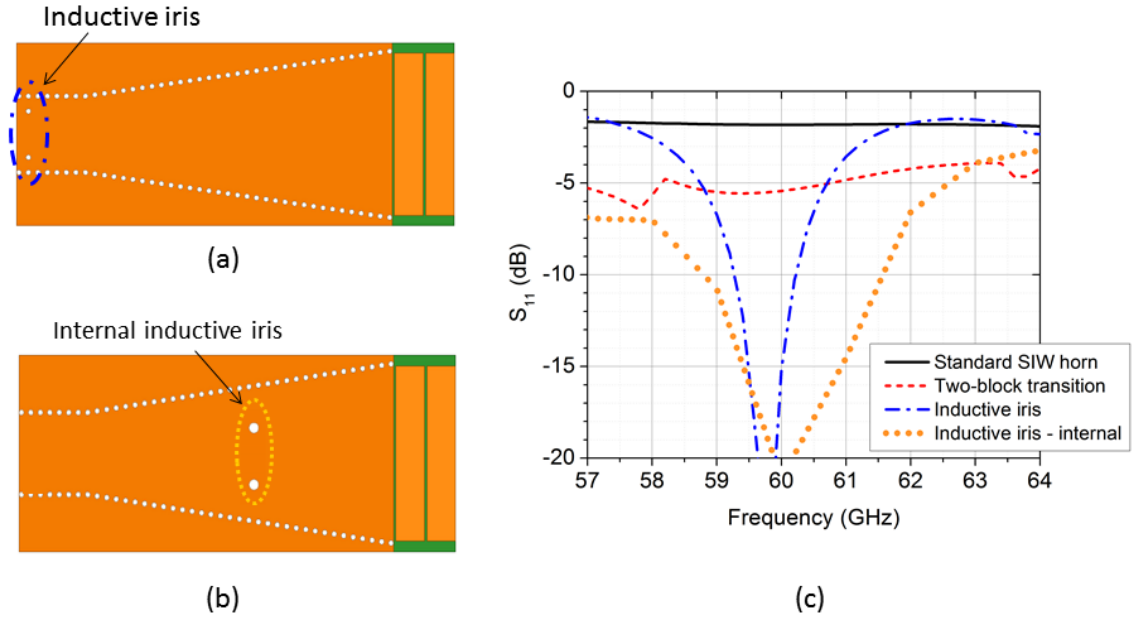


Figure 5.13: SIW Antenna with two-block parallel-plate resonator and inductive iris: Model with *external* iris (a), model with *internal* iris (b), and their simulated S_{11} (c). A comparison with previously introduced antennas is given in the plot.

the simulated and measured S-parameters (Fig. 5.14-b) confirms, as expected, that the matching based on the iris is very accurate in experiments.

SIW Antenna with Grating Transition

As already mentioned at the beginnings of section 5.4.2, the additional degree of freedom obtained by introducing a grating in the resonating blocks (see Fig. 5.15-a) offers the possibility to achieve a better trade-off between RL and FTBR ratio [229]. In fact, by using the grating instead of the full resonators plates, a decrease of the $\epsilon_{r,pp}$ of the resonator is achieved. As a result, the resonators' length L has to be longer than the one used to to guarantee a good FTBR ($L_{FTBR} = 1.21$ mm) and shorter than the one used to achieve a good matching at 60 GHz ($L_{RL} = 1.45$ mm). Using the average value of 1.33 mm as a starting point, optimization has been carried out with the help of HFSS, resulting in a final grating resonator length $L_G = 1.34$ mm. Numerical optimization has been used to determine the other physical parameters of the transition, which are listed in Fig. 5.17-c.

The RL of the antenna with grating resonators is shown in green in Fig. 5.15-b, directly compared with the RL of the other antennas presented so far. It can be seen that, as desired, the antenna shows a broadband matching, with a RL higher than 7 dB in the whole 57-64 GHz range. Its radiation properties are intermediate between the standard SIW and the antenna with two-block transition, as shown in Fig. 5.15-c and 5.15-d, with a FTBR of 17 dB. Figure 5.15-e further shows the gain computed for the end-fire direction in the whole 57-64 GHz, ranging from 5 to 7.5 dBi. Figure 5.16 finally shows the simulated

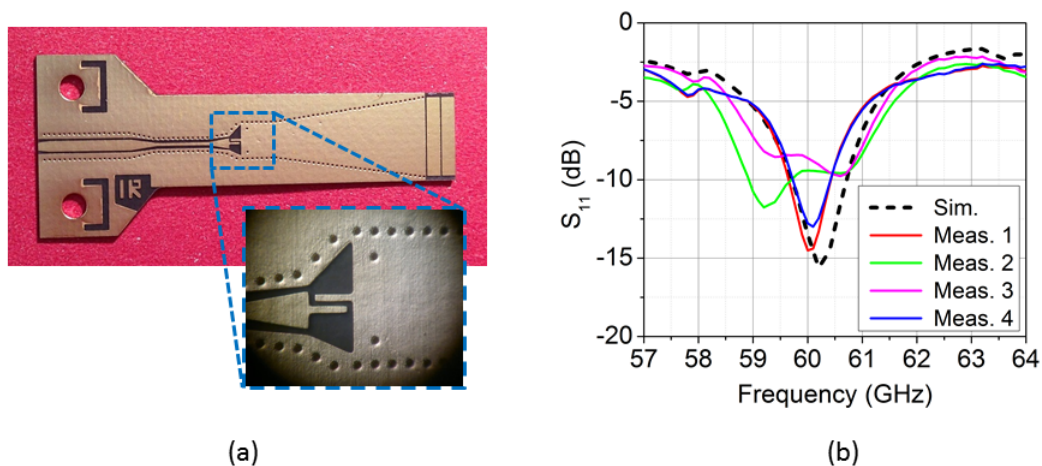


Figure 5.14: SIW antenna with two-block transition and inductive iris (a) and its simulated and measured S_{11} . Both simulated and measured results include the GCPW-to-SIW transition presented in Fig. 5.5, used to feed the signal to the antenna.

radiation pattern of the antenna in the whole band of interest.

The properties of all presented antennas, summarized in table 5.1, show that all improved designs satisfy the radiation requirements introduced in section 5.1. The choice of the most opportune antenna might be dictated by the actual required bandwidth. The design with grating resonators would be preferable for applications that require the whole available 60-GHz band. However, due to the large number of thin, closely spaced elements, this approach could be particularly sensitive to manufacturing inaccuracy, as it will be discussed in the following.

Table 5.1: Characteristics of the presented SIW antennas.

	Standard SIW Horn	Two-Block Transition	Iris Matching	Grating Transition
RL	2 dB	4 dB	10-15 dB (resonant)	7 dB
HPBW (H-Plane)	$\approx 60^\circ$	$\approx 40^\circ$	$\approx 40^\circ$	$\approx 40^\circ$
HPBW (E-Plane)	360°	$\approx 180^\circ$	$\approx 180^\circ$	$\approx 180^\circ$
FTBR	2 dB	21 dB	21 dB	17 dB

In order to validate the design of the antenna with grating transition, two prototypes have been manufactured and measured, as presented in Fig. 5.17-a. Figure 5.17-d shows the measured S_{11} (thin green and purple lines), compared with the simulation's output (black dashed line). The overall response of the antenna clearly shows the desired

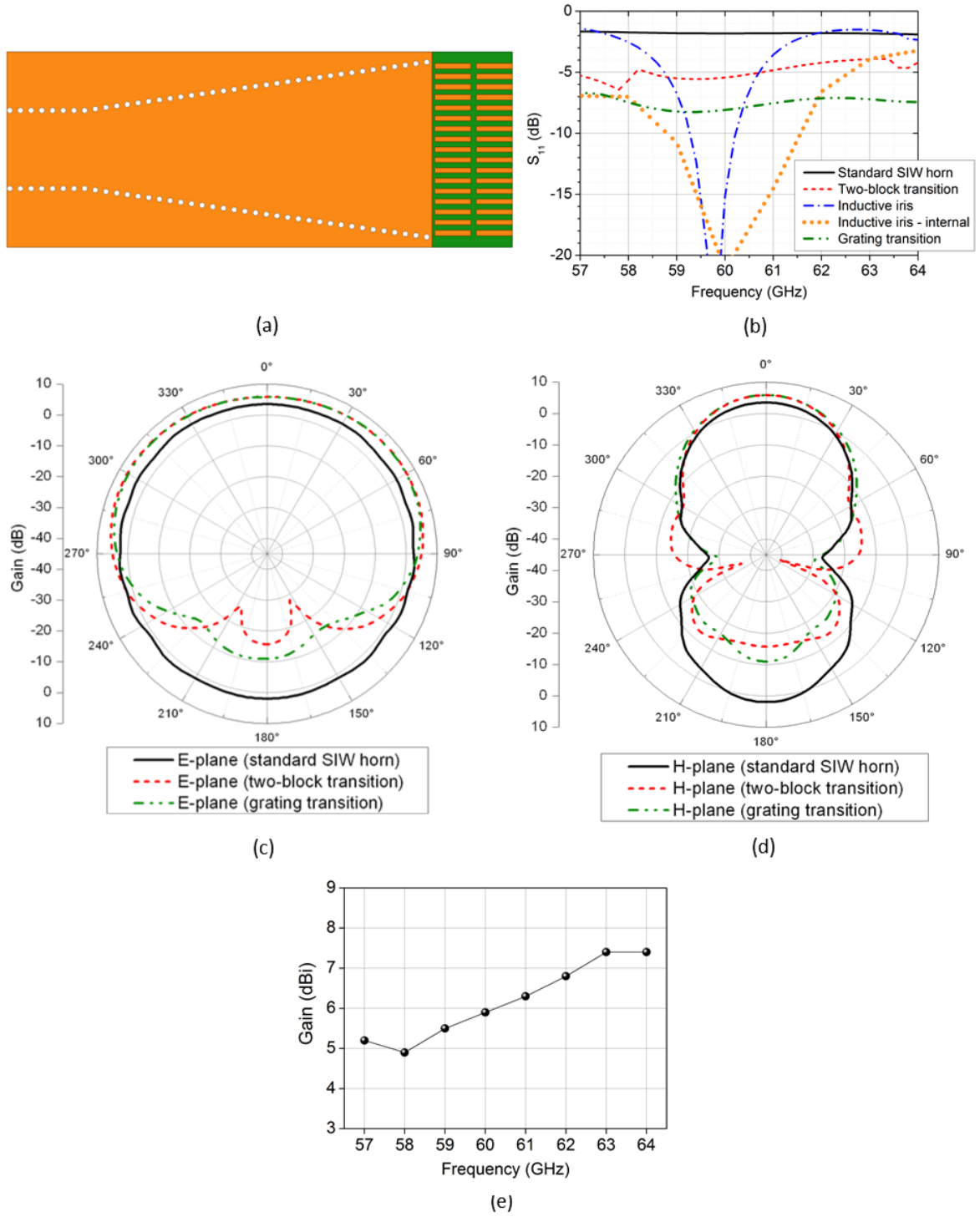


Figure 5.15: SIW Antenna with grating transition: Layout (a), simulated S-parameters (b), E-plane radiation pattern (c), H-plane radiation pattern (d) and simulated gain in the 57-64 GHz range (e). The plots in (b), (c) and (d) also show a comparison with previously introduced antennas.

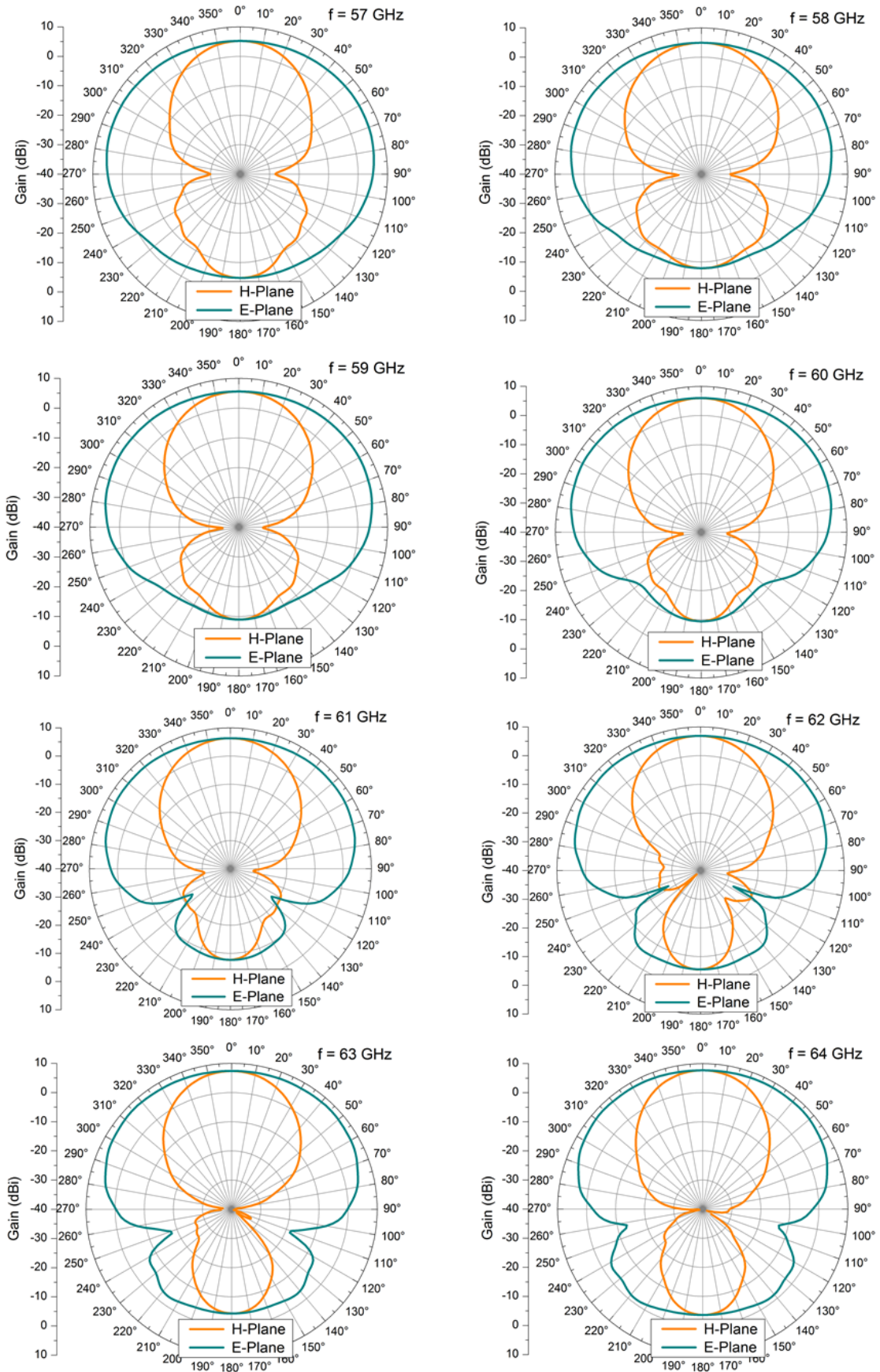


Figure 5.16: Simulated radiation pattern of the SIW antenna with grating transition in the 57-64 GHz range.

broadband matching, although a clear shift in frequency can be noticed in the measured parameter, guaranteeing a RL of 4 dB only for frequencies higher than 58 GHz. The differences are due to manufacturing issues, namely the etching inaccuracy. In fact, as shown in Fig. 5.17-b and 5.17-c, the length of the grating stripes is $50\text{ }\mu\text{m}$ shorter than the optimized size, while a difference from the designed values of up to $40\text{ }\mu\text{m}$ is found for other important parameters (strips' width and gaps) causing changes in $\varepsilon_{r,\text{pp}}$ and radiation efficiency of the slots [100]. By introducing these deviations into the EM model, the result of the simulation (represented by the red dashed line in Fig. 5.17-d) fits closely with the measurements.

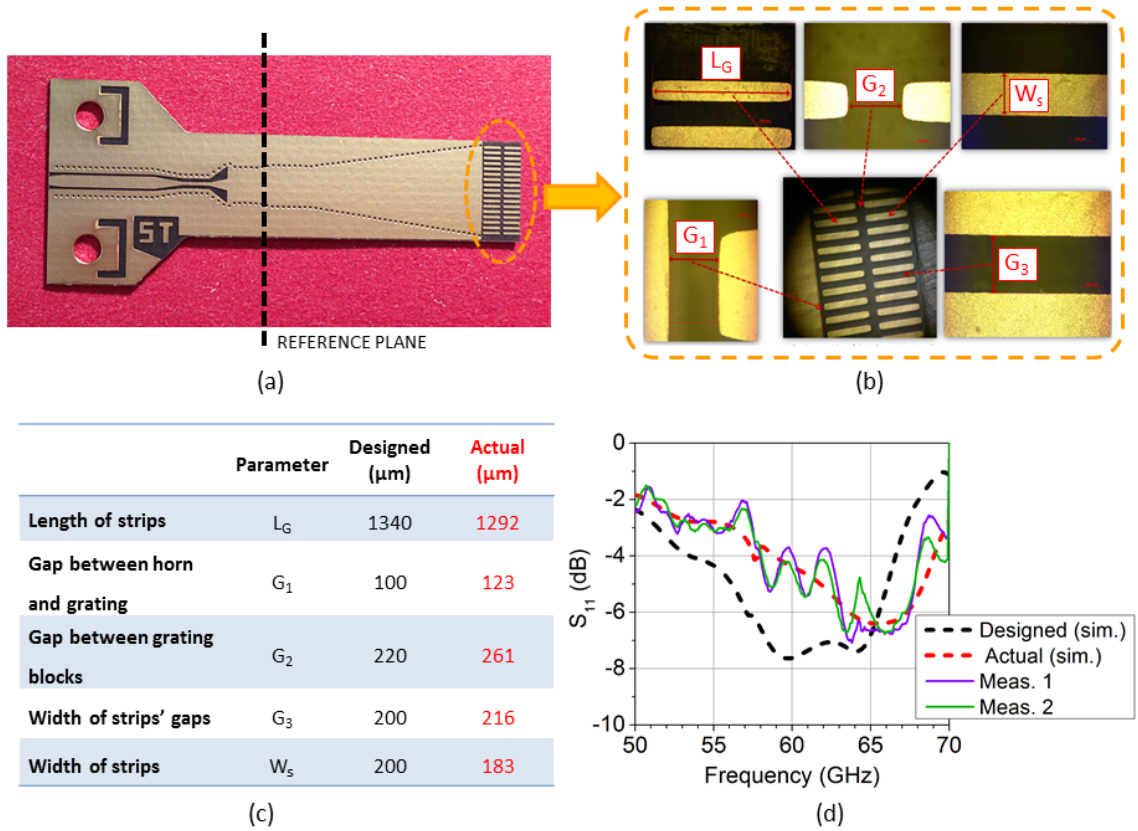


Figure 5.17: SIW antenna with grating transition (a) and its simulated and measured S_{11} (d): Simulated results are shown for the originally designed structure (black dashed line) and for the model modified according to the actual measured dimensions of the prototypes (red dashed line). The deviations of the manufactured layout from the original design are summarized in (b) and (c).

Next, an evaluation of the radiation properties of the antenna has been carried out. It is known that the ground plane and other interconnects can cause diffraction and thus influence the antenna patterns [234], therefore additional simulations have been performed in order to evaluate the impact of the GCPW-to-SIW transition and of the end-launch connector (using the model shown in Fig. 5.18-f) on the radiation pattern of the antenna,

as they cannot be excluded from the measurement environment (see Fig. 5.18-e).

The interaction of the additional structures with the antenna radiation introduces a degree of asymmetry and ripples in the normalized radiation pattern¹³, clearly visible in the simulated E-plane pattern (dark cyan solid line in Fig. 5.18-c); however the sector properties of the pattern are not compromised by the additional elements, as shown by the orange solid line in Fig. 5.18-d (H-plane pattern). The results of an additional simulation, obtained from a model of the transitions featuring the actual dimensions of the prototype listed in Fig. 5.17-c, have been included in the same plots (dashed lines). The antenna radiation pattern has been measured using a VNA ports as both source and detector and using a horn antenna with 25 dBi gain as receiving antenna, as shown in the two setups depicted in Fig. 5.18-a and 5.18-b [100]. The measured patterns (dashed lines with spherical markers) are presented with the corresponding simulated patterns (solid lines) in Fig. 5.18-c and 5.18-d, showing an overall good agreement. Manufacturing defects and etching inaccuracy have modified the radiation pattern in the H-plane by broadening the main lobe¹⁴ to 60° instead of the designed 40° and by introducing a radiation maximum at -15° rather than at 0°. The most notable deviation concerns the FTBR: The measured point at 180° in the H-plane setup shows a difference to the radiation at 0° of only 13 dB rather than the originally simulated 17 dB; by comparing the measurements with the simulation based on the actual dimensions of the prototypes (dashed lines in Fig. 5.18-c and 5.18-d), it can be seen that the FTBR could actually even be reduced 10 dB: The better measured FTBR can be attributed to the shielding effect of the of the additional metal connectors (WR-to-coax transition and WR extension) used to connect the antenna to the VNA port.

In spite of the manufacturing tolerances, the transitions and antennas presented so far have demonstrated a good level of compliance with the required characteristics and confirmed the desired sectoral performance of the improved SIW antenna. Therefore, a full integration platform, composed by a GCPW-to-SIW transition with bias tee and a SIW antenna, will be presented in section 5.5.

5.5 60 GHz SIW Integration Platform

The full layout of the platform featuring the transition and the SIW antenna is shown in Fig. 5.19-a, together with the high-frequency coaxial connector used for characterization of the structure. The dimensions of the integration platform are approximately 2.5 cm x 1 cm. Its simulated S-parameters (see Fig. 5.19-d) show that the RL (refer to the black circles for S_{11}) is larger than 6.5 dB and the IS (refer to the black dotted line for the S_{31}) is at least 27 dB in the band of interest (57-64 GHz). The measured S_{11} for different prototypes is also shown in the same plot (thin solid lines), and it can be seen that an overall good agreement with the simulated results is achieved. The better matching achieved at higher frequencies (>66 GHz), indicates over-etching as the probable cause for the slightly degraded performance around 59 GHz, as discussed for the SIW antenna

¹³Note that all patterns reported in Fig. 5.18-c and Fig. 5.18-d have been normalized to their value found for the 0°-radiation (the theoretical direction of maximum gain).

¹⁴Note that in the measured azimuthal range only half of the main lobe is present.

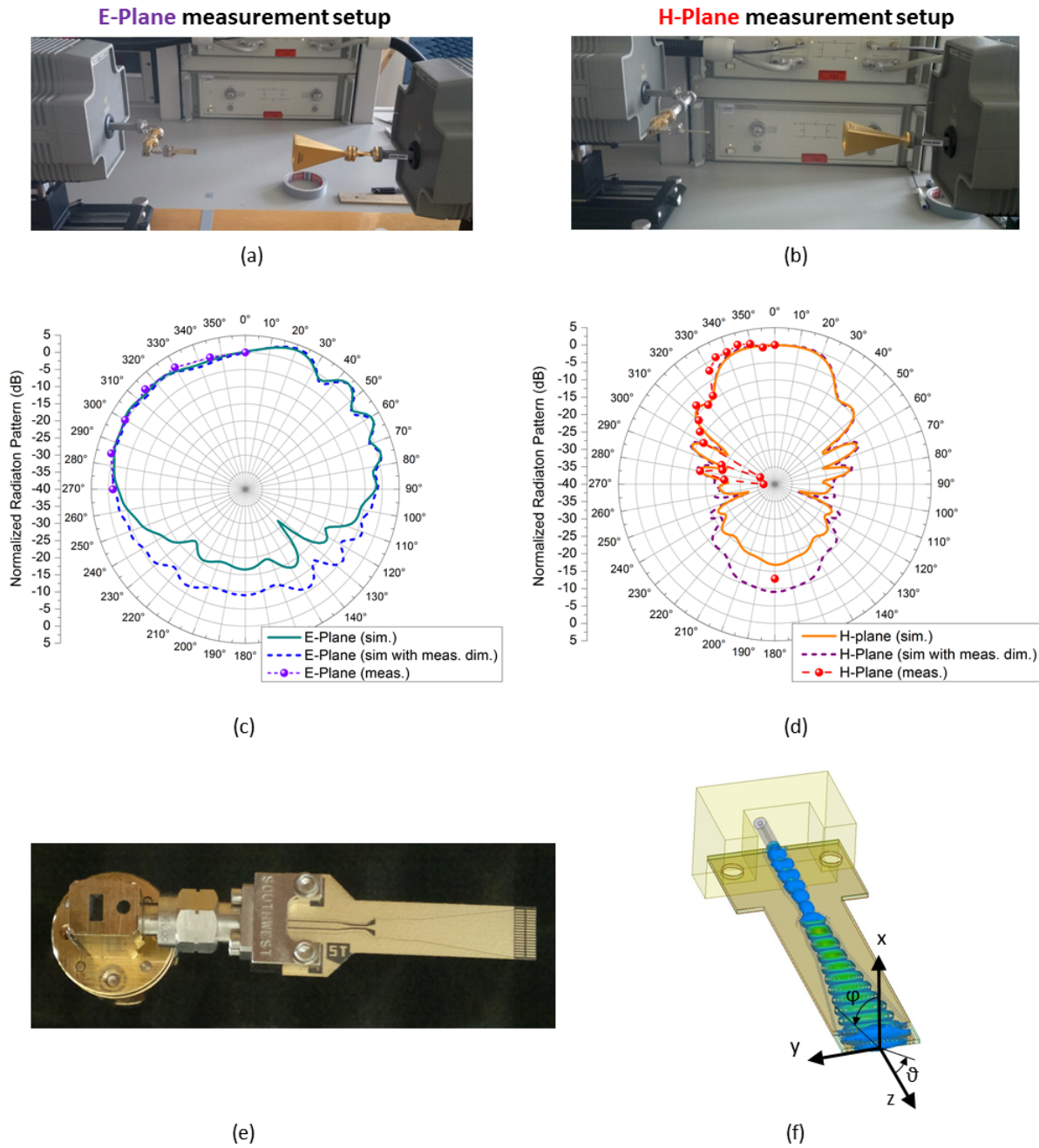


Figure 5.18: Measurements of the 60-GHz radiation pattern of the antenna with grating resonators: Measurement setups (a-b) and measured and simulated normalized radiation patterns (c-d); photograph of the prototype with coaxial and WR connectors (e) and EM model (f).

with grating. A new simulation has been prepared to verify the effect of the actual dimensions of the prototype on the performance of the circuit: In this case, besides the actual dimensions listed in Fig. 5.17-c¹⁵, additional characterization has been performed, in order to also include in the simulation the impact of possible deviation of the CL section [100], as shown in Fig. 5.19-b and 5.19-c. It can be seen that the simulation based on the measured dimensions outputs a lower RL in the band of interest and an improved RL at higher frequencies (refer to the red-filled circles in Fig. 5.19-d for the new S_{11}), as it is the case in reality.

Also in this case the radiation pattern of the SIW antenna is altered by the interaction with the GCPW-to-SIW transition, causing a slight asymmetry and ripples¹⁶. The entity of the fluctuations is not critical (less than 3 dB), however a simple solution to mitigate this effect could be the extension of the SIW section in order to locate the antenna at a farther point from the transition: This solution can be adopted on the basis of the proven low-loss properties of SIW transmission lines.

5.6 Conclusions

In this chapter the suitability of SIW technology based on PCB manufacturing for the development of quasi-hermetic PD modules in the mm-wave range has been investigated for the first time, by introducing a novel integration concept for a 60-GHz photonic transmitter for indoor RoF applications.

Integration of the SIW with other planar lines (especially with a GCPW, which is suitable for the bonding of a PD output) can be achieved by means of planar transitions. At first, a GCPW-to-SIW transition based on a standard tapered layout has been designed and successfully tested. These transitions are easily manufactured and exhibit a broadband and low-loss behavior, with a measured IL of less than 0.6 dB in the 50-65 GHz range; they are therefore suitable for the integration of PDs with integrated bias network and for the characterization of other SIW structures. We have furthermore developed and tested a novel transition featuring a fully-planar bias tee based on a single CL section and an RF-choke, which is a fundamental requirement for the integration of PDs without on-chip bias network: The measured S-parameters have shown excellent agreement with simulations, showing an IL of only 2 dB for a single transition and a RL of at least 12 dB for B2B configurations in the whole 57-64 GHz range.

In order to deliver the signal extracted by from PD to the end-user, SIW H-plane horn antennas have been considered. Their RL and sectoral radiation pattern has been enhanced by loading the output with *block resonators* as well as *grating resonators*, which also offered a possibility to evaluate the influence of etching tolerances in sensitive 60-GHz structures. While the design based on block resonators has shown a good overlap with the results predicted by theory (same frequency resonances and comparable RL ≈ 3.5 -4 dB in the 57-64 GHz range), in the second case deviations of more than 20% from the designed

¹⁵Although the prototypes are different, they have been manufactured within the same batch, therefore it can be assumed that overetching inaccuracy causes comparable effects on the grating structure.

¹⁶The level of asymmetry is lower in this case, as the EL connector has not been included in the simulated model.

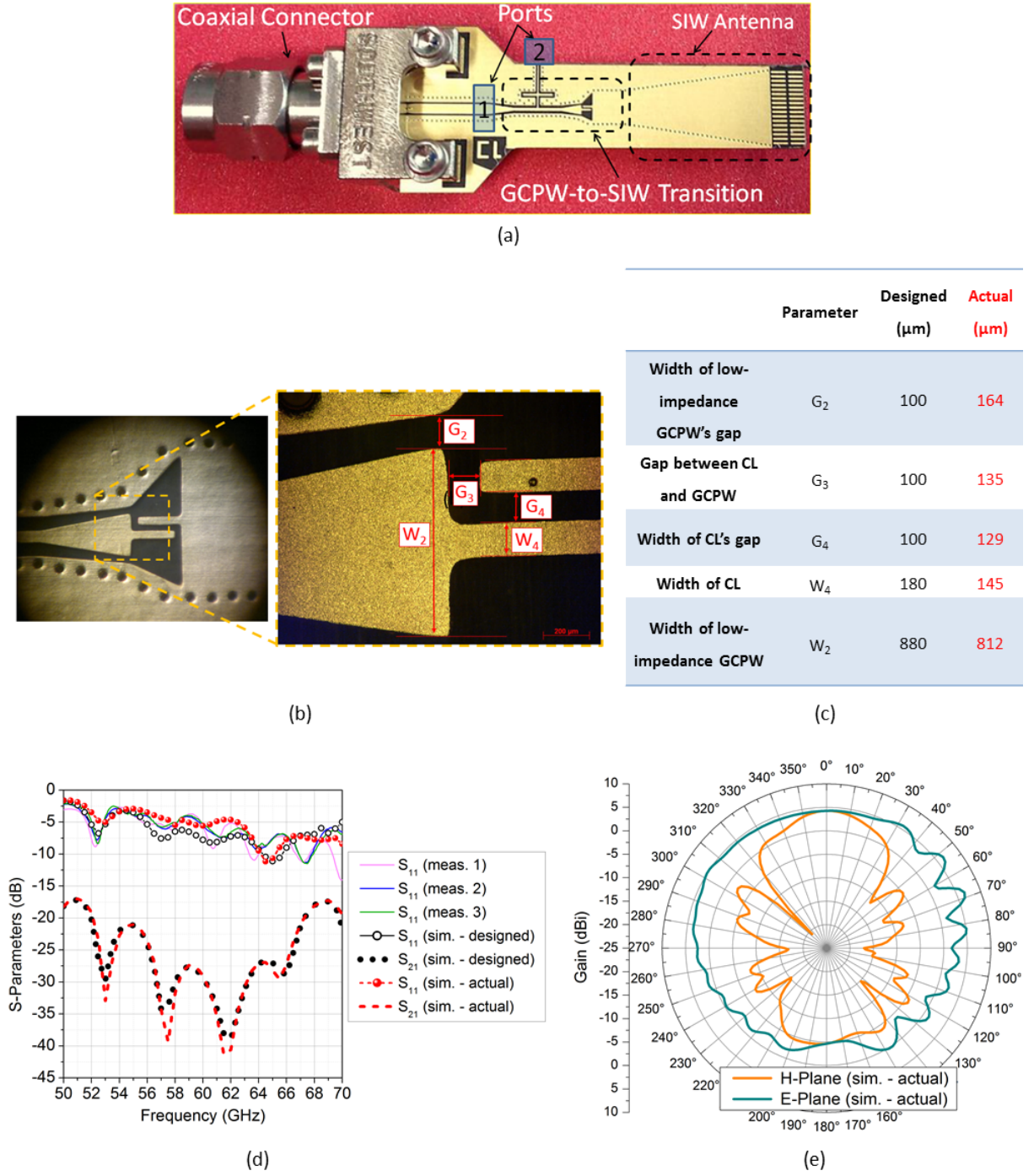


Figure 5.19: Measurements of the SIW integration platform: Prototype (a), zoomed view of the CL section (b) and comparison of designed and actual dimensions (c), measured and simulated S-parameters (d), and simulated radiation pattern based on actual dimensions of the prototype (e).

values of the dimensions of the dense grating area have lead to frequency shifts, reduced RL (4 dB at 57 GHz and 5-6 dB at 64 GHz) and changes in the radiation properties of the antenna (radiation maximum shifted of 20° and FTBR ≈ 13 dB, against the simulated 17 dB).

Nevertheless, measurements of the complete integration platform (transition and improved antenna) show consistency with the simulated results, once the actual dimensions are taken into account, with the RL being at least 4 dB in the 57-64 GHz range and achieving even better matching at higher frequencies, as a result of the over-etching.

In order to improve the reproducibility and accuracy of the manufacture, it is important to use thin metal layers whenever possible, as this simplifies the etching procedure. However, the intrinsic limits of PCB etching accuracy can be improved by taking into account that a few cycles of prototyping can lead to a more reliable process and accurate guidelines for the designer (similarly to the corrections adopted for designs based on co-fired ceramics, described in section 3.4.3), as it has been shown that EM simulations can successfully estimate the impact of the non-idealities, if the correct dimensions are used in the simulated models. This has been confirmed by the design of the complete integration platform (GCPW-to-SIW transition plus SIW antenna): Also in this case, the measured RL, which indicates a clear shift of the resonant range from 57-64 GHz to 64-70-GHz, has been correctly estimated by simulations.

It is important to highlight that the manufacture of SIW filters, cavities and other passive elements generally relies only on the mutual via holes positioning, which is sufficiently accurate even in traditional PCT, as it has been observed in section 5.4.2 by demonstrating excellent antenna matching based on a SIW inductive iris placed before the antenna. In fact, although this solution is by nature relatively narrow-band in comparison to the ones based on external resonators, it has been possible to increase the RL of the antenna to the experimental values of 10-15 dB in at least 1-GHz band, with a very high accuracy in the estimation of the resonance frequency (60 GHz) by means of simulations, as confirmed by several measured prototypes. We have also shown that even better performances can be expected using more refined solutions, such as an iris or filter placed within the antenna, which allow the achievement of similar RL values within a 2.5-GHz bandwidth.

It should be noted that SIWs cannot be used for broadband system (e.g. PD modules working from DC to 110 GHz) as their operational range is imposed by their width and by the dielectric properties of the substrate, which in turn affect their impedance, propagation characteristics and required substrate area. This is not an issue for consumer applications, where the required bandwidth can easily be supported by the one-octave operational range of the SIW.

In this chapter, we have proved that the design flexibility and advantages of PCB SIW make it a promising and reliable technology for the development of future cost-effective, quasi-hermetic, mm-wave RoF modules. Thanks to their proven lower loss and higher predictability, SIWs can improve the performance of systems based on traditional PTLs, and their use is therefore advisable when power loss is a critical issue. Integration of PDs and on-board amplification, as well as improvements and extensions of the antenna designs can lead to the development of compact, low-profile photonic transmitters to support consumer-driven applications [235]. A combination of traditional PTLs and SIWs would

yield the best results, in terms of flexibility, low loss, and interconnectivity with other system components. Recent examples of 60-GHz RoF antenna unit featuring PCB GCPW and SIW elements [129], E-band electronics front-ends [236], and W-band filters [237] and antennas [238] confirm the increasing interest in this technology and its high potential for mm-wave applications.

6 Summary and Outlook

This work addressed the development of mm-wave PD modules based on PCB¹ manufacturing techniques and materials. Theoretical and practical limits of PCB interconnects have been identified and analyzed in order to verify their suitability for mm-wave optoelectronics packaging: Based on current manufacturing possibilities, PCT shows the potential for developing competitive systems up to at least the upper limit of the W-band, with the highest working frequency generally limited by the ability to reliably drill closely spaced via holes.

We have suggested a computationally light modeling approach for traditional PTLs and SIW based on a fictive $\tan \delta$, which has proven to output reliable estimates of the measured performances of the investigated circuits. It has been found that traditional PTLs are more sensitive to manufacturing inaccuracy than the SIW: As a result of surface roughness, etching profiles and dielectric properties of the substrates, up to a threefold increase of the loss has been found for the GCPW, when compared to the one calculated using nominal parameters and perfectly smooth surfaces, while the SIW has shown only $\approx 30\%$ increase in the loss.

For the first time, the employment of cost-effective PCB technologies has been introduced in the packaging of E-band PD modules with WR output. A novel assembly concept which makes use of a GCPW-to-WR transition manufactured using PCT has been presented: The proposed integration technique does not require any mechanical modifications of the waveguide, and the alignment of the PCB to the WR is achieved using the pins of a standard flange, thus dramatically simplifying the assembly procedure when compared to other integration techniques available in literature. Using a quasi-hermetic laminate as substrate for the PCB, this approach enables near-hermetic enclosing of the WR aperture, eliminating the need for radomes at the WR port. Experimental characterization of the GCPW-to-WR transition has been performed, confirming a close correlation with the results obtained from tailored EM simulations, and showing an $IL < 3.2$ dB in the 60-75 GHz range. The impact of drilling tolerances has furthermore been investigated, as this is fundamental for the alignment of the laminate, and it has been shown that misalignments occurring within the current range of industrial drilling accuracy don't compromise the functioning of the transition.

The practical advantages of the usage of PCB for high-end optoelectronic packaging have led to interest of and close cooperation with industrial partners, resulting in the assembly of a pigtailed prototype module featuring a commercially available PD. The

¹All designs presented in this thesis were based on Rogers RT/duroid 5880 laminate, with a thickness of 127 and 381 μm for experiments involving integration of a WR and for designs based on SIW, respectively.

module, which is able to deliver -13.5 dBm of output power at the 1-dB compression point (attained at 9-mA DC photocurrent), has been successfully used in RoF demonstration activities, achieving *error-free* wireless transmission in the 71-76 GHz range with only 1.5 dB of power penalty in laboratory environment.

Several improvements of the design have also been presented and experimentally validated. In particular, the design of a GCPW-to-WR transition with an on-board fully planar bias-tee with only 0.6 dB of additional IL has been introduced, in order to enable the integration of in-house-developed PDs lacking an on-chip bias network. The integration of on-board electrical amplification on the same PCB used for the GCPW-to-WR coupling and the biasing of the PD has also been successfully proved, unlocking the potentiality to increase the output power of the PD module of up to 38 dB, and thus achieving a wider transmission range. Finally, a compact technique to improve the signal coupling into the WR based on reflecting metal lids has been suggested: Simulations, fully backed-up by experimental results, have shown that a 1-dB reduction of the IL can be achieved at essentially no additional assembly burden.

The positive outcomes of the performed experiments suggests that the proposed integration is suitable for the development of cost-effective commercial devices: Performing a redesign of the circuitry and including reflecting metal lids, photonic transmitters equipped with PD, protection circuits, and on-board amplification can be efficiently packaged in standard butterfly packages featuring a WR output and used for the implementation of outdoor RoF links using high-gain antennas [217].

This thesis further explored the use of PCB SIW to overcome the limitations (in particular loss and radiation) of traditional PTLs, and its suitability for the development of compact and potentially hermetic packaging solutions for PD modules in the mm-wave range, leading to the development of a novel integration platform featuring a GCPW-to-SIW transition and an in-package sector antenna.

Traditional (broadband) and innovative (resonant) transitions from GCPW to SIW have been designed and tested, in order to couple the signal from the PD output to the SIW. In particular a novel transition featuring a DC-block (based on a single CL section) and an RF-choke for the integration of 60-GHz PDs has been introduced and experimentally validated, showing less than 2-dB IL in the 57-64 GHz range and a RL of at least 12 dB in B2B configuration in the same frequency range.

To achieve efficient radiation of the signal, sector SIW H-plane horn antennas have been considered. In order to improve the matching and the radiation pattern (HPBW and FTBR) of the antennas, *block resonators* and *grating resonators* have been adopted and their compatibility with mm-wave PCB processing has been assessed, with particular attention to the risks connected to etching inaccuracies. We have proved that both methods are able to increase the RL of the antennas in the whole 60-GHz band, respectively achieving simulated values of 4 and 7 dB. In practice, due to the tolerances of the etching process, the final measured RLs were less than 3.5 and 6 dB, respectively, with an obvious frequency shift of the characteristics in the case of the grating resonators, which are more sensitive to etching inaccuracies. Etching tolerances also influenced the radiation pattern of the antenna which has shown a 20°-tilt of the radiation maximum, and a measured FTBR of 13 dB (against the designed 17 dB). However, it has been demonstrated that

sector radiation patterns with satisfying FTBR and RL of the antenna can be achieved with the used techniques. In order to increase the RL of the antennas, it has also been suggested that matching techniques based only on SIW elements (inductive iris) are particularly accurate at 60 GHz, if compared to printed elements, as they only rely on the positioning of via holes (drilling accuracy). This has been demonstrated by achieving excellent experimental matching ($RL > 10$ dB in a 1-GHz band) using a simple resonant SIW inductive iris placed in front of the antenna input. We have furthermore shown, by means of simulations, that using SIW matching elements *within* the antenna can lead to even better and broader matching ($RL > 10$ dB in at least a 2.5-GHz band).

We have thus proved that the design flexibility and low-loss characteristics of the PCB SIW make it a reliable cost-effective technology for the development of future mm-wave RoF devices. With the integration of optical and electronic chips, the presented SIW designs can lead to the development of compact modules, particularly suitable for local multi-platform data-distribution systems.

The achievements and results presented in this thesis prove that the PCT is a flexible, valid approach for the development of mm-wave optoelectronics devices. In particular, the introduction of the PCB SIW in optoelectronics packaging can help to overcome the difficulties encountered by traditional PCB PTL when working in the mm-wave range, by providing a low-loss, interference-free path for the guidance of the signal. The presented integration solutions for PD modules thus have the potential to facilitate the deployment of high-speed RoF systems required by the increasing diffusion of data-hungry wireless applications.

Bibliography

- [1] J. Zander and P. Maehoenen. Riding the data tsunami in the cloud: myths and challenges in future wireless access. *Communications Magazine, IEEE*, 51(3):145–151, 2013.
- [2] T. Naveh. *Mobile Backhaul: Fiber vs. Microwave*. White paper, Ceragon, 2009.
- [3] J. Wells. Faster than fiber: The future of multi-G/s wireless. *Microwave Magazine, IEEE*, 10(3):104–112, 2009.
- [4] E. Johnson. *Mobile Data Backhaul: The Need For E-Band*. <http://www.microwavejournal.com/ext/resources/whitepapers/2013/february/Sky-Light-Research-E-Band.pdf>, 2013.
- [5] BridgeWave. *The cost and performance benefits of 80 GHz links compared to short-haul 18-38 GHz licensed frequency band products*. White paper, BridgeWave Communications, 2008.
- [6] J. Wells. *Multigigabit Microwave and Millimeter-Wave Wireless Communications*. Artech House, 2010.
- [7] S. K. Yong, P. Xia, and A. Valdes-Garcia. *60 GHz Technology for Gbps WLAN and WPAN: From Theory to Practice*. John Wiley & Sons, 2010.
- [8] S. K. Yong and C. C. Chong. An overview of multigigabit wireless through millimeter wave technology: Potentials and technical challenges. *EURASIP Journal on Wireless Communications and Networking*, 2007(1):078907, 2007.
- [9] E. Perahia. IEEE 802.11n - Development: History, process, and technology. *Communications Magazine, IEEE*, 46(7):48–55, 2008.
- [10] S. Nanda, R. Walton, J. Ketchum, M. Wallace, and S. Howard. A high-performance MIMO OFDM wireless LAN. *Communications Magazine, IEEE*, 43(2):101–109, 2005.
- [11] C. Park and T. S. Rappaport. Short-range wireless communications for next-generation networks: UWB, 60 GHz millimeter-wave WPAN, and ZigBee. *Wireless Communications, IEEE*, 14(4):70–78, 2007.
- [12] T. Kaiser, F. Zheng, and E. Dimitrov. An overview of ultra-wide-band systems with MIMO. *Proceedings of the IEEE*, 97(2):285–312, 2009.

- [13] T. Baykas, C.S. Sum, Z. Lan, J. Wang, M.A. Rahman, H. Harada, and S. Kato. IEEE 802.15.3c: the first IEEE wireless standard for data rates over 1 Gb/s. *Communications Magazine, IEEE*, 49(7):114–121, 2011.
- [14] ITU. *Attenuation by atmospheric gases (ITU-Recommendation P.676-10)*. International Telecommunications Union, September 2013.
- [15] A. Stoechr. Photonic millimeter-wave generation and its applications in high data rate wireless access. In *Microwave Photonics (MWP), 2010 IEEE Topical Meeting on*, pages 7–10, 2010.
- [16] H. Singh, S. Yong, J. Oh, and C. Ngo. Principles of IEEE 802.15.3c: Multi-gigabit millimeter-wave wireless PAN. In *Computer Communications and Networks, 2009*, pages 3–6, 2009.
- [17] J. Wells. New multi-gigabit wireless systems satisfy high-security rapid response applications. Military Embedded Systems, April 2006.
- [18] EIA RS-261-B - Rectangular Waveguides (WR3 to WR2300). Electronic Industries Association of the United States of America, 1979.
- [19] T. Nagatsuma, A. Hirata, Y. Royter, M. Shinagawa, T. Furuta, T. Ishibashi, and H. Ito. A 120-GHz integrated photonic transmitter. In *Microwave Photonics, 2000. MWP 2000. International Topical Meeting on*, pages 225–228, 2000.
- [20] A. Hirata, H. Takahashi, J. Takeuchi, and J. Hirokawa. 120-GHz-band wireless communications field trials. In *Infrared, Millimeter, and Terahertz waves (IRMMW-THz), 2014 39th International Conference on*, pages 1–3, 2014.
- [21] H.-J. Song, K. Ajito, A. Hirata, A. Wakatsuki, T. Furuta, N. Kukutsu, and T. Nagatsuma. Multi-gigabit wireless data transmission at over 200-GHz. In *Infrared, Millimeter, and Terahertz waves (IRMMW-THz), 2009 34th International Conference on*, pages 1–2, 2009.
- [22] S. Koenig, D. Lopez-Diaz, J. Antes, F. Boes, R. Henneberger, A. Leuther, A. Tessmann, R. Schmogrow, D. Hillerkuss, R. Palmer, T. Zwick, C. Koos, W. Freude, O. Ambacher, J. Leuthold, and I. Kallfass. Wireless sub-THz communication system with high data rate enabled by RF photonics and active MMIC technology. In *Photonics Conference (IPC), 2014 IEEE*, pages 414–415, 2014.
- [23] A. Burkert. Tera-Technik fuer die Funknetze der Zukunft. <http://www.springerprofessional.de/tera-technik-fuer-die-funknetze-der-zukunft/4959574.html>, 02 2014. Springer Fachmedien Wiesbaden GmbH.
- [24] D. Jaeger. Microwave photonics. In S. D. Smith and R. F. Neale, editors, *Optical Information Technology*, ESPRIT Basic Research Series, pages 328–333. Springer Berlin Heidelberg, 1993.

- [25] S.Q. Xiao; M.T. Zhou, editor. *Millimeter Wave Technology in Wireless PAN, LAN, and MAN*. CRC Press, 2008.
- [26] I. Stavros, editor. *Microwave Photonics: Devices and Applications*. John Wiley & Sons, 2009.
- [27] S. Weisser, E.C. Larkins, K. Czotscher, W. Benz, J. Daleiden, J. Fleissner, M. Maier, J.D. Ralston, B. Romero, A. Schonfelder, and J. Rosenzweig. 37 GHz direct modulation bandwidth in short-cavity InGaAs/GaAs MQW lasers with C-doped active regions. In *Lasers and Electro-Optics Society Annual Meeting, 1995. 8th Annual Meeting Conference Proceedings, Volume 1., IEEE*, volume 1, pages 91–92 vol.1, 1995.
- [28] H. Ito, T. Ito, Y. Muramoto, T. Furuta, and T. Ishibashi. Rectangular waveguide output untraveling-carrier photodiode module for high-power photonic millimeter-wave generation in the F-band. *Lightwave Technology, Journal of*, 21(12):3456–3462, 2003.
- [29] H. Ito, T. Furuta, T. Ito, Y. Muramoto, K. Tsuzuki, K. Yoshino, and T. Ishibashi. W-band uni-travelling-carrier photodiode module for high-power photonic millimetre-wave generation. *Electronics Letters*, 38:1376–1377, 2002.
- [30] A. Ueda, T. Noguchi, H. Iwashita, Y. Sekimoto, M. Ishiguro, S. Takano, T. Nagatsuma, H. Ito, A. Hirata, and T. Ishibashi. W-band waveguide photomixer using a uni-traveling-carrier photodiode with 2-mW output. *IEEE Transactions on Microwave Theory and Techniques*, 51:1455–1459, 2003.
- [31] H. Ito, K. Yoshino, Y. Muramoto, H. Yamamoto, and T. Ishibashi. Sub-terahertz transceiver module integrating uni-traveling-carrier photodiode, schottky barrier diode, and planar circulator circuit. In *Infrared, Millimeter, and Terahertz waves (IRMMW-THz), 2010 35th International Conference on*, 2010.
- [32] B. Bouhlal, S. Lutzmann, and T. Tekin. Integration platform for 72-GHz photodiode-based wireless transmitter. In *SPIE, RF and Millimeter-Wave Photonics II*, 2012.
- [33] N.-W. Chen, H.-J. Tsai, F.-M. Kuo, and J.-W. Shi. High-speed W-Band integrated photonic transmitter for Radio-Over-Fiber applications. *Microwave Theory and Techniques, IEEE Transactions on*, 59(4):978–986, 2011.
- [34] P. G. Huggard, L. Azcona, A. Laisne, B. N. Ellison, P. Shen, N. J. Gomes, and P. A. Davies. Integrated 1.55 μm photomixer local oscillators for heterodyne receivers at mm wavelengths. In *SPIE, Microwave and Terahertz Photonics*, 2004.
- [35] A. Hirata, T. Kosugi, N. Meisl, T. Shibata, and T. Nagatsuma. High-directivity photonic emitter using photodiode module integrated with HEMT amplifier for 10-Gbit/s wireless link. *IEEE Transactions on Microwave Theory and Techniques*, 52:1843–1850, 2004.

- [36] T. Furuta, T. Ito, Y. Muramoto, H. Ito, M. Tokumitsu, and T. Ishibashi. D-band rectangular-waveguide-output uni-travelling-carrier photodiode module. *Electronics Letters*, 41:715–716, 2005.
- [37] H. Takahashi, T. Kosugi, A. Hirata, J. Takeuchi, K. Murata, and N. Kukutsu. Hermetic sealing technique for F-band waveguides and packages. In *Proc. EuMC*, 2011.
- [38] A. C. Paoella, A. M. Joshi, and A. Bauerle. Photonic modules for millimeter wave communication systems. In *Microwave Photonics, 2000. MWP 2000. International Topical Meeting on*, pages 233–236, 2000.
- [39] Akihiko Hirata, Hiromu Ishii, and Tadao Nagatsuma. Design and characterization of a 120-ghz millimeter-wave antenna for integrated photonic transmitters. *Microwave Theory and Techniques, IEEE Transactions on*, 49(1):2157–2162, 2001.
- [40] D. Ferling, W. Heinrich, W. Kuebart, G. Luz, and F. Buchali. Hybrid integrated fibre-amplifier-antenna module for radio applications at 60 GHz. In *MTT-S Digest*, 1999.
- [41] G. H. Smith, R. B. Waterhouse, A. Nirmalathas, D. Novak, C. Lim, and O. Sevimli. A broadband integrated photonic-antenna interface for multiservice millimeter-wave fiber-wireless applications. In *Microwave Photonics, 2001. MWP '01. 2001 International Topical Meeting on*, pages 173–176, 7-9 Jan. 2002.
- [42] H. Ito, T. Furuta, F. Nakajima, K. Yoshino, and T. Ishibashi. Photonic generation of continuous THz wave using uni-travelling-carrier photodiode. *Journal of Lightwave Technology*, Vol. 23, No. 12:4016–4021, 2005.
- [43] M. Weiss, A. G. Steffan, S. Fedderwitz, G. Tsianos, A. Stoehr, and D. Jaeger. Highly-compact fibre-optic package for 30-300 GHz wireless transmitter modules. In *2nd Electronics System Integration Technology Conference - Greenwich (UK)*, 2008.
- [44] E. Rouvalis, C. C. Renaud, D. G. Moodie, M. J. Robertson, and A. J. Seeds. Traveling-wave uni-traveling carrier photodiodes for continuous wave THz generation. *Optics Express*, 18(11):11105–11110, May 2010.
- [45] N. Ghassemi and K. Wu. Millimeter-wave integrated pyramidal horn antenna made of multilayer printed circuit board (PCB) process. *Antennas and Propagation, IEEE Transactions on*, 60(9):4432–4435, Sept. 2012.
- [46] Z. N. Chen, X. Qing, M. Sun, K. Gong, and W. Hong. 60-GHz antennas on PCB. In *The 8th European Conference on Antennas and Propagation (EuCAP 2014)*, pages 533–536, 6-11 April 2014.
- [47] J. Galiere, J. L. Valard, and E. Estebe. Millimetre-wave MMIC packaging compatible with surface-mount technology (SMT). In *Microwave Conference, 2004. 34th European*, volume 1, pages 353–355, 14-14 Oct. 2004.

- [48] A. Rida, F. Nasri, A. Margomenos, and M. M. Tentzeris. Integration of novel mm-wave components on flexible organic substrates for automotive radar applications. In *Microwave Conference, 2009. EuMC 2009. European*, pages 1327–1330, Sept. 29 2009-Oct. 1 2009.
- [49] R. Hartley. Base materials for high speed, high frequency PC boards. https://www.speedingedge.com/PDF-Files/Materials_RickH2.pdf, Mar. 2002.
- [50] L. A. Belov, S. M. Smolskiy, and V. N. Kochemasov. *Handbook of RF, Microwave, and Millimeter-Wave Components*. Artech House, 2012.
- [51] I. Flammia, C. C. Leonhardt, J. Honecker, A. G. Steffan, and A. Stoehr. Novel E-Band (71-76 GHz) photodiode module featuring a hermetic grounded-coplanar-waveguide-to-rectangular-waveguide transition. In *Microwave Photonics, 2011 International Topical Meeting on & Microwave Photonics Conference, 2011 Asia-Pacific, MWP/APMP*, pages 405–408. IEEE, 2011.
- [52] I. Flammia, B. Khani, and A. Stoehr. A novel transition from grounded coplanar waveguide to substrate integrated waveguide for 60 GHz Radio-over-Fiber photonic transmitters. In *Microwave Techniques (COMITE), 2013 Conference on*, pages 73–76. IEEE, 2013.
- [53] http://portal.uc3m.es/portal/page/portal/grupos_investigacion/optoelectronics/european_projects/mitepho.
- [54] <http://www.iphos-project.eu/>.
- [55] R. E. Collin. *Foundations for Microwave Engineering*. Wiley-Interscience, 2001.
- [56] R. Sorrentino and G. Bianchi. *Microwave and RF Engineering*. John Wiley & Sons, 2010.
- [57] L. F. Chen, C. K. Ong, C. P. Neo, V. V. Varadan, and V. K. Varadan. *Microwave Electronic - Measurement and Materials Characterisation*. John Wiley & Sons, 2004.
- [58] D. M. Pozar. *Microwave Engineering*. John Wiley & Sons, 2012.
- [59] S. Groiss, I. Bardi, O. Biro, K. Preis, and K.R. Richter. Parameters of lossy cavity resonators calculated by the finite element method. *Magnetics, IEEE Transactions on*, 32(3):894–897, 1996.
- [60] T. K. Ishii, editor. *Handbook of Microwave Technology - Volume I - Components and Devices*. Academic Press, 1995.
- [61] B. C. Wadell. *Transmission Line Design Handbook*. Artech House, 1991.
- [62] E. Hammerstad and O. Jensen. Accurate models for microstrip computer-aided design. In *IEEE Microwave Symposium*, pages 407–409, 1980.

- [63] E. Yamashita, K. Atsuki, and T. Hirahata. Microstrip dispersion in a wide frequency range. *IEEE Transactions on Microwave Theory and Techniques*, MTT-29:610–611, 1981.
- [64] D. Mirshekar-Syahkal. An accurate determination of dielectric loss effect in monolithic microwave integrated circuits including microstrip and coupled microstrip lines. *IEEE Transactions on Microwave Theory and Techniques*, MTT-31, No. 11:950–954, 1982.
- [65] M. Kobayashi. A dispersion formula satisfying recent requirements in microstrip CAD. *IEEE Transactions on Microwave Theory and Techniques*, MTT-36:1246–1250, 1988.
- [66] K. Kuang, F. Kim, and S. S. Cahill, editors. *RF and Microwave Microelectronics Packaging*. Springer, 2010.
- [67] RT/duroid - 5870/5880 high frequency laminates. Data sheet, Rogers Corporation. <https://www.rogerscorp.com/documents/606/acm/RT-duroid-5870-5880-Data-Sheet.pdf>, July.
- [68] E. Holzmänn. *Essentials of RF and Microwave Grounding*. Artech House, 2006.
- [69] M. D. Abouzahra and L. Lewin. Radiation from microstrip discontinuities. *IEEE Transactions on Microwave Theory and Techniques*, 27:722–723, 1979.
- [70] J. Coonrod. Insertion loss comparisons of common high frequency PCB constructions. In *IPC APEX EXPO Conference & Exhibition 2013*, 2013.
- [71] Southwest Microwave. *Optimizing Test Boards for 50 GHz End Launch Connectors*, 2007.
- [72] I. Bahl. *Lumped Elements for RF and Microwave Circuits*. Artech House, 2003.
- [73] E. Bogatin, D. DeGroot, P. Huray, and Y. Shlepnev. Which one is better? Comparing options to describe frequency dependent losses. In *DesignCon*, 2013.
- [74] Y. Shlepnev and C. Nwachukwu. Roughness characterization for interconnect analysis. In *Electromagnetic Compatibility (EMC), 2011 IEEE International Symposium on*, pages 518–523, 14-19 Aug. 2011.
- [75] E. H. Fooks and R. A. Zakarevicius. *Microwave Engineering Using Microstrip Circuits*. Prentice Hall, 1990.
- [76] RT/duroid - 6006/6010LM high frequency laminates. Data sheet, Rogers Corporation. <https://www.rogerscorp.com/documents/612/acs/RT-duroid-6006-6010LM-laminate-data-sheet.pdf>.
- [77] S. Hudson and D. Pozar. Grounded coplanar waveguide-fed aperture-coupled cavity-backed microstrip antenna. *Electronics Letters*, 36(12):1003–1005, 8 Jun 2000.

-
- [78] S. Bokhari and H. Ali. On grounded co-planar waveguides as interconnects for 10 Gb/s signals. In *Electromagnetic Compatibility, 2003 IEEE International Symposium on*, volume 2, pages 607–609 vol.2, 18-22 Aug. 2003.
- [79] R. N. Simons. *Coplanar Waveguide Circuits, Components, and Systems*. John Wiley & Sons., 2001.
- [80] Y.C. Shih and M. Maher. Characterization of conductor-backed coplanar waveguide using accurate on-wafer measurement techniques. In *IEEE MTT-S International Microwave Symposium Digest*, 1990.
- [81] W.H. Haydl. On the use of vias in conductor-backed coplanar circuits. *Microwave Theory and Techniques, IEEE Transactions on*, 50(6):1571–1577, 2002.
- [82] T. Tischler, M. Rudolph, A. Kilk, and W. Heinrich. Via arrays for grounding in multilayer packaging - frequency limits and design rules. In *Microwave Symposium Digest, 2003 IEEE MTT-S International*, volume 2, pages 1147–1150 vol.2, 2003.
- [83] J. Hirokawa and M. Ando. Single-layer feed waveguide to excite plane TEM wave for parallel plate slot arrays. Technical Report AP97-31, IEICE, May 1997.
- [84] H. Uchimura, T. Takenoshita, and M. Fujii. Development of a "laminated waveguide". *Microwave Theory and Techniques, IEEE Transactions on*, 46, No. 12:2438–2443, 1998.
- [85] D. Deslandes and K. Wu. Single-substrate integration techniques for planar circuits and waveguide filters. *Microwave Theory and Techniques, IEEE Transactions on*, pages 593–596, February 2003.
- [86] H. J. Tang, W. Hong, Z. C. Hao, J. X. Chen, and Ke Wu. Optimal design of compact millimetre-wave SIW circular cavity filters. *Electronics Letters*, 41, No.19, 2005.
- [87] Y. Cassivi, L. Perregrini, K. Wu, and G. Conciauro. Low-cost and high-Q millimeter-wave resonator using substrate integrated waveguide technique. In *European Microwave Conference*, volume 2, Milan, Sept. 2002.
- [88] S. Germain, D. Deslandes, and K. Wu. Development of substrate integrated waveguide power dividers. In *CCECE*, pages 1921–1924, May 2003.
- [89] Y. Cassivi, D. Deslandes, and K. Wu. Substrate integrated waveguide directional couplers. In *Asia-Pacific Conference*, 2002.
- [90] Z. C. Hao, W. Hong, J. X. Chen, H. X. Zhou, and K. Wu. Single-layer substrate integrated waveguide directional couplers. In *IEEE Proc. Microwaves, Antennas and Propagation*, volume 153, pages 426–431, 2006.
- [91] L. Yan, W. Hong, G. Hua, J. Chen, K. Wu, and T. J. Cui. Simulation and experiment on SIW slot array antennas. *IEEE Microwave and Wireless Components Letters*, 14(9):446–448, Sept. 2004.

- [92] W. Hong, J. Xu, Q. Lai, and P. Chen. Design and implementation of low sidelobe slot array antennas with full and half mode substrate integrated waveguide technology. In *Microwave Conference, 2007. European*, pages 428–429, 9–12 Oct. 2007.
- [93] G. Hua, W. Hong, X. H. Sun, and H. X. Zhou. Design of an omnidirectional line array with SIW longitudinal slot antenna. In *Microwave and Millimeter Wave Technology, 2008. ICMMT 2008. International Conference on*, volume 3, pages 1114–1117, 21–24 April 2008.
- [94] X. P. Chen, K. Wu, L. Han, and F. He. Low-cost high gain planar antenna array for 60-GHz band applications. *Antennas and Propagation, IEEE Transactions on*, 58(6):2126–2129, June 2010.
- [95] A. R. Mallahzadeh and S. Esfandiarpour. Wideband H-plane horn antenna based on ridge substrate integrated waveguide (RSIW). *IEEE Antennas and Wireless Propagation Letters*, 11:85–88, 2012.
- [96] H. Wang, D.-G. Fang, B. Zhang, and W.-Q. Che. Dielectric loaded substrate integrated waveguide (SIW) H-plane horn antennas. *Antennas and Propagation, IEEE Transactions on*, 58(3):640–647, 2010.
- [97] S. R. Ranade and D. U. Nair. Design of a substrate integrated waveguide H plane horn antenna on a PTFE substrate for automotive radar application. In *Applied Electromagnetics Conference (AEMC), 2011 IEEE*, pages 1–4, 2011.
- [98] Y. Seo, T. J.W. Lee, T.K. Lee, and C. S. Cho. An embedded filtering antenna using multiple layers with dielectric lens. In *Microwave Conference, 2009. EuMC 2009. European*, pages 751–754, 2009.
- [99] A. Doghri, A. Ghiotto, T. Djerafi, and K. Wu. Broadband E-plane junction for three-dimensional substrate integrated waveguide circuits and systems. *IEEE Microwave and Wireless Components Letters*, 24(11):739–741, Nov. 2014.
- [100] B. Khani. Design of 60 GHz indoor Radio-over-Fiber photonic transmitter based on substrate integrated waveguide technology. Master’s thesis, University of Duisburg-Essen. Duisburg, Germany, 2013.
- [101] Y. Cassivi. Dispersion characteristics of substrate integrated rectangular waveguides. *IEEE Microwave Wireless Components Letters*, 12:333–335, 2002.
- [102] W. Che. Analytical equivalence between substrate-integrated waveguides and rectangular waveguide. *IET Antenna and Propagation*, 2:35–41, 2008.
- [103] F. Xu and Ke Wu. Guided-wave and leakage characteristics of substrate integrated waveguide. *Microwave Theory and Techniques, IEEE Transactions on*, 51:593–596, 2003.
- [104] R. Garg, I. Bahl, and M. Bozzi. *Microstrip Line and Slotlines*. Artech House, 2013.

- [105] M. Bozzi, L. Perregrini, and K. Wu. Modeling of conductor, dielectric and radiation losses in substrate integrated waveguide by the boundary integral-resonant mode expansion method. *IEEE Tr*, 56:3153–3161, 2008.
- [106] D. Deslandes and K. Wu. Accurate modeling, wave mechanisms, and design considerations of a substrate integrated waveguide. *IEEE Transactions on Microwave Theory and Techniques*, 54(6):2516–2526, June 2006.
- [107] T. P. Pearsall. *Photonic Essentials - An Introduction with Experiments*. McGraw-Hill Professional Publishing, 2002.
- [108] C. H. Cox. *Analog Optical Links - Theory and Practice*. Cambridge University Press, 2006.
- [109] G. P. Agrawal. *Fiber-Optic Communications Systems*. John Wiley & Sons, 2010.
- [110] A. Beling and J. C. Campbell. InP-based high-speed photodetectors. *Journal of Lightwave Technology*, 27, no. 3:343–355, 2009.
- [111] S. O. Kasap. *Optoelectronics And Photonics - Principles and Practices*. Prentice-Hall, 2001.
- [112] H. Ito, S. Kodama, Y. Muramoto, T. Furuta, T. Nagatsuma, and T. Ishibashi. High-speed and high-output InP-InGaAs unitravelling-carrier photodiodes. *Journals of Selected Topics in Quantum Electronics*, 10, no. 4:709–727, 2004.
- [113] A. Madjar, N. Koka, J. Bloch, P. K. L. Yu, A. Stoehr, and D. Jaeger. A UTC-TW photo detector operating at frequencies exceeding 100 GHz. In *Proceedings of the 38th European Microwave Conference*, 2008.
- [114] G. Ghione. *Semiconductor Devices for High-Speed Optoelectronics*. Cambridge University Press, 2009.
- [115] J. Gao. *Optoelectronic Integrated Circuit Design and Device Modelling*. John Wiley & Sons, 2011.
- [116] K.S. Giboney, R.L. Nagarajan, T.E. Reynolds, S.T. Allen, R.P. Mirin, Mark J.W. Rodwell, and J.E. Bowers. Travelling-wave photodetectors with 172-GHz bandwidth and 76-GHz bandwidth-efficiency product. *Photonics Technology Letters, IEEE*, 7(4):412–414, 1995.
- [117] S. Klinger, M. Berroth, M. Kaschel, M. Oehme, and E. Kasper. Ge-on-Si p-i-n photodiodes with a 3-db bandwidth of 49 GHz. *Photonics Technology Letters, IEEE*, 21(13):920–922, 2009.
- [118] K. Kato, A. Kozen, Y. Muramoto, Y. Itaya, and T. NagT. Nagatsuma. Yaita. 110-GHz, 50for a 1.55- μ m wavelength. *Photonics Technology Letters, IEEE*, 6:719–721, 1994.

- [119] A. Umbach, R. Steingruber, A. Seeger, W. Ebert, D. Trommer, and G. Unterborsch. Ultrafast, high-power 1.55 μm side-illuminated photodetector with integrated spot size converter. In *Optical Fiber Communication Conference*, page FG2. Optical Society of America, 2000.
- [120] H. Ito, T. Furuta, S. Kodama, and T. Ishibashi. InP/InGaAs uni-travelling-carrier photodiode with 310 GHz bandwidth. *Electronics Letters*, 36:1809–1810, 2000.
- [121] T. Nagatsuma, H. Ito, and T. Ishibashi. High-power RF photodiodes and their applications. *Laser & Photonics Reviews*, 3(1-2):123–137, 2009.
- [122] M. A. Hollis. Space-charge impedance in photodiodes. *Photonics Technology Letters, IEEE*, 23:1307–1309, 2011.
- [123] T. Nagatsuma, N. Kukutsu, and Y. Kado. Photonics generation of millimeter and terahertz waves and its applications. *Automatika*, 49:51–59, 2008.
- [124] K. S. Giboney, J. W. Rodwell, and J. E. Bowers. Traveling-wave photodetector theory. *IEEE Transactions on Microwave Theory and Techniques*, 45(8):1310–1319, Aug 1997.
- [125] A. Stoehr, Andrei Malcoci, A. Sauerwald, I. C. Mayorga, R. Guensten, and D. S. Jaeger. Ultra-wide-band travelling-wave photodetectors for photonic local oscillators. *Journal of Lightwave Technology*, 21:3062–3070, 2003.
- [126] K. Takahata, Y. Muramoto, H. Fukano, K. Kato, A. Kozen, O. Nakajima, and Y. Matsuoka. 46.5-GHz-bandwidth monolithic receiver OEIC consisting of a waveguide p-i-n photodiode and a HEMT distributed amplifier. *Photonics Technology Letters, IEEE*, 10(8):1150–1152, 1998.
- [127] H. Fukuyarna, K. Murata, K. Sano, H. Kitabayashi, Y. Yamane, T. Enoki, and H. Sugahara. Optical receiver module using an InP HEMT transimpedance amplifier for over 40 Gbit/s. In *Gallium Arsenide Integrated Circuit (GaAs IC) Symposium, 2003. 25th Annual Technical Digest 2003. IEEE*, pages 237–240, 2003.
- [128] M. Ney, editor. *Millimeter Wave in Communication Systems*. Hermes Penton Science, 2002.
- [129] D. Makris, P. Tsiakas, K. Voudouris, M. P. Thakur, and S. Mikroulis. Investigation of the SIW technology for low cost 60 GHz radio over fiber based array antenna units. volume 9387, pages 938707–938707–9, 2015.
- [130] G. Kumar and K.P. Ray. *Broadband Microstrip Antennas*. Artech House, INC., 2003.
- [131] K. Takahata, Y. Muramoto, S. Fukushima, T. Furuta, and H. Ito. Monolithically integrated millimeter-wave photonic emitter for 60-GHz fiber-radio applications. In *Microwave Photonics, 2000. MWP 2000. International Topical Meeting on*, pages 229–232, 2000.

- [132] C. A. Balanis. *Antenna Theory*. Wiley Interscience, 2005.
- [133] E. O. Hammerstad. Equations for microstrip circuit design. In *Proc. Fifth European Microwave Conf.*, 1965.
- [134] W. L. Stutzman and G. A. Thiele. *Antenna Theory and Design*. John Wiley & Sons, 1998.
- [135] D. J. Edwards K.-C. Huang. *Millimetre Wave Antennas for Gigabit Wireless Communications*. John Wiley & Sons, 2008.
- [136] H. Ito, T. Furuta, Y. Hirota, T. Ishibashi, A. Hirata, T. Nagatsuma, H. Matsuo, T. Noguchi, and M. Ishiguro. Photonic millimetre-wave emission at 300 GHz using an antenna-integrated uni-travelling-carrier photodiode. *Electronics Letters*, 38(17):989–990, 2002.
- [137] S. Babel, V. Rymanov, and A. Stoehr. Hybrid integrated photonic millimeter wave emitter. In *Asia-Pacific Microwave Photonics Conference (APMP), Kyoto, Japan*, 2012.
- [138] Z. Barrientos, M. Claudio, G. Calle, H. Victor, J. A. Alvarez, F. P. Mena, J. Vukusic, J. Stake, and E. A. Michael. Vertically illuminated TW-UTC photodiodes for terahertz generation. In *Proc. SPIE 8452, Millimeter, Submillimeter, and Far-Infrared Detectors and Instrumentation for Astronomy VI*, volume 8452, pages 84522I–84522I–11, 2012.
- [139] L. L. Wai, K. M. Chua, A. C. W. Lu, M. Sun, and Y.-P. Zhang. A compact package with integrated patch antenna for single-chip 60-GHz radios. *Progress In Electromagnetics Research C*, 20:227–238, 2011.
- [140] S. Methfessel and L. Schmidt. Design of a balanced-fed patch-excited horn antenna at millimeter-wave frequencies. In *Antennas and Propagation (EuCAP), 2010 Proceedings of the Fourth European Conference on*, pages 1–4, 2010.
- [141] U.R. Pfeiffer, J. Grzyb, Duixian Liu, B. Gaucher, T. Beukema, B.A. Floyd, and S.K. Reynolds. A chip-scale packaging technology for 60-GHz wireless chipsets. *Microwave Theory and Techniques, IEEE Transactions on*, 54(8):3387–3397, 2006.
- [142] B. Pan, Y. Li, G. E. Gonchak, J. Papapolymerou, and M. Tenzeris. A high-gain broadband surface micromachined V-band horn. *Antennas and Propagation, IEEE Transactions on*, 4:1050–1056, 2009.
- [143] A. Lamminen and J. Saily. High gain 60 GHz LTCC chain antenna array with substrate integrated waveguide feed network. In *Antennas and Propagation (EUCAP), 2012 6th European Conference on*, pages 2569–2573, 2012.
- [144] P. Sanchez Olivares, J. L. Masa-Campos, J. A. Ruiz-Cruz, and B. Taha-Ahmed. SIW 2D planar array with four cross slots radiator and tuning vias. *Progress In Electromagnetics Research C*, 40:83–92, 2013.

- [145] R. E. Collin. *Antennas And Radiowave Propagation*. McGraw-Hill Professional Publishing, 1985.
- [146] C.I. Yeh, D.H. Yang, T.H. Liu, J.S. Fu, K.-S. Chin, J.C. Cheng, H.C. Chiu, and C.P. Kao. MMIC compatibility study of SIW H-plane horn antenna. In *Microwave and Millimeter Wave Technology (ICMMT), 2010 International Conference on*, pages 933–936, 2010.
- [147] J.S. Fu. Preliminary study of 60 GHz air-filled SIW H-plane horn antenna. In *Electrical Design of Advanced Packaging and Systems Symposium (EDAPS), 2011 IEEE*, pages 1–4, 2011.
- [148] S. L. Pyshkin and J. M. Ballato, editors. *Optoelectronics - Advanced Materials and Devices*. InTech, 2013.
- [149] R. C. Lasky, A. Singer, and P. Chouta. Packaging assembly techniques. In C. DeCusatis, editor, *Fiber Optic Data Communication: Technological Trends and Advances*. Academic Press, 2002.
- [150] ESIA, KEITA, KSIA, TSIA, and SIA. Assembly and packaging. Technical report, International Technology Roadmap for Semiconductors, 2005.
- [151] R. K. Hoffmann. *Handbook of Microwave Integrated Circuits*. Artech House, 1987.
- [152] IPC Association Connecting Electronic Industries. *IPC-0040: optoelectronic assembly and packaging technology*. Northbrook, IL, 2003.
- [153] R. Sturdivant. *Microwave and Millimeter-Wave Electronic Packaging*. Artech House, 2014.
- [154] A. R. Mickelson, N. R. Basavanahally, and Lee Y.-C., editors. *Optoelectronic Packaging*. John Wiley & Sons, 1997.
- [155] A. Leven, Y. Baeyens, W. Benz, W. Bronner, A. Uelsmann, V. Hurm, T. Jakobus, K. Kohler, M. Ludwig, R. Reuter, J. Rosenzweig, and M. Schlechtweg. GaAs-based pin-HEMT photoreceivers for optical microwave and millimeter-wave transmission at 1.55 μm . In *mt. Topical Meeting on Microwave Photonics (MWP'98), Princeton, NJ, USA, post deadline paper PDOO2*, 1998.
- [156] G.G. Mekonnen, H.-G. Bach, A. Beling, R. Kunkel, D. Schmidt, and W. Schlaak. 80-Gb/s InP-based waveguide-integrated photoreceiver. *Selected Topics in Quantum Electronics, IEEE Journal of*, 11(2):356–360, 2005.
- [157] G. Unterborsch, Th. Engel, D. Rohde, M. Rodhe, D. Bimberg, and G. Grosskopf. Hybrid and monolithic integrated optic/millimeter-wave converters for 60 GHz radio-over-fiber systems. In *Optical Fiber Communication Conference, 1999, and the International Conference on Integrated Optics and Optical Fiber Communication. OFC/IOOC '99. Technical Digest*, volume 1, pages 117–119 vol.1, 1999.

- [158] R. Brown. *RF Microwave Hybrids: Basics, Materials and Processes*. Kluwer Academic Publishers, 2003.
- [159] T.V. Muoi. Integrated fiber optic transmitters and receivers for SONET/ATM applications. In *Electronic Components and Technology Conference, 1995. Proceedings., 45th*, pages 1092–1095, 1995.
- [160] R. S. Khandpur. *Printed Circuit Boards: Design, Fabrication, and Assembly*. McGraw-Hill Professional Publishing, 2005.
- [161] D. Thompson, P. Kirby, J. Papapolymeron, and M.M. Tentzeris. W-band characterization of finite ground coplanar transmission lines on liquid crystal polymer (LCP) substrates. In *Electronic Components and Technology Conference, 2003. Proceedings. 53rd*, pages 1652–1655, 2003.
- [162] D. Thompson, M.M. Tentzeris, and J. Papapolymerou. Packaging of MMICs in multilayer LCP substrates. *Microwave and Wireless Components Letters, IEEE*, 16(7):410–412, 2006.
- [163] F. Bechtold. A comprehensive overview on today’s ceramic substrate technologies. In *Microelectronics and Packaging Conference, 2009. EMPC 2009. European*, pages 1–12, 2009.
- [164] P.G. Huggard, B.N. Ellison, P. Shen, N.J. Gomes, P.A. Davies, W.P. Shillue, A. Vaccari, and J.M. Payne. Efficient generation of guided millimeter-wave power by photomixing. *Photonics Technology Letters, IEEE*, 14(2):197–199, 2002.
- [165] C. Jiang, V. Krozer, H. G. Bach, G. G. Mekonnen, and T. K. Johansen. Broadband packaging of photodetectors for 100 Gb/s ethernet applications. *IEEE Transactions on Components, Packaging and Manufacturing Technology*, 3(3):422–429, March 2013.
- [166] C.Q. Scrantom and J.C. Lawson. LTCC technology: Where we are and where we’re going. II. In *Technologies for Wireless Applications, 1999. Digest. 1999 IEEE MTT-S Symposium on*, pages 193–200, 1999.
- [167] R. Rabe, W. A. Schiller, T. Hochheimer, C. Modes, and A. Kipka. Zero shrinkage of LTCC by self-constrained sintering. *International Journal of Applied Ceramic Technology*, 2(5):374–382, 2005.
- [168] J. Lee, K. Lim, S. Pinel, G. DeJean, R.L. Li, C.H. Lee, M.F. Davis, M. Tentzeris, and J. Laskar. Advanced System-On-Package (SOP) multilayer architectures for RF/wireless systems up to millimeter-wave frequency bands. In *Proceedings of the Asian Pacific Microwave Conference, Seoul, Korea*, 2003.
- [169] J.H. Lee. Highly integrated millimeter-wave passive components using 3-D LTCC System-on-Package (SOP) technology. *Microwave Theory and Techniques, IEEE Transactions on*, 53:2220–2229, 2005.

- [170] D. Lu and C.P. Wong, editors. *Materials for Advanced Packaging*. Springer Science+Business Media, LCC, 2009.
- [171] Copper foils for high frequency materials. White paper, Rogers Corporation, 2015.
- [172] C. F. Coombs, editor. *Printed Circuits Handbook*. McGraw-Hill, 2008.
- [173] N. Kinayman and M. I. Aksun. *Modern Microwave Circuits*. Artech House, 2005.
- [174] H. Legay, C. Sydlo, P. Hall, and O. Lafond. ACE Deliverable 2.1-D3 Report on facilities assessment. Technical report, Antenna Centre of Excellence, 2004.
- [175] O. Lafond and M. Himdi. Substrates characterisation (ϵ_r , $\tan \delta$) up to millimeter-wavelength. In *Proc. ANTEM*, pages 20–23, July 2004.
- [176] D. C. Thompson, O. Tantot, H. Jallageas, G. E. Ponchak, M. M. Tentzeris, and J. Papapolymerou. Characterization of liquid crystal polymer (LCP) material and transmission lines on LCP substrates from 30 to 110 GHz. *Microwave Theory and Techniques, IEEE Transactions on*, 52:1343–1352, 2004.
- [177] I. Maestrojuan, I. Palacios, I. Ederra, and R. Gonzalo. Use of low loss substrate for developing sub-millimeter-wave mixers. In *The 8th European Conference on Antennas and Propagation (EuCAP 2014)*, pages 2650–2652, 6-11 April 2014.
- [178] H. Huang, D. Liu, T. Guan, and X. Liu. Investigating scattering parameters measurements for 50 GHz highspeed printed circuit boards (PCBs). In *Microwave Measurement Conference (ARFTG), 2015 85th*, pages 1–3, 22-22 May 2015.
- [179] A. K. Dutta, N. K. Dutta, and M. Fujiwara, editors. *WDM Technologies - Active Optical Components*. Elsevier Science, 2002.
- [180] K. Chang, editor. *Encyclopedia of RF and Microwave Engineering*, volume I. Wiley-Interscience, 2005.
- [181] T. Kerms. Millimeter-wave performance of chip interconnects using wire bonding and flip chip. In *IEEE MTT-S International Microwave Symposium Digest*, pages 247–250, 1996.
- [182] S. Beer. Design and measurement of matched wire bond and flip chip interconnects for D-band system-in-package applications. In *IEEE MTT-S International Microwave Symposium Digest*, pages 1–4, June 2011.
- [183] C. Kaernfelt, P. Hallbjørner, H. Zirath, and A. Alping. High gain active microstrip antenna for 60-GHz WLAN/WPAN applications. *Microwave Theory and Techniques, IEEE Transactions on*, 54(6):2593–2603, June 2006.
- [184] F. Alimenti, P. Mezzanotte, L. Roselli, and R. Sorrentino. Multi-wire microstrip interconnections: A systematic analysis for the extraction of an equivalent circuit. In *ARFTG Conference Digest-Spring, 51st*, volume 33, pages 167–170, 1998.

- [185] A. Jentzsch and W. Heinrich. Theory and measurements of flip-chip interconnects for frequencies up to 100 GHz. *Microwave Theory and Techniques, IEEE Transactions on*, 49(5):871–878, 2001.
- [186] B K. Gilbert and G. W. Pan. MCM packaging for present and next generation high clock-rate digital and mixed-signal electronic system: Areas for development. *Microwave Theory and Techniques, IEEE Transactions on*, 45:1819–1835, 1997.
- [187] W. T. Khan, A. L. V. Lopez, A. Ulusoy, and J. Papapolymerou. Packaging a W-band integrated module with an optimized flip-chip interconnect on an organic substrate. *IEEE Transactions on Microwave Theory and Techniques*, 62(1):64–72, Jan. 2014.
- [188] W. Menzel and J. Kassner. Novel techniques for packaging and interconnects in mm-wave communication front-ends. In *Packaging and Interconnects at Microwave and mm-Wave Frequencies (Ref. No. 2000/083) IEE Seminar*, pages 1/1–118, 2000.
- [189] P. Dixon. Dampening cavity resonance using absorber material. *RF Design Magazine*, XX:16–19, 2004.
- [190] D.F. Williams. Damping of the resonant modes of a rectangular metal package [mmics]. *Microwave Theory and Techniques, IEEE Transactions on*, 37(1):253–256, 1989.
- [191] P. Dixon. Cavity-resonance dampening. *IEEE Microwave Magazine*, 6(2):74–84, 2005.
- [192] S.-J. Chung and H.-H. Chen. Resonant frequencies of a microwave package with vertical diaphragms attached to the top cover. *Microwave and Optical Technology Letters*, 8(6):300–302, 1995.
- [193] H.-H. Chen, C.-L. Wang, and S.-Y. Chung. A simple method for blocking parasitic modes in a waveguide-packaged microstrip-line circuit. *Microwave Theory and Techniques, IEEE Transactions on*, 46(12):2156–2159, 1998.
- [194] S. Jameson and E. Socher. A packaged 86–98 GHz CMOS transmitter for FMCW radar applications with 30 dBm of EIRP. In *2015 IEEE MTT-S International Microwave Symposium*, pages 1–4, 17-22 May 2015.
- [195] S. Radiom, H. Aliakbarian, P. Reynaert, G. Vandenbosch, and G. Gielen. A fully micromachined W-band waveguide-to-grounded coplanar waveguide transition for 91-113 GHz applications. In *European Microwave Conference (EuMC)*, 2010.
- [196] H. Aliakbarian, A. Enayati, G. A. E. Vandenbosch, and W. De Raedt. Novel low-cost end-wall microstrip-to-waveguide splitter transition. *Progress In Electromagnetics Research*, 75-96:75–96, 2010.
- [197] R. Glogowski, J. F. Zuercher, C. Peixeiro, and J. R. Mosig. Broadband Ka-band rectangular waveguide to substrate integrated waveguide transition. *Electronics Letters*, 49(9):602–604, 2013.

- [198] H. Aliakbarian, G. A. E. Vandenbosch, S. Radiom, G. Gielen, and P. J. Soh. Analysis of the doubled-slot end-wall waveguide to cpw transition. In *Antennas and Propagation (APSURSI), 2011 IEEE International Symposium on*, pages 1–4, 3-8 July 2011.
- [199] I. Flammia, A. Stoehr, C. C. Leonhardt, J. Honecker, and A. G. Steffan. 71-76 GHz grounded CPW to WR-12 transition for quasi-hermetic RoF wireless transmitter. *Electronics Letters*, 48(9):506–508, April 26 2012.
- [200] I. Flammia, T. Kleinfeld, M. Frei, A. Utreras-Rivera, and A. Stoehr. 71-76 GHz grounded-coplanar-waveguide-to-rectangular-waveguide transition with integrated planar bias tee for quasi-hermetic Radio-over-Fiber wireless transmitter. In *Microwave Integrated Circuits Conference (EuMIC), 2012 7th European*, pages 512–515, 29-30 Oct. 2012.
- [201] M. Frei and A. Utreras-Rivera. Design of a built-in bias-tee for an E-band photonic transmitter for Radio-over-Fiber applications by means of circuit-level and planar design tools. Project report, University of Duisburg-Essen. Duisburg, Germany, 2012.
- [202] T. Kleinfeld. Full-wave simulation and optimization of an E-band photonic transmitter with rectangular waveguide output and featuring an integrated bias-tee for Radio-over-Fiber applications. Project report, University of Duisburg-Essen. Duisburg, Germany, 2012.
- [203] 50 GHz Photodetector - XPDV21x0R. Data sheet, Finisar Corporation. https://www.finisar.com/sites/default/files/downloads/xpdv21x0ra_70_ghz_photodetector_product_specification_rev_a1.pdf, 2014.
- [204] I. Flammia, S. Babel, C. C. Leonhardt, J. Honecker, A. G. Steffan, and A. Stoehr. Quasi-hermetic photodiode module featuring a WR12 output for 71-76 GHz Radio-over-Fibre applications. In *Microwave Photonics (MWP), 2012 International Topical Meeting on*, pages 261–264, 11-14 Sept. 2012.
- [205] S. Babel, I. Flammia, A. Stoehr, J. Montero de Paz, L. E. Garcia-Munoz, D. Segovia-Vargas, G. Carpintero, A. Lisauskas, and O. Cojocari. Compact transmitter and receiver modules for E-band wireless links. In *Optical Fiber Communication Conference and Exposition and the National Fiber Optic Engineers Conference (OFC/NFOEC), 2013*, pages 1–3, 17-21 March 2013.
- [206] V. Rymanov, T. Tekin, and A. Stoehr. Double mushroom 1.55- μ m waveguide photodetectors for integrated E-band (60-90 GHz) wireless transmitter modules. volume 8259, pages 82590E–82590E–7, 2012.
- [207] U. H. P. Fischer. *Optoelectronic Packaging*. VDE Verlag GmbH, 2002.
- [208] M. Steeg. Design, development and validation of e-band (71-76 ghz) photonic transmitters for radio-over-fiber applications. Master’s thesis, University of Duisburg-Essen. Duisburg, Germany, 2012.

- [209] I. Flammia, M. Steeg, A. Jankowski, S. Babel, V. Rymanov, and A. Stoehr. Photonic transmitters with rectangular waveguide output for E-Band Radio-over-Fibre communication systems. In *Antennas, Wireless and Electromagnetics, 1st IET Colloquium on*, pages 1–19, 29-29 May 2013.
- [210] GaAs HEMT MMIC Medium Power Amplifier, 71-76 GHz - HMC-AUH318. Data sheet, Analog Devices. <http://www.analog.com/media/en/technical-documentation/data-sheets/hmc-auh318.pdf>, 2013.
- [211] GaAs HEMT LOW NOISE AMPLIFIER, 71-86 GHz - HMC-ALH508. Data sheet, Analog Devices. <http://www.analog.com/media/en/technical-documentation/data-sheets/hmc-alh508.pdf>, 2009.
- [212] B. Khani, V. Rymanov, I. Flammia, M. Miech, and A. Stoehr. Planar bias-tee circuit using single coupled-line approach for 71-76 GHz photonic transmitters. In *German Microwave Conference (GeMIC), 2015*, pages 276–279, 16-18 March 2015.
- [213] B. Khani, V. Rymanov, I. Flammia, and A. Stoehr. Planar 71-76 GHz laminate integration platform for connecting millimeter wave photodiodes to WR-12 waveguides. In *2015 17th International Conference on Transparent Optical Networks (ICTON)*, pages 1–4, 5-9 July 2015.
- [214] B. Khani, V. Rymanov, S. Duelme, I. Flammia, and A. Stoehr. Planar E-band (71-76 GHz) platforms for integrating millimeter wave photodiodes with WR-12 waveguides. *Periodica Polytechnica Electrical Engineering and Computer Science*, 60(1):38–43, 2016.
- [215] I. Flammia, S. Babel, C. C. Leonhardt, J. Honecker, J. Steffan, and A. Stoehr. Novel quasi-hermetic photodiode module featuring an E-band rectangular waveguide (WR-12) output. *Photonics Technology Letters, IEEE*, 25(3):217–219, Feb.1, 2013.
- [216] A. Stoehr, O. Cojucari, F. van Dijk, G. Carpintero, T. Tekin, S. Formont, I. Flammia, V. Rymanov, B. Khani, and R. Chuenchom. Robust 71-76 GHz radio-over-fiber wireless link with high-dynamic range photonic assisted transmitter and laser phase-noise insensitive SBD receiver. In *Optical Fiber Communication Conference, OSA Technical Digest (online)*, page M2D.4, San Francisco, California, 2014. Optical Society of America.
- [217] B. Khani, V. Rymanov, J. Honecker, A. G. Steffan, and A. Stoehr. Compact rectangular-waveguide (WR-12) transition for coherent photonic mixers. In *2016 Global Symposium on Millimeter Waves (GSMM) & ESA Workshop on Millimetre-Wave Technology and Applications*, pages 1–3, 6-8 June 2016.
- [218] I. Flammia, B. Khani, and A. Stoehr. Substrate integrated waveguide integration platform for 60 GHz indoor photonic transmitter. In *German Microwave Conference (GeMIC), 2014*, pages 1–4, 10-12 March 2014.

- [219] S. Lee, S. Jung, and H.-Y. Lee. Ultra-wideband CPW-to-substrate integrated waveguide transition using an elevated-CPW section. *Microwave and Wireless Components Letters, IEEE*, 18(11):746–748, 2008.
- [220] X.-P. Chen and K. Wu. Low-loss ultra-wideband transition between conductor-backed coplanar waveguide and substrate integrated waveguide. In *Microwave Symposium Digest, 2009. MTT '09. IEEE MTT-S International*, pages 349–352, 2009.
- [221] E. Mortazy, F. Xu, M. Meunier, and K. Wu. Millimeter-wave transition of coplanar line to substrate-integrated LiNbO₃ waveguide for traveling-wave electro-optical modulator. *Microwave and Optical Technology Letters*, 51(4):1105–1107, 2009.
- [222] F. Taringou and J. Bornemann. New substrate-integrated to coplanar waveguide transition. In *Microwave Conference (EuMC), 2011 41st European*, pages 428–431, 2011.
- [223] S. Lin, S. Yang, A. E. Fathy, and A. Elsherbini. Development of a novel UWB vivaldi antenna array using SIW technology. *Progress In Electromagnetics Research*, Vol. 90:369–384, 2009.
- [224] T.-Y. Huang, T.-M. Shen, and R.-B. Wu. Design and modeling of microstrip line to substrate integrated waveguide transitions. In *Passive Microwave Components and Antennas*. InTech Open, 2010.
- [225] M. Abdolhamidi, A. Enayati, M. Shahabadi, and R. Faraji-Dana. Wideband single-layer DC-decoupled substrate integrated waveguide (SIW) - to - microstrip transition using an interdigital configuration. In *Microwave Conference, 2007. APMC 2007. Asia-Pacific*, pages 1–4, 2007.
- [226] I. Flammia, B. Khani, and A. Stoehr. Substrate integrated waveguide technology for the development of 60 GHz photonic transmitters. In *Antennas, Wireless and Electromagnetics, 1st IET Colloquium on*, pages 1–19, 29-29 May 2013.
- [227] I. Flammia, B. Khani, S. Arafat, and A. Stoehr. 60 GHz grounded-coplanar-waveguide-to-substrate-integrated-waveguide transition for RoF transmitters. *Electronics Letters*, 50(1):34–35, January 2 2014.
- [228] W. Che, B. Fu, P. Yao, Y. L. Chow, and E. K. N. Yung. A compact substrate integrated waveguide H-plane horn antenna with dielectric arc lens. *International Journal of RF and Microwave Computer-Aided Engineering*, 17(5):473–479, 2007.
- [229] M. Esquiús-Morote, B. Fuchs, and J.R. Mosig. A new type of printed Ku-band SIW horn antenna with enhanced performances. In *Antennas and Propagation (ISAP), 2012 International Symposium on*, pages 223–226, 2012.
- [230] M. Esquiús-Morote. *Horn Antennas and Dual-Polarized Circuits in Substrate Integrated Waveguide (SIW) Technology*. PhD thesis, École Polytechnique Fédérale de Lausanne, Lausanne, Switzerland, 2014.

- [231] P. Benedek and P. Silvester. Capacitance of parallel rectangular plates separated by a dielectric sheet. *Microwave Theory and Techniques, IEEE Transactions on*, 20(8):504–510, 1972.
- [232] M. Esquius-Morote, Zuercher J. F. Fuchs, B. and, and J. R. Mosig. A printed transition for matching improvement of SIW horn antennas. *IEEE Transactions on Antennas and Propagation*, 61(4):1923–1930, April 2013.
- [233] I. Flammia, B. Khani, and A. Stoehr. Substrate integrated waveguide antenna for 60 GHz Radio-over-Fiber transmitter. In *Infrared, Millimeter, and Terahertz Waves (IRMMW-THz), 2013 38th International Conference on*, pages 1–2, 1-6 Sept. 2013.
- [234] D. Liu, B. Gaucher, U. Pfeiffer, and J. Grzyb, editors. *Advanced Millimeter-wave Technologies*. John Wiley & Sons, 2009.
- [235] M. Steeg, B. Khani, V. Rymanov, and A. Stoehr. Novel 50-70 GHz compact PCB leaky-wave antenna with high broadside efficiency and low return loss. In *Infrared, Millimeter, and Terahertz waves (IRMMW-THz), 2016 41st International Conference on*, 2016.
- [236] N. Ghassemi, J. Gauthier, and K. Wu. Low-cost E-band receiver front-end development for gigabyte point-to-point wireless communications. In *Microwave Conference (EuMC), 2013 European*, pages 1011–1014, 6-10 Oct. 2013.
- [237] M. Han, G. Q. Zhao, J. C. Mou, P. Zheng, P. Zhou, N. Yang, W. H. Yu, H. J. Sun, and X. Lv. A W-band substrate-integrated waveguide band-pass filter. In *Microwave and Millimeter Wave Technology (ICMMT), 2012 International Conference on*, volume 2, pages 1–3, 5-8 May 2012.
- [238] N. Ghassemi and K. Wu. Planar high-gain dielectric-loaded antipodal linearly tapered slot antenna for E- and W-band gigabyte point-to-point wireless services. *IEEE Transactions on Antennas and Propagation*, 61(4):1747–1755, April 2013.
- [239] A. K. Ganguly. *Optoelectronic Devices and Circuits: Theory and Applications*. Alpha Science Intl Ltd, 2007.
- [240] D. Kajfez and B. S. Vidula. Design equations for symmetric microstrip DC blocks. *IEEE Transactions on Microwave Theory and Techniques*, 9:974 – 981, 1980.
- [241] R.K. Mongia, I.J. Bahl, P. Bhartia, and J. Hong. *RF and Microwave Coupled-Line Circuits*. Artech House, 2007.
- [242] Y. Huang and K. Boyle. *Antennas from Theory to Practice*. John Wiley & Sons, 2008.
- [243] C. Capps. Near field or far field?, 2001. EDN Network.
- [244] Southwest Microwave. *The Design & Test of Broadband Launches up to 50 GHz on Thin & Thick Substrates*, 2011.

BIBLIOGRAPHY

- [245] Agilent Technologies. *Product Note 8510-8A - Agilent Network Analysis - Applying the 8510 TRL Calibration for Non-Coaxial Measurements.*

Appendices

Appendix A

Electromagnetic Theory

This appendix integrates the fundamental concepts of electromagnetism introduced in chapter 2.

A.1 Maxwell's Equations

The behavior of electromagnetic fields, independently of the frequency (or wavelength) range of interest, can be fully described by an elegant set of equations, namely the *Maxwell's equations*.

For the sake of simplicity, a linear, isotropic, homogeneous and non-dispersive medium will be considered in the following¹, unless otherwise stated. Assuming a harmonic time variation for the EM fields, it is possible to relate the instantaneous fields to their phasor form, eliminating the explicit time dependence from the related equations. For the electric field, expressed in Cartesian coordinates, the following relations apply (similar expressions can be derived for all other time dependent quantities considered in the following):

$$\begin{aligned}\tilde{\mathbf{E}}(x, y, z, t) &\stackrel{\text{def}}{=} \Re\{\mathbf{E}(x, y, z) e^{(j\omega t + \phi)}\} = \\ &= \mathbf{E}(x, y, z) \cos(\omega t + \phi) = (E_x \hat{\mathbf{x}} + E_y \hat{\mathbf{y}} + E_z \hat{\mathbf{z}}) \cos(\omega t + \phi)\end{aligned}\tag{A.1.1a}$$

where E_x, E_y and E_z are the amplitudes of the electric field in the three coordinates identified by the versors $\hat{\mathbf{x}}$, $\hat{\mathbf{y}}$ and $\hat{\mathbf{z}}$ respectively, ω is the angular frequency, t represents the time, ϕ is the phase reference at $t = 0$, and \mathbf{E} is the phasor corresponding to the time-dependent quantity $\tilde{\mathbf{E}}$. Using the phasor representation, it is possible to express the Maxwell's equations in their convenient harmonic-regime differential form:

$$\nabla \times \mathbf{E} = -j\omega \mathbf{B} \tag{A.1.2a}$$

$$\nabla \times \mathbf{H} = j\omega \mathbf{D} + \mathbf{J} \tag{A.1.2b}$$

$$\nabla \cdot \mathbf{D} = \rho \tag{A.1.2c}$$

$$\nabla \cdot \mathbf{B} = 0 \tag{A.1.2d}$$

¹For materials that do not satisfy these properties, more complex mathematical notation in form of tensor matrices is required. For instance, for dispersive materials, the constitutive relation would require a frequency-dependent dielectric constant, while anisotropy would require a formulation in form of tensor matrices [58].

where \mathbf{E} (V/m) is the electric field, \mathbf{B} (Wb/m²) is the magnetic induction, \mathbf{H} (A/m) is the magnetic field, \mathbf{D} (C/m²) is the electric displacement, \mathbf{J} (A/m²) is the current density, and ρ (C/m³) is the electric charge density of the medium.

Maxwell's equations are complemented by the *constitutive relations*, (A.1.3)-(A.1.5), and the *continuity equation* (A.1.6):

$$\begin{aligned}\mathbf{B} &= \mu_0(\mathbf{H} + \mathbf{M}) = \mu_0(1 + \chi_m)\mathbf{H} = \mu_r\mu_r\mathbf{H} = \mu\mathbf{H} = \\ &\stackrel{\text{def}}{=} (\mu' - j\mu'')\mathbf{H}\end{aligned}\tag{A.1.3}$$

$$\begin{aligned}\mathbf{D} &= \varepsilon_0\mathbf{E} + \mathbf{P} = \varepsilon_0(1 + \chi_e)\mathbf{E} = \varepsilon_0\varepsilon_r\mathbf{E} = \varepsilon\mathbf{E} = \\ &\stackrel{\text{def}}{=} (\varepsilon' - j\varepsilon'')\mathbf{E}\end{aligned}\tag{A.1.4}$$

$$\mathbf{J} = \sigma\mathbf{E}\tag{A.1.5}$$

$$\nabla \cdot \mathbf{J} = -j\omega\rho\tag{A.1.6}$$

where \mathbf{M} (H/m) is the magnetic polarization vector, $\mu_0 = 4\pi \cdot 10^{-7}$ H/m is the vacuum's magnetic permeability, χ_m is the magnetic susceptibility, μ_r is the magnetic relative permeability, $\mu = \mu' - j\mu''$ is the magnetic permeability, \mathbf{P} (C/m²) is the electric polarization vector, χ_e is the electric susceptibility, $\varepsilon_0 \approx 8.854 \cdot 10^{-12}$ F/m is the vacuum's dielectric permittivity electric, $\varepsilon = \varepsilon' - j\varepsilon''$ is the dielectric permittivity, ε_r is the relative dielectric permittivity, and σ (S/m) is the electrical conductivity.

The imaginary parts of μ and ε account for the loss in the material due to damping effects in the oscillation of the dipoles. Additional loss can arise from the finite conductivity σ , whose effect can be taken into account by expanding (A.1.2b) using (A.1.4) and (A.1.5):

$$\begin{aligned}\nabla \times \mathbf{H} &= j\omega\varepsilon\mathbf{E} = j\omega(\varepsilon' - j\varepsilon'')\mathbf{E} + \sigma\mathbf{E} = \\ &= j\omega[\varepsilon' - j(\varepsilon'' + \frac{\sigma}{\omega})]\mathbf{E} = \\ &= j\omega\varepsilon'\mathbf{E} + (\omega\varepsilon'' + \sigma)\mathbf{E}\end{aligned}\tag{A.1.7}$$

Electromagnetic loss is an important factor to be considered in microwave and mm-wave applications. A practical quantity to describe the loss in a medium, the *loss tangent*, can be conveniently defined as follows:

$$\tan \delta \stackrel{\text{def}}{=} \frac{\omega\varepsilon'' + \sigma}{\omega\varepsilon'}\tag{A.1.8}$$

It is important to notice that the contribution of dipole oscillation damping and conductivity cannot be distinguished by external measurements of power dissipation, therefore the dielectric permittivity is often redefined as:

$$\varepsilon \stackrel{\text{def}}{=} \varepsilon'(1 - j \tan \delta) = \varepsilon_r\varepsilon_0(1 - j \tan \delta)\tag{A.1.9}$$

where $\varepsilon_r = \varepsilon'_r$ (relative permittivity) is now a real number. From (A.1.8) and (A.1.9) it can be seen that the $\tan \delta$ expresses the ratio of the the imaginary and real parts of ε , as shown in Fig. A.1:

$$\tan \delta = \frac{\varepsilon''}{\varepsilon'}\tag{A.1.10}$$

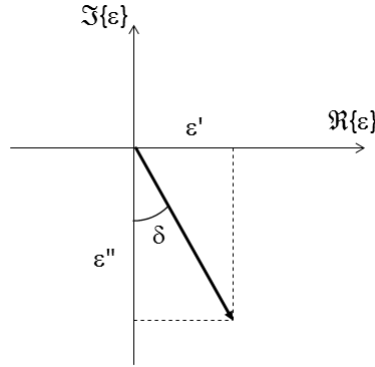


Figure A.1: Loss tangent ($\tan \delta$)

The loss tangent is an important parameter for substrates commonly used for high-frequency applications and is usually included in the data sheets² by the manufacturers, together with the relative permittivity ε_r . The complex dielectric permittivity can thus be calculated using equation (A.1.9). The effect of these parameters on EM waves and signals traveling in a transmission line are analyzed in section 2.1.1.

A.2 Electromagnetic Waves

Electromagnetic signals propagate in form of waves obtained as solution of the *wave equations*. In order to derive a possible expression for an EM wave, it is useful to consider the Maxwell's equations in a lossless ($\sigma = 0$, $\varepsilon'' = 0$ and $\mu'' = 0$), and source-free medium ($\rho = 0$ and $\mathbf{J} = 0$):

$$\nabla \times \mathbf{E} = -j\omega\mu\mathbf{H} \quad (\text{A.2.1a})$$

$$\nabla \times \mathbf{H} = j\omega\varepsilon\mathbf{E} \quad (\text{A.2.1b})$$

$$\nabla \cdot \mathbf{E} = 0 \quad (\text{A.2.1c})$$

$$\nabla \cdot \mathbf{B} = 0 \quad (\text{A.2.1d})$$

By taking the curl of (A.2.1a) and using (A.2.1b) it is possible to derive:

$$\begin{aligned} \nabla \times \nabla \times \mathbf{E} &= -j\omega\mu\nabla \times \mathbf{H} \implies \\ &\implies \nabla^2 \mathbf{E} = -j\omega\mu j\omega\varepsilon\mathbf{E} \implies \\ &\implies \nabla^2 \mathbf{E} = -\omega^2\mu\varepsilon\mathbf{E} \end{aligned} \quad (\text{A.2.2})$$

where the vector identity $\nabla \times \nabla \times \mathbf{E} = \nabla(\nabla \cdot \mathbf{E}) - \nabla^2 \mathbf{E}$ has been used. Defining the *wave number* $k = \omega\sqrt{\mu\varepsilon}$ (m^{-1}), it is possible to write the *Helmoltz equation* for the electric field

$$\nabla^2 \mathbf{E} + k^2 \mathbf{E} = 0 \quad (\text{A.2.3})$$

²Some manufacturers provide a *dissipation factor* (DF) to characterize their substrates. It is defined by modifying the formula of the loss tangent neglecting the role of atomic oscillation (i.e. ε''), thus yielding: $DF \stackrel{\text{def}}{=} \sigma/(\omega\varepsilon')$ [153]. This approximation is acceptable at lower frequencies and for most of the commonly used substrate materials, although substantial differences might arise in the mm-wave range.

and its equivalent for the magnetic field:

$$\nabla^2 \mathbf{H} + k^2 \mathbf{H} = 0 \quad (\text{A.2.4})$$

Assuming an $(x-y-z)$ Cartesian coordinates system, equation (A.2.3) can be broken down into three scalar equations, each related to the i -th scalar component of the field

$$\nabla^2 \mathbf{E}_i + k^2 \mathbf{E}_i = 0 \quad (\text{A.2.5})$$

Solutions of physics relevance to (A.2.5) can be found using the *method of variables separation* [56] and they can be written in the following form:

$$\mathbf{E}(x, y, z) = \mathbf{E}_0 e^{-j\mathbf{k} \cdot \mathbf{r}} = \mathbf{E}_0 e^{-j\boldsymbol{\beta} \cdot \mathbf{r}} e^{-\boldsymbol{\alpha} \cdot \mathbf{r}} \quad (\text{A.2.6})$$

where $\mathbf{r} = x\hat{\mathbf{x}} + y\hat{\mathbf{y}} + z\hat{\mathbf{z}}$ is the *position vector*, and the *propagation vector* $\mathbf{k} \stackrel{\text{def}}{=} \boldsymbol{\beta} - j\boldsymbol{\alpha} = k_x\hat{\mathbf{x}} + k_y\hat{\mathbf{y}} + k_z\hat{\mathbf{z}}$ has to satisfy the *separability condition*

$$\mathbf{k} \cdot \mathbf{k} = k_x^2 + k_y^2 + k_z^2 = \omega^2 \mu \varepsilon \quad (\text{A.2.7})$$

where $\boldsymbol{\alpha}$ and $\boldsymbol{\beta}$ are the *attenuation vector*³ and the *phase vector*, respectively. From equation A.2.6, the magnetic field can be expressed as:

$$\mathbf{H}(x, y, z) = \frac{1}{\omega \mu} \mathbf{k} \times \mathbf{E}_0 e^{-j\mathbf{k} \cdot \mathbf{r}} = \mathbf{H}_0 e^{-j\mathbf{k} \cdot \mathbf{r}} = \mathbf{H}_0 e^{-j\boldsymbol{\beta} \cdot \mathbf{r}} e^{-\boldsymbol{\alpha} \cdot \mathbf{r}} \quad (\text{A.2.8})$$

and the ratio $\eta = E_0/H_0 = \sqrt{\mu/\varepsilon}$ is defined as *intrinsic impedance* of the propagation medium (for the vacuum: $\eta_0 = \sqrt{\mu_0/\varepsilon_0} \approx 377 \, \Omega$). Equations A.2.6 and A.2.8 describe an important solution called *plane wave* (because its constant-phase surfaces are planes identified by $\boldsymbol{\beta} \cdot \mathbf{r} = \text{constant}$) and can be used to describe the EM wave emitted by any source at a point sufficiently distant in space.

A.3 Guided Electromagnetic Propagation

Transmission lines are structures used to carry and guide electromagnetic signals. In order to describe how the fields propagate within them, we can model them as generic cylindrical structures, with a constant cross-section along the linear axial coordinate of propagation (the z axis in the Cartesian coordinates system shown in Fig. A.2).

Assuming a propagation in the positive z -direction ($\boldsymbol{\beta} = \beta\hat{\mathbf{z}}$), we can express the fields in their transverse and axial components as [56]:

$$\mathbf{E} = \mathbf{E}_t + \mathbf{E}_z \quad (\text{A.3.1})$$

$$\mathbf{E} = \mathbf{E}_t + \mathbf{E}_z \quad (\text{A.3.2})$$

³The reader should be aware that alternative definitions of the *attenuation constant* are given by different authors in different fields. In particular, in optical applications it is common to define a *power attenuation constant* $\alpha_p = 1/L \cdot \ln(P_{\text{in}}/P_{\text{out}})$, with $P_{\text{in/out}}$ being the power at two given *input* and *output* points separated by a distance L [239]. Therefore the following relations subsist: $\alpha = \alpha_p/2$ and $\mathbf{k} = \boldsymbol{\beta} - j\boldsymbol{\alpha}_p/2$. More information concerning loss in optical fibers is given in Section 2.1.7.

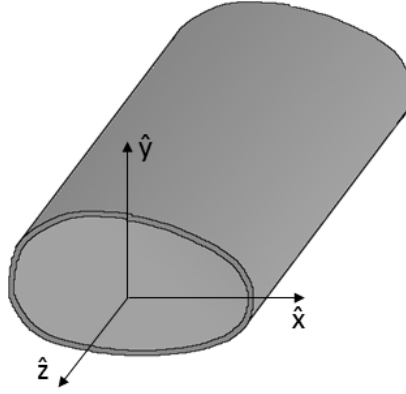


Figure A.2: Transmission line concept.

and the separability condition (A.2.7) becomes:

$$k^2 = k_t^2 + k_z^2 = \omega^2 \mu \epsilon \quad (\text{A.3.3})$$

By considering the Helmholtz equations A.2.3 and A.2.4, it is possible to derive special solutions, which take into account particular properties of the fields, as described in the following.

Transverse Electromagnetic (TEM) Waves A transverse electromagnetic wave is characterized by the fact that $\mathbf{E}_z = \mathbf{H}_z = 0$, i.e. the electromagnetic field has no components in the direction of propagation. This leads to the condition that

$$k_t^2 = 0 \implies k_z = k = \omega \sqrt{\mu \epsilon} \quad (\text{A.3.4})$$

and the wave impedance can be expressed as:

$$\eta_{\text{TEM}} = \eta \quad (\text{A.3.5})$$

where η is the intrinsic impedance of the propagation medium. Equations A.3.4 and A.3.5 show that a TEM wave is essentially equivalent to a plane wave propagating in the z -direction and there is no cut-off frequency, i.e. a TEM wave can propagate for any frequency $f \geq 0$. The relationship between electric and magnetic field is given by:

$$\mathbf{E}_{\text{T}} = -\eta_{\text{TEM}} \mathbf{H}_{\text{T}} \quad (\text{A.3.6})$$

Transverse Electric (TE) Waves A transverse electric wave has no component of the electric field in the direction of propagation, i.e. $\mathbf{E}_z = 0$, while no assumption is made for the magnetic field. The fields for such a wave can be described as [57]:

$$\mathbf{H}_{\text{T}} = -\frac{j k_z}{k^2 - k_z^2} \nabla_{\text{T}} H_z \quad (\text{A.3.7})$$

$$\mathbf{E}_{\text{T}} = \frac{j \omega \mu}{k^2 - k_z^2} \hat{\mathbf{z}} \times \nabla_{\text{T}} H_z = -\frac{\omega \mu}{k_z} \hat{\mathbf{z}} \times \mathbf{H}_{\text{T}} \quad (\text{A.3.8})$$

and the wave impedance can be defined as:

$$\eta_{\text{TE}} = \frac{\omega\mu}{k_z} = \frac{\omega\sqrt{\varepsilon\mu}}{k_z} \sqrt{\frac{\mu}{\varepsilon}} = \frac{k}{k_z} \eta \quad (\text{A.3.9})$$

For TE waves, the propagation constant can be calculated from:

$$k_z = \sqrt{k^2 - k_t^2} = \sqrt{\omega^2\mu\varepsilon - k_t^2} \quad (\text{A.3.10})$$

where k_t has to be derived by solving the *eigenvalue* problem of the transverse boundary condition due to the actual configuration of the guiding structure. It can be noticed that k_z can only be a real number (which implies an actual propagating wave) if $\omega^2\mu\varepsilon - k_t^2 > 0$. This condition identifies the cut-off frequency f_c , starting from which propagation in the guiding line is actually allowed, as:

$$2\pi f_c = \omega_c \stackrel{\text{def}}{=} \frac{k_t}{\mu\varepsilon} \quad (\text{A.3.11})$$

Equations A.3.10 and A.3.11 can be combined to express

$$k_z = \sqrt{\omega^2\mu\varepsilon - \omega_c^2\mu\varepsilon} = \omega \sqrt{1 - \frac{\omega_c^2}{\omega^2}} = \omega \sqrt{1 - \frac{f_c^2}{f^2}} \quad (\text{A.3.12})$$

which shows that TE solutions are dispersive, i.e. their propagation characteristics depend on the operation frequency. This also affects the guided-wave wavelength λ_g , which can be computed as:

$$\lambda_g = \frac{2\pi}{k_z} = \frac{1}{\sqrt{1 - \left(\frac{f_c}{f}\right)^2}} = \frac{1}{\sqrt{1 - \left(\frac{\lambda_0}{\lambda_c}\right)^2}} \quad (\text{A.3.13})$$

with $\lambda_0 = 2\pi/\beta_0 = 1/(f\sqrt{\mu\varepsilon})$ being the free-space wavelength and $\lambda_c = 1/(f_c\sqrt{\mu\varepsilon})$ being the wavelength at the cut-off frequency.

Transverse Magnetic (TM) Waves A transverse magnetic wave has no component of the magnetic field in the direction of propagation, i.e. $\mathbf{H}_z = 0$, while no assumption is made for the electric field. The fields of TM waves can be expressed as [57]:

$$\mathbf{E}_T = -\frac{jk_z}{k^2 - k_z^2} \nabla_T E_T \quad (\text{A.3.14})$$

$$\mathbf{H}_T = \frac{j\omega\mu}{k^2 - k_z^2} \hat{\mathbf{z}} \times \nabla_T H_z = \frac{\omega\varepsilon}{k_z} \hat{\mathbf{z}} \times \mathbf{E}_T \quad (\text{A.3.15})$$

and the wave impedance can be defined as:

$$\eta_{\text{TM}} = \frac{k_z}{\omega\varepsilon} = \frac{k_z}{\omega\sqrt{\varepsilon\mu}} \sqrt{\frac{\mu}{\varepsilon}} = \frac{k_z}{k} \eta \quad (\text{A.3.16})$$

For TM modes, considerations on the propagation constant, cut-off frequency and dispersion apply, which are equivalent to the ones derived for the TE modes.

TE, TM and TEM modes can be used to represent and analyze the behaviour of common transmission-line structures.

A.4 Microstrip Coupled Lines

Coupled lines (CLs) are useful elements used to design filters, implement DC-block functionalities and even achieve impedance matching in high-frequency engineering. They are based on the principle that closely spaced lines (schematically represented as transmission lines in Fig. A.3) exchange EM energy without the need for ohmic contact. Their behavior can be examined considering the even and odd-modes excitation [56]. In the first case, due the symmetrical excitation, no current will flow between the two strips, and therefore an *even-mode capacitance* C_e can be determined, allowing to define an *even-mode characteristic impedance* $Z_{0e} = \frac{1}{v_e C_e}$. In the second case, the opposite excitation of the two strips establishes an electrical field across the two lines, with a voltage null in the middle: therefore an *odd-mode capacitance* C_o can be defined as allowing to define an *odd-mode characteristic impedance* $Z_{0o} = \frac{1}{v_o C_o}$. The characteristics of a CL section can be calculated using formulas available in literature (e.g. in [61]) and are implemented in many CAD programs.

An interesting feature of CLs is that they can provide impedance transformation (i.e. matching between *input* and *output impedances*) if properly designed. Considering the circuit shown in Fig. A.3, the transmission coefficient from the *generator* with impedance Z_{in} and the load with impedance Z_{out} can be expressed as [240]:

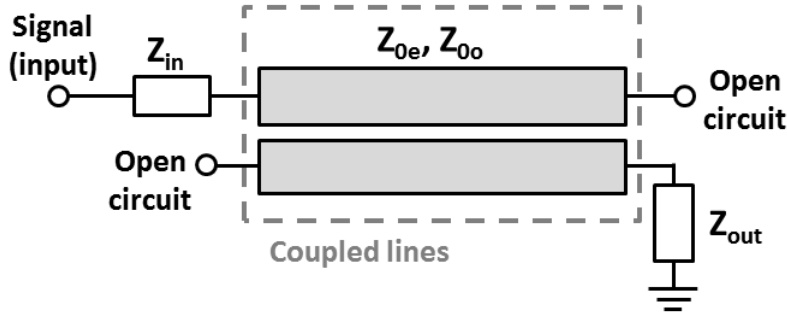


Figure A.3: Coupled-lines transformer.

$$S_{21} = \frac{2(Z_{0e} \csc \theta_e - Z_{0o} \csc \theta_o)}{N} \quad (A.4.1)$$

$$N = \left(\frac{Z_{out}}{Z_{in}} + \frac{Z_{in}}{Z_{out}} \right) (Z_{0e} \cot \theta_e + Z_{0o} \cot \theta_o) + j \left[\frac{Z_{0e}^2 + Z_{0o}^2}{2\sqrt{Z_{in}Z_{out}}} - \frac{Z_{0e}Z_{0o}}{\sqrt{Z_{in}Z_{out}}} (\csc \theta_e \csc \theta_o + \cot \theta_e \cot \theta_o) + 2\sqrt{Z_{in}Z_{out}} \right] \quad (A.4.2)$$

where $\theta_e = 2\pi/\lambda_0 L \sqrt{\epsilon_{r,e}}$ and $\theta_o = 2\pi/\lambda_0 L \sqrt{\epsilon_{r,o}}$ are the electrical lengths of the CL section corresponding to the even and odd-mode respectively, with $\epsilon_{r,e}$ and $\epsilon_{r,o}$ representing the effective dielectric constants of the two modes and λ_0 being the free-space wavelength. Choosing $\theta_e \approx \theta_o = \pi/2$ and assuming a loss-less configuration, by imposing that $|S_{21}| = 1$, it can be shown that the following condition must be satisfied in order to guarantee the maximum power transfer from the generator (Z_{in}) to the load (Z_{out}) [241]:

$$Z_{0e} = Z_{0o} + 2\sqrt{Z_{in}Z_{out}} \quad (\text{A.4.3})$$

Equation A.4.3 represents a powerful expression for the design of CL impedance transformers, putting in direct relation the even and odd impedances of the CL with the input and output impedances connected to its terminals.

A.5 Antennas

Antennas are structures that are specifically designed to radiate (or collect) an electromagnetic signal (see Fig. A.4).

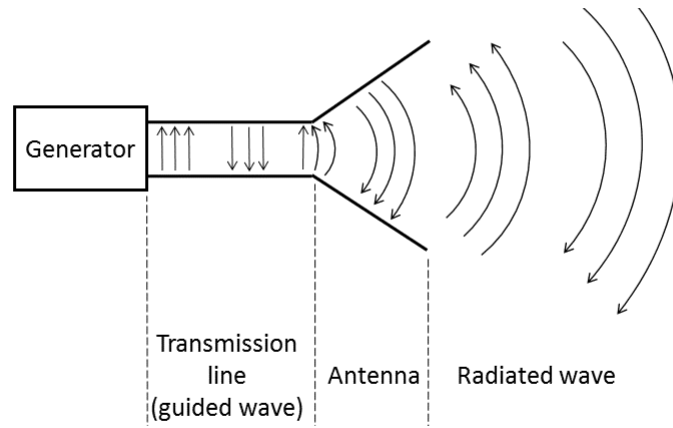


Figure A.4: Antenna concept. Adapted from [132].

Antennas are described by a set of useful parameters, that will be discussed in the following. At first, it is useful to establish different regions (whose limits are generally dependent on the operating frequency or wavelength) in the space surrounding the antenna, in which the emitted EM field assumes different characteristics. A traditional and simplified characterization⁴ comprises [132]:

- *Reactive near-field region*: the closest area surrounding the antenna, where the fields have a reactive behavior. It is generally identified assuming as external limit the distance $R = 0.62\sqrt{D^3/\lambda}$, where D is the largest dimension of the antenna and λ is the wavelength under consideration.
- *Radiative near-field region* or *Fresnel region*: is the next identifiable region, in which the fields assume a radiative behavior but their angular field distribution is dependant on the distance from the antenna and its radial component might be non-negligible. Its external boundary is generally assumed to be given by $R = 2D^2/\lambda$.
- *Far-field region* or *Fraunhofer region*: this region starts at the same limit defining the external boundary of the Fresnel region, and is characterized by the fact that

⁴The interested reader can find a more detailed treatise and accurate delimitation of the three regions in [242, 243].

the radiated fields are essentially independent of the distance from the antenna and their radial component is negligible, thus allowing a description of the EM field in terms of planar wave:

$$\mathbf{E}(r, \theta, \phi) = \mathbf{E}(\theta, \phi) \frac{e^{-jkr}}{r} \quad (\text{A.5.1})$$

The Fraunhofer region is often the most important region in communication applications and, if not otherwise stated, any other considerations in this thesis related to antennas will assume an observation point located in this region.

A fundamental concept used to describe the behavior of an antenna is the *radiation pattern*⁵, which is a function of the spatial coordinates used to represent the generated fields or the emitted power of the antenna in a given direction. It is possible to define *field patterns* as well as *power pattern*, the latter simply being a measure, as a function of direction, of the average power density radiated by the antenna [132], which can be expressed as the average Poynting vector $\mathbf{S}_{\text{av}} \stackrel{\text{def}}{=} \frac{1}{2} \Re\{\mathbf{E} \times \mathbf{H}^*\}$, with \mathbf{H}^* denoting the complex conjugate of \mathbf{H} . The total radiated power can be calculated integrating the Poynting vector over an entire close surface enclosing the antenna as:

$$\mathbf{P}_{\text{rad}} = \oint\oint_s \mathbf{S} \cdot d\mathbf{s} = \frac{1}{2} \oint\oint_s \Re\{\mathbf{E} \times \mathbf{H}^*\} \cdot d\mathbf{s} \quad (\text{A.5.2})$$

It is useful to define the *radiation intensity* U as the power radiated per unit solid angle, i.e.:

$$U = r^2 S \quad (\text{A.5.3})$$

in order to define a normalized radiation pattern $P_n(\theta, \phi)$ that is independent of the variable r :

$$P_n(\theta, \phi) \stackrel{\text{def}}{=} \frac{U(\theta, \phi)}{U_{\text{max}}} \quad (\text{A.5.4})$$

It is also convenient to introduce the concept of *isotropic radiator*, i.e. an ideal source that radiates the same amount of power in all directions (this is an obvious abstraction, as such an antenna cannot be built in practice, but it is a useful reference when analyzing the characteristic of actual antennas), i.e. its average power density can be expressed as [132]:

$$\mathbf{S}_{\text{iso}} = \hat{\mathbf{a}}_r \frac{P_{\text{rad}}}{4\pi r^2} \quad (\text{A.5.5})$$

and its radiation intensity as:

$$U_{\text{iso}} = \frac{P_{\text{rad}}}{4\pi} \quad (\text{A.5.6})$$

From equations A.5.3 to A.5.6, the *directivity*⁶ of the antenna can be defined as

$$D(\theta, \phi) = \frac{U(\theta, \phi)}{U_{\text{iso}}} = \frac{4\pi U}{P_{\text{rad}}} \quad (\text{A.5.7})$$

⁵Radiation patterns are often presented in normalized form (i.e. normalized with respect to their maximum) and in decibel scale, to facilitate the view of their characteristics.

⁶Note that the directivity and the gain of antennas are quantities usually defined as a ratio to the corresponding characteristic of an isotropic radiator, therefore they are measured in dBi.

i.e. as the ratio of the radiation intensity in a given direction⁷ to the radiation intensity of an isotropic radiator emitting the same average power P_{rad} . Furthermore, an *antenna gain* can be defined, by introducing the antenna efficiency e_{ant} , as:

$$G(\theta, \phi) \stackrel{\text{def}}{=} e_{\text{ant}} U(\theta, \phi) = e_{\text{ant}} U(\theta, \phi) \quad (\text{A.5.8})$$

where the antenna efficiency is always smaller than 1 and accounts for losses due to mismatch and to conductor or dielectric power attenuation occurring within the antenna structure.

The directivity pattern of antennas generally presents *lobes*, i.e. regions of the solid angle in which the radiation is particularly intense. The main lobe is the one in which the radiation has its maximum and the antenna is generally designed to radiate in that region. The half-power beamwidth (HPBM) is delimited by the points in which the radiated power is the half of that in the maximum direction and measures the ability of the antenna to radiate only in a specific region, an important feature for *sector antennas*. In this cases, the front-to-back ratio (FTBR) is also an important figure of merit, defined as the ration between the power radiated in the maximum directivity direction to the power radiated in the diametrically opposite direction.

When modeling the antenna as a circuit element, it is particularly useful to use the concept of *radiation resistance*, that allows to represent the antenna as a load connected to a transmission line. The radiation resistance is generally a complex quantity, whose real part represents both the radiated fields and the energy lost within the antenna, while its imaginary part represents the energy stored as reactive fields in proximity of the antenna:

$$Z_{\text{ant}} = R_{\text{ant}} + jX_{\text{ant}} = R_{\text{rad}} + R_{\text{loss}} + jX_{\text{ant}} \quad (\text{A.5.9})$$

⁷Note that if no direction is specified, the direction of maximum radiation intensity is implicitly assumed.

Note that point C (corresponding to the center of the WR) in Fig. B.1 is a center of vertical symmetry and can also be used as a reference for the placement of the ground slots and other parts of the transition. In the bottom view, the contour of a WR-12 waveguide is also visible.

B.2 GCPW-to-WR-12 Transition with Bias Tee

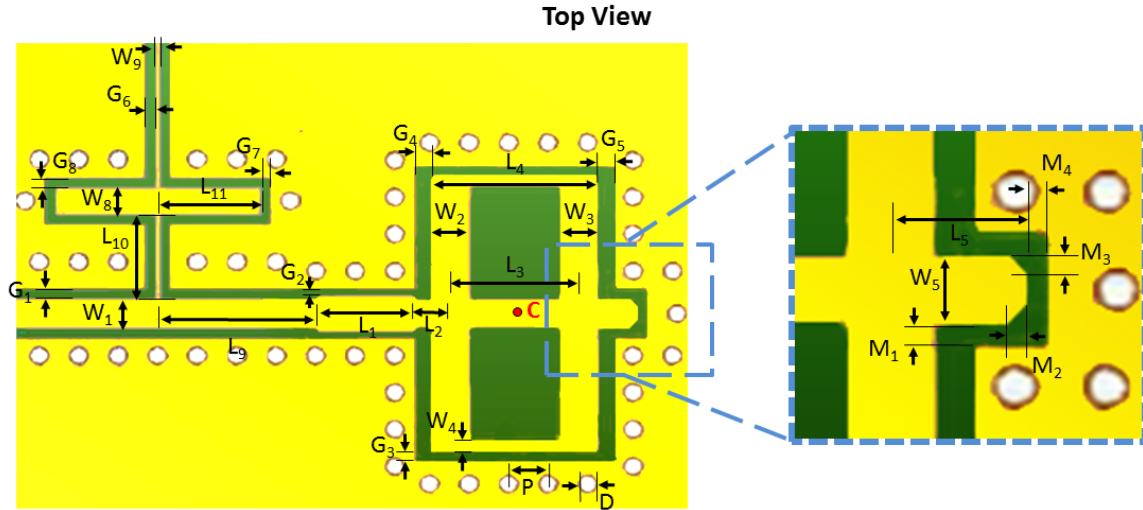


Figure B.2: Layout of GCPW-to-WR-12 transition with bias tee.

With respect to Fig. B.2, the design parameters expressed in μm of the GCPW-to-WR-12 transition with bias tee introduced in section 4.2.1 are:

$$W_1 = 320 \mu\text{m}, W_2 = 410 \mu\text{m}, W_3 = 410 \mu\text{m}, W_4 = 140 \mu\text{m},$$

$$W_5 = 250 \mu\text{m}, W_6 = \mu\text{m}, W_7 = \mu\text{m}, W_8 = \mu\text{m}, W_9 = 100 \mu\text{m}$$

$$L_1 = 1040 \mu\text{m}, L_2 = 350 \mu\text{m}, L_3 = 1300 \mu\text{m}, L_4 = 890 \mu\text{m},$$

$$L_5 = 1300 \mu\text{m}, L_6 = 2500 \mu\text{m}, L_7 = 1500 \mu\text{m}, L_8 = 900 \mu\text{m},$$

$$L_9 = 1530 \mu\text{m}, L_{10} = 850 \mu\text{m}, L_{11} = 1000 \mu\text{m},$$

$$G_1 = 100 \mu\text{m}, G_2 = 60 \mu\text{m}, G_3 = 100 \mu\text{m},$$

$$G_4 = 150 \mu\text{m}, G_5 = 150 \mu\text{m}, G_7 = 100 \mu\text{m}, G_8 = 100 \mu\text{m},$$

$$M_1 = 100 \mu\text{m}, M_2 = 100 \mu\text{m}, M_3 = 100 \mu\text{m}, M_4 = 100 \mu\text{m},$$

$$D = 200 \mu\text{m}, P = 400 \mu\text{m}.$$

Note that point C (corresponding to the center of the WR) in Fig. B.2 is a center of vertical symmetry (with the exception of the RF-choke structure) and can also be used as a reference for the placement of the ground slots and other parts of the transition. The structure of the bottom layer (not shown in Fig. B.2) of the transition and the dimensions of the corresponding elements (W_6 , W_7 , L_6 , L_7 , L_8) are identical to the ones depicted in Fig. B.1 and listed in section B.1.

Appendix C

Layouts of SIW Designs

C.1 GCPW-to-SIW Transition with Tapered Line

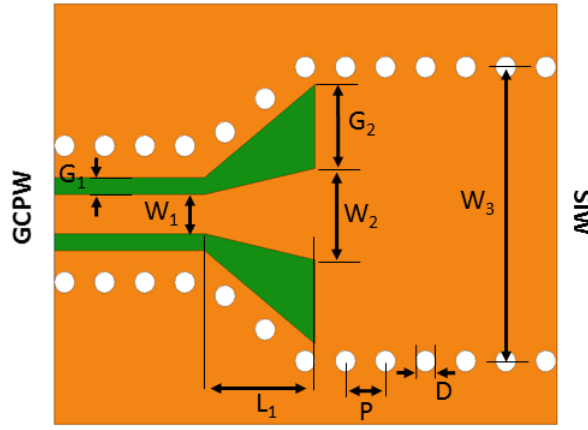


Figure C.1: Layout of tapered GCPW-to-SIW transition.

With respect to Fig. C.1, the design parameters of the GCPW-to-SIW transition with tapered line introduced in section 5.3 are:

$$W_1 = 250 \mu\text{m}, W_2 = 850 \mu\text{m}, W_3 = 3000 \mu\text{m}, L_1 = 1280 \mu\text{m},$$

$$G_1 = 230 \mu\text{m}, G_2 = 900 \mu\text{m}, D = 200 \mu\text{m}, P = 400 \mu\text{m}.$$

C.2 GCPW-to-SIW Transition with Bias-Tee

With respect to Fig. C.2, the design parameters of the GCPW-to-SIW transition introduced in section 5.3.1 are:

$$W_1 = 250 \mu\text{m}, W_2 = 880 \mu\text{m}, W_3 = 420 \mu\text{m}, W_4 = 180 \mu\text{m},$$

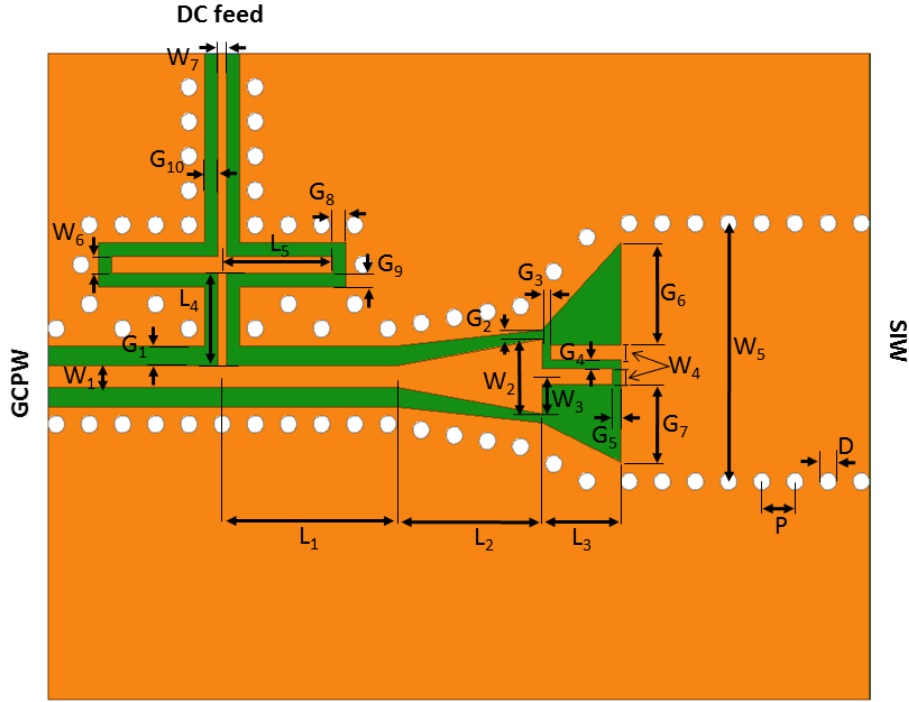


Figure C.2: Layout of GCPW-to-SIW transition with bias tee.

$$W_5 = 3000 \mu\text{m}, W_6 = 190 \mu\text{m}, W_7 = 100 \mu\text{m},$$

$$L_1 = 200 \mu\text{m}, L_2 = 1750 \mu\text{m}, L_3 = 850 \mu\text{m}, L_4 = 1085 \mu\text{m}, L_5 = 1330 \mu\text{m},$$

$$G_1 = 230 \mu\text{m}, G_2 = 100 \mu\text{m}, G_3 = 100 \mu\text{m}, G_4 = 100 \mu\text{m},$$

$$G_5 = 100 \mu\text{m}, G_6 = 1180 \mu\text{m}, G_7 = 900 \mu\text{m}, G_8 = 165 \mu\text{m},$$

$$G_9 = 165 \mu\text{m}, G_{10} = 165 \mu\text{m}, D = 200 \mu\text{m}, P = 400 \mu\text{m}.$$

C.3 Standard H-Plane SIW Horn Antenna

With respect to Fig. C.3, the design parameters of the standard SIW H-plane horn antenna introduced in section 5.4.1 are:

$$W_1 = 3000 \mu\text{m}, W_2 = 6700 \mu\text{m},$$

$$L_1 = 2800 \mu\text{m}, L_2 = 13000 \mu\text{m}, D = 200 \mu\text{m}, P = 400 \mu\text{m}.$$

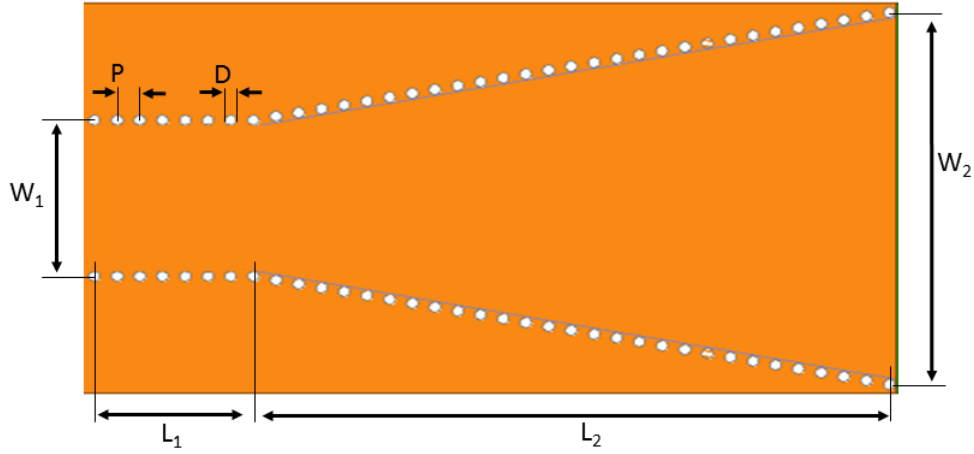


Figure C.3: Layout of standard SIW H-plane horn antenna.

C.4 SIW H-Plane Horn Antennas with Matching Irises

C.4.1 SIW H-Plane Horn Antennas with External Iris

With respect to Fig. C.4, the design parameters expressed in μm of the antenna with external matching iris introduced in section 5.4.2 (page 116) are:

$$L_1 = 2400 \mu\text{m}, W_1 = 1900 \mu\text{m}.$$

All other design parameters are identical to the ones reported in section 5.4.2 for the SIW antenna with two-block transition (page 113).

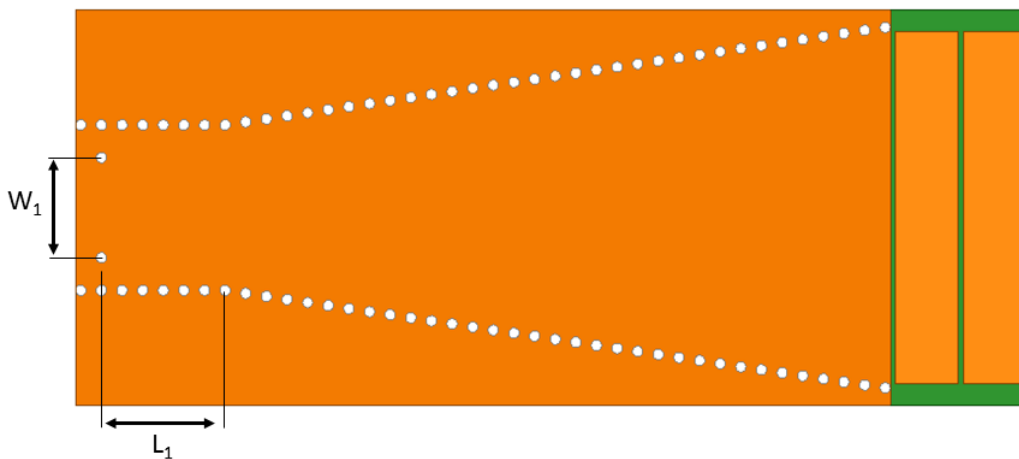


Figure C.4: Layout of SIW H-plane horn antenna with external matching iris.

C.4.2 SIW H-Plane Horn Antennas with Internal Iris

With respect to Fig. C.5, the design parameters of the antenna with internal matching iris introduced in section 5.4.2 (page 116) are:

$$L_1 = 7200 \mu\text{m}, W_1 = 2500 \mu\text{m}, D_{\text{iris}} = 400 \mu\text{m}.$$

All other design parameters are identical to the ones reported in section 5.4.2 for the SIW antenna with two-block transition (page 113).

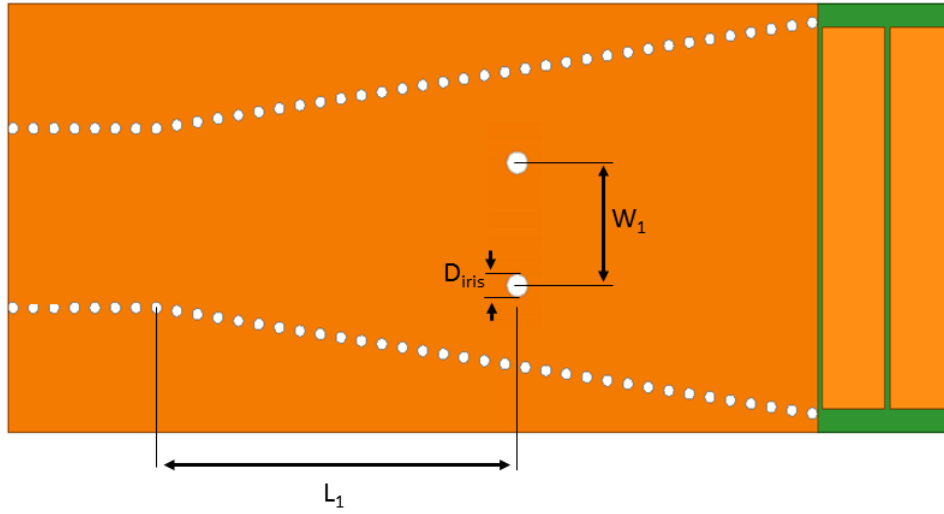


Figure C.5: Layout of SIW H-plane horn antenna with internal matching iris.

Appendix D

Calibration Sets

In some cases, end-launch coaxial connectors commercially available from Southwest Microwave Inc. (series number 1492-01A-5 and 1492-02A-5) have been used to excite a signal on planar transmission lines (GCPW or SIW) in order to perform experimental characterization of the designs presented in this thesis. The transitions from the coaxial connector to the laminate have been based on the guidelines given by the manufacturer [244] and optimized using HFSS [100].

Several Thru-Reflect-Line (TRL) calibration sets have been specifically designed to allow the de-embedding of connectors from the performed VNA measurements. All calibration sets introduced in the following sections have been designed according to the guidelines given in [245].

D.1 Calibration Set 1

The calibration set shown in Fig. D.1 is used to de-embed the effect of the end-launch coaxial connectors from the measurements, setting the reference plane at the GCPW line on 127- μm -thick Rogers RT/duroid 5880 laminates. The *reflect* standard is a short-circuited transmission line (based on grounding via holes).

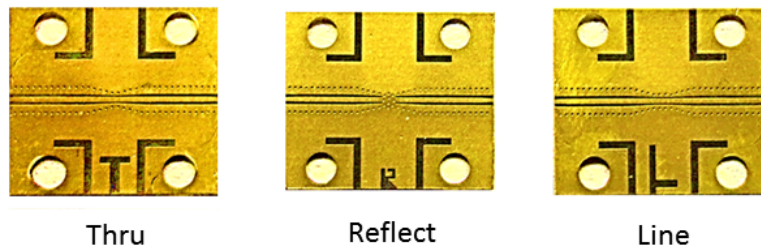


Figure D.1: Calibration set 1.

D.2 Calibration Set 2

This calibration set (shown in Fig. D.2-a) is used to de-embed the effect of the end-launch coaxial connectors from the measurements, setting the reference plane at the GCPW

line on 381- μm -thick Rogers RT/duroid 5880 laminates. The *reflect* standard is a short-circuited transmission line (based on grounding via holes).

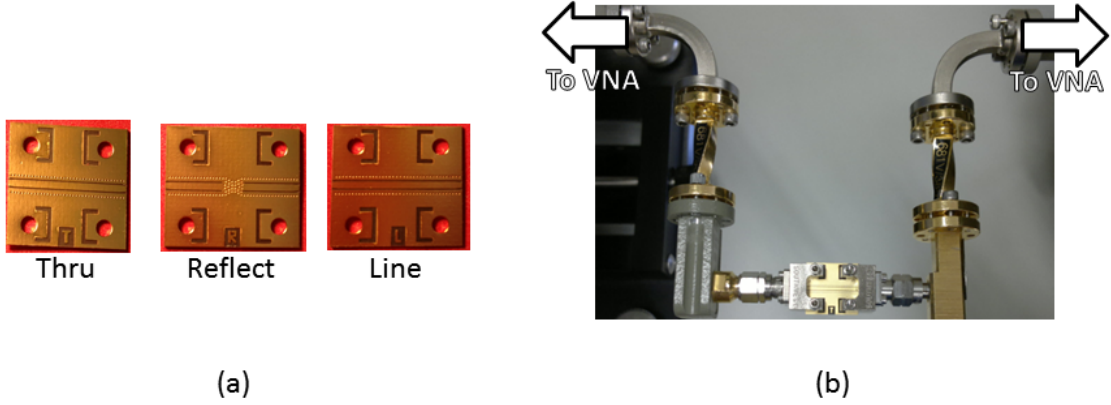


Figure D.2: Calibration set 2 (a) and measurement of the *thru* standard (b).

D.3 Calibration Set 3

This calibration set (shown in Fig. D.3) is used to de-embed the effect of the end-launch coaxial connectors and of the tapered GCPW-to-SIW transition introduced in section 5.3 from the measurements, setting the reference plane at the SIW on 381- μm -thick Rogers RT/duroid 5880 laminates. The *reflect* standard is a short-circuited transmission line (based on grounding via holes).

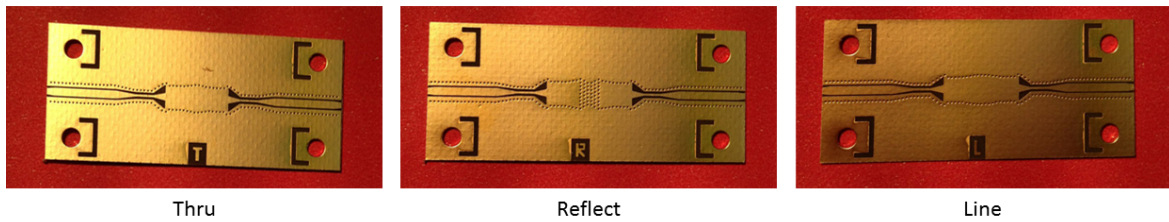


Figure D.3: Calibration set 3.

Biography

Der Lebenslauf ist in der Online-Version aus Gründen des Datenschutzes nicht enthalten.

List of Publications

1. B. Khani, V. Rymanov, S. Dülme, **I. Flammia**, and A. Stöhr. Planar E-band (71-76 GHz) platforms for integrating millimeter wave photodiodes with WR-12 waveguides. *Periodica Polytechnica Electrical Engineering and Computer Science*, 60(1):38–43, 2016.
2. B. Khani, V. Rymanov, **I. Flammia**, and A. Stöhr. Planar 71-76 GHz laminate integration platform for connecting millimeter wave photodiodes to WR-12 waveguides. In *2015 17th International Conference on Transparent Optical Networks (ICTON)*, pages 1–4, 5-9 Jul. 2015.
3. B. Khani, V. Rymanov, **I. Flammia**, M. Miech, and A. Stöhr. Planar bias-tee circuit using single coupled-line approach for 71-76 GHz photonic transmitters. In *German Microwave Conference (GeMIC), 2015*, pages 276–279, 16-18 Mar. 2015.
4. A. Stöhr, O. Cojucari, F. van Dijk, G. Carpintero, T. Tekin, S. Formont, **I. Flammia**, V. Rymanov, B. Khani, and R. Chuenchom. Robust 71-76 GHz radio-over-fiber wireless link with high-dynamic range photonic assisted transmitter and laser phase-noise insensitive SBD receiver. In *Optical Fiber Communication Conference*, OSA Technical Digest (online), page M2D.4, San Francisco, California, 9–13 Mar. 2014. Optical Society of America.
5. **I. Flammia**, B. Khani, and A. Stöhr. Substrate integrated waveguide integration platform for 60 GHz Indoor Photonic Transmitter. In *German Microwave Conference (GeMIC), 2014*, pages 1–4, 10-12 Mar. 2014.
6. **I. Flammia**, B. Khani, S. Arafat, and A. Stöhr. 60 GHz grounded-coplanar-waveguide-to-substrate-integrated-waveguide transition for RoF transmitters. *Electronics Letters*, 50(1):34–35, 2 Jan. 2014.
7. **I. Flammia**, S. Babel, C. C. Leonhardt, J. Honecker, J. Steffan, and A. Stöhr. Novel quasi-hermetic photodiode module featuring an E-band rectangular waveguide (WR-12) output. *Photonics Technology Letters, IEEE*, 25(3):217–219, 1 Feb. 2013.
8. S. Babel, **I. Flammia**, A. Stöhr, J. Montero de Paz, L. E. Garcia-Munoz, D. Segovia-Vargas, G. Carpintero, A. Lisauskas, and O. Cojocari. Compact transmitter and receiver modules for E-band wireless links. In *Optical Fiber Communication Conference and Exposition and the National Fiber Optic Engineers Conference (OFC / NFOEC), 2013*, pages 1–3, 17-21 Mar. 2013.

9. **I. Flammia**, M. Steeg, A. Jankowski, S. Babel, V. Rymanov, and A. Stöhr. Photonic transmitters with rectangular waveguide output for E-Band Radio-over-Fibre communication systems. In *Antennas, Wireless and Electromagnetics, 1st IET Colloquium on*, pages 1–19, 29 May 2013.
10. **I. Flammia**, B. Khani, and A. Stöhr. Substrate integrated waveguide technology for the development of 60 GHz photonic transmitters. In *Antennas, Wireless and Electromagnetics, 1st IET Colloquium on*, pages 1–19, 29 May 2013.
11. **I. Flammia**, B. Khani, and A. Stöhr. A novel transition from grounded coplanar waveguide to substrate integrated waveguide for 60 GHz Radio over-Fiber photonic transmitters. In *Microwave Techniques (COMITE), 2013 Conference on*, pages 73–76. IEEE, 17–18 Apr. 2013.
12. **I. Flammia**, B. Khani, and A. Stöhr. Substrate integrated waveguide antenna for 60 GHz Radio-over-Fiber transmitter. In *2013 38th International Conference on Infrared, Millimeter, and Terahertz Waves (IRMMW-THz)*, pages 1–2, 1-6 Sept. 2013.
13. **I. Flammia**, T. Kleinfeld, M. Frei, A. Utreras-Rivera, and A. Stöhr. 71-76 GHz grounded-coplanar-waveguide-to-rectangular-waveguide transition with integrated planar bias tee for quasi-hermetic Radio-over-Fiber wireless transmitter. In *Microwave Integrated Circuits Conference (EuMIC), 2012 7th European*, pages 512–515, 29-30 Oct. 2012.
14. **I. Flammia**, S. Babel, C. C. Leonhardt, J. Honecker, A. G. Steffan, and A. Stöhr. Quasi-hermetic photodiode module featuring a WR12 output for 71-76 GHz Radio-over-Fiber applications. In *Microwave Photonics (MWP), 2012 International Topical Meeting on*, pages 261–264, 11-14 Sept. 2012.
15. **I. Flammia**, A. Stöhr. Quasi-hermetic photonic transmitter with WR12-output for Radio-over-Fiber applications In *Marie Curie Actions, ESOF 2012*, Dublin, Ireland, 10- 15 Jul. 2012.
16. **I. Flammia**, A. Stöhr, C. C. Leonhardt, J. Honecker, and A. G. Steffan. 71-76 GHz grounded CPW to WR-12 transition for quasi-hermetic RoF wireless transmitter. *Electronics Letters*, 48(9):506–508, 26 Apr. 2012.
17. A Jankowski, V. Rymanov, **I. Flammia**, S. Babel, A. Garcia, and A. Stöhr. Optical THz generation and its applications. In *Photonics Event 2012, Safe and Security and Session*, Nieuwegein, The Netherlands, 27–28 Mar. 2012.
18. **I. Flammia**. Design and evaluation of millimeter-wave photonic transmitter modules for Radio-over-Fiber applications. In *Winter College on Optics: Advances in Nano-Optics and Plasmonics, LAMP Seminar Series - Session II*, Miramare - Trieste, Italy, 6 - 17 Feb. 2012.

-
19. **I. Flammia**, C. C. Leonhardt, J. Honecker, A. G. Steffan, and A. Stöhr. Novel E-Band (71-76 GHz) photodiode module featuring a hermetic grounded-coplanar-waveguide-to-rectangular-waveguide transition. In *Microwave Photonics, 2011 International Topical Meeting on & Microwave Photonics Conference, 2011 Asia-Pacific, MWP/APMP*, pages 405–408. IEEE, 18-21 Oct. 2011.